

Analysis of Adiabatic Frequency Conversion and Polarization Coupling in Integrated Lithium Niobate Resonators

by

Luis Enrique Cortés Herrera

Submitted in Partial Fulfillment of the

Requirements for the Degree

Doctor of Philosophy

Supervised by

Govind P. Agrawal

The Institute of Optics

Arts, Sciences and Engineering

Edmund A. Hajim School of Engineering and Applied Sciences

University of Rochester

Rochester, New York

2024

Dedicated to my dad, mom, and brother

Table of Contents

Biographical sketch	vii
Acknowledgments	ix
Abstract	xi
Contributors and funding sources	xiii
1 Introduction	1
1.1 Overview of electro-optical frequency conversion	1
1.2 Overview of adiabatic frequency conversion	3
1.3 Thesis outline	5
2 Spatial coupled-mode theory	7
2.1 Motivation for coupled-mode theories	7
2.2 Maxwell' equations and the constitutive relations	8
2.3 Decomposition of Maxwell's curl equations into longitudinal and transverse components	9
2.4 Propagation equation for the transverse fields	10
2.5 Derivation of the coupled-mode equations	12
3 Temporal coupled-mode theory	13
3.1 Derivation of the coupled-mode equations	13
3.2 Coupled-mode description of AFC	16
3.3 Coupling between two discrete resonant modes	18
3.4 Coupling between resonant mode and waveguide	19
3.5 Input-output analysis of resonator-waveguide coupling	21
4 Polarization dynamics in a uniaxial ring resonator	27
4.1 Intuitive description and the zero-bending model	27
4.2 Polarization coupling in the ZBM	29
4.2.1 Perturbation due to permittivity reorientation	29
4.2.2 Resonance condition for microring resonators	30
4.3 Approximate Analytic Solution of Coupled-Mode Equations	30
4.3.1 Simplification of the coupled-mode equations	30
4.3.2 Analysis of the simplified coupled-mode equations	31
4.3.3 Perturbative regime	33
4.3.4 Resonant regime	34
4.3.5 Adiabatic regime	35
4.4 A Practical Example	36
4.4.1 Local effective indices and comparison with FEM calculations	36
4.4.2 Influence of slab thickness	40
4.4.3 Polarization evolution along the microring	41
4.5 Conclusions	42

5	Oblique uniaxial waveguide as a polarization rotator	45
5.1	Proposed design and SCMT analysis	46
5.1.1	Polarization rotator geometry	46
5.1.2	CMT-based design of the tilted segment	47
5.1.3	Residual crosstalk due to finite curvature at the joints	48
5.1.4	Differences between configurations	48
5.2	Numerical analysis of a LNOI rotator	49
5.2.1	Polarization parameters and tilt-segment orientation	49
5.2.2	Effective coupling coefficient and rotator bandwidth	50
5.2.3	Residual crosstalk due to finite curvature at the joints	52
5.3	Conclusion	53
6	AFC in an all-pass resonator	55
6.1	Analysis of the governing equations	55
6.2	Upper limit on the Energy Efficiency	57
6.3	Pulsed input of fixed shape	59
6.3.1	Partial parameter sweeps	60
6.3.2	Global parameter sweep	61
6.4	Continuous-wave input	63
6.5	Conclusion	65
6.6	Justification for the condition in Eq. (6.8)	65
7	Simultaneous AFC in coupled rings	67
7.1	Description of the photonic circuit and the AFC linear operator	67
7.2	Inner-product analysis of the AFC linear operator and its efficiencies	70
7.3	AFC matrix representation and singular value decomposition	73
7.4	Numerical analysis of the two-ring impulse-response functions	76
7.5	Numerical SVD of the loading and unloading maps	80
7.6	Numerical SVD of the AFC operator	86
7.7	Efficiency analysis of AFC of a symmetric single-lobe pulse	88
7.8	Conclusion	95
8	Cascaded AFC in coupled rings	97
8.1	Description of the photonic circuit and coupled-mode equations for CAFC	98
8.2	Description of a sample CAFC process	100
8.3	Inner-product analysis of the CAFC efficiency	102
8.3.1	Limit of large inter-ring detuning	104
8.4	Optimization of the CAFC timescales	105
8.5	Convergence analysis of the CAFC efficiency	109
8.6	Modeling of the CAFC efficiency as a polynomial function	115
8.7	Conclusion	118
9	Conclusion and future work	121
9.1	Conclusion	121
9.2	Future work	122
A	Guided modes and coupling coefficients of the uniaxial slab	125
A.1	Guided modes along principal axes of the asymmetric birefringent slab	125
A.1.1	Transverse-electric modes	125
A.1.2	Transverse-magnetic modes	127
A.2	Matrix elements of perturbation for the uniaxial dielectric slab	129
A.2.1	Out-of-plane slab	130
A.2.2	In-plane slab	131

B	Quantum-inspired analyses of polarization coupling	133
B.1	Resonant polarization coupling	133
B.1.1	Simplified case of constant detuning	134
B.2	Berry phase for the in-plane slab ring	135
B.3	Crosstalk due to polarization coupling along the curved joints	136
C	Mathematical expressions and analyses for the SVD of simultaneous AFC	139
C.1	Characterization of the impulse-response functions	139
C.2	Gram-Schmidt orthonormalization of AFC image and coimage	142
C.3	Partial analytical SVD of the loading and unloading matrices	144
C.4	Proof of submultiplicative property of maximum and minimum singular values	145
D	Quantum-optical description of AFC in coupled microrings	149
D.1	Hamiltonian and constants of the motion	149
D.2	General input-output formalism	150
D.3	Input-output analysis of a coherent waveguide state	152
E	Analytical expression for the CAFC output	155
E.1	Exact solution for piece-wise constant detuning	155
E.2	Output before modulation	156
E.3	Output during modulation	157
E.4	Output after modulation	158
F	Mathematical description and optimization of CAFC	159
F.1	Analysis of the complex-valued frequency splitting for large inter-ring detuning	159
F.2	Optimization of the duration of inter-ring energy exchange	160
F.3	Analytical optimization of the input bus coupling	163
F.4	Expression for frequency-converted energy under finite inter-ring detuning	166
F.5	Output bus coupling efficiency in the high-modulation limit	167
G	Analyticity of the CAFC efficiency	169
G.1	Derivation of the polynomial model for the CAFC efficiency	169
G.2	Sufficient conditions for the real analyticity of the CAFC efficiency	171
H	Efficiency limit of serial AFC	173
	Bibliography	174

Biographical sketch

The author was born in Monterrey, Nuevo León, Mexico. He attended the Instituto Tecnológico y de Estudios Superiores de Monterrey (ITESM) and graduated with a Bachelor of Science degree in Physics Engineering in December of 2015. During his undergraduate studies, he spent the summers of 2014 and 2015 performing theoretical and numerical research in Professor Anthony Hoffman's group at University of Notre Dame on chaotic ray dynamics in rotationally asymmetric multipass cells. In Fall of 2016, he enrolled in a Masters program at ITESM. During this program, he worked with Professor Israel de León in the theoretical and numerical modelling of the temporal dynamics of the non-linear response of indium tin oxide in its epsilon-near-zero wavelength regime due to intraband electronic absorption. He graduated with a Masters of Science degree in Electronics Engineering summa cum laude in May of 2018.

The author began his doctoral studies in Optics at the University of Rochester in Fall of 2018. He joined Professor Govind Agrawal's Nonlinear Photonics group in November of 2018. In Professor Agrawal's group, the author investigated the theoretical modeling and engineering of optical processes in integrated photonics. In collaboration with Professor Jaime Cardenas and his doctoral student Xiaotong He, and under the supervision of Professor Agrawal, the author researched polarization coupling and adiabatic frequency conversion in lithium-niobate-on-insulator ring resonators.

The following publications were a result of work conducted during the author's doctoral study:

Peer-reviewed journal articles

Luis Cortes-Herrera, Xiaotong He, Jaime Cardenas, and Govind P. Agrawal. Coupled-mode theory of the polarization dynamics inside a microring resonator with a uniaxial core. *Physical Review A*, 103(6):063517, 2021.

Luis Cortes-Herrera, Xiaotong He, Jaime Cardenas, and Govind P. Agrawal. Design of an X-cut thin-film lithium niobate waveguide as a passive polarization rotator. *Optics Express*, 29(26):44174–44188, 2021.

Luis Cortes-Herrera, Xiaotong He, Jaime Cardenas, and Govind P. Agrawal. Optimization of adiabatic frequency conversion in an all-pass resonator. *Physical Review A*, 106(2):023517, 2022.

Luis Cortes-Herrera, Xiaotong He, Jaime Cardenas, and Govind P. Agrawal. Theory of high-efficiency adiabatic frequency conversion in coupled microrings. *Physical Review A*, 108(6):063514, 2023.

Luis Cortes-Herrera, Xiaotong He, Jaime Cardenas, and Govind P. Agrawal. Proposal and efficiency analysis of cascaded adiabatic frequency conversion in coupled microrings. *Physical Review A*, 109(6):063510, 2024.

Contributed conference presentations

Luis Cortes-Herrera, Xiaotong He, Jaime Cardenas, and Govind P. Agrawal. Coupled-mode theory of the polarization dynamics inside a microring resonator with a uniaxial core. In *Conference on Lasers and Electro-Optics*, page STu1F.6. Optica Publishing Group, 2021.

Luis Cortes-Herrera, Xiaotong He, Jaime Cardenas, and Govind P. Agrawal. Optimization of adiabatic frequency conversion in an all-pass resonator. In *Frontiers in Optics + Laser Science 2022 (FIO, LS)*, page JW4A.57. Optica Publishing Group, 2022.

Luis Cortes-Herrera, Xiaotong He, Jaime Cardenas, and Govind P. Agrawal. Passive polarization rotator in thin-film lithium niobate. In *Frontiers in Optics + Laser Science 2022 (FIO, LS)*, page JW4A.58. Optica Publishing Group, 2022.

Luis Cortes-Herrera, Xiaotong He, Jaime Cardenas, and Govind P. Agrawal. Cascaded adiabatic frequency conversion in coupled lithium niobate microring resonators. In *Conference on Lasers and Electro-Optics*, page JW2A.74. Optica Publishing Group, 2023.

Acknowledgments

I wish to thank some of the numerous people who supported me throughout my doctoral studies.

I am very thankful to my doctoral advisor, Professor Govind Agrawal, for granting me the opportunity to be a member of his Nonlinear Photonics Group at the Institute of Optics. He has been a great professional mentor. He is always willing to listen to my concerns and provide advise either about my research or my professional career in general. I appreciate the trust and support he has given me as a researcher.

I am grateful to Professor Jaime Cardenas of the Institute of Optics. The work of this thesis was part of a collaboration between Prof. Cardenas and Prof. Agrawal's groups; and Prof. Cardenas often demonstrated interest and support for my work. Though often busy, Prof. Cardenas always made sure to set time to discuss my research with me, despite not being directly under his supervision. I admire that he genuinely cares about helping his students improve their professional skills.

I am thankful to my fellow members of Prof. Agrawal's Nonlinear Photonics Group. I thank Dr. Aku Antikainen for welcoming me into the group in my first year. Though we interacted only briefly, I truly appreciate his amicability. I am grateful to Dr. Amira Ahsan. She was always glad to share her with me her professional experience and advice. Lastly, I am thankful to Junchi Zhang. He overlapped the most with me in our time in Prof. Agrawal's group, so we shared many experiences. I am grateful for our many discussions about optics, physics, and research in general.

I am also grateful to many fellow doctoral students outside of Prof. Agrawal's group. I am thankful to Dr. Xiaotong He, former member of Prof. Cardenas's group, who shared with me her insight from experimental experience as we worked on our research project. I am thankful to Samuel Arroyo, member of Prof. Boyd's group, who shared with me the victories and setbacks of his own work. I am thankful to Dr. Alexis Sparapani, former member of Prof. Diego Grosz's group at Instituto Balseiro, who shared with our group his fresh perspective on research from the other end of the globe.

I thank Professor Qiang Lin of the Department of Electrical and Computer Engineering and Professor Machiel Blok of the Department of Physics and Astronomy for serving as member and chair, respectively, of my thesis committee. I recognize their work is completely voluntary, yet absolutely essential for my thesis defense to take place.

I am thankful to the faculty outside of University of Rochester who have motivated me to pursue a career in optics and photonics. In particular, I would like to thank Professor Israel de León and Professor Sergio Camacho from Instituto Tecnológico y de Estudios Superiores de Monterrey (ITESM) and Professor Anthony Hoffman from the University of Notre Dame.

In general, I am grateful to the faculty and staff at the Institute of Optics. They made me feel welcome and invited to delve into the intriguing world of optics and photonics. In particular, I am thankful to Kai Davies, Optics's Graduate Program Coordinator. They were always happy to lend me a hand any time I needed help navigating the administrative side of the university.

Last but not least, I am thankful to my father, mother, and brother. Their unconditional trust and support gave me confidence to continue my work.

Abstract

Adiabatic frequency conversion (AFC) is a promising mechanism for integrated, electro-optical, tunable frequency shifting. AFC is the phenomenon in which light excites an optical cavity, the cavity's refractive index is modulated, and light follows the cavity's instantaneous resonance frequency. To realize electro-optical AFC, we propose the material platform of lithium-niobate on insulator (LNOI), which enables high-quality, electro-optically tunable ring resonators. Our objective is to analyze and optimize electro-optical AFC in LNOI ring resonators.

As a preliminary, we study polarization coupling in a LNOI ring resonator induced by lithium niobate's material anisotropy using spatial coupled-mode theory. We show that the resulting equations are isomorphic to the Schrödinger equation describing an optically driven two-level atom modulated sinusoidally in frequency. We leverage this isomorphism to characterize the polarization-coupling dynamics. As a corollary, we design a polarization rotator consisting of a straight LNOI waveguide at an oblique angle with lithium niobate's optical axis.

We analyze the energy efficiency of AFC in a single ring resonator utilizing temporal coupled-mode theory. We show the AFC efficiency depends on the inner product of the input pulse and the resonator's time-reversed impulse-response, and it is thus limited through a Schwarz inequality. We show that the AFC efficiency for a symmetric, single-lobe (SSL) pulse has a maximum of 80%. This limit is a consequence of the mismatch between the SSL input and the ideal input for 100% AFC efficiency.

We propose two extensions of single-ring AFC. First, we propose inducing AFC simultaneously over two coupled rings to overcome the efficiency limit of 80% for a SSL input. We show that simultaneous AFC over two rings can attain an energy efficiency of 97% for a SSL input. To explain this result, we analyze two-ring AFC as a linear operator, and we examine its singular value decomposition. Second, we propose inducing cascaded AFC along a chain of coupled, yet initially detuned rings. We show that the energy efficiency of cascaded AFC depends on the input pulse shape through a Schwarz inequality, just as in single-ring AFC. We show that this maximum efficiency is identical to that for single-ring AFC.

Contributors and funding sources

This work was supported by Professor Govind P. Agrawal of the Institute of Optics as thesis advisor, along with Professor Jaime Cardenas of the Institute of Optics and Professor Qiang Lin of the Department of Electrical and Computer Engineering as thesis committee members. Portions of this dissertation have been published elsewhere. The publications were co-authored with Professor Govind P. Agrawal, Professor Jaime Cardenas, and Dr. Xiaotong He. All co-authors assisted with manuscript editing. Dr. Xiaotong He also obtained the numerical finite-element-method data used for Figure 4.3. The material is based on work supported by the National Science Foundation under Grant No. ECCS-1807735 and by Mexico's National Council of Science and Technology (CONAHCYT).

Chapter 1

Introduction

This chapter contains the thesis's introduction. In Section 1.1, we motivate the investigation of integrated electro-optically induced frequency conversion of optical signals and we discuss various physical mechanisms which have been proposed to realize it. In Section 1.2, we introduce adiabatic frequency conversion, the physical mechanism for frequency conversion analyzed in this thesis. In Section 1.3, we present the outline of the remaining chapters of this thesis.

1.1 Overview of electro-optical frequency conversion

In photonics, frequency conversion is usually achieved via wave mixing, mediated by a nonlinear polarization response [1–3]. In particular, the advent of integrated photonics has spurred broadband, high-efficiency wave mixing in a compact footprint [4–7]. Integrated wave mixing offers two critical advantages over its free-space counterpart. First, the high confinement in integrated systems drastically enhances the optical intensity, which leads to more efficient nonlinear interaction. Second, in integrated wave mixing, modal dispersion can be engineered to extend the frequency-conversion bandwidth by tuning the waveguide geometry.

Despite the successes of integrated wave mixing, it has three inherent limitations [1–3]. First, it demands a high-power optical pump, which impedes on-chip integration. Second, wave mixing must obey conservation of photon energy. Hence, to change the output signal frequency, one must change either the pump frequency or the input signal frequency. Evidently, this merely displaces the problem of frequency conversion. Third, efficient wave mixing requires phase matching. This requirement restricts both the waveguide geometry and the range of possible output frequencies.

An ideal frequency converter would be integrable, tunable, electrically controlled, and would not necessitate an optical pump or phase matching. Ideally such a device would operate based on the linear electro-optic (EO) effect, also known as the Pockels effect. This is mainly because of two reasons. First, the Pockels effect typically exhibits remarkably short response time. In lithium niobate, for instance, the Pockels effect has a response time in the femtosecond scale [8]. Second, modulation via the Pockels effect introduces no additional optical losses, in contrast to, for example, modulation via charge-carrier injection [9, 10]. Such an EO frequency converter could transform network routing in optical telecommunication by enabling efficient channel switching and tuning of light beyond a laser's gain bandwidth.

On-chip EO frequency shifting can be realized via modulation of light in waveguides or resonators. First, we discuss the former and then the latter. The main advantage of realizing EO frequency-shifting in waveguides compared to resonators is that waveguides are non-resonant devices. So the optical input to frequency-shift is, in principle, unrestricted in frequency. Consequently, waveguide-based EO shifting may achieve a large bandwidth, restricted mostly by waveguide dispersion. The main disadvantage is that, similar to static non-resonant phase modulators [11], non-resonant EO frequency shifting requires long waveguides and electrodes so the EO modulation can accumulate upon propagation. Clearly, this hinders the goal of compact on-chip integration. Furthermore, large electrodes generally result in a larger electrical capacitance. This implies a larger RC circuit time constant and slower possible electrical modulation. Waveguide-based EO frequency shifting can be engineered under two different approaches: sideband generation and spectral shearing.

In sideband generation [12, 13], the optical waveguide is modulated by a (stationary or traveling) sinusoidal electrical control of frequency Ω and simultaneously excited by an optical wave of bandwidth smaller than Ω . As a result, the input optical power is distributed in a frequency comb, consisting of a series of sidebands [14] separated in frequency by the modulation frequency Ω . In the framework of nonlinear wave-mixing [3], this process can be understood as a cascade of sum-frequency and difference-frequency generation processes which are all simultaneously phase-matched due to the smallness of the electrical frequency modulation relative to the bandwidth at which optical group velocity dispersion is appreciable [14]. Usually, the excitation of more than one output sideband is undesirable. A scheme to partially suppress these undesired sidebands consists of splitting the signal into four waveguide arms, inducing sideband generation over each arm, and recombining the output of each one. If the phase of the optical wave and the modulation amplitude of each arm are set correctly, three of every four sidebands can be suppressed via destructive interference [12, 13]. This approach to EO frequency shifting has several limitations. Most obviously, the input power is distributed over a theoretically-infinite set of sidebands. Even with the interference-based scheme for sideband suppression, only a small fraction of power can be transferred to a single sideband, with a theoretical maximum of 33.81% [12, 13]. Furthermore, as mentioned above, the input optical bandwidth must be smaller than the electrical modulation frequency Ω .

Spectral shearing [15, 16] is an alternative to sideband generation for EO waveguide-based frequency shifting. For spectral shearing, the applied electrical control varies linearly in time, rather than oscillate sinusoidally like in sideband generation. As a consequence, an optical pulse propagating along the waveguide is subject to a propagation constant that increases in time, resulting in a frequency shift [15]. In contrast to sideband generation with an upper efficiency limit of 33.81%, spectral shearing has the advantage that it can theoretically achieve 100% efficiency. Nonetheless, spectral shearing has its own set of limitations. Naturally, the electrical control cannot increase indefinitely in amplitude. Thus, this linear modulation must have a start time and an end time. Consequently, the optical input for spectral shearing is necessarily pulsed and the EO modulation must be synchronized with the input optical pulse. Furthermore, the modulation's rise time must be large compared to the input pulse duration for the whole pulse to undergo the frequency shift. Yet the rise time must be comparable to the propagation time of the pulse in the waveguide for a large frequency shift to accumulate [15]. Hence the waveguide used needs to be long enough for the pulse's propagation time to be large compared to the pulse's duration. Lastly, deviation from linearity in time of the increase of the electrical signal results in distortion of the frequency-shifted output [15].

Compared to waveguide-based frequency-shifting, resonator-based frequency-shifting has its own advantages and disadvantages. The clearest advantage is that resonator-based shifting can be achieved with a smaller footprint, which allows for easier on-chip integration. Additionally, a smaller footprint generally results in a smaller capacitance for the electrical drive, and hence a smaller RC time constant and faster electrical control. Another feature is that the response of optical resonators is frequency-selective. This can be leveraged for frequency-multiplexing frequency shifts, i.e., selectively applying frequency shifts among different optical frequency channels in a common waveguide. Relative to waveguide-based shifting, a disadvantage of resonator-based shifting is that it requires coupling of light to a resonator normal mode, which is efficient only for narrowband optical inputs. Furthermore, the frequency-shifted output is also similarly narrowband. Lastly, resonator-based shifting requires EO-driven resonators with high intrinsic quality, which are challenging to fabricate [11, 17].

Resonator-based EO frequency conversion can be accomplished with either a sinusoidal or monotonic modulation. Conversely, frequency conversion with sinusoidal modulation can be done on a single resonator or on multiple coupled resonators. Frequency conversion via sinusoidal modulation of a single resonator can be accomplished in the following way [18]. One couples continuous-wave light into a resonator of static resonance frequency ω_0 through a bus waveguide while the resonator is modulated sinusoidally with frequency Ω . Then, the modulated resonator acts as a scattering element, accepting narrowband inputs at the frequencies $\omega_0 + j\Omega$ for integer j , and scattering them among these same frequencies. Hence, continuous-wave light resonant with any one of the frequencies $\omega_0 + j\Omega$ scatters into the infinite set of sidebands. This scheme is then analogous to the aforementioned scheme of sideband generation via sinusoidal modulation of a waveguide [12–14]. The advantage of this scheme is that it is simple to implement, as it requires only a single resonator and single-tone sinusoidal modulation. The disadvantage is that, as in waveguide-based sideband generation, the output consists of an infinite set of sidebands. Hence, the scheme is inefficient and requires filtering, as one is usually interested in a single-sideband output.

Alternatively, one can induce frequency conversion via sinusoidal modulation of two coupled resonators, rather than one single resonator [8, 19]. In this approach, two identical resonators are strongly coupled, with a coupling rate larger than their decay rates. Hence, they can be described as a photonic molecule, with two resonant supermodes, i.e., a symmetric supermode, where the resonator amplitudes are in phase, and an anti-symmetric supermode, where the

resonator amplitudes are out of phase. Then, the resonators are modulated at the same frequency, but with opposite electrical amplitudes. If the modulation frequency equals the frequency difference between the supermodes, then light in the molecule undergoes Rabi oscillation between the supermodes. The system is analogous to a two-level atom driven by a resonant optical field [20], with the photonic molecule acting as the atom; and the applied electric field, as the resonant optical field. Resonant modulation of a photonic molecule has its relative advantages and disadvantages. Compared to sinusoidal modulation of a single ring, the clearest advantage is that inter-ring coupling suppresses most sideband generation. Thus, in contrast to the single-ring case, resonant modulation of the molecule can theoretically reach 100%. Furthermore, under this scheme a large frequency shift (equal to the supermode splitting) can be obtained with small modulation strength, so long as the modulation is approximately resonant. Its disadvantages are mainly two. First, the magnitude of frequency shift is set by the supermode splitting, i.e., the inter-ring coupling rate. Thus it is not dynamically tunable, but fixed upon device fabrication. Second, Rabi oscillation between the supermodes only occurs when the rotating wave approximation (RWA) [20, 21] is accurate. In this case, the RWA only holds for when the modulation amplitude is small compared to the supermodes' splitting. This limitation constrains frequency conversion time or bandwidth, as we explain below.

So far, two approaches have been proposed to leverage Rabi oscillation in a photonic molecule for optical frequency conversion [8, 19]. They mainly differ in when the input light is injected with respect to the electro-optical modulation. In the first approach [8], light is injected into one of the supermodes of the photonic molecule. Then the molecule is modulated with an electrical π -pulse to take it to the state orthogonal to the initial one. The advantage of this approach is that is suitable for pulsed optical inputs, as then the duration of Rabi oscillation can be tailored to optimize the energy in the target output supermode. Conversely, a disadvantage is that it is unsuitable for a continuous-wave input, as once the π -pulse ends, no further input power can be frequency-shifted. A second disadvantage is that Rabi oscillation requires finite time, inversely proportional to modulation strength. Furthermore, the RWA restricts the modulation strength to small values compared to the supermodes' frequency splitting. Thus, this approach fundamentally requires a non-zero modulation time and hence higher intrinsic-quality resonators, which may restrict the use in fast processing for optical telecommunications. Finally, to apply this scheme to optical pulses, the modulation needs to be synchronized with the arrival of the optical pulse to the resonator.

In the second approach [19], the photonic molecule is constantly modulated: before, during, and after the arrival of the optical input. Then, as in single-ring modulation, the photonic molecule acts as a scattering element (or beam splitter), now scattering inputs at the supermode frequencies into each other. Compared to the first approach, this beamsplitter scheme has the advantages that it requires no synchronization with respect to the optical input and that it can be applied to continuous-wave inputs. A disadvantage, however, is that the frequency-conversion bandwidth is now further constrained. For complete frequency conversion, the detuning between the input and the initial supermode must be small compared to the modulation strength [19]. However, the RWA constrains the modulation strength to small values compared to the supermode splitting. Hence, the optical bandwidth for this scheme is vastly smaller than the supermode splitting for this beam-splitter approach to be efficient.

As mentioned above, EO frequency shifting can also be accomplished by monotonic (rather than sinusoidal) modulation of a single optical resonator or set of coupled resonators. This modulation scheme results in adiabatic frequency conversion [10, 22, 23], which is the focus of this thesis and is discussed in the following section.

1.2 Overview of adiabatic frequency conversion

Adiabatic frequency conversion (AFC) is a promising mechanism for frequency shifting. AFC is the phenomenon in which light excites an optical cavity's mode, the cavity's refractive index is modulated, and light follows the cavity's instantaneous resonance frequency [22, 24]. This process is called adiabatic because it was numerically shown [22] that it preserves the adiabatic invariant U/ω of the harmonic oscillator [25, 26], where U is the mode's energy and ω is the mode's frequency. However, AFC need not occur adiabatically, i.e., slowly. In fact, AFC occurs as rapidly as the cavity modulation. If n is the cavity's refractive index before modulation and Δn is the change in refractive index achieve after modulation, the change $\Delta\omega$ in frequency ω is given by $\Delta\omega = -\omega(\Delta n)/n$ [22, 23].

To observe AFC in a dynamically modulated cavity, there exist three criteria [22, 23]. First, coupling to other cavity modes must be inhibited [27]. This occurs either when the cavity's modulation is spatially homogeneous or when modulation is slow compared to the difference in the modes' frequencies. Second, the cavity modulation must occur over a time shorter than the cavity's photon lifetime τ_{ph} . Otherwise, just a small fraction of the original energy

actually undergoes the frequency shift. Third, the shift in resonance frequency must be larger than τ_{ph}^{-1} . Otherwise, the shift in frequency cannot be resolved. This last criterion implies that AFC can only occur in cavities with high quality factor (Q). For this reason, AFC has only begun attracting attention in the past two decades [22, 28]. In contrast to nonlinear wave mixing, AFC does not require either an optical pump or phase matching. Furthermore, being a resonator-based approach to frequency-shifting, it is highly compact. Lastly, in contrast to EO frequency-shifting based on photonic-molecule modulation, the output frequency can be tuned by adjusting the strength of modulation to the cavity. Hence, AFC can be used to realize integrated, tunable frequency conversion.

AFC has been demonstrated in on-chip silicon cavities [10, 29–31] and semiconductor-based metasurfaces [32]. For these demonstrations, the cavities were modulated via charge-carrier injection in the following manner: a short and strong optical pulse was focused into the silicon cavity, its power was absorbed, and charge carriers were generated upon optical absorption. The effect was also demonstrated by electrical injection of carriers through a p-i-n junction [28]. The demonstrations based on optically-induced carrier injection are impractical and can only be considered proofs of principle. This is because they use a strong optical pump, focused from outside the chip. Evidently, packaging of the pump and focusing elements limits the scalability of these systems. Additionally, the use of carrier-injection limits the repetition rate of AFC. This is because injected carriers diffuse slowly [33], so cavity takes a long time to return to its original state. AFC has also been induced in a silica toroidal cavity via the optical Kerr effect [33]. Though this approach is lossless and has a high repetition rate, it still requires the use of an optical pump. Hence, the resulting device cannot be fully integrated on-chip.

For this research, we propose and analyze novel techniques for electro-optical (EO) AFC, induced via the Pockels effect. This approach is ideal for on-chip integration, due to several reasons. First and most evidently, the Pockels effect is induced electrically. Thus AFC induced via the Pockels effect can be manipulated through an easily tunable electrical control, rather than a high-power optical pump of fixed frequency. As a result, fine and tunable control can be exerted over the the output frequency. Second, the Pockels effect typically possesses a remarkably short response time as mentioned above. This feature is critical because AFC is energy-efficient only if it is performed in a timescale shorter than the cavity mode’s photon lifetime, as discussed previously. Third, in contrast to carrier injection, modulation via the Pockels effect induces no additional optical loss. Therefore, AFC induced via the Pockels effect is fundamentally more energy-efficient than that induced via carrier-injection. Fourth, EO AFC can be controlled by compact electrodes placed around the modulated cavity. This allows multiple cavities with separate electrodes to be coupled. Thus, AFC can be performed independently in each cavity to effectively control the coupling between neighboring cavities by tuning the frequency-mismatch between them. AFC induced through the Pockels effect has been demonstrated in a bulk, lithium niobate, whispering-gallery mode resonator [34], yielding shifts of 5 GHz. However, larger frequency shifts and a smaller footprint should be possible by using a high index-contrast material platform.

To realize AFC induced via the Pockels effect, we focus on the use of the material platform of lithium-niobate on insulator (LNOI) [11]. LNOI is a thin-film, high index-contrast platform. In LNOI, as the name implies, lithium niobate (LN) is used as a guiding layer; and a low-index dielectric like silicon dioxide, as cladding. LNOI is an emerging material platform recently enabled by the development of “smart-cut” fabrication technology [11, 17]. LNOI combines the large Pockels coefficient of LN and the strong field confinement of a high-index-contrast platform. This enables the fabrication of ring resonators with high quality factors and susceptible to efficient EO modulation. These have been leveraged for applications such as resonant EO modulation [35–37], EO frequency comb generation [38, 39], photonic molecules with EO control [8], EO quantum transduction [40, 41], and synthetic-dimension photonics [42]. Recently, EO AFC in a LNOI ring resonator was demonstrated [43], where tunable frequency shifts of up to 14.3 GHz were attained.

AFC has been analyzed using three different approaches. The first and most direct approach is the numerical solution of the time-dependent Maxwell’s equations, employing the finite-difference time-domain (FDTD) method [22, 44]. This numerical approach has the advantage of being free of any approximation beyond discretization, which can always be refined. Nonetheless, FDTD analysis is computationally demanding, time-consuming, and limited in the insight it offers.

Another approach is offered by heuristic traveling-wave models [45–47]. In these, an intuitive ansatz for optical wave propagation in a dynamic medium is proposed, inferred from generalizing wave propagation in static cavities. The main advantage of this approach is that it is intuitive by construction. However, it is unclear how to derive their ansatz from Maxwell’s equations. So their accuracy cannot be judged without comparing directly with experiment or an independent analysis. Additionally, this approach is unsuitable to analyze an array of coupled cavities, as the complexity of the analysis grows rapidly with the number of cavities under consideration.

The third analytical approach is based on temporal coupled-mode theory (TCMT), which describes the time evo-

lution of a discrete set of resonant modes [18, 23, 27, 48, 49]. The main advantage of TCMT is the simplicity of the resulting equations, which reduce the electromagnetic field to a finite (or countably infinite) number of degrees of freedom. Remarkably, this simplicity is preserved even when an array of coupled cavities is considered [8, 50], rather than just a single cavity. Moreover, this approach can be derived directly from Maxwell's equations [23, 27]. Hence, conditions sufficient for its validity can be obtained, and its accuracy can be assessed a priori.

TCMT still has limitations, though. First, for the method to be practical, one must choose the modes of a static cavity (usually, the considered cavity in the absence of modulation) as the expansion basis that generates the coupled-mode equations. Evidently, this is an approximation, valid only when the modulation inducing AFC is small. Second, for numerical evaluation of the coupled-mode equations, one must truncate the number of examined resonant modes to a finite number. This truncation restricts the bandwidth of the optical source exciting the cavity subject to AFC. Third, it is unfeasible to include the continuum of unconfined electromagnetic modes in the analysis. Thus, the method's analysis is inherently limited.

For this research, we analyze AFC utilizing TCMT. The main reasons for this choice is the relative simplicity of the coupled-mode equations, and their scalability with increasing number of coupled resonators. This last quality is critical, as we aim to examine cascaded AFC, where light repeatedly couples to a cavity mode and undergoes AFC. We only need to be mindful of the method's previously listed limitations, as we analyze its results.

1.3 Thesis outline

We close this introductory chapter by explaining the organization of the remaining chapters. In Chapters 2 and 3, we derive and examine the equations governing spatial coupled-mode theory (SCMT) and temporal coupled-mode theory (TCMT), respectively, from Maxwell's macroscopic equations and the constitutive relations. These chapters are foundational to this thesis, as the analyses in Chapters 4 to 8 are based completely on either SCMT or TCMT. Most of the content of Chapters 2 and 3 consists of review of previously published theory. However, Sections 3.4 and 3.5 contain derivations of the input-output description of coupling between a discrete resonant mode of a cavity and the continuum resonance modes of a waveguide that are original to this thesis.

LN is a uniaxial birefringent material. Thus, when a LNOI waveguide is patterned with a LN core at an oblique angle with LN's optical axis, non-trivial polarization coupling can occur as light propagates along the waveguide. In particular, when a circular LNOI ring resonator is patterned, the angle between the core's propagation axis and LN's optical axis changes continuously. This induces longitudinally-varying modulation and coupling of the LNOI waveguide's polarization modes. In general, these polarization phenomena modify the frequencies of a LNOI ring's optical resonances, and the polarization required to excite them. Thus, the analysis of this polarization coupling is relevant to the engineering of photonic processes in LNOI ring resonators, in general; and to the realization of AFC in LNOI ring resonators, in particular.

In Chapter 4, we utilize the SCMT of Chapter 2 to study polarization coupling in such a ring resonator with a uniaxial core. We show that the SCMT equations are isomorphic to the Schrödinger equation describing a two-level atom modulated sinusoidally in frequency and driven by a classical optical field. Thus, we examine polarization coupling along the ring using techniques popular in the context of two-level atoms under resonant optical excitation. In this manner, we identify and characterize three parameter regimes where the polarization-coupling dynamics are approximately integrable: a perturbative regime, a resonant regime, and an adiabatic regime. Then, we utilize this SCMT formalism to examine the material system of interest to this thesis of a LNOI ring resonator.

In Chapter 5, we take a brief detour from the analysis of AFC and we leverage the SCMT of Chapter 2 and the polarization-coupling analysis of Chapter 4 to design a LNOI waveguide as a passive fundamental-mode polarization rotator. Specifically, this polarization rotator consists of an X-cut LNOI waveguide with a propagation axis at an oblique angle with the LN core's optic axis. We choose this oblique angle so that LN's material anisotropy compensates for the waveguide's geometrical anisotropy and induces phase-matched polarization rotation. We discuss the rotator's ideal-device length, crosstalk, and bandwidth. We show that the proposed design can yield compact (shorter than 1 mm), low-loss, passive polarization rotators for telecom wavelengths.

In Chapters 6 to 8, we employ the TCMT of Chapter 3 to examine the optimization of AFC in ring resonators. First, in Chapter 6, we study AFC in an all-pass resonator, realized in integrated photonics as a single ring resonator coupled to a single bus waveguide. In particular, we analyze comprehensively the energy efficiency of the AFC process. We show that this efficiency is proportional to the squared modulus of the inner product of two squared-integrable

functions. The first is the input pulse. The second is the resonator's impulse response, reversed in time at the instant when index modulation is applied to induce AFC. Thus, it follows from Schwarz's inequality that the AFC efficiency increases with respect to the input pulse when its projection along the time-reversed impulse response increases, in accordance with the matched-filter principle of electrical circuits [51, 52]. We discuss the AFC efficiency's dependence on the process's timescales for a symmetric, single-lobe pulse of fixed shape. We show that, for such a shape, the maximum AFC efficiency attainable is of 80%, limited by the mismatch between the input pulse shape, and the ideal input shape for 100% AFC efficiency. Furthermore, we demonstrate that maximum AFC efficiency requires overcoupling of the resonator to a degree dependent on the input pulse's duration. We compare and contrast the requirements for optimal AFC for pulsed and continuous-wave inputs.

In Chapter 7, we propose and analyze inducing AFC simultaneously over two coupled rings to overcome the fundamental efficiency limit of 80% for a symmetric, single-lobe input pulse. We show that simultaneous AFC over two rings can attain an energy efficiency of 97% in the limit of negligible intrinsic ring loss. To explain this higher AFC efficiency, we analyze two-ring AFC as a linear operator of rank two in the vector space of finite-energy optical pulses. We represent this AFC operator as a 2×2 matrix using orthonormal representation theory. Then, we examine the matrix's (and hence, the operator's) singular value decomposition (SVD). We show that this SVD governs the efficiency of AFC in the two-ring system. With this analysis, we explain the dependence of the two-ring AFC efficiency on the input pulse shape and the system's TCMT timescales.

In Chapter 8, we propose and analyze a scheme to induce cascaded AFC (CAFC) along a chain of coupled, yet initially detuned rings, without requiring unloading the optical signal into a bus waveguide between successive modulations. In this way, we can accomplish multiple instances of AFC, without compromising the process's energy efficiency. For concreteness, we examine thoroughly the simplest non-trivial case of a chain of two rings, and briefly discuss the generalization to a chain of an arbitrary number of rings. We examine the transformation of the input into the frequency-shifted output as a rank-one linear operator in the vector space of finite-energy pulses. In this way, we show that the energy efficiency of CAFC depends on the input pulse shape through a Schwarz inequality, just as in single-ring AFC. We propose a numerical scheme to maximize the CAFC efficiency with respect to the process's timescales and discuss the physics involved. We show that the resulting CAFC efficiency converges in a polynomial manner to a maximum as the process becomes progressively idealized. Furthermore, we show that this maximum efficiency is identical to that for single-ring AFC, e.g., 80% for a symmetric, single-lobe input pulse. Thus, we show that CAFC can become more efficient than multiple instances of single-ring AFC in series. We explain the polynomial convergence of the CAFC efficiency as a consequence of its real-analyticity as a function of the process's timescales under our scheme. We leverage this polynomial convergence to model the CAFC efficiency as a simple polynomial in few normalized timescales. We then utilize this polynomial model to predict optimal values for the remaining free parameters, and the scaling of the CAFC with the inter-ring detuning.

In Chapter 9, we present the thesis's conclusion and describe possible directions for future work.

Chapter 2

Spatial coupled-mode theory

In this chapter, we derive the equations governing spatial coupled-mode theory (SCMT) starting from Maxwell's macroscopic equations. For this thesis, we are only concerned with the coupling among modes of a single waveguide, rather than modes of multiple different waveguides. Hence, we find it possible and preferable to derive SCMT from orthogonality relations, rather than on a variational principle [53, 54]. Furthermore, we only analyze coupling due to material imperfections, rather than geometry changes. Hence, we find it accurate to formulate SCMT in terms of ideal modes, rather than local modes [55]. In our derivation, we follow Refs. [56–58] and utilize an abstract inner-product vector space description of the frequency-domain Maxwell's equations. This has the benefit of yielding the waveguide modes' properties simply and directly from the algebraic form of Maxwell's equations. This analysis is equivalent, yet more succinct, to that of Refs. [55, 59, 60] which directly analyze Maxwell's equations employing vector calculus. We aim to utilize SCMT to analyze waveguides with a core of LN, an anisotropic material. Hence, we explicitly consider material anisotropy in our analysis.

This chapter is organized as follows. In Section 2.1, we explain the concepts of resonance modes of an optical resonator, and propagation modes of an optical waveguide. Then, we motivate the development of spatial and temporal coupled-mode theories. In Section 2.2, we introduce and examine Maxwell's macroscopic equations and the material constitutive relations for dielectric, non-dispersive, anisotropic media. In Section 2.3, we discuss a scheme to decompose Maxwell's frequency-domain equations into transverse and longitudinal vector components, even in the presence of general dielectric anisotropy. In Section 2.4, we leverage this decomposition to pose optical propagation in an arbitrary anisotropic medium as a single initial-value problem. In this form, we derive the modes' orthogonality relations. In Section 2.5, we utilize these orthogonality relations to derive the spatial coupled-mode equations, describing the modulation and coupling of a waveguide's propagation modes due to a small material perturbation.

2.1 Motivation for coupled-mode theories

In integrated photonics, light is usually confined via total internal reflection or destructive interference to optical resonators and waveguides [61]. An optical resonator possesses a discrete set of electromagnetic field distributions localized in the vicinity of the resonator. For a localized field distribution to exist, it must interfere constructively with itself as it propagates in the around the resonator. This can only occur when the optical field oscillates at a particular discrete set of frequencies. These frequencies are the resonator's resonance frequencies; and the corresponding optical field distributions are the resonator's optical modes. This existence of resonant modes at discrete frequencies is analogous to the fact that, in quantum mechanics, a particle can only have localized wavefunctions at a discrete set of energies [21].

An optical waveguide can be understood as an optical resonator elongated along a single direction, which becomes the waveguide's propagation axis [62, 63]. As a consequence of this elongation, the spectral spacing between resonance frequencies of the resonator turned waveguide decreases. This is usually to the point that the resonance frequencies can be treated as a continuum. In this elongation, the resonance modes are no longer confined along the direction of propagation, so they can be considered as propagating optical modes.

If unperturbed, the modes of a resonator remain invariant under time evolution; as do those of a waveguide upon propagation. They merely increase linearly in phase, with their corresponding resonance frequency or propagation

constant, respectively. But if perturbations are introduced to either, this ceases to be true. In general, studying the exact time evolution of the optical field in a perturbed resonator, or its propagation along a perturbed waveguide, is a challenging problem. Thus, this often requires numerical solution of Maxwell's macroscopic equations. Nonetheless, if the perturbations can be considered small, then one can argue the system's modes remain approximate solutions to Maxwell's equations, and the perturbations merely modulates them and couples them to each other. Coupled-mode theory (CMT) is the mathematical framework used to quantitatively analyze the effect of small material perturbations to the optical modes' evolution [53, 54, 64, 65]. Specifically, temporal coupled-mode theory (TCMT) studies the modulation and coupling of resonator modes as they evolve in time; and spatial coupled-mode theory (SCMT), the modulation and coupling of waveguide modes as they propagate in space.

In subsequent chapters, we employ both TCMT and SCMT for our analysis of LNOI ring resonators and AFC in these devices. Hence, we derive and discuss SCMT in the current chapter, and TCMT in the next one. We utilize fewer results from SCMT, so we discuss it first, and then discuss TCMT.

2.2 Maxwell' equations and the constitutive relations

In integrated photonics [61], the propagation of optical fields is described by the source-free Maxwell's macroscopic equations [66, 67]. These can be divided in two sets. One set consists of the divergence equations

$$\begin{aligned}\nabla \cdot \mathbf{D} &= 0, \\ \nabla \cdot \mathbf{B} &= 0;\end{aligned}\tag{2.1}$$

and the other, of the curl equations

$$\begin{aligned}\nabla \times \mathbf{E} &= -\frac{\partial \mathbf{B}}{\partial t}, \\ \nabla \times \mathbf{H} &= \frac{\partial \mathbf{D}}{\partial t}.\end{aligned}\tag{2.2}$$

In Eqs. (2.1) and (2.2), \mathbf{D} is the electric displacement field; \mathbf{B} , the magnetic induction field; \mathbf{E} , the electric vector field; and \mathbf{H} , the magnetic vector field [67]. A rigorous derivation of Maxwell's macroscopic equations from their microscopic version is given in Ref. [66].

In the absence of free charges, the divergence equations (2.1) can be considered initial conditions. If the fields \mathbf{D} and \mathbf{B} satisfy them at some initial time, they will continue do so for any subsequent time. To see this, one need only integrate the curl equations (2.2) in time and take the divergence of the resulting expression. Thus, we need only focus on the curl equations (2.2) to describe time evolution and propagation of an optical field.

To describe the propagation medium, we must complement Eq. (2.2) with constitutive relations connecting \mathbf{D} and \mathbf{B} to \mathbf{E} and \mathbf{H} . For this thesis, we restrict attention to non-magnetic media which respond linearly to the electric field, but are generally anisotropic. Furthermore, we consider media which are non-dispersive over the bandwidth of interest. Hence, we write the constitutive relations as

$$\begin{aligned}\mathbf{D} &= \varepsilon_0 \overset{\leftrightarrow}{\varepsilon} \cdot \mathbf{E}, \\ \mathbf{B} &= \mu_0 \mathbf{H}.\end{aligned}\tag{2.3}$$

In Eq. (2.3), ε_0 is vacuum's electric permittivity; and μ_0 , vacuum's magnetic permeability. Additionally, $\overset{\leftrightarrow}{\varepsilon}$ is the relative permittivity dyadic.

To describe optical propagation in a linear, time-invariant media, we may decompose the time-dependence of the optical field into a superposition of monochromatic fields, analyze propagation for each frequency component, and synthesize the field via inverse Fourier transform after propagation [67]. Hence, we assume all fields in Maxwell's equations have the harmonic time dependence $\exp(-i\omega t)$. Then, the curl equations (2.2) become

$$\begin{aligned}\nabla \times \mathbf{E} &= i\omega \mathbf{B}, \\ \nabla \times \mathbf{H} &= -i\omega \mathbf{D}.\end{aligned}\tag{2.4}$$

2.3 Decomposition of Maxwell's curl equations into longitudinal and transverse components

As is conventional [53, 55, 60, 65], we denote with z the Cartesian coordinate along the waveguide's axis, and thus, the direction of propagation for the optical field. Given Eq. (2.4), it is then possible and convenient to express the longitudinal field components \mathbf{E}_z and \mathbf{H}_z in terms of the transverse field components \mathbf{E}_t and \mathbf{H}_t [55, 56, 58, 59]. To this end, we first decompose the fields \mathbf{E} and \mathbf{H} , their curls into transverse and longitudinal components; and the permittivity dyadic $\overset{\leftrightarrow}{\epsilon}$, according to how it relates transverse and longitudinal vector components.

Thus, we write the fields \mathbf{E} and \mathbf{H} as

$$\begin{aligned}\mathbf{E} &= \mathbf{E}_t + \mathbf{E}_z, \\ \mathbf{H} &= \mathbf{H}_t + \mathbf{H}_z.\end{aligned}\tag{2.5}$$

Here, the transverse field \mathbf{E}_t and the longitudinal field \mathbf{E}_z are defined so that $\mathbf{E}_t \cdot \hat{\mathbf{z}} = 0$, and $\mathbf{E}_z = \hat{\mathbf{z}}(\hat{\mathbf{z}} \cdot \mathbf{E}_z)$. Analogously for \mathbf{H}_t and \mathbf{H}_z . Correspondingly, the curl of the electric field, $(\nabla \times \mathbf{E})$, is decomposed into its transverse part, $(\nabla \times \mathbf{E})_t$, and its longitudinal part, $(\nabla \times \mathbf{E})_z$, as

$$\begin{aligned}(\nabla \times \mathbf{E})_t &= \nabla_t \times \mathbf{E}_z + \hat{\mathbf{z}} \times \frac{\partial \mathbf{E}_t}{\partial z}, \\ (\nabla \times \mathbf{E})_z &= \nabla_t \times \mathbf{E}_t.\end{aligned}\tag{2.6}$$

Here, $\nabla_t \times$ is the transverse curl operator. It maps transverse vectors into longitudinal ones, and longitudinal vectors into transverse ones. Explicitly, in Cartesian coordinates x, y, z it is given by the relation

$$\begin{aligned}\nabla_t \times \mathbf{E}_t &= \hat{\mathbf{z}} \left(\frac{\partial E_y}{\partial x} - \frac{\partial E_x}{\partial y} \right), \\ \nabla_t \times \mathbf{E}_z &= \hat{\mathbf{x}} \frac{\partial E_z}{\partial y} - \hat{\mathbf{y}} \frac{\partial E_z}{\partial x},\end{aligned}\tag{2.7}$$

where $\mathbf{E}_t = E_x \hat{\mathbf{x}} + E_y \hat{\mathbf{y}}$ and $\mathbf{E}_z = \hat{\mathbf{z}} E_z$. Of course, equations analogous to (2.6) and (2.7) hold for the curl of \mathbf{H} , with \mathbf{H} replacing \mathbf{E} .

As stated above, we need also decompose the relative permittivity dyadic $\overset{\leftrightarrow}{\epsilon}$ based on how it relates transverse and longitudinal vector components for our analysis of field propagation. This decomposition is given by the equation [58, 59, 68]

$$\overset{\leftrightarrow}{\epsilon} = \overset{\leftrightarrow}{\epsilon}_t + \vec{\epsilon}_{tz} \hat{\mathbf{z}} + \hat{\mathbf{z}} \vec{\epsilon}_{zt} + \epsilon_z \hat{\mathbf{z}} \hat{\mathbf{z}}.\tag{2.8}$$

Here, $\overset{\leftrightarrow}{\epsilon}_t$ is the purely transverse component of $\overset{\leftrightarrow}{\epsilon}$, mapping transverse components of \mathbf{E} to transverse components of \mathbf{D}/ϵ_0 . $\vec{\epsilon}_{tz}$ and $\vec{\epsilon}_{zt}$ are two, generally different, transverse vectors. And ϵ_z is a scalar. In Eq. (2.8) and henceforth in this thesis, juxtaposition of two vectors indicates their tensor product. The relation between $\overset{\leftrightarrow}{\epsilon}$ and the parameters $\overset{\leftrightarrow}{\epsilon}_t$, $\vec{\epsilon}_{tz}$, $\vec{\epsilon}_{zt}$, and ϵ_z is bijective. Hence, the latter set is uniquely determined if $\overset{\leftrightarrow}{\epsilon}$ is given. Explicitly, these quantities are given by

$$\begin{aligned}\epsilon_z &= \hat{\mathbf{z}} \cdot \overset{\leftrightarrow}{\epsilon} \cdot \hat{\mathbf{z}}, \\ \epsilon_{tz} &= \hat{\mathbf{z}} \cdot \overset{\leftrightarrow}{\epsilon} - \hat{\mathbf{z}} \epsilon_z, \\ \epsilon_{zt} &= \overset{\leftrightarrow}{\epsilon} \cdot \hat{\mathbf{z}} - \epsilon_z \hat{\mathbf{z}}, \\ \overset{\leftrightarrow}{\epsilon}_t &= \overset{\leftrightarrow}{\epsilon} - \vec{\epsilon}_{tz} \hat{\mathbf{z}} - \hat{\mathbf{z}} \vec{\epsilon}_{zt} - \epsilon_z \hat{\mathbf{z}} \hat{\mathbf{z}}.\end{aligned}\tag{2.9}$$

Next we substitute Eqs. (2.5), (2.6), and (2.8) into the constitutive relations of Eq. (2.3) and into the longitudinal part of Eq. (2.4). In this manner, we express the longitudinal field components, \mathbf{E}_z and \mathbf{H}_z , in terms of the transverse ones, \mathbf{E}_t and \mathbf{H}_t , as

$$\begin{aligned}\mathbf{E}_z &= \frac{i}{\omega \epsilon_0 \epsilon_z} \nabla_t \times \mathbf{H}_t - \hat{\mathbf{z}} \frac{\vec{\epsilon}_{zt} \cdot \mathbf{E}_t}{\epsilon_z}, \\ \mathbf{H}_z &= - \frac{i}{\omega \mu_0} \nabla_t \times \mathbf{E}_t.\end{aligned}\tag{2.10}$$

Given Eq. (2.10), we may substitute it into the transverse parts of Maxwell's curl equations (2.4) to express them purely in terms of the transverse fields \mathbf{E}_t and \mathbf{H}_t . We need only then solve the resulting equations for \mathbf{E}_t and \mathbf{H}_t , and then evaluate \mathbf{E}_z and \mathbf{H}_z via Eq. (2.10) to obtain the full vector fields \mathbf{E} and \mathbf{H} .

2.4 Propagation equation for the transverse fields

Leveraging the field decomposition of Section 2.3, we next write the transverse parts of the curl equations as a differential equation in the transverse fields \mathbf{E}_t and \mathbf{H}_t as functions of the longitudinal coordinate z . In Dirac's bra-ket notation this equation is written as [56, 58]

$$-i \frac{\partial}{\partial z} \hat{Z} |\psi\rangle = \hat{E} |\psi\rangle. \quad (2.11)$$

Here the ket vector $|\psi\rangle$ specifies the optical field in a plane transverse to $\hat{\mathbf{z}}$. It is given in terms of the transverse fields, \mathbf{E}_t and \mathbf{H}_t , by the four-component vector field

$$|\psi\rangle \equiv \begin{pmatrix} \sqrt{\epsilon_0} \mathbf{E}_t \\ \sqrt{\mu_0} \mathbf{H}_t \end{pmatrix}. \quad (2.12)$$

The factors of $\sqrt{\epsilon_0}$ and $\sqrt{\mu_0}$ are included in Eq. (2.12) so that all components of $|\psi\rangle$ share the same units. In Eq. (2.11), \hat{Z} and \hat{E} are two linear operators in the vector space spanned by vectors $|\psi\rangle$ of the form (2.12). Specifically, \hat{Z} and \hat{E} are given by

$$\hat{Z} = \begin{pmatrix} 0 & -\hat{\mathbf{z}} \times \\ \hat{\mathbf{z}} \times & 0 \end{pmatrix}, \quad \hat{E} = \begin{pmatrix} \hat{E}_{ee} & \hat{E}_{eh} \\ \hat{E}_{he} & \hat{E}_{hh} \end{pmatrix}. \quad (2.13)$$

In Eq. (2.13), \hat{E}_{ee} , \hat{E}_{eh} , \hat{E}_{he} , and \hat{E}_{hh} are operators in the vector space of two-component transverse fields, e.g., $\sqrt{\epsilon_0} \mathbf{E}_t$ and $\sqrt{\mu_0} \mathbf{H}_t$. The explicit expressions for these operators are

$$\begin{aligned} \hat{E}_{ee} &= k_0 \left(\overset{\leftrightarrow}{\epsilon}_t - \frac{\vec{\epsilon}_{tz} \vec{\epsilon}_{zt}}{\epsilon_z} \right) - k_0^{-1} \nabla_t \times \nabla_t \times, \\ \hat{E}_{eh} &= i \left(\frac{\vec{\epsilon}_{tz} \hat{\mathbf{z}}}{\epsilon_z} \right) \cdot (\nabla_t \times), \\ \hat{E}_{he} &= -i \nabla_t \times \left(\hat{\mathbf{z}} \frac{\vec{\epsilon}_{zt}}{\epsilon_z} \right), \\ \hat{E}_{hh} &= k_0 - k_0^{-1} \nabla_t \times \left(\frac{1}{\epsilon_z} \nabla_t \times \right), \end{aligned} \quad (2.14)$$

where $k_0 \equiv \omega \sqrt{\epsilon_0 \mu_0}$ is the vacuum wavenumber of the optical field.

To exploit the mathematical machinery of quantum mechanics, the inner product $\langle \psi_a | \psi_b \rangle$ of the two transverse fields $|\psi_a\rangle$ and $|\psi_b\rangle$ needs to be defined. We define it as the positive-definite Hermitian form [56, 58]

$$\langle \psi_a | \psi_b \rangle \equiv \frac{1}{4} \iint (\eta_0^{-1} \mathbf{E}_{ta}^* \cdot \mathbf{E}_{tb} + \eta_0 \mathbf{H}_{ta}^* \cdot \mathbf{H}_{tb}) \, dx \, dy, \quad (2.15)$$

In Eq. (2.15), $\eta_0 = \sqrt{\mu_0 / \epsilon_0}$ is the impedance of vacuum, and integration is taken over the full two-dimensional plane perpendicular to $\hat{\mathbf{z}}$. The operator \hat{Z} is self-adjoint under the inner product (2.15), i.e.,

$$\langle \psi_a | \hat{Z} | \psi_b \rangle = \langle \psi_b | \hat{Z} | \psi_a \rangle^*, \quad (2.16)$$

as long as the integral $\langle \psi_a | \hat{Z} | \psi_b \rangle$ exists. The definition (2.15) of the inner product has the additional property that $\langle \psi | \hat{Z} | \psi \rangle$ gives the time-averaged power carried by the electromagnetic field $|\psi\rangle$ along z .

On the other hand, \hat{E} satisfies

$$\langle \psi_a | \hat{E} | \psi_b \rangle = \langle \psi_b | \hat{E} | \psi_a \rangle^*, \quad (2.17)$$

and is thus self-adjoint under the inner product (2.15), if two conditions are satisfied [58, 59]. The first condition is that $\overset{\leftrightarrow}{\boldsymbol{\varepsilon}}$ is Hermitian, i.e.,

$$\mathbf{E}_a^* \cdot \overset{\leftrightarrow}{\boldsymbol{\varepsilon}} \cdot \mathbf{E}_b = (\mathbf{E}_b^* \cdot \overset{\leftrightarrow}{\boldsymbol{\varepsilon}} \cdot \mathbf{E}_a)^*, \quad (2.18)$$

for any electric fields \mathbf{E}_a and \mathbf{E}_b . Based on Eq. (2.8) and (2.9), an equivalent condition to (2.18) is for $\overset{\leftrightarrow}{\boldsymbol{\varepsilon}}_t$ to be Hermitian, $\overset{\leftrightarrow}{\boldsymbol{\varepsilon}}_{tz} = (\overset{\leftrightarrow}{\boldsymbol{\varepsilon}}_{zt})^*$, and for ε_z to be real valued. For this thesis, we are interested only in media with real-valued and symmetric permittivity $\overset{\leftrightarrow}{\boldsymbol{\varepsilon}}$, so Eq. (2.18) is satisfied. The second condition for \hat{Z} to be self-adjoint is that the any pair of fields $|\psi_a\rangle$ and $|\psi_b\rangle$ over which it operates satisfy [59, 60]

$$\oint (\mathbf{E}_a^* \times \mathbf{H}_b) \cdot \hat{\mathbf{n}} ds = 0. \quad (2.19)$$

In Eq. (2.19), \mathbf{E}_a is the full (transverse and longitudinal) electric field corresponding to ψ_a ; and \mathbf{H}_b , the full magnetic field corresponding to ψ_b . In Eq. (2.19), the integral is a closed line integral on a surface normal to $\hat{\mathbf{z}}$ enclosing a circle of infinite radius. The differential ds is the length differential along this line and $\hat{\mathbf{n}}$ is the outward unit vector normal to both $\hat{\mathbf{z}}$ and to the line. The integral in Eq. (2.19) vanishes if either \mathbf{E}_a or \mathbf{H}_b correspond to a guided mode of the waveguide described by $\overset{\leftrightarrow}{\boldsymbol{\varepsilon}}$ [58–60]. If both \mathbf{E}_a and \mathbf{H}_b correspond to radiation modes of the waveguide, then Eq. (2.19) vanishes in the sense of a delta function of nonzero argument [59, 60], i.e., as a distribution or generalized function [69]. The combined set of guided modes and radiation modes (including evanescent radiation modes) form a complete basis [55] for the vector space of optical fields in a waveguide. Thus, Eq. (2.19) is satisfied for any fields \mathbf{E}_a and \mathbf{H}_b obeying Maxwell's equations.

The result that \hat{E} and \hat{Z} are self-adjoint under the inner product (2.15), i.e., they satisfy Eqs. (2.17) and (2.16), is significant. For instance, it immediately implies that, for any optical fields $|\psi_a\rangle$ and $|\psi_b\rangle$

$$\frac{d}{dz} \langle \psi_a | \hat{Z} | \psi_b \rangle = 0. \quad (2.20)$$

In other words, the matrix element $\langle \psi_a | \hat{Z} | \psi_b \rangle$ is conserved along z . In particular, it implies that $\langle \psi | \hat{Z} | \psi \rangle$, i.e., the power carried along z by $|\psi\rangle$, is conserved along z . We note that this result holds even when the waveguide described by $\overset{\leftrightarrow}{\boldsymbol{\varepsilon}}$ and \hat{E} varies along z . This property is analogous to the unitary nature of time-evolution of quantum-mechanical states obeying Schrödinger's equation [21, 70].

Though more importantly for this thesis, we can utilize Eqs. (2.16) and (2.17) along with the propagation equation Eq. (2.11) to characterize the normal modes of a longitudinally invariant waveguide. The z dependence of a normal mode $|\beta\rangle$ of a waveguide is $\exp(i\beta z)$ for some propagation constant β [55, 61]. Substituting this longitudinal dependence on the propagation equation (2.11), the normal mode $|\beta\rangle$ must satisfy the relation

$$\beta \hat{Z} |\beta\rangle = \hat{E} |\beta\rangle. \quad (2.21)$$

As identified in Refs. [56, 58], Eq. (2.21) is a generalized eigenvalue equation [71] for the operator pair $\{\hat{Z}, \hat{E}\}$, with eigenvalue β and eigenvector $|\beta\rangle$.

From the generalized eigenvalue equation (2.21) and the self-adjoint relations (2.16) and (2.17), we obtain two important results [56, 58]. The first is that two generally distinct normal modes, $|\beta\rangle$ and $|\beta'\rangle$, are power-orthogonal if $\beta' \neq \beta^*$, i.e.,

$$\langle \beta | \hat{Z} | \beta' \rangle = 0, \quad \text{if } \beta' \neq \beta^*. \quad (2.22)$$

The second is that for any normal mode $|\beta\rangle$,

$$\beta \text{ is purely real, if } \langle \beta | \hat{Z} | \beta \rangle \neq 0. \quad (2.23)$$

In other words, β is necessarily real if the normal mode $|\beta\rangle$ carries non-zero (either positive or negative) power along z . We note that, generally, waveguides do have normal modes which carry exactly zero power along z . These are the evanescent radiation modes [55, 60] of the waveguide. These modes are not restricted by Eq. (2.23) and thus have generally complex propagation constant β . Eqs. (2.22) and (2.23) are analogous to the well-known results from quantum mechanics that the eigenstates of a self-adjoint operator with different eigenvalue are mutually orthogonal, and that the eigenvalue spectrum of a self-adjoint operator is purely real [21, 70].

To prove Eqs. (2.22) and (2.23), we evaluate Eq. (2.21) for $|\beta\rangle$ and $|\beta'\rangle$. Then we take the product of the first resulting equation with $\langle\beta'|\$ and the product of the second resulting equation with $\langle\beta|\$. In this way, we obtain

$$\begin{aligned}\beta\langle\beta'|\hat{Z}|\beta\rangle &= \langle\beta'|\hat{E}|\beta\rangle, \\ \beta'\langle\beta|\hat{Z}|\beta'\rangle &= \langle\beta|\hat{E}|\beta'\rangle.\end{aligned}\tag{2.24}$$

Then, we compare the left-hand sides of Eq. (2.24) utilizing Eq. (2.16) and (2.17) to obtain

$$(\beta' - \beta^*)\langle\beta|\hat{Z}|\beta'\rangle = 0.\tag{2.25}$$

From Eq. (2.25), then Eq. (2.22) follows. From Eq. (2.25) with $\beta = \beta'$, then Eq. (2.23) follows.

2.5 Derivation of the coupled-mode equations

In this thesis, we are mostly concerned with the coupling between guided, co-propagating modes carrying positive power along z . Thus, we rescale the normal modes $|\beta\rangle$ to carry unit power. Then, utilizing Eq. (2.22) and the fact that degenerate eigenvectors $|\beta\rangle$ can always be chosen to be orthogonal [21, 70], we express the matrix elements of \hat{Z} with respect to these guided modes as

$$\langle\beta|\hat{Z}|\beta'\rangle = \delta_{\beta,\beta'}.\tag{2.26}$$

In Eq. (2.26), $\delta_{\beta,\beta'}$ equals 1 if $\beta = \beta'$ and 0 otherwise. If the propagation-coefficient spectrum β exhibits degeneracy, the right-hand side of (2.26) is non-zero only when the modes are identical. In Eq. (2.26), we normalize the propagation modes $|\beta\rangle$ so they carry unit power along z .

Given the relations (2.21) and (2.26), we implement the procedure of quantum-mechanical time-dependent perturbation theory [21, 70] to develop a CMT for birefringent waveguides. In this approach, the transverse field $|\psi(z)\rangle$ is approximated as a coherent superposition of the normal modes $|\beta_n\rangle$ even when the operator \hat{E} becomes a z -dependent operator $\hat{E}'(z)$ in Eq. (2.11). Hence, we write

$$|\psi(z)\rangle \approx \sum_n \tilde{a}_n(z) |\beta_n\rangle.\tag{2.27}$$

In contrast to the case of quantum-mechanics, Eq. (2.27) is indeed only an approximation, and not an exact expansion. This is because the normal modes $|\beta_n\rangle$ are only a complete set of the transverse electromagnetic fields in the medium corresponding to the original, ideal waveguide with z -independent operator \hat{E} , even when all guided modes, radiation modes, and evanescent modes are included. To see this, it is sufficient to note that all the normal modes of a given \hat{E} satisfy a specific set of boundary conditions at the exact location of material discontinuities specified by the dielectric dyadic $\overset{\leftrightarrow}{\epsilon}$ which defines \hat{E} . Thus, if $\overset{\leftrightarrow}{\epsilon}$ and thus \hat{E} change, the modes do not generally satisfy the changed boundary conditions. And thus, they are no longer exact solutions of Maxwell's equations. However, the error resulting from this approximation is small if the difference between the original, ideal $\overset{\leftrightarrow}{\epsilon}$ and the perturbed, z -dependent $\overset{\leftrightarrow}{\epsilon}'$ determining $\hat{E}'(z)$ is small [53–55, 65]. As we verify in Chapter 4, this is the case for the problem of interest in this thesis, so the approximation in Eq. (2.27) is accurate.

Substituting the expansion (2.27) into Eq. (2.11) (with $\hat{E}'(z)$ instead of \hat{E}), and utilizing the orthonormality relation (2.26) for the normal modes $|\beta_n\rangle$, we obtain the following set of coupled equations for the mode amplitudes $\tilde{a}_n(z)$,

$$-i\frac{d\tilde{a}_n}{dz} = \beta_n\tilde{a}_n + \sum_m D_{nm}(z)\tilde{a}_m.\tag{2.28}$$

Here $D_{nm}(z) \equiv \langle\beta_n|\hat{D}(z)|\beta_m\rangle$ are the matrix elements of the perturbation operator $\hat{D}(z) \equiv \hat{E}'(z) - \hat{E}$. We use these coupled-mode equations to study polarization mode coupling in waveguiding structures etched on a uniaxial core. Specifically, in Chapter 4 we consider polarization coupling in a microring resonator; and in Chapter 5, polarization coupling in an waveguide at an oblique angle with the core's optical axis.

Chapter 3

Temporal coupled-mode theory

In this chapter, we derive temporal coupled-mode theory (TCMT) directly from Maxwell’s curl equations (2.2) and the constitutive relations (2.3). Our approach is similar to that in References [23, 27, 72, 73] and partially to that in Ref. [74]. However, in analogy to our analysis of spatial coupled-mode theory (SCMT) of Chapter 2, we emphasize the algebraic properties of the problem. This allows us to identify and highlight the similarities and differences between SCMT and TCMT.

In the photonics literature, TCMT is often derived phenomenologically [74–79], starting from general assumptions about the resonant modes and waveguides, and principles such as energy conservation and time-reversal symmetry. The phenomenological approach is attractive because it is simple, intuitive, and seemingly general. Nonetheless, we find it worthwhile to complement the phenomenological approach with our more direct approach based on Maxwell’s equations and orthogonality relations. This is because the latter analysis provides us with results not obtainable from the phenomenological theory. Two of these results are of particular importance to this thesis. The first is an integral expression for the magnitude of the frequency shift induced via AFC. This expression is given in Section 3.2. The second are sufficient conditions for resonator-waveguide coupling to be described by input-output relations, even when AFC is induced. These conditions are presented and discussed in Section 3.5.

This chapter is organized as follows. In Section 3.1, we pose the time-domain macroscopic Maxwell’s equations as a differential equation in time, and we adapt the procedure of Sections 2.4 and 2.5 to derive temporal coupled-mode equations. In Section 3.2, we utilize the TCMT equations of Section 3.1 to analyze AFC. We obtain explicit expressions for the dependence on the adiabatic frequency shift on the resonance mode and the dielectric perturbation. In Section 3.3, we examine the coupled-mode equations for the time evolution of two coupled resonances. In particular, we discuss sufficient and necessary conditions for these equations to preserve the system’s electromagnetic energy, as is necessary in the absence of time-dependent material modulation.

Although most of this chapter consists of a review of previously published analyses, Sections 3.4 and 3.5 contain analysis original to this thesis. In Section 3.4, we describe a waveguide as an optical resonator of large length L along its propagation axis. This allows us to adapt techniques of solid state physics [80] and quantum optics [62, 63] to derive coupled-mode equations between a discrete optical resonant mode and the continuum of modes in a waveguide. In Section 3.5, we identify the coupled-mode equations between a discrete resonant mode and a waveguide’s continuum of modes as isomorphic to the Schrödinger equation of a discrete state coupled to a continuum of states [21], as in spontaneous emission and the photoelectric effect. Thus, analogous to the input-output formalism of quantum optics [81–84], we employ the Weisskopf-Wigner analysis [21, 85], usually applied to these quantum mechanical systems, to derive input-output relations between the optical resonator and waveguide.

3.1 Derivation of the coupled-mode equations

In this section, we analyze the time-dependent Maxwell’s equations as a first-order differential equation in time in an inner-product vector space. We examine the consequences of this characterization of Maxwell’s equations in the conservation of electromagnetic energy in a medium undergoing temporal modulation. We show the resonance modes of a lossless dielectric optical resonator can be chosen to all obey a common orthogonality condition and that they all

have real-valued resonance frequencies. Lastly, we leverage this orthogonality relation to derive temporal coupled-mode equations, accurate when the medium undergoes small time-dependent modulation.

The analysis of this section closely follows that of Sections 2.4 and 2.5. This allows us to emphasize the similarities and differences between this formulation of TCMT and that of SCMT in Sections 2.4 and 2.5.

Analogously to Section 2.4, we start by combining Maxwell's equations with the medium's constitutive relations, and write the result in a simple, abstract form more amenable for subsequent analysis. Thus, we substitute Eq. (2.3) into Eq. (2.2), and again adopt Dirac's bra-ket notation, to obtain

$$i \frac{\partial}{\partial t} |\psi\rangle = \hat{C} \hat{H} |\psi\rangle. \quad (3.1)$$

In Eq. (3.1), $|\psi\rangle$ is the full time-dependent electromagnetic field at time t . We specify it in terms of the electric displacement \mathbf{D} and the magnetic induction \mathbf{B} as the six-component vector field

$$|\psi\rangle = \begin{pmatrix} \mathbf{D}/\sqrt{\epsilon_0} \\ \mathbf{B}/\sqrt{\mu_0} \end{pmatrix}. \quad (3.2)$$

As in Eq. (2.12), the factors of $1/\sqrt{\epsilon}$ and $1/\sqrt{\mu_0}$ are introduced so that all components of ψ share the same units. In Eq. (3.1), \hat{C} and \hat{H} are two linear operators in the vector space spanned by vectors $|\psi\rangle$ of the form (3.2). They are given by

$$\hat{C} = \begin{pmatrix} 0 & ic_0 \nabla \times \\ -ic_0 \nabla \times & 0 \end{pmatrix}, \quad \hat{H} = \begin{pmatrix} \overset{\leftrightarrow}{\eta} & 0 \\ 0 & 1 \end{pmatrix}. \quad (3.3)$$

In Eq. (3.3), $c_0 = 1/\sqrt{\epsilon_0 \mu_0}$ is the speed of light in vacuum; and $\overset{\leftrightarrow}{\eta}$, the relative impermeability dyadic, equal to the inverse of the relative permittivity dyadic, i.e., $\overset{\leftrightarrow}{\eta} = \overset{\leftrightarrow}{\epsilon}^{-1}$.

We choose to define the electromagnetic field $|\psi\rangle$ in Eq. (3.2), and hence Maxwell's equations in Eq. (3.1), in terms of the electric displacement \mathbf{D} and magnetic induction \mathbf{B} rather than in terms of the electric field \mathbf{E} and the magnetic field \mathbf{H} . This is because, from Maxwell's curl equations, \mathbf{D} and \mathbf{B} are continuous in time, even in the presence of time modulation [86]. Thus the resulting formulation of TCMT yields a direct integral expression for the frequency-shift of a resonance mode upon temporal modulation. This is of interest for our study of AFC, and would not be possible if we analyzed the field in terms of \mathbf{E} and \mathbf{H} in Eq. (3.1), and further approximations would be required, as in Ref. [23]. Additionally, representing $|\psi\rangle$ in terms of \mathbf{D} and \mathbf{H} allows us to obtain a simpler result in Eq. (3.9) when discussing energy conservation in time-modulated media, as we explain below.

As in Section 2.4, we define an inner product $\langle \psi_a | \psi_b \rangle$ between two electromagnetic fields $|\psi_a\rangle$ and $|\psi_b\rangle$ so we may leverage the mathematical techniques of quantum mechanics. For this section's analysis, it proves convenient to define it as the positive-definite Hermitian form

$$\langle \psi_a | \psi_b \rangle \equiv \frac{1}{4} \iiint (\epsilon_0^{-1} \mathbf{D}_a^* \cdot \mathbf{D}_b + \mu_0^{-1} \mathbf{H}_a^* \cdot \mathbf{H}_b) \, \mathbf{d}\mathbf{x}, \quad (3.4)$$

where integration is taken over all of three-dimensional space. Clearly, the operator \hat{H} is self-adjoint under the inner product (3.4), i.e.,

$$\langle \psi_a | \hat{H} | \psi_b \rangle = \langle \psi_b | \hat{H} | \psi_a \rangle^*, \quad (3.5)$$

if and only if $\langle \psi_a | \hat{H} | \psi_b \rangle$ exists and $\overset{\leftrightarrow}{\eta}$ is Hermitian. By definition, $\overset{\leftrightarrow}{\eta}$ is Hermitian if

$$\mathbf{D}_a^* \cdot \overset{\leftrightarrow}{\eta} \cdot \mathbf{D}_b = \left(\mathbf{D}_b^* \cdot \overset{\leftrightarrow}{\eta} \cdot \mathbf{D}_a \right)^* \quad (3.6)$$

for any displacement fields \mathbf{D}_a and \mathbf{D}_b . If $\overset{\leftrightarrow}{\epsilon} = \overset{\leftrightarrow}{\eta}^{-1}$ exists, which is usually the case, Eq. (3.6) is equivalent to Eq. (2.18). The definition (3.4) has the additional property that $\langle \psi | \hat{H} | \psi \rangle$ equals the time-averaged energy of the electromagnetic field $|\psi\rangle$ in the medium with impermeability $\overset{\leftrightarrow}{\eta}$.

On the other hand, if \hat{H} is invertible (usually the case) and self-adjoint, then \hat{C} satisfies

$$\langle \psi_a | \hat{C} | \psi_b \rangle = \langle \psi_b | \hat{C} | \psi_a \rangle^* \quad (3.7)$$

and is thus self-adjoint if and only if and $\hat{H}\hat{C}\hat{H}$ itself is self-adjoint. The operator product $\hat{H}\hat{C}\hat{H}$ is self-adjoint under the inner product (3.4) if and only if, for any electric field \mathbf{E}_a and magnetic field \mathbf{H}_b corresponding to electromagnetic fields $|\psi_a\rangle$ and $|\psi_b\rangle$, respectively,

$$\oint (\mathbf{E}_a^* \times \mathbf{H}_b - \mathbf{H}_a^* \times \mathbf{E}_b) \cdot \hat{\mathbf{n}} d\sigma = 0. \quad (3.8)$$

In Eq. (3.8), integration is over a surface containing the dielectric medium under analysis and extending towards infinity. The unit vector $\hat{\mathbf{n}}$ points outward on this surface, and $d\sigma$ is the differential area along this surface. Substituting $\mathbf{E}_b = \mathbf{E}_a$ and $\mathbf{H}_b = \mathbf{H}_a$ into Eq. (3.8), then a necessary condition for $\hat{H}\hat{C}\hat{H}$ (and thus \hat{C}) to be self-adjoint is for the considered fields to radiate a net time-averaged power of zero into the environment at infinity. Thus, $\hat{H}\hat{C}\hat{H}$ and \hat{C} can be self-adjoint only in dielectric resonators with high quality factor. We assume this to be the case henceforth. If needed, deviation of $\hat{H}\hat{C}\hat{H}$ and \hat{C} from self-adjoint behavior can be treated a posteriori as a perturbation [74].

Having established sufficient and necessary conditions for \hat{C} and \hat{H} to be simultaneously self-adjoint, it is interesting to note one of its consequences. In Eq. (2.20) of Section 2.4, we showed that the self-adjoint property of the operators \hat{Z} and \hat{E} in the propagation equation directly implied conservation of power upon propagation for any initial configuration of the transverse electromagnetic field. It is then of interest to determine whether there exists an analogous conservation relation for energy, rather than power, for the time-dependent Maxwell's equations, when \hat{C} and \hat{H} are self-adjoint. To do so, we assume \hat{C} and \hat{H} are self-adjoint and evaluate the time derivative of the matrix element $\langle \psi_a | \hat{H} | \psi_b \rangle$. In this way, leveraging the assumed self-adjoint nature of \hat{C} and \hat{H} , we obtain

$$\frac{d}{dt} \langle \psi_a | \hat{H} | \psi_b \rangle = \langle \psi_a | \frac{\partial \hat{H}}{\partial t} | \psi_b \rangle. \quad (3.9)$$

This result contrasts with that of Eq. (2.20). Even when the medium is inhomogeneous along the direction of propagation, the matrix element $\langle \psi_a | \hat{Z} | \psi_b \rangle$ is conserved for any fields $|\psi_a\rangle$ and $|\psi_b\rangle$. In particular, power is always conserved. In contrast, Eq. (3.9) states that when the medium is modulated in time, the matrix element $\langle \psi_a | \hat{H} | \psi_b \rangle$ generally also changes in time, and in particular, so does the energy $\langle \psi | \hat{H} | \psi \rangle$ of an electromagnetic field $|\psi\rangle$. It is when the material properties remain static that the electromagnetic energy always remains constant. This contrast between Eqs. (2.20) and (3.9) arises because the operator \hat{H} depends on the medium's properties, but \hat{Z} of Section 2.4 does not.

Next, as in Section 2.4, we analyze the consequence of the self-adjoint nature of \hat{C} and \hat{H} on the resonant modes of a dielectric time-invariant medium. These time dependence of a resonance mode $|\omega\rangle$ is, by definition, $\exp(-i\omega t)$ for some resonance frequency ω . Substituting this time dependence on the time-dependent Maxwell's equations, (3.1), the resonance mode $|\omega\rangle$ must satisfy the relation

$$\omega \hat{H} |\omega\rangle = \hat{H}\hat{C}\hat{H} |\omega\rangle. \quad (3.10)$$

Similarly to Eq. (2.21), Eq. (3.10) is a generalized eigenvalue equation, now for the operator pair $\{\hat{H}, \hat{H}\hat{C}\hat{H}\}$, with eigenvalue ω and eigenvector $|\omega\rangle$.

From the generalized eigenvalue equation (3.10) and the self-adjoint relations (3.5) and (3.7), we derive properties for the resonance modes $|\omega\rangle$ analogous to those of Eqs. (2.22) and (2.23) for the propagation modes $|\beta\rangle$ in Section 2.4. The first is that two generally distinct resonance modes, $|\omega\rangle$ and $|\omega'\rangle$, are energy-orthogonal if $\omega' \neq \omega$, i.e.,

$$\langle \omega | \hat{H} | \omega' \rangle = 0, \quad \text{if } \omega \neq \omega'. \quad (3.11)$$

The second is that, for any resonance mode $|\omega\rangle$ with resonance frequency ω ,

$$\omega \text{ is purely real.} \quad (3.12)$$

The properties (3.11) and (3.12) can be proven in just the same way as Eqs. (2.22) and (2.23) of Section 2.4. The only difference between these proofs is that, in contrast to the operator \hat{Z} from Section 2.4, \hat{H} is assumed positive definite. This follows when $\overset{\leftrightarrow}{\eta}$ is itself a positive-definite dyadic, which is usually the case for dielectric media with negligible dispersion.

Next, we follow as in Section 2.5 and leverage the orthogonality relation (3.11) between resonant modes $|\omega\rangle$ to derive coupled mode equations for a resonant system undergoing temporal modulation. We restrict attention to localized resonance modes $|\omega\rangle$ of finite energy. Then, we utilize (3.11) and the fact that any degenerate modes $|\omega\rangle$ can be chosen as orthogonal [21, 70] to express the matrix elements of \hat{H} with respect to these resonant modes as

$$\langle \omega | \hat{H} | \omega' \rangle = \delta_{\omega, \omega'}. \quad (3.13)$$

In Eq. (3.13), $\delta_{\omega,\omega'}$ equals 1 if $\omega = \omega'$ and 0 otherwise. If the resonance spectrum exhibits degeneracy, the right-hand side of (3.13) is non-zero only when the modes are identical. In Eq. (3.13), we leverage the resonant modes $|\omega\rangle$ to contain unit energy. We note that, in contrast to the propagation modes $|\beta\rangle$, which may carry zero or negative power along z , the resonant modes $|\omega\rangle$ always have positive energy $\langle\omega|\hat{H}|\omega\rangle$, so the normalization $\langle\omega|\hat{H}|\omega\rangle = 1$ is always possible if $|\omega\rangle$ contains finite energy.

Given the eigenvalue equation (3.10) and the orthonormality relation (3.13), we do as in Section (2.5) and leverage them to develop TCMT for media under temporal modulation employing the procedure of quantum-mechanical time-dependent perturbation theory [21, 70]. In this approach, we aim to solve Maxwell's curl equations in the form of Eq. (3.1) with a time-dependent impermeability $\overleftrightarrow{\eta}(t)$ and thus operator $\hat{H}(t)$. Then, we approximate the time-dependent electromagnetic field $|\psi(t)\rangle$ in Eq. (3.1) as a coherent superposition of the resonant modes $|\omega_n\rangle$ of the medium in the absence of temporal modulation. Thus, we write

$$|\psi(t)\rangle \approx \sum_n a_n(t) |\omega_n\rangle. \quad (3.14)$$

As in Section 2.5, we recognize that the expansion of Eq. (3.14) in terms of the modes of a static medium is not exact, but only an approximation. This follows from the same argument that the resonant modes of the static structure satisfy a given set boundary conditions, which generally differ from those of the temporally-modulated medium. Nonetheless, the argument still holds that if the material modulation is of small, then the expansion in Eq. (3.14) is accurate.

Substituting the expansion (3.14) into Eq. (3.1) with a time-dependent operator $\hat{H}(t)$, and utilizing the orthonormality relation (3.13) for the resonance modes $|\omega_n\rangle$, we obtain the following set of coupled equations for the mode amplitudes $a_n(t)$,

$$i \frac{da_n}{dt} = \omega_n a_n(t) + \sum_m D_{nm}(t) a_m(t). \quad (3.15)$$

Similarly to Eq. (2.28), in Eq. (3.15), $D_{nm}(t) \equiv \langle\omega_n|\hat{D}(t)|\omega_m\rangle$ are the matrix elements of the perturbation operator. Though in the case of TCMT, $\hat{D}(t)$ is given by

$$\hat{D}(t) = \hat{H}_0 \hat{C} \Delta \hat{H}(t), \quad (3.16)$$

where $\Delta \hat{H}(t) = (\hat{H}(t) - \hat{H}_0)$ is the difference between the instantaneous operator $\hat{H}(t)$ and the static one \hat{H}_0 , representing the static medium for which the fields $|\omega_n\rangle$ are exact resonant modes. In the next section, we employ Eqs. (3.15) and (3.16) to analyze AFC resulting from modulation of a dielectric resonator.

3.2 Coupled-mode description of AFC

In this section, we utilize the TCMT of Section 3.1 to obtain an integral expression for the adiabatic frequency shift the resonant mode of a dielectric resonator undergoes when the resonator is modulated in time. For this analysis, we assume that only one resonance mode is initially excited and that the modulation is spatially homogeneous so, there is no significant coupling to other resonance modes. Hence, we approximate the time-dependent optical field $|\psi(t)\rangle$ as $a(t)|\omega\rangle$ and Eq. (3.15) simplifies to

$$i \frac{da}{dt} = [\omega + \Delta\omega(t)] a(t), \quad (3.17)$$

where the time-dependent frequency shift $\Delta\omega(t)$ is given by

$$\Delta\omega(t) = \langle\omega|\hat{D}(t)|\omega\rangle. \quad (3.18)$$

The rest of this section aims to analyze and simplify the expression (3.18) for $\Delta\omega(t)$.

First, we recall that, by definition, the optical field $|\omega\rangle$ satisfies the eigenvalue equation (3.10), with \hat{H} replaced by \hat{H}_0 . Then, we assume that \hat{H}_0 is invertible (which is the case if the static impermeability $\overleftrightarrow{\eta}$ itself is an invertible dyadic). Thus $|\omega\rangle$ satisfies $\omega|\omega\rangle = \hat{C}\hat{H}_0|\omega\rangle$. And, because both \hat{C} and \hat{H}_0 are self-adjoint, $\omega\langle\omega| = \langle\omega|\hat{H}_0\hat{C}$. Then, utilizing this observation and substituting Eq. (3.16) for $\hat{D}(t)$ into Eq. (3.18), we obtain

$$\Delta\omega(t) = \omega\langle\omega|\Delta\hat{H}(t)|\omega\rangle. \quad (3.19)$$

In Section 3.1, we normalized the resonant modes $|\omega\rangle$ to possess unit time-averaged energy. For this section, however, it is useful to make this normalization explicit. Thus, Eq. (3.19) becomes

$$\frac{\Delta\omega(t)}{\omega} = \frac{\langle\omega|\Delta\hat{H}(t)|\omega\rangle}{\langle\omega|\hat{H}_0|\omega\rangle}. \quad (3.20)$$

Evaluating then the explicit expressions for the Hermitian forms in the right-hand side of (3.20), we get

$$\frac{\Delta\omega(t)}{\omega} = \frac{\iiint d\mathbf{x} \mathbf{D}_\omega^*(\mathbf{x}) \cdot \Delta\overset{\leftrightarrow}{\eta}(\mathbf{x}, t) \cdot \mathbf{D}_\omega(\mathbf{x})}{4\epsilon_0(U_{E\omega} + U_{M\omega})}. \quad (3.21)$$

In Eq. (3.21), $\mathbf{D}_\omega(\mathbf{x})$ is the displacement field of the resonant mode with frequency ω , and $\overset{\leftrightarrow}{\eta}(\mathbf{x}, t)$ is the perturbation to the impermeability dyadic inducing the frequency shift. $U_{E\omega}$ and $U_{M\omega}$ are the time-averaged electric energy and magnetic energy, respectively, of the resonant mode $|\omega\rangle$ in the absence of modulation. These are given by

$$\begin{aligned} U_{E\omega} &= \frac{1}{4\epsilon_0} \iiint d\mathbf{x} \mathbf{D}_\omega^*(\mathbf{x}) \cdot \overset{\leftrightarrow}{\eta}(\mathbf{x}) \cdot \mathbf{D}_\omega(\mathbf{x}), \\ U_{M\omega} &= \frac{1}{4\mu_0} \iiint d\mathbf{x} \mathbf{H}_\omega^*(\mathbf{x}) \cdot \mathbf{H}_\omega(\mathbf{x}). \end{aligned} \quad (3.22)$$

To simplify Eq. (3.21) further, we require a relation between the electric energy $U_{E\omega}$ and the magnetic energy $U_{M\omega}$ [23]. We assume $\overset{\leftrightarrow}{\eta}$ is Hermitian, i.e., it satisfies (3.6). Of course, this is consistent with our analysis of Section 3.1, as it is necessary for \hat{H} to be self-adjoint. Then, the required relation between $U_{E\omega}$ and $U_{M\omega}$ is given by the complex Poynting's theorem [87]

$$2\omega(U_{E\omega} - U_{M\omega}) = \oint \text{Im}\{\mathbf{E}_\omega^* \times \mathbf{H}_\omega\} \cdot \hat{\mathbf{n}} d\sigma. \quad (3.23)$$

The integral in the right-hand side of Eq. (3.23) is over a surface enclosing the dielectric resonator and extending towards infinity. \mathbf{E}_ω and \mathbf{H}_ω are respectively the electric and magnetic fields associated to the mode $|\omega\rangle$. Again, $\hat{\mathbf{n}}$ is the outward unit vector on the integration surface, and $d\sigma$ is the differential area of the integration surface. Again, we focus on dielectric resonators of high intrinsic quality, so we assume that the fields \mathbf{E}_ω and \mathbf{H}_ω decay sufficiently fast (i.e., at least as $1/r$, where r is the distance from the surface to the resonator) for the integral on the right-hand side of Eq. (3.23) to vanish. Then, we may take the electric energy $U_{E\omega}$ and the magnetic energy $U_{M\omega}$ of $|\omega\rangle$ in the absence of modulation as equal [23, 74]. Taking then $U_{M\omega} = U_{E\omega}$, and substituting the expression for the latter from Eq. (3.22) into Eq. (3.21), we obtain

$$\frac{\Delta\omega(t)}{\omega} = \frac{\iiint d\mathbf{x} \mathbf{D}_\omega^*(\mathbf{x}) \cdot \Delta\overset{\leftrightarrow}{\eta}(\mathbf{x}, t) \cdot \mathbf{D}_\omega(\mathbf{x})}{2 \iiint d\mathbf{x} \mathbf{D}_\omega^*(\mathbf{x}) \cdot \overset{\leftrightarrow}{\eta}(\mathbf{x}) \cdot \mathbf{D}_\omega(\mathbf{x})}. \quad (3.24)$$

To continue simplifying Eq. (3.24), we make some specific assumptions about the forms of the static impermeability $\overset{\leftrightarrow}{\eta}(\mathbf{x})$ and the perturbation $\Delta\overset{\leftrightarrow}{\eta}(\mathbf{x}, t)$. First, we restrict attention to the isotropic case, where both $\overset{\leftrightarrow}{\eta}(\mathbf{x})$ and $\Delta\overset{\leftrightarrow}{\eta}(\mathbf{x}, t)$ are proportional to the identity dyadic $\overset{\leftrightarrow}{I}$. Then, the medium's dielectric properties are characterized by its refractive index $n(\mathbf{x}, t) = 1/\sqrt{\overset{\leftrightarrow}{\eta}(\mathbf{x}, t)}$, where $\overset{\leftrightarrow}{\eta}(\mathbf{x}, t) = \eta(\mathbf{x}, t)\overset{\leftrightarrow}{I}$. Then, by differentiation, $\Delta\eta(\mathbf{x}, t)/\eta(\mathbf{x}) \approx -2\Delta n(\mathbf{x}, t)/n(\mathbf{x})$. Furthermore, we assume that the ratio $\Delta n(\mathbf{x}, t)/n(\mathbf{x})$ is independent of position \mathbf{x} over a modulation region R . Hence, we write [23]

$$\frac{\Delta\omega(t)}{\omega} \approx -\frac{\Delta n(t)}{n} F_{E\omega}^{(R)}, \quad (3.25)$$

where $F_{E\omega}^{(R)}$ is the electric-energy fraction

$$F_{E\omega}^{(R)} = \frac{\iiint_R d\mathbf{x} \eta(\mathbf{x}) |\mathbf{D}_\omega(\mathbf{x})|^2}{\iiint d\mathbf{x} \eta(\mathbf{x}) |\mathbf{D}_\omega(\mathbf{x})|^2} \leq 1. \quad (3.26)$$

Of course, when modulation with the same ratio $\Delta n(t)/n$ is applied to the whole region where light is confined, then the electric-energy fraction $F_{E\omega}^{(R)}$ in Eq. (3.26) equals unity, and (3.25) reduces to $\Delta\omega(t)/\omega = -\Delta n(t)/n$.

Eq. (3.25) with $F_{E\omega}^{(R)} = 1$ has been validated in previous theoretical [24], numerical [22], and experimental [10, 34] investigations of AFC. We note that Eq. (3.24) and its simplified approximation, Eq. (3.25), agree with the first-order approximation in time-independent perturbation theory of the instantaneous resonance-frequency shift of mode $|\omega\rangle$ [74]. This corroborates the intuitive statement that light in the resonance mode $|\omega\rangle$ follows the instantaneous frequency of the resonator [10, 22, 88].

3.3 Coupling between two discrete resonant modes

In this section we analyze the coupled-mode equations for the time evolution of two coupled resonances. We analyze their coupling in the absence of temporal modulation, and at the end, we describe how medium-modulation can be incorporated into the model.

We consider a resonant system comprised of two neighboring dielectric cavities. In the absence of the other, each of them supports a set of resonant modes $|\omega_n\rangle$. If they are sufficiently close in space, then the two set of resonant modes begin to hybridize. From time-independent perturbation theory [21, 70], we know that only the modes which original resonance frequencies are initially close hybridize substantially. Usually, specially if the resonators are similar to each other, the modes hybridize in pairs, one per resonator, as the remaining modes are comparatively far in frequency.

The two coupled modes then hybridize and form two new resonant modes of the overall, two-cavity dielectric system. Spectrally, this coupling results in an anti-crossing of their resonant frequencies [8, 21, 65]. Let ω_+ and ω_- denote the resonant frequencies of the hybridized modes, $|\omega_+\rangle$ and $|\omega_-\rangle$, of the two-cavity system. Then, because they each are exact resonant modes of the two-cavity system, their amplitudes $a_{\pm}(t)$ evolve in time according to the differential equation

$$i \frac{da_{\pm}}{dt} = \omega_{\pm} a_{\pm}. \quad (3.27)$$

As proved in Section (3.1), the modes $|\omega_{\pm}\rangle$ are energy-orthogonal. So the electromagnetic energy of the system equals $|a_+|^2 + |a_-|^2$. Furthermore, this energy is time-invariant, so we have

$$\frac{d}{dt} (|a_+|^2 + |a_-|^2) = 0. \quad (3.28)$$

Though the description in terms of the resonant modes $|\omega_{\pm}\rangle$ is exact and complete, one often desires an alternative one in terms of modes localized in each of the two constituent dielectric cavities. This is the case, for example, when one of the cavities is simultaneously coupled to a waveguide or undergoing temporal modulation, as is of interest to this thesis.

So, instead of describing the field in the two-cavity system a sum of the hybrid modes $|\omega_{\pm}\rangle$, we describe it in terms of the field distributions $|\omega_1\rangle$ and $|\omega_2\rangle$. The latter are defined as linear combinations of the hybrid modes $|\omega_{\pm}\rangle$ so that $|\omega_1\rangle$ is mostly localized in Cavity 1, and $|\omega_2\rangle$ in Cavity 2.

The fields $|\omega_1\rangle$ and $|\omega_2\rangle$ are not resonant modes of the two-cavity system. So they do not evolve harmonically in time. Nonetheless, they are linear combinations of two resonant modes. So applying the corresponding linear transformation to the linear differential equations (3.27), we find they must satisfy differential equations of the form

$$\begin{aligned} i \frac{da_1}{dt} &= \omega_1 a_1 + \kappa_{12} a_2, \\ i \frac{da_2}{dt} &= \kappa_{21} a_1 + \omega_2 a_2. \end{aligned} \quad (3.29)$$

It is usually desirable to retain the property that the sum of the squared norms equals the total energy of the two-dielectric system. So we constrain the linear mapping from $|\omega_+\rangle$ and $|\omega_-\rangle$ to $|\omega_1\rangle$ and $|\omega_2\rangle$ so that the corresponding map from the column vector $(a_+(t), a_-(t))^T$ to the column vector $(a_1(t), a_2(t))^T$ is unitary. Thus, Eq. (3.28) becomes

$$\frac{d}{dt} (|a_1|^2 + |a_2|^2) = 0. \quad (3.30)$$

Substituting Eq. (3.29) into Eq. (3.30), we find that the latter is satisfied if and only if

$$\text{Im}\{\omega_1 |a_1|^2 + \omega_2 |a_2|^2 + \kappa_{12} a_1^* a_2 + \kappa_{21} a_2^* a_1\} = 0. \quad (3.31)$$

Eq. (3.30) must hold for any initial value of a_1 and a_2 . Thus, so must Eq. (3.31). This is the case if and only if

$$\begin{aligned} \text{Im}\{\omega_1\} &= 0, \\ \text{Im}\{\omega_2\} &= 0, \\ \kappa_{12} &= \kappa_{21}^*. \end{aligned} \quad (3.32)$$

To prove that Eq. (3.32) is sufficient for Eq. (3.31) to hold for any value of a_1 and a_2 , one need only substitute (3.32) into (3.31) and verify that the latter is then satisfied identically. To prove that Eq. (3.32) is necessary, we substitute

into (3.31) for (a_1, a_2) the specific values $(1, 0)$, $(0, 1)$, $(1, 1)$ and $(1, i)$. We then find that, for Eq. (3.31) to hold for these particular values of (a_1, a_2) , Eq. (3.32) must hold.

If any or both of the resonators are modulated in time, then their corresponding instantaneous resonance frequencies ω_j ($j = 1, 2$) change in time. To account for this phenomenon, we modify the static frequencies ω_j in Eq. (3.29) as $\omega_j \rightarrow \omega_j + \Delta\omega_j(t)$, with $\Delta\omega_j(t)$ given by expression Eq. (3.24). Of course, the modal displacement fields $\mathbf{D}_\omega(\mathbf{x})$ in (3.24) are then replaced with those of the mode in Cavity j in the absence of the other cavity. This is only an approximation, even to the accuracy of TCMT, because it does not account for inter-cavity coupling. But we expect the error in this approximation to scale as $|\kappa_{12}|\Delta\omega/\omega^2$, and hence to be accurate. This approximation has been found to be accurate for experimental work [8, 19].

3.4 Coupling between resonant mode and waveguide

In this section, we modify the TCMT description of coupling between two discrete resonant modes to describe coupling between the discrete mode of a localized dielectric cavity and the one-dimensional continuum of resonant modes of an optical waveguide. We begin by describing the waveguide as a dielectric cavity, of large length L along one direction which becomes its propagation axis. As a result, the finite-length waveguide supports a large number of modes within the bandwidth of interest which all couple to the modes of the localized dielectric cavity. We write the TCMT equations for this system by generalizing those of Section 3.3. Then, we take the limit of large L , where the discrete set of modes of the waveguide can be approximated as a continuum. To analyze this limit, we introduce a spectral density of modes, as in the solid-state physics theory of electrons in metals [80] and renormalize the modal amplitudes and coupling coefficients as in the theory of quantum optics of a one-dimensional continuum [62, 63]. We emphasize that the analysis of this section is original to this thesis.

As stated above, we model the waveguide as a dielectric cavity of large length L along its propagation axis. Furthermore, we do as in solid-state physics [80] and continuum quantum optics [62] and impose periodic boundary conditions at the ends of the waveguide. Then, the waveguide supports families of discrete set of traveling-wave modes with propagation constant β_n . For simplicity, we assume the waveguide is single-moded and we consider only one polarization. Furthermore, for this thesis we are interested only in coupling of waveguides to ring resonators. Hence, we need only consider modes along one propagation direction. This assumptions and restrictions allow us to restrict attention to just one family of modes of the waveguide, corresponding to a single propagation mode with different frequency and hence propagation constant. Let β_n be the discrete set of propagation constants for this set of traveling-wave modes. Then, as a consequence of the periodic boundary conditions, and length L of the waveguide, these are restricted to the values [80]

$$\beta_n = 2\pi n/L, \quad (3.33)$$

for integer n . The periodic boundary condition for the waveguide field is clearly unphysical. However, it has been shown in solid-state physics that in the large L limit, the choice of boundary conditions does not affect the properties of the system [80]. So the choice of boundary condition is mostly one of mathematical convenience.

We assume that the dielectric cavity coupled to the waveguide only supports one resonant mode on the frequency bandwidth of the optical excitation. Thus, we consider only one resonant mode for the cavity. Thus, the electromagnetic energy U of the cavity-waveguide system consists of a sum of infinite terms, as we include an infinite set of waveguide modes in our analysis. As in Section 3.3, we approximate the cavity and waveguide modes as unitary transformations of the exact modes of the complete cavity-waveguide system. Thus, they are energy-orthogonal and U is expressible as

$$U = |a_r|^2 + \sum_{n=-\infty}^{\infty} |\tilde{a}_n|^2. \quad (3.34)$$

Here a_r is the energy-normalized amplitude of the cavity mode; and \tilde{a}_n , the energy-normalized amplitude of the n th waveguide resonant mode.

The TCMT equations for time evolution of the cavity mode a_r and the waveguide modes a_n can be derived via a generalization of the argument of Section 3.3. Specifically, we impose the requirement that the energy U in Eq. (3.34) be time-independent, in particular when any linear combination of the cavity amplitude a_r and any waveguide mode

\tilde{a}_n is excited. Thus, we obtain

$$\begin{aligned} i \frac{da_r}{dt} &= \omega_r a_r + \sum_{n=-\infty}^{\infty} \tilde{\kappa}_n \tilde{a}_n, \\ i \frac{d\tilde{a}_n}{dt} &= \omega_n \tilde{a}_n + \tilde{\kappa}_n^* a_r. \end{aligned} \quad (3.35)$$

Eqs. (3.34) and (3.35) form a complete description of the time evolution of the cavity-waveguide system. However, they can usually be considerably simplified when the length L of the waveguide is large by introducing the input-output formalism, popular in quantum optics [81–83]. To do so, we first must take the continuum limit of Eqs. (3.34) and (3.35), when L tends to infinity.

We introduce this continuum limit as in the conduction-electron theory of metals [80]. We note that, as L increases, the spacing $\Delta\beta = \beta_{n+1} - \beta_n = 2\pi/L$ between allowed propagation constants in Eq. (3.33) becomes progressively small. However, we assume that the bandwidth of the optical excitation remains fixed and the dispersion relation $\omega = \omega(\beta)$ of the waveguide modes is monotonic. Then, as L increases, the number of waveguide resonant modes over this bandwidth increases accordingly, and the mode amplitudes \tilde{a}_n and the coupling coefficients $\tilde{\kappa}_n$ gradually become slowly varying functions of the waveguide mode number n .

Thus, let $f(\omega_n)$ be a function of the resonance frequency ω_n of the n th waveguide mode. If L is sufficiently large so that the frequency spacing $\Delta\omega$ between waveguide modes is small compared to the extent and bandwidth over which $f(\omega_n)$ varies, then we may accurately approximate the following sum as

$$\sum_{n=-\infty}^{\infty} f(\omega_n) \approx \int_{-\infty}^{\infty} d\omega g(\omega) f(\omega). \quad (3.36)$$

In Eq. (3.36), we introduce the spectral density of modes $g(\omega)$. If we assume the coupling between the cavity and the waveguide is weak, we can then approximate $g(\omega)$ by the density of modes in the absence of the cavity. Then, utilizing (3.33), we have

$$g(\omega) \approx \frac{L}{2\pi} \frac{d\beta}{d\omega} = \frac{L}{2\pi v_g(\omega)}, \quad (3.37)$$

where $v_g(\omega) = d\omega/d\beta$ is the waveguide's group velocity.

We may now substitute Eq. (3.36) into Eq. (3.34) to express the electromagnetic energy U in the continuum limit. Then, the integral in Eq. (3.34) of the waveguide energy becomes $\int_{-\infty}^{\infty} d\omega g(\omega) |\tilde{a}(\omega)|^2$. Here, $|\tilde{a}(\omega)|^2$ is the energy of the waveguide mode with resonance frequency ω . Nonetheless, for Section 3.5, it is convenient to renormalize the mode amplitude $\tilde{a}(\omega)$ to a new variable $a(\omega)$ so that $|a(\omega)|^2$ (rather than $g(\omega) |\tilde{a}(\omega)|^2$) equals the spectral energy density. Thus, we make a change of dependent variable from $\tilde{a}(\omega)$ to $a(\omega)$, with the latter given as

$$a(\omega) = \tilde{a}(\omega) \sqrt{g(\omega)}. \quad (3.38)$$

Then, by construction, the total electromagnetic energy of the system is

$$U = |a_r|^2 + \int_{-\infty}^{\infty} d\omega |a(\omega)|^2. \quad (3.39)$$

Next, substituting Eqs. (3.36) and (3.38) into the TCMT equation for da_r/dt , (3.35), we find the second term in the right-hand side of (3.35) becomes $\int_{-\infty}^{\infty} d\omega \sqrt{g(\omega)} \tilde{\kappa}(\omega) a(\omega)$. Similarly, we evaluate $da(\omega)/dt$ by combining Eqs. (3.35) and (3.38), and we find $a(\omega)$ is driven by a term proportional to $\tilde{\kappa}^*(\omega) \sqrt{g(\omega)} a_r$. Thus, it is convenient to define the spectral coupling coefficient $\kappa(\omega)$ as

$$\kappa(\omega) = \tilde{\kappa}(\omega) \sqrt{g(\omega)}. \quad (3.40)$$

Then, substituting Eqs. (3.36), (3.38) and (3.40) into the TCMT equations (3.35), the latter take the form

$$\begin{aligned} i \frac{da_r}{dt} &= \omega_r a_r + \int_{-\infty}^{\infty} d\omega \kappa(\omega) a(\omega), \\ i \frac{da(\omega)}{dt} &= \omega a(\omega) + \kappa^*(\omega) a_r. \end{aligned} \quad (3.41)$$

In Section 3.5 and later chapters of this thesis, we examine the case of a time-modulated cavity mode $a_r(t)$. Then, as explained in Section 3.3, we replace the cavity resonance frequency ω_r by the time-dependent expression $\omega_r + \Delta\omega_r(t)$, with $\Delta\omega_r(t)$ estimated by Eq. (3.24).

3.5 Input-output analysis of resonator-waveguide coupling

Eq. (3.41) is an infinite system of coupled differential equations for the field amplitudes $a_r(t)$ and $a(\omega, t)$. Thus, it is challenging to obtain its exact solution for arbitrary initial conditions. Hence, we wish to simplify them under suitable approximations. In particular, we aim to obtain an approximate uncoupled equation for the cavity amplitude $a_r(t)$. When the system is time-invariant, this can be accomplished via the Weisskopf-Wigner (WW) method [21, 85] to rigorously derive the input-output relations of TCMT [75, 78, 79]. In this section we illustrate how to do so. Furthermore, we include original discussion explaining how to extend this derivation to account for a cavity with a time-dependent resonance frequency $\omega_r(t)$.

Following the WW method, we first integrate Eq. (3.41) for $a(\omega, t)$ to obtain

$$\begin{aligned} a(\omega, t) = & a(\omega, t_0) \exp[-i\omega(t - t_0)] \\ & - i\kappa^*(\omega) \int_{t_0}^t dt' a_r(t') \exp[-i\omega(t - t')]. \end{aligned} \quad (3.42)$$

Then, we substitute the right-hand side (RHS) of Eq. (3.42) into Eq. (3.41) for $a(\omega, t)$. This yields the integro-differential equation for the cavity field amplitude $a_r(t)$

$$\begin{aligned} \frac{da_r(t)}{dt} = & -i\omega_r a_r(t) \\ & - i \int_{-\infty}^{\infty} d\omega \kappa(\omega) a(\omega, t_0) \exp[-i\omega(t - t_0)] \\ & - \int_{-\infty}^{\infty} d\omega \int_{t_0}^t dt' |\kappa(\omega)|^2 a_r(t') \exp[-i\omega(t - t')]. \end{aligned} \quad (3.43)$$

Because $a(\omega, t_0)$ (i.e., field amplitude of the mode ω at time t_0) is known, it can be taken as an initial condition. Then, Eq. (3.43) formally achieves the objective of an uncoupled equation for $a_r(t)$, without introducing any approximations. However, its solution is still generally challenging, so we must introduce approximations to simplify it.

To do so, we first examine the second term on the RHS of Eq. (3.43). As usual in optics, we assume that the initial waveguide modes $a(\omega, t_0)$ constitute a narrowband excitation. Specifically, we assume that $a_r(\omega, t_0)$ has a bandwidth B small compared to its carrier frequency ω_0 . Additionally, we suppose that

$$B \ll B_\kappa, \quad (3.44)$$

where B_κ is the bandwidth over which $\kappa(\omega)$ changes noticeably in value. In this case, we may write

$$\begin{aligned} \int_{-\infty}^{\infty} d\omega \kappa(\omega) a(\omega, t_0) \exp[-i\omega(t - t_0)] \\ \approx \sqrt{2\pi} \kappa(\omega_0) \bar{a}(t - t_0, t_0), \end{aligned} \quad (3.45)$$

where $\bar{a}(t - t_0, t_0)$ is defined as

$$\bar{a}(t, t') \equiv \frac{1}{\sqrt{2\pi}} \int_{-\infty}^{\infty} d\omega a(\omega, t') \exp(-i\omega t). \quad (3.46)$$

Note that, from Eq. (3.46), $\bar{a}(t, t')$ is a dynamical field variable at time t' . Its first argument t is merely a label for its degree of freedom.

Next, we aim to simplify the third term on the RHS of Eq. (3.43). To do so, we temporarily change the dependent variable $a_r(t)$ in (3.43) from the rapidly oscillating $a_r(t)$ to the slowly-varying $\tilde{a}_r(t)$. These are related by

$$a_r(t) = \tilde{a}_r(t) \exp(-i\omega_r t). \quad (3.47)$$

Then, substituting Eq. (3.47) into Eq. (3.43), the latter becomes

$$\begin{aligned} \frac{d\tilde{a}_r(t)}{dt} = & -i\sqrt{2\pi} \kappa(\omega_0) \exp(i\omega_r t) \bar{a}(t - t_0, t_0) \\ & - \int_{-\infty}^{\infty} d\omega \int_{t_0}^t dt' |\kappa(\omega)|^2 \tilde{a}_r(t') \\ & \times \exp[-i(\omega - \omega_r)(t - t')]. \end{aligned} \quad (3.48)$$

Now, we employ the Weisskopf-Wigner (WW) method [21, 89, 90] to simplify the second term on the RHS of Eq. (3.48). In particular, we follow the analysis of Cohen-Tannoudji et al. in Ref. [21], and extend it to allow for a time-dependent resonance frequency ω_r at the end of this section. First, we change the order of integration in the second term on the RHS of Eq. (3.48). Thus, it becomes

$$\int_{t_0}^t dt' \tilde{a}_r(t') \int_{-\infty}^{\infty} d\omega |\kappa(\omega)|^2 \exp[-i(\omega - \omega_r)(t - t')]. \quad (3.49)$$

As in Ref. [21], we note that the integral over ω in Eq. (3.49) is negligible if $2\pi/(t - t')$ is small compared to B_κ , the bandwidth over which $|\kappa(\omega)|^2$ changes. Therefore, in (3.49), we need only consider values of $(t - t')$ such that $B_\kappa(t - t') \lesssim 2\pi$. Then, we make the Markovian (memory-less) approximation

$$\tilde{a}_r(t') \approx \tilde{a}_r(t), \quad \text{for } t - t' \lesssim 2\pi/B_\kappa. \quad (3.50)$$

We evaluate its accuracy later in this section.

Substituting Eq. (3.50) into Eq. (3.49) and recalling that t for which $(t - t') \gg 2\pi/B_\kappa$ can be neglected, Eq. (3.49) can be written as

$$\tilde{a}_r(t) \int_{-\infty}^{\infty} d\omega |\kappa(\omega)|^2 \left\{ \int_0^{\infty} dt' \exp[-i(\omega - \omega_r)t'] - \int_{t-t_0}^{\infty} dt' \exp[-i(\omega - \omega_r)t'] \right\}. \quad (3.51)$$

In addition, we choose t_0 , the time from which Eq. (3.42) for $a(\omega, t)$ is integrated, such that

$$t - t_0 \gg 2\pi/B_\kappa. \quad (3.52)$$

In this case, the argument of the exponential in the second term inside brackets in Eq. (3.51) oscillates too fast with ω , so its contribution is negligible. Hence, we need only retain the first integral over t' , going from 0 to ∞ , which is the Fourier transform of the Heaviside step function and can be evaluated exactly as [21, 91]

$$\int_0^{\infty} dt' \exp[-i(\omega - \omega_r)t'] = \pi\delta(\omega - \omega_r) - i\text{P.V.} \left(\frac{1}{\omega - \omega_r} \right), \quad (3.53)$$

where $\text{P.V.}(\cdot)$ denotes Cauchy principal value.

In summary, if both Eqs. (3.50) and (3.52) are satisfied, then the second term of the RHS of Eq. (3.48) can be approximated as

$$\int_{t_0}^t dt' \tilde{a}_r(t') \int_{-\infty}^{\infty} d\omega |\kappa(\omega)|^2 \exp[-i(\omega - \omega_r)(t - t')] \approx (\gamma + i\delta) \tilde{a}(t), \quad (3.54)$$

where the decay rate γ and the frequency shift δ are given by

$$\begin{aligned} \gamma &= \pi |\kappa(\omega_r)|^2, \\ \delta &= \text{P.V.} \int_{-\infty}^{\infty} d\omega \frac{|\kappa(\omega)|^2}{\omega_r - \omega}. \end{aligned} \quad (3.55)$$

Correspondingly, if Eqs. (3.50) and (3.52) are satisfied, the integro-differential Equation (3.48) can be approximated by the first-order differential equation

$$\begin{aligned} \frac{da_r(t)}{dt} &= -(i\omega_r + i\delta + \gamma) a_r(t) \\ &\quad - i\sqrt{2\gamma} \exp(i\phi_\kappa) \bar{a}(t - t_0, t_0), \end{aligned} \quad (3.56)$$

where we have changed back from the slowly-oscillating $\tilde{a}_r(t)$ to the rapidly-oscillating $a_r(t)$ as the dependent variable via their relation, Eq. (3.47). In writing Eq. (3.56), we have assumed, for simplicity, that $|\omega_r - \omega_0| \ll B_\kappa$, so $\kappa(\omega_r) \approx \kappa(\omega_0)$, and we defined ϕ_κ so that $\kappa(\omega_r) = \exp(i\phi_\kappa) \sqrt{\gamma/\pi}$.

We now discuss sufficient conditions for the WW approximation, Eq. (3.50), to hold. Writing Eq. (3.56) for the slowly-varying operator $\tilde{a}_r(t)$, we get

$$\begin{aligned} \frac{d\tilde{a}_r(t)}{dt} = & -(i\delta + \gamma)\tilde{a}_r(t) \\ & - i\sqrt{2\gamma}\exp(i\phi_\kappa)\exp(i\omega_r t)\tilde{a}(t-t_0, t_0). \end{aligned} \quad (3.57)$$

Clearly, for Eq. (3.50) to hold, the change in $\tilde{a}_r(t)$ induced by the terms on the RHS of Eq. (3.57) over a time period of the order of $2\pi/B_\kappa$ needs to be relatively small. For the first term to induce small change over a period of $2\pi/B_\kappa$, a sufficient condition is that

$$|\delta| \ll B_\kappa, \quad |\gamma| \ll B_\kappa. \quad (3.58)$$

A sufficient condition for the second term to induce a small relative change in $\tilde{a}_r(t)$, assuming that $\omega_r \approx \omega_0$, is that

$$|\gamma B| \ll B_\kappa^2; \quad (3.59)$$

where, again B is the bandwidth of $a(\omega, t_0)$. Evidently, Eq. (3.59) is satisfied if Eqs. (3.44) and (3.58) are already satisfied.

Equation (3.56) is a differential equation for the cavity field amplitude $a_r(t)$ at time t in terms of the waveguide field $\tilde{a}(t-t_0, t_0)$ at the past time t_0 and with ‘‘degree of freedom’’ $(t-t_0)$, as defined in Eq. (3.46). This time t_0 must necessarily satisfy $t_0 < t$, in order to satisfy Eq. (3.52). Conversely, we may integrate Eq. (3.42) from the present time t to a future time t_1 (such that $t < t_1$), rather than from the past time t_0 to the present time t (such that $t_0 < t$). Then, following the same procedure to derive Eq. (3.56), we obtain the ‘‘time-reversed’’ equation [81, 82]

$$\begin{aligned} \frac{da_r(t)}{dt} = & -\left(i\omega_r + i\delta - \frac{\gamma}{2}\right)a_r(t) \\ & - i\sqrt{\gamma}\exp(i\phi_\kappa)\tilde{a}(t-t_1, t_1). \end{aligned} \quad (3.60)$$

Similarly to Eq. (3.52) for the past time t_0 , the future time t_1 is required to satisfy

$$t_1 - t \gg 2\pi/B_\kappa. \quad (3.61)$$

Thus, Equation (3.60) is a differential equation for $a_r(t)$ at time t , in terms of $\tilde{a}(t-t_1, t_1)$ at the future time t_1 . We then subtract Eq. (3.56) from Eq. (3.60) to obtain

$$\tilde{a}(t-t_1, t_1) = \tilde{a}(t-t_0, t_0) - i\sqrt{2\gamma}\exp(-i\phi_\kappa)a_r(t). \quad (3.62)$$

Equation (3.62) is the so-called input-output relation [81, 82]. It is an algebraic equation for $\tilde{a}(t-t_1, t_1)$ at the future time t_1 in terms of the past time t_0 , and the resonator operator $a_r(t)$ at the present time t ($t_0 < t < t_1$).

Next, we examine how to extend the WW analysis of this section to yield a first-order differential equation similar to Eq. (3.56) when the cavity has a time-dependent frequency $\omega_r(t) = \omega_r + \Delta\omega_r(t)$, rather than a constant value ω_r .

As we discuss below, there are two distinct conditions under which it is still possible to obtain a first-order differential equation for $a_r(t)$, even if its resonance frequency ω_r varies with time. The first is if its deviation $\Delta(t)$ from its static value ω_r is sufficiently small in magnitude. The second is if $\omega(t)$ varies slowly enough in time.

We first consider the case where $\Delta(t)$ is of small magnitude. In this case, we still change from $a_r(t)$ to the slowly-varying $\tilde{a}_r(t)$ using Eq. (3.47), where ω_r is the some average, value for $\omega_r(t)$. Then, we recover Eq. (3.48), albeit with an additional term of $-i\Delta(t)\tilde{a}_r(t)$ in its RHS. We again employ the WW approximation (3.50) and repeat the same analysis to reach Eq. (3.54). The only change is that now, for the WW approximation to hold, we need $\Delta(t)$ to have sufficiently small magnitude so $a(t')$ does not deviate significantly from $a(t)$ as a result. In other words, we require

$$\int_{t'}^t dt'' \Delta\omega_r(t'') \ll 2\pi, \quad t-t' \lesssim 2\pi/B_\kappa, \quad (3.63)$$

for the WW approximation, Eq. (3.50), to still be accurate. Clearly, a sufficient condition for (3.63) to hold is

$$|\Delta\omega_r(t)| \ll B_\kappa. \quad (3.64)$$

Alternatively, $\Delta\omega_r(t)$ may have large magnitude so Eq. (3.64) is not satisfied, so long as it changes rapidly in sign for Eq. (3.63) to still hold.

If $\Delta\omega_r(t)$ does not satisfy Eq. (3.63), a first-order differential equation can still be derived if $\Delta\omega_r(t)$ (and hence $\omega_r(t)$) changes slowly over a time period of $2\pi/B_\kappa$; that is, if

$$\left| \frac{d\omega_r}{dt} \right| \ll \frac{2\pi\omega_r(t)}{B_\kappa}. \quad (3.65)$$

In this case, we may replace $\omega_r t$ by $\int_0^t dt' \omega_r(t')$ in Eq. (3.47). Then, the phase in the integrand of Eq. (3.49) becomes

$$\omega(t-t') - \int_{t'}^t dt'' \omega(t'') \approx [\omega - \omega(t)](t-t'). \quad (3.66)$$

Here, we make use of the fact that we need only consider the phase for $(t-t') \lesssim 2\pi/B_\kappa$. This is because when $(t-t') \gg 2\pi/B_\kappa$ the integral over ω becomes negligible, if $\omega(t)$ changes slowly, as assumed.

Then, the rest of the WW analysis can be carried out as in the case of static ω_r , resulting in a time-dependent relaxation rate $\gamma(t)$ and resonance shift $\delta(t)$, given by Eq. (3.55) with a time-dependent resonance $\omega_r(t)$. Note that, in this case, the factor of $\sqrt{\gamma} \exp(i\phi_\kappa)$ in the second term of the RHS of Eq. 3.56 remains constant, as it depends on the carrier frequency ω_0 of $\bar{a}(t-t_0, t_0)$, and not on the resonator's time-dependent frequency $\omega_r(t)$.

To close this section, we discuss the physical interpretation of the field amplitudes $\bar{a}(t, t')$, defined through Eq. (3.46). As mentioned following Eq. (3.46), $\bar{a}(t, t')$ is a dynamical field variable with ‘‘degree of freedom’’ t at time t' . First, we show how it is related to the electromagnetic field at some point \mathbf{x} of the waveguide and time t . Since the waveguide supports a continuum of modes with propagation constant $\beta(\omega)$ and amplitude $a(\omega, t)$ at time t at time t , the electric field $\mathbf{E}(\mathbf{x}, t)$ and magnetic field $\mathbf{H}(\mathbf{x}, t)$ are given by

$$\begin{pmatrix} \mathbf{E}(\mathbf{x}, t) \\ \mathbf{H}(\mathbf{x}, t) \end{pmatrix} = \frac{1}{\sqrt{2\pi}} \int_{-\infty}^{\infty} d\omega a(\omega, t) \exp[i\beta(\omega)z] \begin{pmatrix} \mathbf{e}(\omega, x, y) \\ \mathbf{h}(\omega, x, y) \end{pmatrix}. \quad (3.67)$$

Here, $\mathbf{e}(\omega, x, y)$ and $\mathbf{h}(\omega, x, y)$ are the transverse electric and magnetic profiles, depending on the transverse coordinates x and y , of the waveguide mode with resonant frequency ω .

As usual in the theory of waveguide propagation [92, 93], we model the frequency-dependence of the propagation constant and the modal profiles by expanding them to first and zeroth order in ω around the carrier frequency ω_0 . Thus, we write

$$\begin{aligned} \beta(\omega) &\approx \omega_0/v_p + (\omega - \omega_0)/v_g, \\ \begin{pmatrix} \mathbf{e}(\omega, x, y) \\ \mathbf{h}(\omega, x, y) \end{pmatrix} &\approx \begin{pmatrix} \mathbf{e}(\omega_0, x, y) \\ \mathbf{h}(\omega_0, x, y) \end{pmatrix}, \end{aligned} \quad (3.68)$$

where v_p is the phase velocity of the waveguide mode at frequency ω_0 ; and v_g , the group velocity at ω_0 . Substituting Eq. (3.68) into Eq. (3.67), we obtain

$$\begin{pmatrix} \mathbf{E}(\mathbf{x}, t) \\ \mathbf{H}(\mathbf{x}, t) \end{pmatrix} \approx \bar{a}(-z/v_g, t) \exp[i\omega_0 z(v_p^{-1} - v_g^{-1})] \begin{pmatrix} \mathbf{e}(\omega_0, x, y) \\ \mathbf{h}(\omega_0, x, y) \end{pmatrix}. \quad (3.69)$$

Thus, $\bar{a}(t, t')$ can be interpreted as the optical field amplitude at time t' and position $-v_g t$, sans a z -dependent phase factor $\exp[i\omega_0 z(v_p^{-1} - v_g^{-1})]$.

Lastly, we examine the relation of the squared modulus $|\bar{a}(t, t')|^2$ and the waveguide's electromagnetic energy U_w . For weak coupling, the latter is given by the integral in Eq. (3.39). By the Fourier relation Eq. (3.46) and Parseval's theorem, this integral can be evaluated in terms of $|\bar{a}(t, t')|^2$ as

$$U_w(t_1) = \int_{-\infty}^{\infty} d\omega |a(\omega, t_1)|^2 = \int_{-\infty}^{\infty} dt |a(t-t_1, t_1)|^2. \quad (3.70)$$

Furthermore, we note that the input-output relation Eq. (3.62) holds for any future time t_1 which satisfies Eq. (3.61). Thus, $\bar{a}(t-t_1, t_1)$ is independent of t_1 so long as this condition is satisfied and depends only on t . Hence, we write

$$|\bar{a}(t-t_1, t_1)|^2 = P(t). \quad (3.71)$$

Substituting Eq. (3.71) into Eq. (3.70), we obtain

$$U_w = \int_{-\infty}^{\infty} dt |a(t-t_1, t_1)|^2 = \int_{-\infty}^{\infty} dt P(t) = \int_{-\infty}^{\infty} dt |a(t_1, t-t_1)|^2. \quad (3.72)$$

In the RHS of (3.72), the condition of Eq. (3.61) becomes

$$-t_1 \gg 2\pi/B_\kappa. \quad (3.73)$$

In terms of the interpretation of Eq. (3.69), Eq. (3.73) only means that the RHS of Eq. (3.72) is accurate when the distance from the cavity, $z = -v_g t_1$, is large compared to the length $2\pi v_g/B_\kappa$. Hence, from the RHS of Eq. (3.72), we find that $dt |\bar{a}(t_1, t - t_1)|^2$ is the contribution to the waveguide energy U_w at time $(t - t_1)$ and longitudinal position $z = -v_g t_1$. Thus, $|\bar{a}(t_1, t - t_1)|^2$ is the instantaneous power in the waveguide at this time and longitudinal position.

Chapter 4

Polarization dynamics in a uniaxial ring resonator

Lithium niobate (LN) is a uniaxial crystal, with its crystallographic Z axis as its extraordinary axis. At the telecom wavelength of 1550 nm, it has an ordinary refractive index of 2.21 and an extraordinary refractive index of 2.14 [11, 94]. To achieve efficient EO modulation in LNOI, as required for AFC, the LN wafer is fabricated as X-cut (or Y-cut), i.e., with its Z axis lying in the plane of the wafer [11, 35, 37, 94]. This generally results in coupling between the transverse-electric (TE) and transverse-magnetic (TM) modes of the LNOI waveguide [95–99]. When the X-cut LN is patterned into a ring cavity, the cavity’s orientation changes continuously with respect to LN’s extraordinary axis along the ring’s circumference. This continuous reorientation can induce non-trivial polarization dynamics along the LNOI ring. These dynamics due to polarization coupling may shift the resonances’ frequencies and alter the state-of-polarization required to excite them [94]. In this chapter, we develop a spatial coupled-mode theory (SCMT) description of the polarization dynamics resulting from the curvature of a uniaxial microring resonator and their effect in the resonant modes of an X-cut LNOI cavity.

Modes of uniaxial planar waveguides have been studied for over forty years [95–100]. It has been found that the mode hybridization depends on the relative orientation of the optic axis with respect to the plane of the core layer and the direction of propagation. Of course, even an isotropic planar waveguide exhibits geometric birefringence due to the difference in the effective refractive indices of its TE and TM modes. When an anisotropic material is used to form a planar waveguide, the modal birefringence is determined by a combination of both geometric and material properties. In a microring resonator, the curvature of the ring waveguide leads to additional complication when the optic axis of the material lies in the plane of the core layer. In this case, the angle between the optic axis and the direction of propagation varies continuously as light propagates along the ring. In general, this continuous rotation complicates the polarization evolution of the guided radiation, as we discuss below.

This chapter is organized as follows. In Section 4.1, we provide an intuitive description of the physics governing the polarization-mode dynamics and introduce the zero-bending model which replaces the ring waveguide with a straight waveguide in which the optic axis changes continuously. In Section 4.2, we determine the coupling matrix due to the continuous optic axis reorientation and discuss the effect of polarization coupling on the resonances of a microring resonator. In Section 4.3, we approximate the modes with those of a slab waveguide and demonstrate that the resulting polarization dynamics are isomorphic to those of a frequency-modulated two-level atom driven by a classical optical field. We exploit this analogy and study polarization coupling in a microring resonator using well-known techniques and concepts of quantum mechanics such as time-dependent perturbation theory, the rotating-wave approximation, and adiabatic following. In Section 4.4, we demonstrate the usefulness of our theory by applying it to the case of a LN waveguide with a silica (SiO_2) substrate and air cladding. In Section 4.5, we summarize the chapter’s results.

4.1 Intuitive description and the zero-bending model

We consider a microring resonator of radius r as sketched in Fig. 4.1. A straight bus waveguide is used to inject light into this resonator at the location where the ring comes closest to the bus waveguide. Generally, the injected light excites a coherent sum of the TE and TM modes of the ring waveguide, depending on its state of polarization (SOP). The core of the ring waveguide is made of an uniaxial anisotropic material. The extraordinary (optic) axis of this uniaxial material lies in the plane of the ring in a fixed direction \hat{u}_e (see Fig. 4.1). As the injected light travels along

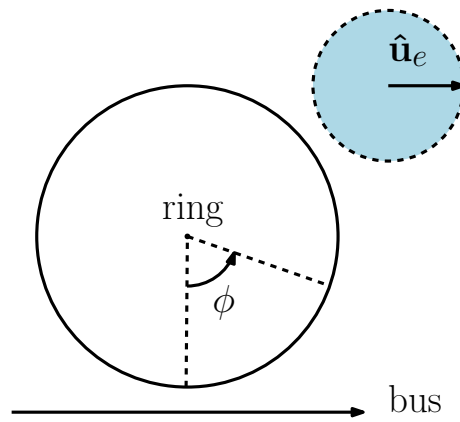
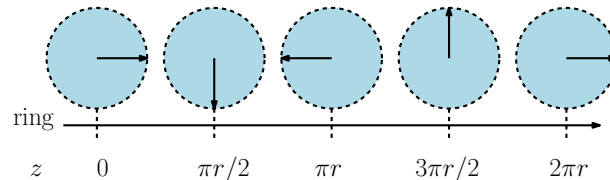
Figure 4.1: A uniaxial microring resonator and the orientation of its optic axis $\hat{\mathbf{u}}_e$.

Figure 4.2: Rotation of the optic axis in the zero-bending model (ZBM) that replaces the curved uniaxial ring with an equivalent straight waveguide.

the ring, sweeping the arc angle ϕ , its SOP changes continuously. This occurs because the relative angle between the optic axis and the direction of propagation varies along the ring.

To understand the evolution of the SOP, one may examine the components of the permittivity dyadic $\overleftrightarrow{\epsilon}$ of the guiding core in a coordinate frame rotating with the ring waveguide. In this rotating frame, the diagonal components of $\overleftrightarrow{\epsilon}$ oscillate, causing an analogous oscillation in the effective indices of the local guided modes. In the rotating frame, the permittivity also develops non-diagonal components, also oscillating in magnitude along the ring. If these non-diagonal elements link electric-field components of different guided modes, these become locally coupled and exchange power. This intuitive description will be given mathematical precision in the sections that follow. The analysis of light propagation even in an isotropic curved waveguide is known to be challenging [101]. Adding material anisotropy to such a waveguide makes the problem even more difficult. It is then desirable to find an equivalent formulation that preserves the fundamental physics. For this purpose, we propose the “zero-bending model” (ZBM), illustrated by Figure 4.2. Effectively, the ZBM replaces the curved waveguide with a straight waveguide along which the extraordinary axis rotates continuously with propagation distance z forming a rotation angle $\phi = z/r$. At a distance $z = 2\pi r$, corresponding to one round trip inside the microring resonator, the optic axis returns to the initial orientation, so the ZBM waveguide is periodic along z with a period $2\pi r$.

The mathematical simplification afforded by the ZBM comes at a cost. This consists of the neglect any effect of the finite curvature of the ring on light propagation other than the continuous reorientation of the optic axis. The most prominent among the neglected effects are the bending loss and the field displacement [101]. The impact of these two effects scales with the ring’s curvature. Hence, we expect the results obtained via the ZBM to be accurate when the ring radius r is large compared to both the wavelength of light, λ , and the characteristic dimension d of the waveguide’s cross-section. This conclusion follows from dimensional analysis, as these are the only other characteristic lengths of the problem, and has been proven to be correct for isotropic bent waveguides [101]. Both conditions, $r \gg \lambda$ and $r \gg d$, are usually satisfied in practice, indicating that our ZBM-based description is applicable to most experimental situations. Of course, higher index contrast between the ring core and substrate results in lower bending losses. So we expect the ZBM to be more accurate in higher-contrast microrings, all else being equal.

If we wished to forgo the ZBM, we could write Maxwell’s curl equations in cylindrical coordinates and consider propagation of the optical field along the azimuthal coordinate ϕ of the ring. Then, we could rederive SCMT as in Chapter 2, but considering propagation along the azimuthal angle ϕ , rather than the Cartesian coordinate z . Then, for

example, the decomposition of $\overset{\leftrightarrow}{\boldsymbol{\epsilon}}$ in Eq. (2.8) would single out the azimuthal component, rather than one along z . The main theoretical difficulty in such a SCMT formulation arises from the fact that the propagation constant β becomes complex, on account of bending loss [60]. This implies that the analog of operator \hat{E} in Eq. (2.11) is not Hermitian and the orthogonality relations (2.26) need no longer hold for curved waveguides. Although orthogonality relations have been obtained for curved waveguides with simplified geometries [102, 103], the presence of bending loss prohibits the formulation of orthogonality relations for a general waveguide cross-section. Of course, one may decide to neglect bending losses and treat \hat{E} as approximately Hermitian, and, consequently, have the orthogonality relations (2.26) hold as an approximation. In such case, however, the ZBM should be accurate and result in simpler calculations.

4.2 Polarization coupling in the ZBM

4.2.1 Perturbation due to permittivity reorientation

Adopting the ZBM, we analyze light propagation in a straight birefringent waveguide oriented along the direction of propagation $\hat{\mathbf{z}}$. Then, we may directly employ the SCMT of Chapter 2 to describe polarization coupling due to the continuous reorientation of the optical axis along the effective straight waveguide.

Equation (2.28) describes how the mode amplitudes $\tilde{a}_n(z)$ are coupled through the dielectric perturbation $\hat{D}(z) = \hat{E}'(z) - \hat{E}$. The next step is to find an expression for $\hat{D}(z)$. For both the unperturbed and perturbed systems, the permittivity is a symmetric dyadic with a value n_o^2 along the two ordinary axes and n_e^2 along the extraordinary (optic) axis. For the unperturbed system, we take the optic axis along the z axis. This orientation matches $\phi = 0$ in Fig. 4.1 (and $z = 0$ in Fig. 4.2). With this choice, the unperturbed basis-modes are TE- and TM-polarized modes; this identification aids subsequent physical interpretation. In the perturbed system, the optic axis rotates on the x - z plane, forming the angle $\phi = z/r$ with respect to the z axis, as depicted in Fig. 4.2.

Based on this description, we write the core's unperturbed and perturbed permittivities, $\overset{\leftrightarrow}{\boldsymbol{\epsilon}}$ and $\overset{\leftrightarrow'}{\boldsymbol{\epsilon}}$, as

$$\begin{aligned}\overset{\leftrightarrow}{\boldsymbol{\epsilon}} &= n_o^2(\hat{\mathbf{x}}\hat{\mathbf{x}} + \hat{\mathbf{y}}\hat{\mathbf{y}}) + n_e^2\hat{\mathbf{z}}\hat{\mathbf{z}}, \\ \overset{\leftrightarrow'}{\boldsymbol{\epsilon}}(\phi) &= n_o^2(\hat{\mathbf{u}}_o(\phi)\hat{\mathbf{u}}_o(\phi) + \hat{\mathbf{y}}\hat{\mathbf{y}}) + n_e^2\hat{\mathbf{u}}_e(\phi)\hat{\mathbf{u}}_e(\phi),\end{aligned}\tag{4.1}$$

where the unit vectors $\hat{\mathbf{u}}_o(\phi)$ and $\hat{\mathbf{u}}_e(\phi)$ are given by

$$\begin{aligned}\hat{\mathbf{u}}_o(\phi) &= \cos\phi\hat{\mathbf{x}} + \sin\phi\hat{\mathbf{z}}, \\ \hat{\mathbf{u}}_e(\phi) &= -\sin\phi\hat{\mathbf{x}} + \cos\phi\hat{\mathbf{z}}.\end{aligned}\tag{4.2}$$

We substitute Eq. (4.1) into Eq. (2.14) to evaluate both \hat{E} and \hat{E}' and use them to write the perturbation \hat{D} in the form

$$\hat{D}(z) = \sum_{n=1}^3 \hat{D}^{(n)} f_n(\phi, \zeta),\tag{4.3}$$

where $\zeta \equiv (n_e^2 - n_o^2)/(n_e^2 + n_o^2)$ is a measure of the guiding core's material birefringence and $\hat{D}^{(n)}$ are z -independent Hermitian operators defined as

$$\begin{aligned}\hat{D}^{(1)} &= \begin{pmatrix} k_0 \bar{\boldsymbol{\epsilon}} C(x, y) \hat{\mathbf{x}}\hat{\mathbf{x}} & 0 \\ 0 & 0 \end{pmatrix}, \\ \hat{D}^{(2)} &= \begin{pmatrix} 0 & -iC(x, y) \hat{\mathbf{x}}\hat{\mathbf{z}} \cdot (\nabla_t \times) \\ i\nabla_t \times [\hat{\mathbf{z}}\hat{\mathbf{x}}C(x, y)] & 0 \end{pmatrix}, \\ \hat{D}^{(3)} &= \begin{pmatrix} 0 & 0 \\ 0 & (k_0 \bar{\boldsymbol{\epsilon}})^{-1} \nabla_t \times [C(x, y) \nabla_t \times] \end{pmatrix}.\end{aligned}\tag{4.4}$$

Here, $\bar{\boldsymbol{\epsilon}} = (n_e^2 + n_o^2)/2$ and $C(x, y)$ is a generalized function (or distribution) that equals unity inside the waveguide's

cross-section and zero outside of it. The scalar functions $f_n(\phi, \zeta)$ in Eq. (4.3) depend on $z = r\phi$ through

$$\begin{aligned} f_1(\phi, \zeta) &= \zeta(1 - \cos 2\phi) - \zeta^2 f(\phi, \zeta) \sin^2 2\phi, \\ f_2(\phi, \zeta) &= \zeta f(\phi, \zeta) \sin 2\phi, \\ f_3(\phi, \zeta) &= (1 + \zeta)^{-1} - f(\phi, \zeta), \end{aligned} \tag{4.5}$$

where the auxiliary function $f(\phi, \zeta)$ is defined as

$$f(\phi, \zeta) \equiv (1 + \zeta \cos 2\phi)^{-1}. \tag{4.6}$$

Equations (4.3) to (4.6) indicate that the z dependence of $\hat{D}(z)$ comes only from the ϕ dependence of the scalars $f_n(\phi, \zeta)$, which are periodic in $\phi = z/r$ with a period of π . Therefore, $\hat{D}(z)$ is periodic in z with period πr . This agrees with physical intuition, as the ring in Figure 4.1 is invariant when rotated by 180 degrees around the axis normal to the plane of propagation.

In Fig. 4.1, we assumed the bus waveguide to be aligned with the optic axis, so it was natural to define $\phi = 0$ at the point on the ring closest to the bus. In practice, one could have the bus perpendicular to the optic axis, as the bus would still possess independent TE and TM modes. Of course, our analysis can still be applied to such a configuration. The net effect is that formulas (4.3) to (4.6) still apply, provided the birefringence parameter ζ is replaced with $-\zeta$. In Fig. 4.1, we also assumed that light is injected into the bus from the left side, so that it travels counterclockwise along the ring. Our analysis can also be used when light is injected from the right side and travels clockwise inside the ring. It is easy to verify that Eqs. (4.3) to (4.6) can still be used if replace ϕ with $-\phi$. If the bus is perpendicular to the optic axis and light travels clockwise inside the ring, one needs to replace both ζ with $-\zeta$ and ϕ with $-\phi$.

4.2.2 Resonance condition for microring resonators

In Chapter 2, we found that the mode amplitudes $\tilde{a}_n(z)$ satisfy the coupled-mode equations (2.28). These equations can be solved to find the field amplitudes at any point $z = r\phi$ along the ring, if we know their values at some $z_0 = r\phi_0$. Because the coupled-mode equations are linear, we can write their solution in the form

$$\tilde{a}(\phi) = \tilde{U}(\phi, \phi_0) \tilde{a}(\phi_0), \tag{4.7}$$

where $\tilde{a}(\phi)$ is a column vector whose n -th element equals $\tilde{a}_n(\phi)$ and $\tilde{U}(\phi, \phi_0)$ is a square matrix. The evolution matrix $\tilde{U}(\phi, \phi_0)$ is unitary because the propagation constants β_n are real and the perturbation operator $\hat{D}(z)$ is Hermitian. As is well known, a unitary matrix has a complete set of orthonormal eigenvectors and all its eigenvalues have unit magnitude.

The microring's resonance frequencies are implicitly determined by the round-trip matrix $\tilde{U}(2\pi, 0)$, which maps the initial amplitudes $\tilde{a}(0)$ to those obtained after one round trip around the ring. To see this, observe that the eigenvectors of $\tilde{U}(2\pi, 0)$ represent the polarization states that reproduce themselves after each round trip up to a phase factor equal to the corresponding eigenvalue. If this eigenvalue equals one, the eigenstate reproduces itself exactly after a round trip, i.e., $\tilde{a}(2\pi) = \tilde{a}(0)$. This is the resonance condition. Recall that $\hat{D}(z)$ depends on frequency through the wavenumber $k_0 \equiv \omega/c$ in Eq. (4.4), and consequently so does $\tilde{U}(2\pi, 0)$. Hence, there exists a discrete set of values of the frequency ω for which one of the eigenvalues of $\tilde{U}(2\pi, 0)$ equals one. These values of ω constitute the resonance frequencies of the microring resonator. Because coupling between the TE and TM modes changes the eigenvalues of $\tilde{U}(2\pi, 0)$, we expect this coupling to shift the ring's resonance frequencies.

4.3 Approximate Analytic Solution of Coupled-Mode Equations

4.3.1 Simplification of the coupled-mode equations

Given the form of the perturbation operator \hat{D} in Eq. (4.3), the coupled-mode equations (2.28) in general must be solved numerically. In theory, one could leverage the periodicity of $\hat{D}(z)$ to employ Floquet theory [104]. However,

this approach obscures the physics and still require new approximations like the truncation of an infinite Fourier series. In this section we find approximate analytical solutions to Eqs. (2.28) after introducing suitable simplifications.

The approximations we make are as follows. First, we assume that the originally unbent ring waveguide (the unperturbed waveguide in the ZBM) either supports only fundamental TE and TM modes or only these two modes are excited by the light injected into the ring. Even in the presence of higher-order modes, this assumption holds if the difference between the effective indices of different order is sufficiently large that coupling between them is phase-mismatched. For brevity, we follow convention and denote the fundamental TE and TM modes by s and p , respectively.

Second, we assume that the material anisotropy is small, so the anisotropy parameter ζ satisfies $|\zeta| \ll 1$ and we can expand $f_n(\phi, \zeta)$ in Eq. (4.3) in a power series in ζ and retain only terms up to the first order. This assumption is consistent with the use of SCMT and usually holds in practice. For example, $|\zeta| = 0.032$ for a LN waveguide at wavelengths near 1550 nm [94].

Third, we assume that the cross section of the ring waveguide is such that its one dimension is much larger than the other one, i.e., the modes are strongly confined only along one dimension. Hence, we may approximate the waveguide cross-section as one dimensional by taking the larger dimension as infinite. These assumptions facilitate numerical calculations and reduces the number of free parameters in the problem.

Next we examine again the geometry of the ring waveguide in Fig. 4.2, where both the ring and the optic axis lie in the x - z plane and the y axis is normal to this plane. To approximate the waveguide cross-section as one-dimensional, we could extend it infinitely in either the x or y direction. If the waveguide is kept narrow in the x direction but is much thicker in the y -direction, we call it as an out-of-plane slab waveguide. If the waveguide is relatively thin but much wider in the x -direction, we refer to as an in-plane slab. We find that these two configurations behave quite differently from the standpoint of mode coupling.

In Section A.2, we show that the matrix element $D_{sp}(z)$ (as introduced in Eq. (2.28) of Section 2.5) vanishes for the out-of-plane slab waveguide, indicating that the s and the p modes do not couple in such waveguides. In fact, the only effect of the permittivity reorientation is a shift of the propagation constant for the p mode. This agrees with previous theoretical investigations of the normal modes of such slab waveguides [105]. In contrast, the s and the p modes generally undergo coupling for in-plane slab waveguides. Thus, unless otherwise stated, we focus subsequent analysis only on in-plane waveguides which widths are much larger than their thicknesses. This is also often the case in practice, so the in-plane waveguide is the configuration of technological interest too.

This distinction between the coupling behavior of in-plane and out-of-plane waveguides can be understood by analyzing the electric-field components of the guided modes for each waveguide geometry. The electric field of the TE mode of the in-plane waveguide lies in the plane of propagation. So does the longitudinal electric field of its TM mode. These two fields are coupled by the anisotropic permittivity dyadic, as it possesses non-diagonal components mapping transverse fields to longitudinal ones and vice versa. In contrast, the out-of-plane waveguide has the electric field of its TE mode normal to the plane of propagation. Rotation of the direction of propagation relative to the in-plane optic axis cannot result in non-diagonal permittivity elements mapping this TE field into the plane. Consequently, in an out-of-plane waveguide, a TE mode cannot couple to a TM mode, which electric field lies completely in the plane of propagation.

We should also mention that the TE-TM mode coupling depends on whether the in-plane waveguide's cladding and substrate (assumed isotropic) have the same or different refractive indices. If these indices are the same (symmetric case), the TE (TM) modes have definite spatial parity and even orders couple only to TM (TE) modes of odd orders (see Section A.2). If such a waveguide supports only fundamental modes, no coupling occurs between its TE- and TM-polarized modes to the accuracy of SCMT. If the cladding and substrate refractive indices differ (asymmetric case), though, the modes no longer have definite parity so the fundamental TE- and TM-modes couple.

4.3.2 Analysis of the simplified coupled-mode equations

With the preceding simplifications, the amplitude vector $\tilde{a}(\phi)$ becomes two dimensional, with elements $\tilde{a}_s(\phi)$ and $\tilde{a}_p(\phi)$, and can be interpreted as a Jones vector. Of course, one should be careful with this interpretation, as the guided modes possess non-homogeneous spatial distributions and longitudinal components due to mode confinement. In addition, each polarization-mode is normalized to carry unit power, rather than keeping a constant intensity ratio at any point in space. Hence, the electric field generally does not trace the traditional polarization ellipse as in plane-wave optics.

Next, we consider the matrix elements $D_{nm}^{(l)}$ of the operators $\hat{D}^{(l)}$ ($l = 1, 2, 3$) with n, m taking values s or p . As proved in Section A.2, for the in-plane geometry, only four of the twelve possible matrix elements are non-vanishing. These are $D_{ss}^{(1)}$, $D_{sp}^{(2)}$, $D_{ps}^{(2)} = [D_{sp}^{(2)}]^*$ and $D_{pp}^{(3)}$. Also, $D_{ss}^{(1)}$ and $D_{pp}^{(3)}$ are purely real because the matrices $D^{(l)}$ are Hermitian.

To further simplify the problem, we introduce a new column vector $a(\phi)$ via

$$\tilde{a}(\phi) = \exp[i\theta(\phi)]a(\phi), \quad (4.8)$$

where $\theta(\phi)$ is the common phase acquired by $\tilde{a}(\phi)$ during propagation along the ring:

$$\theta(\phi) = \frac{1}{2}r(\beta_s + \beta_p)\phi + \frac{1}{2}r\zeta \left(D_{ss}^{(1)} - D_{pp}^{(3)} \right) \left(\phi - \frac{1}{2}\sin 2\phi \right), \quad (4.9)$$

where we have performed a small ζ truncation, as discussed in Subsection 4.3.1.

Then, setting $\phi = z/r$ as the independent variable, the coupled-mode equations become

$$-i \frac{da}{d\phi} = H(\phi)a, \quad (4.10)$$

where $H(\phi)$ is a ϕ -dependent 2×2 matrix, akin to a time-dependent Hamiltonian in quantum mechanics. It may be written in terms of the Pauli spin matrices σ_n ($n = 1, 2, 3$) as

$$H(\phi) = \frac{1}{2}(\Delta_0 + \Delta_1 \cos 2\phi) \sigma_1 + (\kappa \sin 2\phi) \sigma_3, \quad (4.11)$$

where

$$\sigma_1 = \begin{pmatrix} 1 & 0 \\ 0 & -1 \end{pmatrix}, \quad \sigma_2 = \begin{pmatrix} 0 & 1 \\ 1 & 0 \end{pmatrix}, \quad \sigma_3 = \begin{pmatrix} 0 & -i \\ i & 0 \end{pmatrix}. \quad (4.12)$$

We follow optics convention [106, 107] and label the Pauli matrices such that the Stokes parameters S_n are obtained through $S_n = a^\dagger \sigma_n a$.

In Eq. (4.11), we introduced three parameters that govern polarization dynamics of the microring. These are the ring-averaged detuning Δ_0 ; the detuning-oscillation amplitude Δ_1 ; and the coupling coefficient κ . The three parameters can be explicitly evaluated from the relations

$$\begin{aligned} \Delta_0 &= r(\beta_s - \beta_p) - \Delta_1, \\ \Delta_1 &= -r\zeta \left(D_{ss}^{(1)} + D_{pp}^{(3)} \right), \\ \kappa &= -r\zeta \operatorname{Im} \left\{ D_{sp}^{(2)} \right\}, \end{aligned} \quad (4.13)$$

where, naturally, β_s and β_p are the propagation constants of the unperturbed s and p modes, respectively.

Expressions (4.10) and (4.11) constitute the main result of this section. They describe how the amplitudes of TE and TM modes evolve along a microring resonator with the angle ϕ . These equations are mathematically equivalent to those governing a frequency-modulated two-level atom driven by a classical optical field [108]. The first term, proportional to σ_1 , represents a local mode detuning that oscillates between $(\Delta_0 - \Delta_1)$ and $(\Delta_0 + \Delta_1)$ along the ring. The last term represents polarization coupling whose magnitude oscillates between $-\kappa$ and κ . As shown later, the combination of these two effects leads to complicated polarization dynamics on the Poincaré sphere.

We find that the form of the matrix $H(\phi)$ in Eq. (4.11) agrees with the intuitive description of polarization coupling in Section 4.1. The oscillation of its diagonal term, modeling local detuning, is a consequence of the oscillation in the diagonal components of the permittivity in the frame rotating with the ring waveguide. Observe that the detuning extrema occur when ϕ is an integer multiple of $\pi/2$, when the direction of propagation is either parallel or perpendicular to the optic axis, so the diagonal permittivity elements are themselves extremized. On the other hand, the oscillation of the non-diagonal term of $H(\phi)$, proportional to σ_3 , occurs due to the oscillation of the non-diagonal permittivity elements in the rotating frame. Thus, mode coupling is strongest when ϕ is an odd multiple of $\pi/4$, just where the non-diagonal permittivity elements are extremized.

Note that $H(\phi)$ varies in the three-dimensional parameter space spanned by Δ_0 , Δ_1 , and κ . Since $H(\phi)$ alone governs the polarization dynamics in Eq. (4.10), the polarization dynamics also vary in this space. Generally, Eq. (4.10)

must be solved numerically. Nonetheless, approximate analytic solutions can be obtained in certain regions of the parameter space by employing analytic tools for quantum systems with a time-dependent Hamiltonian [70]. In the following subsections, we discuss these approximate solutions and their regions of validity.

Again, as Eq. (4.10) is linear with the Hermitian $H(\phi)$, we may write its solution as $a(\phi) = U(\phi, 0)a(0)$, where $U(\phi, 0)$ is unitary and satisfies

$$-i \frac{dU}{d\phi} = H(\phi)U(\phi, 0), \quad (4.14)$$

with the initial condition $U(0, 0) = 1$. Of course, we may relate this $U(\phi, 0)$ to the full round-trip matrix $\tilde{U}(\phi, 0)$ of Subsection 4.2.2 through the relation

$$\tilde{U}(\phi, 0) = \exp[i\theta(\phi)]U(\phi, 0), \quad (4.15)$$

with $\theta(\phi)$ given by Eq. (4.9). In what follows, we provide approximate expressions for $U(\phi, 0)$ and investigate its properties and the corresponding polarization eigenstates of the ring.

4.3.3 Perturbative regime

One way to solve Eq. (4.14) approximately is using a perturbative approach. As is known from quantum mechanics [70], this type of solution is accurate when $H(\phi)$ can be written as $H = H_0 + V$, where V is a small perturbation. Then, we may write the solution in the form of a rapidly-converging Dyson series:

$$U(\phi, 0) = \sum_{l=0}^{\infty} U^{(l)}(\phi, 0), \quad (4.16)$$

where the l th terms $U^{(l)}(\phi, 0)$ scales as the l -th power of the perturbation.

The zeroth-order term $U^{(0)}(\phi, 0)$ is defined as the evolution operator for zero perturbation. So we can evaluate this term analytically, we take H_0 as the first term on the right-hand-side of Eq. (4.11) (proportional to σ_1). It follows that

$$V(\phi) = (\kappa \sin 2\phi)\sigma_3. \quad (4.17)$$

and

$$\begin{aligned} U^{(0)}(\phi, 0) &= \exp\left(i \int_0^\phi d\phi' H_0(\phi')\right), \\ &= \exp\left[\frac{1}{2}i\sigma_1 \left(\Delta_0\phi + \frac{1}{2}\Delta_1 \sin 2\phi\right)\right]. \end{aligned} \quad (4.18)$$

The first-order correction $U^{(1)}(\phi, 0)$ is then given by [70]

$$U^{(1)}(\phi, 0) = i \int_0^\phi d\phi' U^{(0)}(\phi, \phi') V(\phi') U^{(0)}(\phi', 0). \quad (4.19)$$

Substituting $V(\phi)$ and $U^{(0)}$ from Eqs. (4.17) and (4.18), the integration in Eq. (4.19) can be performed employing the Jacobi–Anger expansion [109]

$$\exp(iz \sin \theta) = \sum_{n=-\infty}^{\infty} J_n(z) \exp(in\theta), \quad (4.20)$$

and taking its derivative with respect to z , where $J_n(z)$ is the Bessel function of the first kind and integer order n , evaluated at z . Thus, we obtain

$$\begin{aligned} U^{(1)}(\phi, 0) &= i\kappa\phi \sum_{n=-\infty}^{\infty} J'_n(\Delta_1/2) \text{sinc}[\phi(n + \Delta_0/2)] \\ &\quad \times (\sigma_2 \cos \chi_n - \sigma_3 \sin \chi_n). \end{aligned} \quad (4.21)$$

Here, $J'_n(z)$ is defined as the derivative of $J_n(z)$ with respect to z ; the function $\text{sinc}(x)$, as

$$\text{sinc}(x) \begin{cases} \sin(x)/x, & \text{for } x \neq 0, \\ 1, & \text{for } x = 0; \end{cases} \quad (4.22)$$

and the angle $\chi_n(\phi)$, as

$$\chi_n(\phi) \equiv \frac{1}{4}\Delta_1 \sin 2\phi - n\phi. \quad (4.23)$$

As is usual in quantum dynamics, we can neglect terms of order higher than one in the Dyson series (4.16) for a small perturbation V .

The most striking feature of Eq. (4.21) is the appearance of an infinite number of coupling resonances occurring when $n + \Delta_0/2 = 0$ for some integer n . Each of these resonances is the product of three factors. One factor is the unitary matrix $(\sigma_2 \cos \chi_n - \sigma_3 \sin \chi_n)$. The second one is the sinc term representing the decrease in strength of the resonance as $\Delta_0/2$ moves away from $-n$. This kind of dependence is typical for a quantum-mechanical system driven by a sinusoidal classical field [110]. The third factor is the weighting function $J'_n(\Delta_1/2)$. Using the recurrence relation $J'_n(z) = [J_{n-1}(z) - J_{n+1}(z)]/2$ and the property $J_n(0) = \delta_{n,0}$ [109], we find that when $\Delta_1 = 0$, $J'_n(0) = (\delta_{n,1} - \delta_{n,-1})/2$, and the infinite sum reduces to only two terms with $n = \pm 1$. As Δ_1 deviates from zero, new resonances appear for other values of n . Even though the amplitudes of original two resonances decrease, they remain prominent for small values of $|\Delta_1|$.

As discussed in Section 4.2.2, $U(2\pi, 0)$ determines the ring's polarization eigentates and the resonances of the microring resonator. From Eq. (4.18), $U^{(0)}(2\pi, 0) = \exp(i\pi\Delta_0\sigma_1)$. From Eq. (4.21), the first-order term $U^{(1)}(2\pi, 0)$ becomes proportional to σ_2 because $\chi_n = -2\pi n$ and the σ_3 term vanishes. Furthermore, when Δ_0 is an integer, $U^{(1)}(2\pi, 0)$ simplifies to

$$U^{(1)}(2\pi, 0) = \begin{cases} 0, & \text{for } \Delta_0 \text{ odd,} \\ i2\pi\kappa\sigma_2 J'_m(\Delta_1/2), & \text{for } \Delta_0 \text{ even,} \end{cases} \quad (4.24)$$

where m is the integer satisfying

$$\Delta_0 + 2m = 0. \quad (4.25)$$

So when Δ_0 is an odd integer, the first-order correction to the round -trip matrix $U(2\pi, 0)$ vanishes and $U(2\pi, 0) \approx \exp(i\pi\Delta_0\sigma_1)$ to the first order in V . In addition, note that even for fixed Δ_1 and κ , the maximum amplitude of $U^{(1)}(2\pi, 0)$ does not necessarily align with even values of Δ_0 , as Eq. (4.24) seems to suggest. This is because, as Δ_0 moves away from $-2m$, the resonant term $n = m$ diminishes in strength but the other terms of the infinite sum in Eq. (4.21) become nonzero and start to contribute to $U^{(1)}(2\pi, 0)$.

We briefly address the validity of the perturbative solution. We truncated the Dyson series in Eq. (4.16) to its first two terms. This series is known to converge rapidly when the perturbation V is small. From Eq. (4.17), V can be said to be small for any ϕ only if κ is small. How small κ must be is a subtle question. A necessary condition is that the power transferred between the TE and TM modes must be negligible, i.e., $|U_{12}(\phi, 0)|^2 \ll 1$. Assuming that $J'_n(\Delta_1/2) \sim 1$ for the coupling resonance with n closest to $-\Delta_0/2$, we get $|\kappa| \ll 2$ as a necessary condition for the perturbative approximation to be valid.

4.3.4 Resonant regime

As we just saw, the modulation of level spacing induced by Δ_1 results in an infinite set of coupling resonances in the perturbative regime. It turns out that this conclusion holds even beyond the accuracy of the first-order perturbation. When Δ_0 approximately satisfies Eq. (4.25) for some integer m , the m th resonance in Eq. (4.21) is most strongly excited. It follows that, if the coupling strength κ is small enough, it is justified to neglect all other coupling resonances, since only the m -th resonance has its effect accumulate and become non-negligible as ϕ varies from 0 to 2π .

Under this approximation, we show in Section B.1 that $U(\phi, 0)$ is found to be given by

$$U(\phi, 0) \approx \exp[i\sigma_1\chi_m(\phi)] \exp(i\phi H_{\text{RWA}}), \quad (4.26)$$

where $\chi_m(\phi)$ is defined in Eq. (4.23) and the matrix H_{RWA} is given by

$$H_{\text{RWA}} = \frac{1}{2}(\Delta_0 + 2m)\sigma_1 + \kappa J'_m(\Delta_1/2)\sigma_2. \quad (4.27)$$

The neglect of the non- resonant terms of $H(\phi)$ is known as the rotating-wave approximation (RWA) in quantum mechanics [108].

Recalling from Eq. (4.23) that $\chi_m(2\pi) = -2\pi m$, we find

$$U(2\pi, 0) \approx \exp(i2\pi H_{\text{RWA}}). \quad (4.28)$$

Thus, the eigenvectors of H_{RWA} are approximately those of $U(2\pi, 0)$. After a round-trip, they each acquire a phase of $\theta(2\pi) \pm \pi\Delta_{\text{RWA}}$, where $\theta(2\pi)$ is the common round-trip phase from Eq. (4.9) and is Δ_{RWA} the difference between the eigenvalues of H_{RWA} . It is straightforward to verify that

$$\Delta_{\text{RWA}} = \sqrt{(\Delta_0 + 2m)^2 + 4\kappa^2 [J'_m(\Delta_1/2)]^2}. \quad (4.29)$$

In particular, when Eq. (4.25) is nearly satisfied, H_{RWA} is close to proportional to σ_2 , and its polarization eigenstates approximately correspond to the Jones vectors $(1, 1)^T/\sqrt{2}$ and $(1, -1)^T/\sqrt{2}$. These are also approximately the polarization eigenstates of the round-trip matrix $U(2\pi, 0)$, if the RWA applies.

To understand these results, we note that, in the absence of coupling ($\kappa = 0$), TE and TM modes are independent and acquire different phases after a round trip. When Eq. (4.25) is satisfied, they acquire the same phase (up to a multiple of 2π). Hence, a non-zero coupling lifts the phase-factor degeneracy and determines the eigenvector structure of $U(2\pi, 0)$.

We refer to the region where Eq. (4.25) approximately applies and $|\kappa|$ is small enough for Eq. (4.26) to hold as the resonant regime. If $|\kappa|$ becomes too large, the contributions to $H(\phi)$ neglected in the RWA may noticeably alter the polarization dynamics, despite their effect not accumulating over ϕ . This pair of conditions may appear stricter than those governing the perturbative regime, which requires only $|\kappa|$ to be small. However, this is not the case because Eq. (4.26) is valid for values of $|\kappa|$ larger than those for which Eq. (4.19) holds. To see this, note that the expression in Eq. (4.26) is unitary, while the two-term Dyson series $U \approx U^{(0)} + U^{(1)}$ is not. This feature implies that Eq. (4.26) automatically conserves the total power $a^\dagger a$, while the sum $U^{(0)} + U^{(1)}$ only approximately does so if $|\kappa| \ll 2$.

4.3.5 Adiabatic regime

In the adiabatic regime, if the polarization state $a(\phi)$ is an eigenstate of the matrix $H(\phi)$, it continuously follows the local eigenstate of $H(\phi)$ as ϕ increases and $H(\phi)$ varies. Let $a^{(\pm)}(\phi)$ be the local eigenstates, i.e., the two Jones vectors satisfying the eigenvalue equation

$$H(\phi)a^{(\pm)}(\phi) = k_{\pm}(\phi)a^{(\pm)}(\phi), \quad (4.30)$$

with eigenvalues $k^{(\pm)}(\phi)$ depending on ϕ . The adiabatic theorem states that, in the limit $|k_+(\phi) - k_-(\phi)| \rightarrow \infty$, $U(\phi, 0)$ tends toward [70, 111]

$$U_A(\phi, 0) = \sum_{n \in \{+, -\}} \exp \left[i \int_0^\phi d\phi' k_n(\phi') \right] \times \exp[i\gamma_n(\phi)] a^{(n)}(\phi) \left[a^{(n)}(0) \right]^\dagger, \quad (4.31)$$

The argument of the first exponential in this expression is known as the dynamic phase; and the argument of the second one, $\gamma_n(\phi)$, as the geometric phase. In the adiabatic approximation [111], $U(\phi, 0) \approx U_A(\phi, 0)$. A good rule of thumb [70, 112] for its validity is that the difference in eigenvalues should be much larger than the characteristic frequency at which $H(\phi)$ changes. For our problem, this condition requires $|k_+ - k_-| \gg 2$ from Eq. (4.11).

The calculation of the geometric phase $\gamma_n(\phi)$ in Eq. (4.31) is generally cumbersome. Nevertheless, following Berry [113], we can evaluate its value when $H(\phi)$ returns to its original value $H(0)$. For our microring resonator, this happens when ϕ is an integer multiple of π . Applying Berry's general result, we show in Section B.2 that

$$\exp[i\gamma_{\pm}(\pi)] = \begin{cases} -1, & |\Delta_0| < |\Delta_1| \\ +1, & |\Delta_0| > |\Delta_1| \end{cases} \quad (4.32)$$

and

$$\exp[i\gamma_{\pm}(2\pi)] = \exp[i2\gamma_{\pm}(\pi)] = 1, \quad \text{for } |\Delta_0| \neq |\Delta_1|. \quad (4.33)$$

No expression for the geometric phase exists when $|\Delta_0| = |\Delta_1|$, because the adiabatic approximation does no longer hold in that case, as explained in Section B.2.

Naturally, the round-trip matrix $U(2\pi, 0)$ can be approximated with $U_A(2\pi, 0)$ in the adiabatic regime. Additionally, it takes a substantially simpler form compared to the general expression in Eq. 4.31. To see this, recall from Eq. (4.11) that the eigenstates of $H(0) = H(2\pi)$ are $(1, 0)^T$ and $(0, 1)^T$. Also, it is easy to see that the trace of $H(\phi)$ vanishes. Hence, its eigenvalues satisfy $k_+(\phi) = -k_-(\phi) = \Delta(\phi)/2$ where $\Delta(\phi)$ is the eigenvalue difference. From Eq. (4.11), $\Delta(\phi)$ is readily found to be

$$\Delta(\phi) = \sqrt{[\Delta_0 + \Delta_1 \cos(2\phi)]^2 + 4\kappa^2 \sin^2(2\phi)}. \quad (4.34)$$

Using this result, one gets the simple expression:

$$U_A(2\pi, 0) = \exp \left[\pm i\sigma_1 \int_0^\pi d\phi \Delta(\phi) \right], \quad (4.35)$$

In Eq. (4.35), \pm is taken as $+$ if the TE mode at $\phi = 0$ has higher effective index than the TM mode; and is taken as $-$ otherwise.

So we find that, in the adiabatic regime, the ring's polarization eigenstates are always TE and TM polarizations. The net effect of the polarization coupling induced by κ is merely to alter the phase difference after a round-trip according to Eqs. (4.34) and (4.35).

4.4 A Practical Example

To illustrate the usefulness of our coupled-mode formalism, we examine a specific example and focus on a material platform based on LN [94]. More precisely, we model a microring resonator made with a waveguide whose LN core with silicon dioxide (SiO_2) substrate and air cladding. The resonator is excited with a laser operating at the 1550-nm wavelength. At this wavelength, the ordinary and extraordinary refractive indices of LN are $n_o = 2.21$ and $n_e = 2.14$, respectively. Silicon dioxide is isotropic with a refractive index of 1.444 for this wavelength. Air is isotropic with a refractive index of unity. We consider waveguides of different thickness, but for concreteness, we fix the ring radius to 100 μm .

To observe interesting polarization dynamics, Δ_0 must be of the order of unity. Otherwise, the dynamics become adiabatic with local eigenstates never deviating far from fully-TE and fully-TM modes. This requirement on Δ_0 between the fundamental modes leads us to consider multi-moded LN waveguides with thicknesses in the range of 0.7 to 1.0 μm , in agreement with previous experimental work [94]. However, we neglect higher-order modes in our analysis and examine coupling only between the fundamental TE and TM modes. As mentioned in Subsection 4.3.1, this is legitimate if the difference in propagation constants between the fundamental and higher-order modes is much larger than the matrix elements $\zeta D_{mn}^{(l)}$ of the perturbation, which we assume to be true. The validity of this assumption is verified in Subsection 4.4.1.

4.4.1 Local effective indices and comparison with FEM calculations

To validate our coupled-mode description, we compare its predictions with those obtained with commercial numerical software. Specifically, we calculate the effective indices $n_{\text{eff}}^{(+)}$ and $n_{\text{eff}}^{(-)}$ for the two modes of the ring waveguide as a function of the ϕ and use them to compute the angle-dependent polarization-averaged index $\bar{n}_{\text{eff}} = (n_{\text{eff}}^{(+)} + n_{\text{eff}}^{(-)})/2$ and the modal birefringence $B(\phi) = n_{\text{eff}}^{(+)} - n_{\text{eff}}^{(-)}$. From our SCMT, we have

$$B(\phi) = \Delta(\phi)/(k_0 r) \quad (4.36)$$

with $\Delta(\phi)$ given by Eq. (4.34). In the absence of material's birefringence, $B(\phi)$ does not depend on ϕ and reduces to the geometric birefringence due to mode confinement. In the presence of material anisotropy, $B(\phi)$ varies with ϕ and reveals key features of the polarization coupling, as we will see shortly. To evaluate \bar{n}_{eff} , we use Eqs. (4.8) and (4.9) to obtain

$$\bar{n}_{\text{eff}}(\phi) = \bar{\beta}(\phi)/k_0 = (k_0 r)^{-1} d\theta/d\phi, \quad (4.37)$$

where

$$\bar{\beta}(\phi) = \bar{\beta}_0 + \bar{\beta}_1 \cos 2\phi, \quad (4.38)$$

along with

$$\begin{aligned} \bar{\beta}_1 &= -\zeta(D_{ss}^{(1)} - D_{pp}^{(3)})/2, \\ \bar{\beta}_0 &= (\beta_s + \beta_p)/2 - \bar{\beta}_1. \end{aligned} \quad (4.39)$$

As stated, we want to compare the SCMT results for $\bar{n}_{\text{eff}}(\phi)$ and $B(\phi)$ with numerical values calculated with commercial software. We wish to show that our simplified SCMT of polarization coupling, with Hamiltonian matrix (4.11), is legitimate not only for in-plane slab waveguides, but also for thin waveguides with a finite two-dimensional cross-section. To do this, we evaluate the matrix elements $D_{ss}^{(1)}$, $D_{sp}^{(2)}$, and $D_{pp}^{(3)}$ for the TE and TM modes of ridge waveguides with fully 2-D cross-sections, assuming that they are wide enough for all other matrix elements to be comparatively negligible. We then calculate the parameters Δ_0 , Δ_1 , and κ from Eq. (4.13) for in-plane slabs, and calculate $B(\phi)$ using Eqs. (4.34) and (4.36) and $\bar{n}_{\text{eff}}(\phi)$ using Eqs. (4.37) and (4.38). For the numerical computations, we use the fully tensorial version of the finite-element method (FEM) mode solver in Photon Design's FIMMWAVE software suite.

The results are displayed in Figure 4.3 (top and middle) over the half ring $-\pi/2 \leq \phi \leq \pi/2$. Only half of the ring need be considered because the local modes are periodic in ϕ with period π , as evidenced, for instance, by Eq. (4.5). In Fig. 4.3, SCMT results are depicted with solid lines and FEM results are shown with circles. We consider ridge waveguides, all with a common thickness (height) of $1 \mu\text{m}$ and ridge widths of 1.6, 1.8 and $2.0 \mu\text{m}$. For reference, we also depict $\bar{n}(\phi)$ and $B(\phi)$ for an in-plane slab with the same thickness of $1 \mu\text{m}$. We set $1 \mu\text{m}$ for the thickness of the LN film because then $\Delta_0 \approx 0$ for the in-plane slab at 1550 nm causing the effects of polarization coupling to be more evident. The bottom part of Fig. 4.3 shows an expanded view $B(\phi)$ over a narrower range, $\pi/6 \leq \phi \leq \pi/4$. This auxiliary plot allows us to resolve the minima in $B(\phi)$ around $\phi = \pi/4$. These minima are important because they reveal information about the coupling strength, as we elaborate below.

Figure 4.3 shows that there is close agreement between the SCMT and the FEM curves for both $\bar{n}(\phi)$ and $B(\phi)$. From this, we can draw two conclusions. First, we confirm that Eqs. (4.34) and (4.38) accurately predict the ϕ -dependence of $\Delta(\phi)$ and $\bar{\beta}(\phi)$, even for waveguides of two-dimensional cross-section, so long as they are sufficiently thin. Second, we deduce that Eqs. (4.13) and (4.39) are accurate expressions for the parameters determining the local effective indices. Both conclusions support our SCMT description of the polarization dynamics.

Note that the middle plot in Fig. 4.3, of $B(\phi)$ over the half ring, is not useful to determine the coupling strength κ . This is because $|\kappa/\Delta_1| \sim 0.01$ for our LN waveguides, so the effect of a non-zero κ is negligible everywhere except in the regions where $(\Delta_0 + \Delta_1 \cos 2\phi) \approx 0$. This occurs when $\phi \approx \pm\pi/4$ because $(\Delta_0/\Delta_1) \approx 0$. Thus, we need to examine $B(\phi)$ around $\phi = \pm\pi/4$ to determine whether the SCMT values for κ are accurate. This is why the bottom part of Fig. 4.3 is useful. The good agreement between the SCMT and FEM values for $B(\phi)$ in Fig. 4.3 (bottom) legitimizes the use of Eq. (4.13) for the coupling strength κ for our LN films.

In aggregate, the plots of Fig. 4.3 confirm that $H(\phi)$ gives an accurate prediction for the local effective indices along the ring, despite neglecting coupling with higher-order modes, as argued in the opening paragraphs of this section. This is legitimate if the matrix elements $\zeta D_{mn}^{(l)}$ inducing coupling are much smaller than the difference in propagation constants between modes of different order. In the evaluation of the local indices, this condition follows from quantum mechanical stationary perturbation theory [21]. The good agreement between the SCMT and FEM results shows that this neglect of higher-order modes is valid for the LN waveguides under consideration.

Observe that the in-plane slab curves for $\bar{n}(\phi)$ and $B(\phi)$ have generally the same shape as those for the ridge waveguides with finite width. However, the slab curves are noticeably distinct for the ridge widths considered. The $\bar{n}(\phi)$ curve for the slab, in particular, is visibly off-set from the three $\bar{n}(\phi)$ curves for ridge waveguides. Nonetheless, this off-set can be intuitively understood as a consequence of decreased transversal confinement. Because the optical modes of the slab waveguide are less confined than those of a ridge waveguide but obey the same wave equation inside the core, they acquire a larger phase per longitudinal translation, i.e., they possess larger effective indices. This argument also explains the monotonic increase in $\bar{n}(\phi)$ for fixed ϕ and increasing ridge width in Fig. 4.3 (top).

In contrast, the difference between $B(\phi)$ (Fig. 4.3 (middle)) for the slab waveguide and that for ridge waveguides is not as significant as that for $\bar{n}(\phi)$ (Fig. 4.3 (top)). Thus, even if it might be imprecise to use the an in-plane slab model to calculate the phase accumulated along the ring, it may still yield accurate predictions for the polarization dynamics.

In Fig. 4.3, $B(\phi)$ approaches zero near $\phi = \pm\pi/4$. As explained above, it never vanishes because of the intermodal coupling due to κ , as can be verified from Eq. (4.34). Hence we expect the effective indices to exhibit an anti-crossing

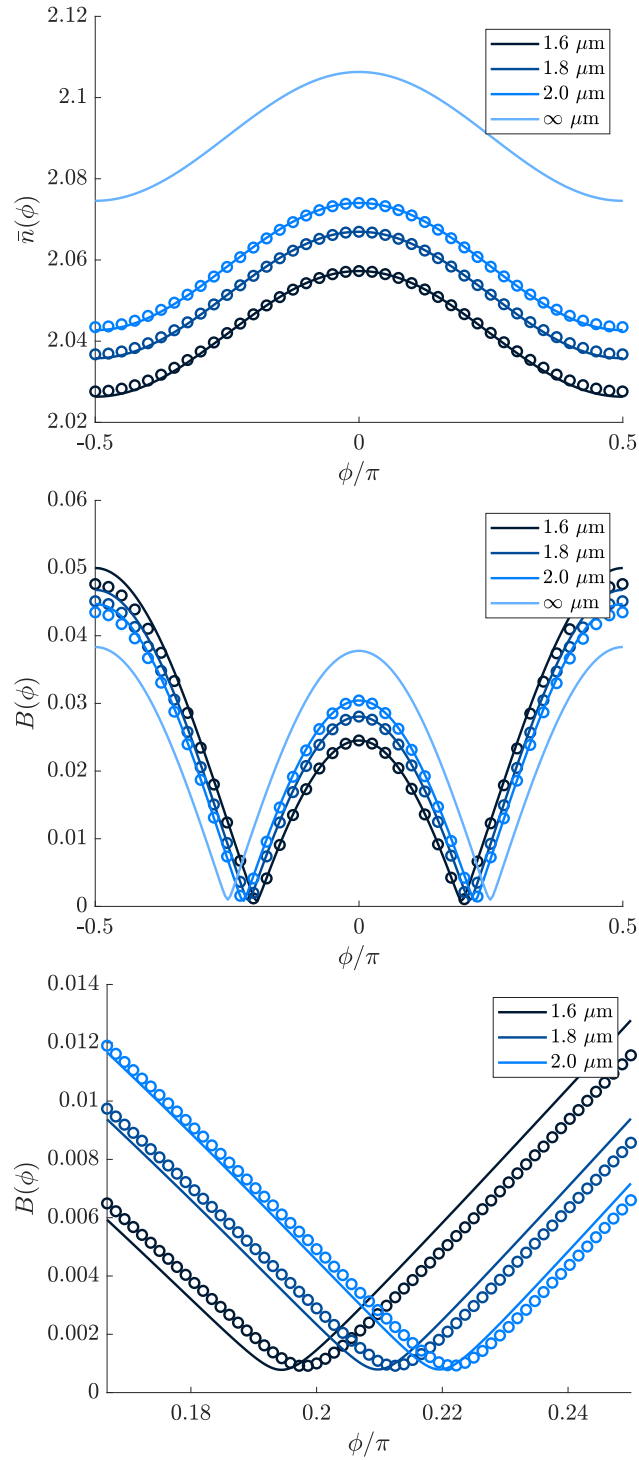


Figure 4.3: Variation of the polarization-averaged effective index $\bar{n}(\phi)$ (top) and the modal birefringence $B(\phi)$ (middle) as a function of the microring angle ϕ for different ridge waveguide widths. The bottom plot depicts $B(\phi)$ in the neighborhood of the index anti-crossings. Solid lines correspond to coupled-mode theory (SCMT) results. Circles correspond to finite-element method (FEM) results.

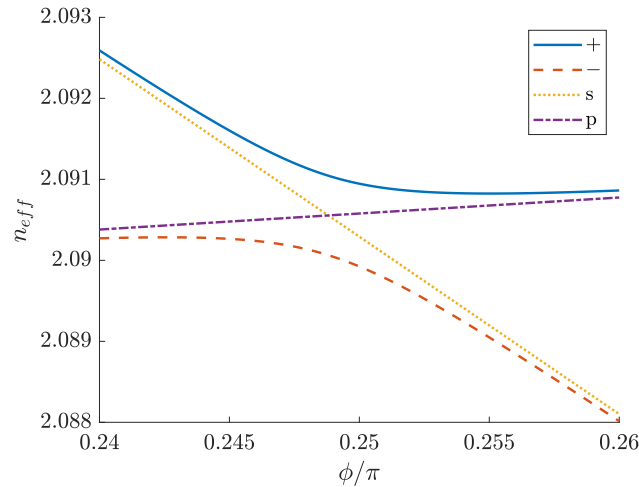


Figure 4.4: Effective-index anti-crossing in a LN microring resonator modeled as an in-plane slab with a thickness of $1 \mu\text{m}$. The solid line and dashed line show the effective indices of the two modes (+ and –, respectively) as a function of the ring angle ϕ . The dotted curve and dash-dot line shows the indices of the hypothetical bare TE (s polarization) and TM (p polarization) modes, respectively, in the absence of polarization coupling ($\kappa = 0$).

behavior, well-known in the context of quantum-mechanical two-level systems. Figure 4.4 shows this feature by plotting the effective indices of the eigenmodes of $H(\phi)$ for the in-plane slab in the region near $\phi = \pi/4$ in solid and dashed lines. For comparison, the dotted and dash-dot lines depict the effective indices of the “bare” TE and TM modes when the coupling is absent (i.e., κ is artificially set to zero). The curves depict the typical anti-crossing behavior of a two-level system [21]: $n_{\text{eff}}^{(+)}$ starts close to $n_{\text{eff}}^{(s)}$ for $\phi < \pi/4$, but deviates from it in a parabolic manner as ϕ approaches the crossing point near $\phi = \pi/4$. After the crossing, $n_{\text{eff}}^{(+)}$ asymptotically approaches $n_{\text{eff}}^{(p)}$. The opposite transition occurs for $n_{\text{eff}}^{(-)}$.

There are two reasons why analysis of the anti-crossing in Fig. 4.4 is worthwhile. First, one may use the anti-crossing effect to estimate the coupling coefficient κ from numerical data. If $H(\phi)$ has the form given in Eq. (4.11), the level-spacing minima (the anti-crossing point) occur when $2\phi = \pm\pi + \arccos[\Delta_0\Delta_1/(\Delta_1^2 + 4\kappa^2)]$. To first order in κ , one finds that Δ_{min} , the value of $\Delta(\phi)$ at these minima, is given by

$$\Delta_{\text{min}} = 2|\kappa|\sqrt{1 - (\Delta_0/\Delta_1)^2}, \quad (4.40)$$

under the assumption that $|\Delta_0/\Delta_1| \leq 1$. Thus, one can use Eq. (4.40) to determine $|\kappa|$ if Δ_0 and Δ_1 are known or if $\Delta_0 = 0$.

Second, examination of the anti-crossings elucidates the nature of the local modes. For instance, from the proximity of $n_{\text{eff}}^{(+)}$ to $n_{\text{eff}}^{(s)}$ for $\phi < \pi/4$ (and far from the intended crossing), we deduce that $n_{\text{eff}}^{(+)}$ is a mostly s -polarized mode by a perturbation argument [21]. Similarly, we deduce this mode becomes mostly p -polarized after it passes the anti-crossing. We also infer that the + mode is fully-hybridized at the anti-crossing. In fact, it can be regarded as circularly polarized, if the caveats outlined in Subsection 4.3.2 are respected. This is easily verified by diagonalizing $H(\phi)$ in Eq. (4.11) for $\Delta_0 + \Delta_1 \cos(2\phi) = 0$, as this is a necessary condition for the anti-crossing to appear. These observations suggest that, if the ring radius r is large enough for the polarization dynamics to be adiabatic, one would observe s -polarized light become circularly polarized (again, recalling the caveats of Subsection 4.3.2) and then p -polarized as it passes the anti-crossing. Similarly, p -polarized light would become circularly-polarized (of opposite handedness) and then s -polarized as it traverses the anti-crossing.

Note, though, that for this adiabatic evolution to occur, the adiabatic condition $\Delta(\phi) \gg 2$ should hold for all ϕ , so the minimum value Δ_{min} from Eq. (4.40) must satisfy $\Delta_{\text{min}} \gg 2$. Conversely, this requires $|\kappa| \gg 1$. Since κ is proportional to the ring radius r , the adiabatic condition bounds r from below. For instance, we find in Subsection 4.4.2, from Figure 4.5, that $|\kappa|$ is in the order of 0.3 for LN microrings with radius of $100 \mu\text{m}$. Thus, satisfying $|\kappa| \gg 1$ for the same ring cross-section requires increasing r to, at least, between 1 and 3 millimeters. This should still be experimentally feasible, though, as losses in LN waveguides have been reported to be in the order of 0.1 dB/cm

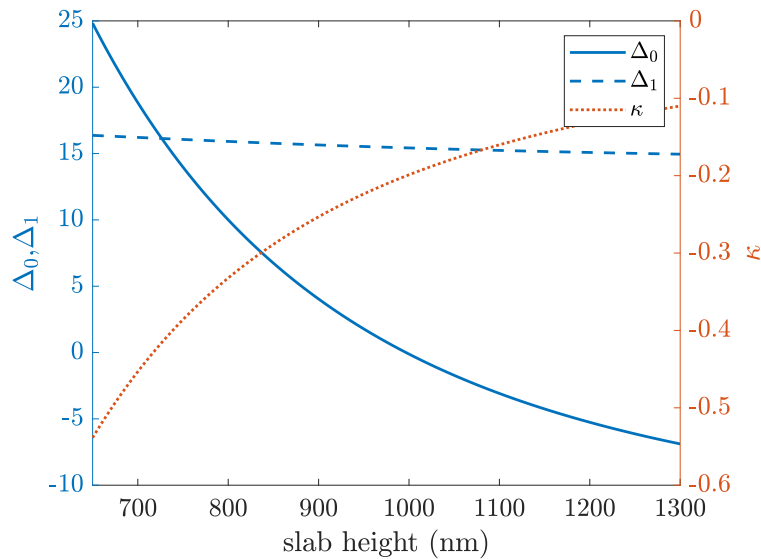


Figure 4.5: Hamiltonian parameters plotted as a function of the waveguide thickness $2d$.

[11].

4.4.2 Influence of slab thickness

In this subsection, we analyze the effect of the waveguide's geometry on the Hamiltonian parameters Δ_0 , Δ_1 and κ and the concomitant polarization dynamics along a ring round-trip. Staying in the in-plane slab model, the only geometrical parameters to vary are the ring radius r and the slab thickness (or height) $2d$, keeping notation consistent with Appendix A. Given Eq. (4.13), it is clear that changes in the ring radius r only rescale the Hamiltonian matrix. Although such rescaling can change the polarization dynamics (say, by taking it from the resonant to the adiabatic regime), this change is easily predictable. For this reason, we keep the ring's radius fixed at $100 \mu\text{m}$ and focus on dependence of the polarization dynamics on the waveguide's thickness.

Figure 4.5 shows how the parameters Δ_0 , Δ_1 and κ vary as a function of $2d$. Both Δ_0 and κ vary appreciably as thickness is varied from 600 to 1300 nm; Δ_0 even changes its sign. The coupling parameter κ decreases in magnitude by a factor of 5 over this thickness range. In contrast, Δ_1 maintains a comparatively constant value of approximately 16 over the entire thickness range.

In particular, the large variation in Δ_0 from 25 to -5 suggests drastic changes in the polarization evolution as $2d$ varies from 600 to 1300 nm. Recall from Section 4.3.5 that the evolution falls in the adiabatic regime when the eigenvalue difference $\Delta(\phi)$ is large compared to 2. It follows from Eq. (4.34) that this is the case when $(|\Delta_0| - |\Delta_1|) \gg 2$. Since this applies in the neighborhood of 600 nm, we expect the dynamics fall in the adiabatic regime in this thickness range. As $2d$ increases past 600 nm, Δ_0 rapidly decreases toward zero. Because we always have $|\kappa| < 1$, the decrease in $|\Delta_0|$ causes the dynamics to leave the adiabatic regime, as it is no longer true that $\Delta(\phi) \gg 2$ for all ϕ . The polarization dynamics are then susceptible to the excitation of coupling resonances when Δ_0 approaches an even integer, as discussed in Section 4.3.4. In the thickness range 800–1300 nm, $|\Delta_0|$ has relatively small values, in the order of unity. Consequently, we expect the excited resonances to have non-negligible weights $J'_n(\Delta_1/2)$ and polarization coupling to be most pronounced when such resonances occur.

To verify these predictions, we solved the coupled-mode equations (4.10) numerically over one round trip with the initial condition that the pure TE (TM) mode is excited initially at $\phi = 0$ for $2d$ from 600 nm to 1300 nm. As ϕ increases, the mode coupling leads to the transfer of power to the TM (TE) mode. We denote the fraction power transferred as $P_{sp}(\phi)$ and use it to calculate two quantities: the round-trip power (RTP), $P_{sp}(2\pi)$ and the mean coupled power (MCP), i.e., the fraction of coupled power averaged over a round trip $(2\pi)^{-1} \int_0^{2\pi} d\phi P_{sp}(\phi)$. Because of the unitary evolution of the Jones vector along the ring, both the RTP and the MCP are independent of whether TE or TM light is injected at $\phi = 0$. Though both the RTP and the MCP are measures of the polarization hybridization, they

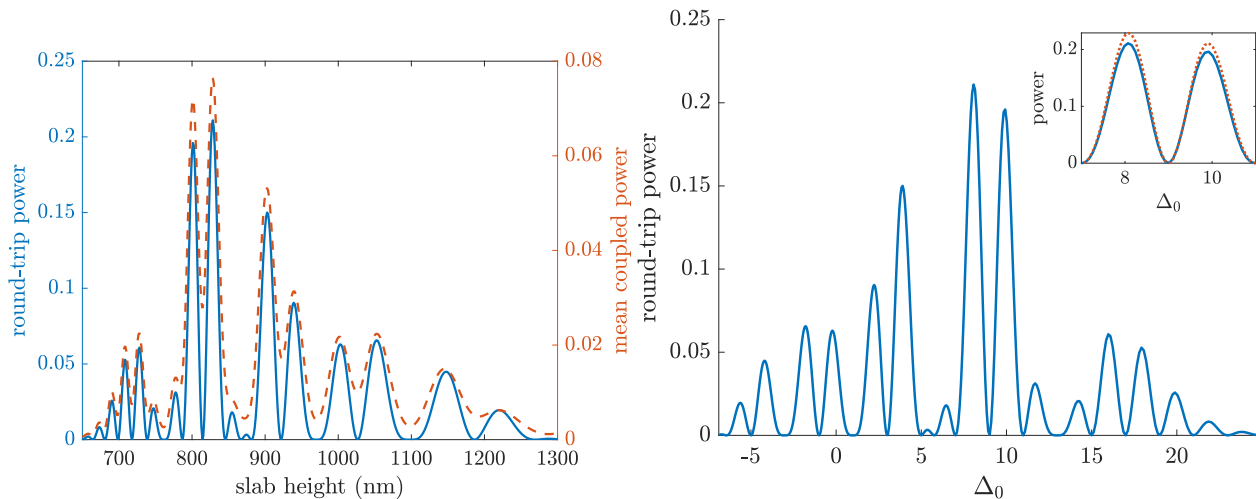


Figure 4.6: Round-trip power (solid blue line) and mean coupled power (dashed orange line) as a function of slab height $2d$ (top). Round-trip power as a function of Δ_0 (bottom). Inset compares the numerically calculated round-trip power (solid blue line) with that predicted by first-order perturbation (dotted orange line).

provide different information. The RTP measures the net hybridization after one round trip and the hybridization of the ring's polarization eigenstates. On the other hand, the MCP is a global measure of the average hybridization over the ring.

Figure 4.6 depicts the RTP and MCP as a function of $2d$. Both quantities exhibit multiple aligned peaks representing resonances. From the previous discussion, we expect these resonances to appear when Δ_0 approaches an even integer. The solid trace in Figure 4.6 confirms this by plotting RTP as a function of Δ_0 . Even though the RTP peaks mostly align with even integer values of Δ_0 , the alignment is not perfect and deviates occasionally from Eq. (4.28). As explained in Subsection 4.3.3, such deviations are due to the effect of neighboring resonances on the polarization evolution. This can be verified through comparison of the numerically calculated RTP with that predicted by the perturbative formula, Eq. (4.21).

As seen in the inset of Fig. 4.6, the perturbative calculation mostly retraces the RTP. The inset zooms into the $\Delta_0 \approx 8, 10$ peaks so the difference between the numerical and perturbative RTP can be resolved. Small deviations arise only from a slight overestimation of the maxima's magnitudes. This difference is most pronounced for these two peaks because they are the largest in magnitude, but it exists for all the resonance peaks. The slight overshoot of the perturbative RTP is explained by noting that the perturbative approximation $U(2\pi, 0) \approx U^{(0)}(2\pi, 0) + U^{(1)}(2\pi, 0)$ neglects coupling saturation, i.e., it assumes the power of the launched TE or TM polarization is not depleted because of polarization coupling. The close agreement between the perturbative and numerical RTP and the location of the RTP minima at odd-integer Δ_0 values allows us to interpret the RTP minima as a consequence of Eq. (4.24). Thus, we verify that the slab thicknesses corresponding to odd-integer Δ_0 possess TE- and TM-polarized round-trip eigenstates.

Returning to the upper plot in Fig. 4.6, we note that the resonance peaks are tightly packed in the neighborhood of $2d = 600$ nm and progressively spread out as $2d$ increases. Inspecting Fig. 4.5, we can attribute this behavior to the fact that, although Δ_0 varies monotonically with $2d$, the variation is nonlinear. For smaller values of d , Δ_0 changes more rapidly with d . This argument is confirmed in the lower trace. When we plot the RTP with respect to Δ_0 , the resonance valleys and peaks become evenly spaced.

4.4.3 Polarization evolution along the microring

Our SCMT can be used to study how an initial SOP evolves along the microring, as it is affected by the competing geometrical and material birefringence. In this subsection, we analyze the polarization dynamics along the microring in the resonant and adiabatic regimes of the parameter-space and verify the validity of the approximate solutions given in Sections 4.3.4 and 4.3.5.

First, we investigate the resonant regime and fix the waveguide thickness at 800 nm, for which $\Delta_0 \approx 10$, and a

coupling resonance results with $m = -5$ (see Section 4.3.4). We numerically integrate the coupled-mode equations (4.10) with an initially TE-polarized mode ($a(0) = (1, 0)^T$) and plot the resulting Stokes vector $\mathbf{S}(\phi)$, with components $S_j(\phi) = a^\dagger(\phi)\sigma_j a(\phi)$, on the Poincaré sphere to track the evolution of the SOP. The resulting plot is presented in Figure 4.7 (top). The numerically computed $\mathbf{S}(\phi)$ is represented by the solid blue curve, while the behavior predicted by the RWA solution, obtained from Eq. (4.26), is drawn with a dashed orange curve.

Although the numerical and the RWA curves in Fig. 4.7 trace noticeably different trajectories on the Poincaré sphere, they both describe a similar overall nutation of the SOP away from the initial TE-polarization. This is seen in the lower plot of Fig. 4.7, where we plot the fraction of power transferred to the initially unexcited TM-polarization as a function of ϕ , i.e., $P_{sp}(\phi)$ in the notation of Subsection 4.4.2. It is evident that the RWA solution successfully describes the accumulating effect of the polarization coupling, while ignoring the small mode-power oscillations of the numerical solution. These oscillations are associated with the off-resonant terms of the Hamiltonian matrix, which are neglected in the RWA.

Lastly, we examine a case where the polarization dynamics lie in the adiabatic regime by choosing $2d = 500$ nm. In this case, $\Delta_0 = 52.4$ and $\Delta_1 = 16.6$, hence $\Delta(\phi) \geq (|\Delta_0| - |\Delta_1|) \gg 2$ for all ϕ . Once again, we evaluate the fraction of power $P_{sp}(\phi)$ coupled into the TM mode when the TE mode is excited at $\phi = 0$. Figure 4.8 presents $P_{sp}(\phi)$ as computed from a numerical solution of Eq. (4.10) and compares it with the values predicted from the adiabatic approximation. Clearly, there is very good agreement between the two curves for all ϕ . The only features that the adiabatic approximation does not reproduce are the rapid, small-amplitude oscillations on top of the accumulated power. These can be understood as artifacts of a finite (contrary to infinitely small) rate of change of the Hamiltonian matrix.

4.5 Conclusions

We developed a theoretical framework for studying the evolution of polarization inside a microring resonator whose waveguide has a core made with a uniaxial birefringent material. We introduced a zero-bending model that replaces the ring waveguide with a straight one, but retains the continuous reorientation of the optic axis relative to the direction of propagation. We wrote Maxwell's equations in the form of a Schrödinger equation and used it to obtain the equations governing the resulting coupling between TE and TM polarizations.

We solved the coupled-mode equations in the simple case when only fundamental TE and TM modes are coupled due to the reorientation of the optic axis. We found that the resulting coupled-mode equations are identical to the Schrödinger equation of a two-level atom under optical excitation and external frequency modulation. We leveraged this isomorphism and used analytical tools from quantum mechanics to study the polarization dynamics inside the microring under different parameter regimes. Our formalism can be used to characterize the polarization properties of microrings made with a uniaxial material such as lithium niobate. The study of such microrings is of great technological importance, since they are the building block of many electro-optical and nonlinear optical devices.

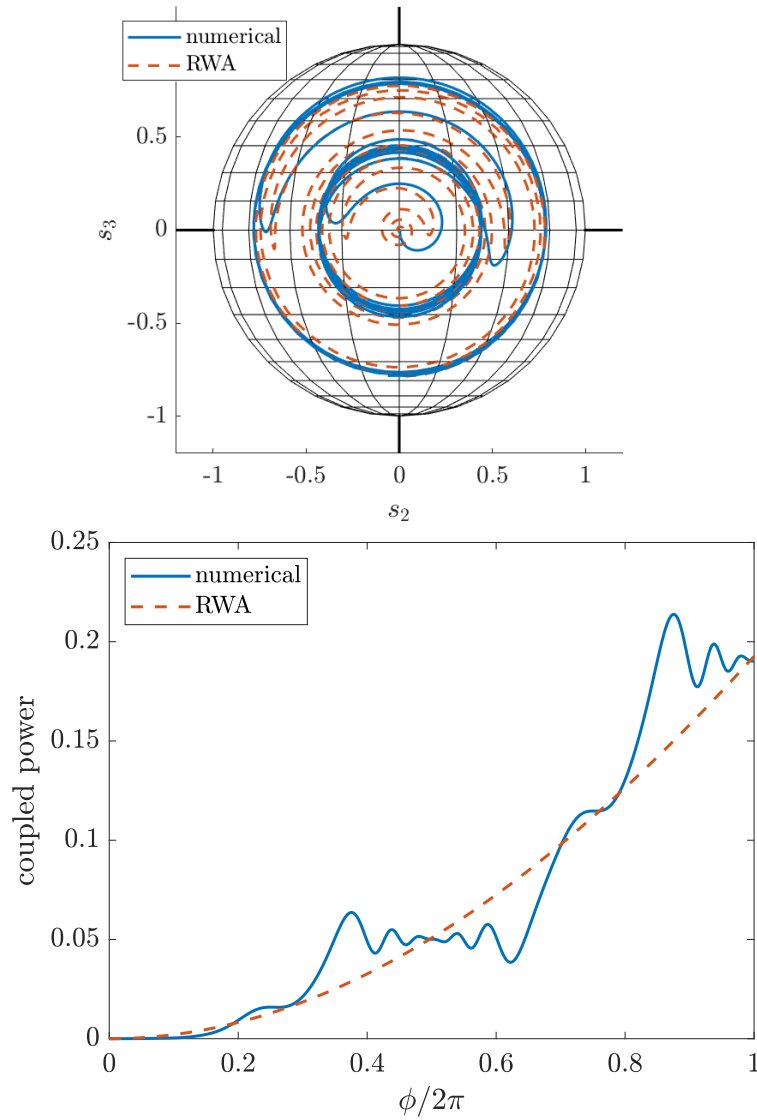


Figure 4.7: Evolution of the SOP on the Poincaré sphere of initially s -polarized light for $2d = 800$ nm (top). Fractional power transfer as a function of angle ϕ (bottom). The solid blue trace shows the numerically-evaluated evolution; the dashed orange trace shows the evolution under the RWA.

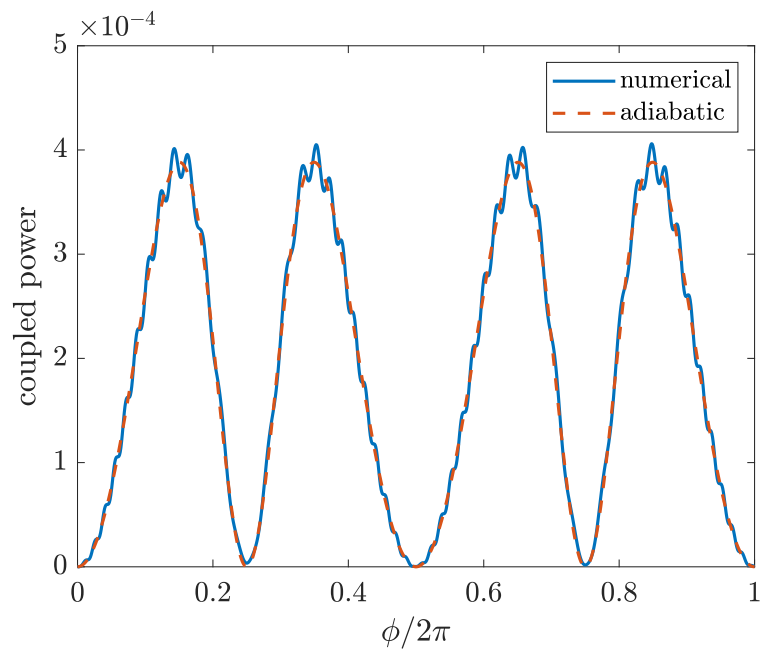


Figure 4.8: Fraction of power coupled into the initially-unexcited polarization for $2d = 500$ nm, calculated numerically (solid blue line) and via the adiabatic approximation (dashed orange line)

Chapter 5

Oblique uniaxial waveguide as a polarization rotator

In Chapter 4, we developed a spatial coupled-mode theory (SCMT), describing coupling between the transverse-electric (TE) and transverse-magnetic (TM) modes when the lithium-niobate (LN) core of a lithium-niobate-on-insulator (LNOI) ring is either X-cut or Y-cut and its crystallographic Z-axis (i.e., its optic axis) makes an oblique angle with the etched waveguide. In this chapter, we utilize this theory to design a passive polarization rotator, which directly transfers power from its fundamental TE mode to its fundamental TM mode. Essentially, the rotator consists of an X-cut LNOI waveguide tilted at an optimum angle with respect to its Z-axis, such that the core's material anisotropy induces both polarization coupling and a vanishing modal birefringence, resulting in phase-matched polarization conversion.

The guided modes of anisotropic waveguides have been analyzed for decades [95, 97, 98, 114, 115]. In particular, the effect of LN's material birefringence on the polarization properties of X-cut LNOI waveguides has been the topic of several theoretical and experimental investigations [94, 116–118]. It has also been utilized to design polarization-engineering devices such as TE/TM-pass polarizers [119, 120], polarization beam splitters [121–123], and birefringence-free waveguides [124, 125]. Polarization rotation via the electro-optic effect in LNOI [126] and via material anisotropy of oblique deposition of columnar thin films [127] have also been proposed. However, a design for a passive LNOI polarization rotator utilizing LN's material birefringence has yet to be presented. That is the objective of this chapter.

The influence of LN's material birefringence on the polarization characteristics of guided modes has also been investigated for bulk titanium-indiffused lithium niobate (Ti:LiNbO_3) waveguides. In this context, slight off-Z-axis propagation was originally proposed [128] so material birefringence compensates for residual geometric birefringence in electro-optical polarization rotators. In that work, it was also identified that off-Z-axis propagation induces passive polarization coupling. Later, both the change in polarization effective indices and polarization coupling in off-Z-axis Ti:LiNbO_3 waveguides were analyzed [129–131] using SCMT [59]. A passive polarization rotator based on passive coupling in Ti:LiNbO_3 waveguides was even proposed and characterized through a vectorial beam propagation method [132].

However, the optical guiding properties of LNOI differ drastically from those of Ti:LiNbO_3 , so polarization rotation in LNOI waveguides must be examined independently, as we do in this chapter. This is because LNOI waveguides have an index contrast much larger than that of Ti:LiNbO_3 waveguides, roughly by an order of magnitude [11]. Consequently, LNOI waveguides possess much larger geometric birefringence, so polarization-mode phase-matching can be achieved at much greater deviations from the Z-axis. This, we find, results in correspondingly more efficient polarization rotation. Additionally, larger index contrast permits the etching of sharp waveguide bends [11]. This allows one to tightly delimit the polarization rotator length with such bends, as in our proposed design, depicted below.

The remainder of this chapter is organized as follows. In Section 5.1, we describe the geometry of the proposed polarization rotator, and examine analytically its polarization properties via SCMT. In Section 5.2, we evaluate the SCMT design numerically and study the resulting characteristics of the polarization rotator such as device length, crosstalk, and bandwidth. In Section 5.3, we present our conclusions.

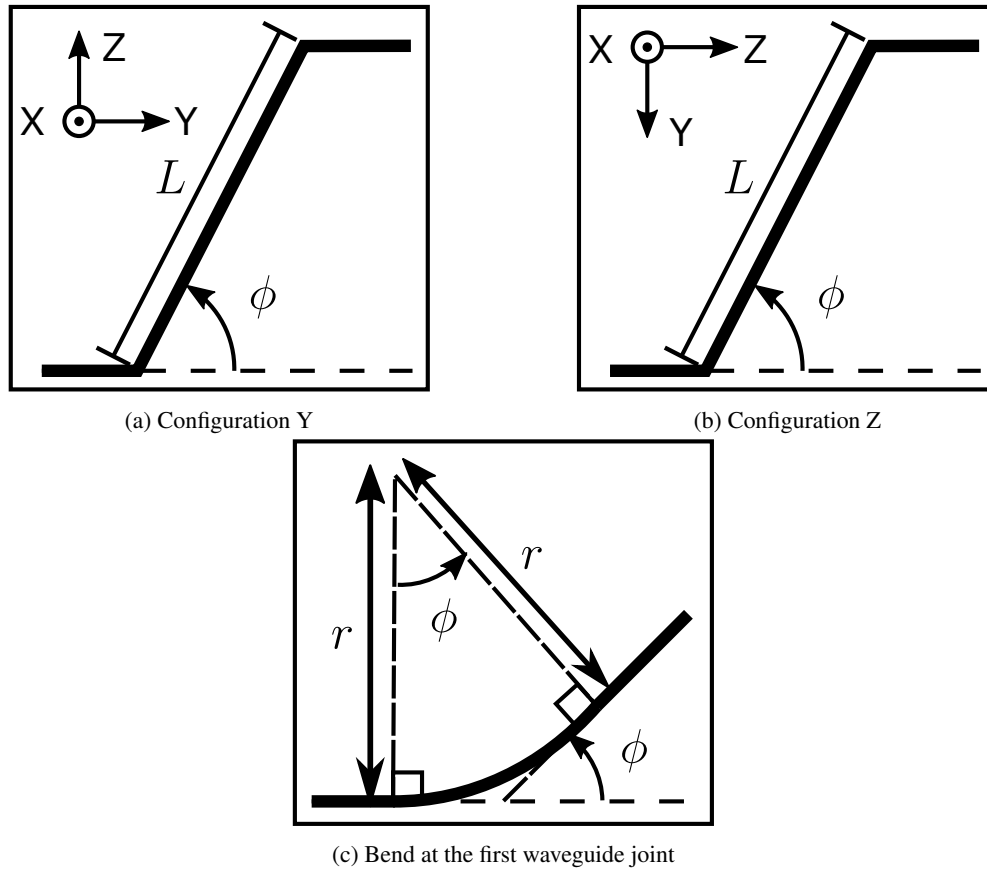


Figure 5.1: (a,b) Geometry of the proposed passive polarization rotator under its two possible configurations. L is the length of the tilted segment. ϕ is the angle between the tilted segment and the corresponding LN crystallographic axis. The orientation of the crystallographic axes for each configuration is shown in the upper left corner. Light propagates from left to right. (c) Geometry of the circular bend at the first waveguide joint. r is the joint's bending radius.

5.1 Proposed design and SCMT analysis

5.1.1 Polarization rotator geometry

Our proposed design is shown in Figures 5.1a and 5.1b in its two possible configurations. It consists of a LNOI waveguide with a tilted section of length L , joined at its two ends by untilted (or straight) segments. The direction of propagation along the tilted segment makes an oblique angle ϕ with that along the straight sections. Along the straight segments, the direction of propagation is parallel to either LN's Y-axis or Z-axis, depending on the chosen configuration. In Configuration Y (Fig. 5.1a), the direction of propagation is parallel to the Y-axis. In Configuration Z (Fig. 5.1b), it is parallel to the Z-axis. The SCMT of polarization coupling in Sections 5.1.2 and 5.1.3 applies equally well to both configurations. The differences in performance between both configurations are few and are summarized in Sections 5.1.4 and 5.2.3.

In practice, each joint consist of a circular arc, as shown for the first joint in Figure 5.1c. The second joint is bent similarly to the first. Note that the deviation angle ϕ is equal to the angle spanned by the curved segment with radius of curvature r . Naturally, the radii of curvature r must be large enough to avoid noticeable bending losses. In our analytical design, we assume that the radii are still small enough so polarization coupling in each of the circular joints is negligible. However, the finite curvature of these joints induces residual crosstalk. In Section 5.1.3, we provide a perturbative expression and a simple bound for this residual crosstalk. In Section 5.2.3, we evaluate these numerically for a LNOI polarization rotator.

5.1.2 CMT-based design of the tilted segment

To analyze polarization rotation in the tilted waveguide segment, we use our coupled-mode formalism, originally developed for a curved uniaxial waveguide [116]. For simplicity, we assume that only the fundamental TE mode and the fundamental TM mode are initially excited and denote their amplitudes with a_s and a_p , respectively. Coupling to higher-order modes can be safely neglected, because generally it is heavily phase-mismatched. We consider the column vector $a \equiv (a_s, a_p)^T$, which can be loosely interpreted as a Jones vector [116]. The basis TE and TM modes are normalized so $a^\dagger a = |a_s|^2 + |a_p|^2$ equals the total power carried in the direction of propagation.

Because the angle ϕ , between the waveguide direction and its core's optic axis, is constant along the straight oblique segment, the corresponding coupled-mode equations have constant coefficients. Thus, they can be readily integrated to relate $a(L)$, the Jones vector at the end of the oblique segment, to $a(0)$, the Jones vector at its beginning. This yields the relation

$$a(L) = \exp[iM(\phi)L]a(0). \quad (5.1)$$

Recall from Fig. 5.1 that L is the length of the oblique segment. $M(\phi)$ is a 2×2 Hermitian matrix that depends on ϕ and has the form [116]

$$M(\phi) = \begin{pmatrix} \Delta(\phi)/2 & -i\kappa(\phi) \\ i\kappa(\phi) & -\Delta(\phi)/2 \end{pmatrix}, \quad (5.2)$$

where $\Delta(\phi)$ and $\kappa(\phi)$ are the real-valued functions of ϕ

$$\Delta(\phi) = \Delta_0 + \Delta_1 \cos 2\phi, \quad \kappa(\phi) = \kappa_0 \sin 2\phi. \quad (5.3)$$

Equation (5.1) is analogous to that obtained for directional couplers. It shows that power is periodically exchanged between the TE and TM polarizations when $\kappa(\phi)$ is non-zero.

Physically, the functions $\Delta(\phi)$ and $\kappa(\phi)$ are, respectively, the ϕ -dependent detuning in propagation constants between the TE and TM modes; and the ϕ -dependent coupling coefficient. Correspondingly, Δ_0 , Δ_1 , and κ_0 are three real-valued, ϕ -independent coefficients, henceforth referred to as ‘‘polarization parameters’’. They represent, respectively: the direction-averaged detuning; the amplitude of oscillation in detuning with varying ϕ ; and the coupling coefficient when $\sin 2\phi = 1$. These parameters can be calculated in terms of the TE and TM modes' field distributions at $\phi = 0$ and their corresponding propagation constants, as described in Chapter 2 and as done in Chapter 4.

Given Eqs. (5.1) and (5.2), the oblique waveguide segment of length L acts as a full polarization rotator if and only if

$$\Delta(\phi) = 0, \quad (5.4)$$

$$L\kappa(\phi) = \pi(2n+1)/2, \quad (5.5)$$

for some integer n . Equation (5.4) can be interpreted as requiring the TE and TM modes of the oblique waveguide to be phase-matched, and it restricts ϕ to a discrete set of values. If Eq. (5.4) is satisfied, then ϕ is fixed by it, and Eq. (5.5) becomes a constraint on L . This constraint is analogous to setting the length of a directional coupler equal to an odd-integer multiple of its minimum length for full power transfer.

As stated, Eq. (5.4) can only be met by a discrete set of tilt angles ϕ . For concreteness, we restrict ϕ to lie in the first quadrant, i.e., $\phi \in [0, \pi/2]$. Then ϕ satisfying Eq. (5.4) becomes unique and given by

$$\phi = \frac{1}{2} \arccos\left(-\frac{\Delta_0}{\Delta_1}\right) = \frac{\pi}{4} + \frac{1}{2} \arcsin\left(\frac{\Delta_0}{\Delta_1}\right), \quad (5.6)$$

where $\arccos(x) \in [0, \pi]$ and $\arcsin(x) \in [-\pi/2, \pi/2]$ for $x \in [-1, 1]$. Alternative polarization-rotator designs can be made because solutions ϕ for Eq. (5.4) can be found in any quadrant $[m\pi/2, (m+1)\pi/2]$ for integer m . These alternative values are found through the transformations $\phi \rightarrow -\phi$, $\phi \rightarrow \phi - \pi$, and $\phi \rightarrow -\phi + \pi$. The first of these transformations results in a rotator with identical performance. The last two are comparatively undesirable: they only increase $|\phi|$, which leads to longer circular arcs at the joints, and, thus, larger insertion loss.

Of course, Eq. (5.6) yields a real-valued ϕ if and only if $|\Delta_0/\Delta_1| \leq 1$. Additionally, $|\Delta_0/\Delta_1|$ cannot be unity, because then $\kappa(\phi)$ vanishes and Eq. (5.5) cannot be satisfied. Hence, a necessary condition for Eqs. (5.4) and (5.5) to be satisfied simultaneously is

$$|\Delta_0/\Delta_1| < 1. \quad (5.7)$$

As evident from the formulas in Chapters 2 and 5, the polarization parameters depend implicitly on the optical frequency and the waveguide cross-section. Hence, Eq. (5.7) is a necessary condition on these parameters for the waveguide segment to function as a full polarization rotator for some orientation angle ϕ .

Given Eq. (5.6) for ϕ , the second condition for full power transfer, i.e., Eq. (5.5), can be satisfied if the tilted-segment length L is set equal to

$$L = \frac{\pi}{2|\kappa_{\text{eff}}|}, \quad \text{where} \quad \kappa_{\text{eff}} \equiv \kappa_0 \sqrt{1 - (\Delta_0/\Delta_1)^2}. \quad (5.8)$$

As our notation suggests, κ_{eff} acts as the effective coupling constant along the tilted segment.

Of course, Eq. (5.5) is still satisfied if L is set equal to an odd-integer multiple of the right-hand side of Eq. (5.8). Nonetheless, just as in directional-coupler design, the smallest possible L is preferable because it results in the largest bandwidth for polarization-conversion and incurs the lowest possible material loss.

If ϕ was chosen to lie outside the first quadrant, the sign of the radical (and hence that of κ_{eff}) in Eq. (5.8) might change. Such a change in sign does not change the power exchange between polarization modes, however.

5.1.3 Residual crosstalk due to finite curvature at the joints

Let r be the bending radius of both of the curved segments joining the tilted segment to one of the straight segments in Fig. 5.1. In Section 5.1.2, we assumed r to be small enough that polarization coupling along the curved segments is negligible. However, polarization coupling along these segments does occur, resulting in residual crosstalk X_r , i.e., a non-zero normalized power remaining in the original polarization mode after propagation along the rotator. In Section B.3, we show that, to first-order perturbation theory in $r|\kappa_0|$, X_r is given by

$$X_r = 4r^2 \left| \int_0^\phi d\phi' \kappa(\phi') \exp \left[ir \int_0^{\phi'} d\phi'' \Delta(\phi'') \right] \right|^2. \quad (5.9)$$

Hence, neglect of the curved segments is accurate if $X_r \ll 1$. In deriving Eq. (5.9), we assume r to be common to both joints for simplicity. This simplification is sufficient because we are mostly interested in studying the effect of finite curvature on X_r , rather than the interference due to mismatch in the joints' curvatures.

The right-hand side of Eq. (5.9) is a complicated transcendental function of r . However, it admits a simple bound, quadratic in r , given by

$$X_r \leq (r/r_0)^2, \quad \text{where} \quad r_0 \equiv \frac{1}{2|\kappa_0| \sin^2 \phi}. \quad (5.10)$$

Thus, if $r \ll r_0$, then $X_r \ll 1$. As discussed in Section B.3, the crosstalk X_r approaches its upper bound in Eq. (5.10) if the accumulated phase-mismatch, i.e., the argument of the exponential in Eq. (5.9), is negligible.

In addition to introducing polarization crosstalk, waveguide curvature at the rotator's joints induces bending losses and mode distortion [101]. Neither of these effects are modeled by our SCMT description of mode coupling, as discussed in Ref. [116]. However, these effects can be inhibited in LNOI by leveraging the platform's large index contrast [11]. Nonetheless, if the bending radius r becomes comparable to the waveguide width and/or the optical wavelength, bending loss and mode distortion may become prominent [101]. Bending loss, in particular, may noticeably increase the rotator's insertion loss if r is chosen too small. Thus, there exists a trade-off between bending loss and residual polarization crosstalk one should engineer when fabricating a rotator using our proposed design.

5.1.4 Differences between configurations

In the framework of SCMT, the difference between the two configurations of Fig. 5.1 lies in their respective values for the polarization parameters. Because the core's (LN's) material birefringence is small, SCMT in general, and Eq. (5.3) in particular, are accurate for any orientation ϕ . Hence, we can estimate the polarization parameters for one configuration from those for the other by applying the shifts $\Delta(\phi) \rightarrow \Delta(\phi \pm \pi/2)$ and $\kappa(\phi) \rightarrow \kappa(\phi \pm \pi/2)$ and matching the resulting expressions to the original form, Eq. (5.3). Thus, to the accuracy of SCMT, the polarization parameters transform as

$$\Delta_0 \rightarrow \Delta_0, \quad \Delta_1 \rightarrow -\Delta_1, \quad \kappa_0 \rightarrow -\kappa_0, \quad (5.11)$$

when going from Configuration Y to Configuration Z, or vice versa.

Of course, even if accurate, SCMT is only approximate so Eq. (5.11) is not exact. Nonetheless, we have verified Eq. (5.11) to be accurate for small normalized material birefringence, i.e., when

$$|n_e^2 - n_o^2| \ll n_e^2 + n_o^2, \quad (5.12)$$

where n_e (n_o) is the core's extraordinary (ordinary) index of refraction. This is unsurprising as when Eq. (5.12) holds, the perturbation due to the reorientation of the permittivity dyadic is small, so SCMT is expected to hold. For LN at a wavelength near 1550 nm, $n_e = 2.14$ and $n_o = 2.21$ [11], so Eq. (5.12) is well satisfied.

Next, we examine the effect of Eq. (5.11) on the design of the polarization rotator. Under the transformation of Eq. (5.11), Eq. (5.8) for L remains invariant; and Eq. (5.6) for ϕ is reflected about $\pi/4$.

The change in ϕ makes intuitive sense, as this shift in ϕ geometrically corresponds to one of two cases. In one case, the new value for ϕ corresponds to the original orientation, measured from the new axis reference: Z instead of Y , or vice versa. In the second case, the new ϕ corresponds to a direction given by one of the quadrant transformations discussed in the paragraph following Eq. (5.6). Ultimately, polarization rotation along the tilted segment is unaltered by the choice of configuration.

On the other hand, the geometry of the curved joints does change between configurations. Applying Eq. (5.11) to Eq. (5.6), it follows that if $|\phi| < \pi/4$ for one configuration, we have $\pi/4 < |\phi| \leq \pi/2$ for the other, and vice versa. Thus, for a fixed bending radius r , the length $r|\phi|$ spanned by each curved segment changes between configurations. For fixed r , larger $|\phi|$ implies longer propagation length and hence, larger propagation loss.

Hence, one would expect that the configuration resulting in smaller $|\phi|$ would be preferable, as it would result in smaller propagation loss and smaller crosstalk X_r due to residual polarization coupling. However, such conclusion is generally incorrect for two reasons. First, LNOI's high index-contrast enables bent waveguides with small r and low losses. Hence, propagation losses along the curved joints can be made negligible compared to those along the tilted segment, independent of the configuration. Thus, the main criterion to choose the rotator configuration should be to minimize X_r . Second, phase-mismatch between the polarization-modes along the curved segments may result in the configuration with larger $|\phi|$ having the smaller X_r . This point is further discussed in Section 5.2.3.

5.2 Numerical analysis of a LNOI rotator

In this section, we evaluate numerically the polarization parameters of a particular LNOI waveguide and examine its resulting polarization properties. The waveguide consists of a LN core with silicon-dioxide as bottom cladding and air as top cladding. We design the LNOI polarization rotator to operate at telecom wavelength, $\lambda_0 = 1550$ nm. At this wavelength, LN has the ordinary and extraordinary refractive indices of 2.21 and 2.14, respectively [11]; and silicon dioxide has a refractive index of 1.44.

For simplicity, we assume the core layer to be wide enough so its width can be taken as infinite. Hence, its height (or thickness) h is the only geometrical parameter characterizing the waveguide cross-section. This assumption facilitates numerical evaluation of the polarization parameters, while still yielding results close to those for rectangular waveguides with finite width. In Ref. [116], this approximation was examined numerically and found to be accurate for the LNOI platform. This infinite-width simplification is also consistent with the observation that waveguide width has negligible effect on polarization coupling, so long as it is larger than twice its height, as reported in Ref. [118].

For concreteness, we design the rotator using Configuration Y. As discussed in Section 5.1.4, the only significant difference between configurations is the residual crosstalk X_r due to finite joint curvature. X_r for both configurations is calculated and compared in Section 5.2.3.

5.2.1 Polarization parameters and tilt-segment orientation

To let our results be general, we normalize the polarization parameters by dividing them by the optical wavenumber $k_0 = 2\pi/\lambda_0$. Once normalized, these parameters depend not on the height h and the wavelength λ_0 separately, but only on the optical thickness h/λ_0 . This follows from the scale invariance of Maxwell's equations [74].

Figure 5.2a shows the dependence of the polarization parameters on h/λ_0 in the range of 0.4–0.8. In this interval, the ratio Δ_0/Δ_1 has a magnitude of the order of unity, which allows the condition in Eq. (5.7) to be satisfied over an

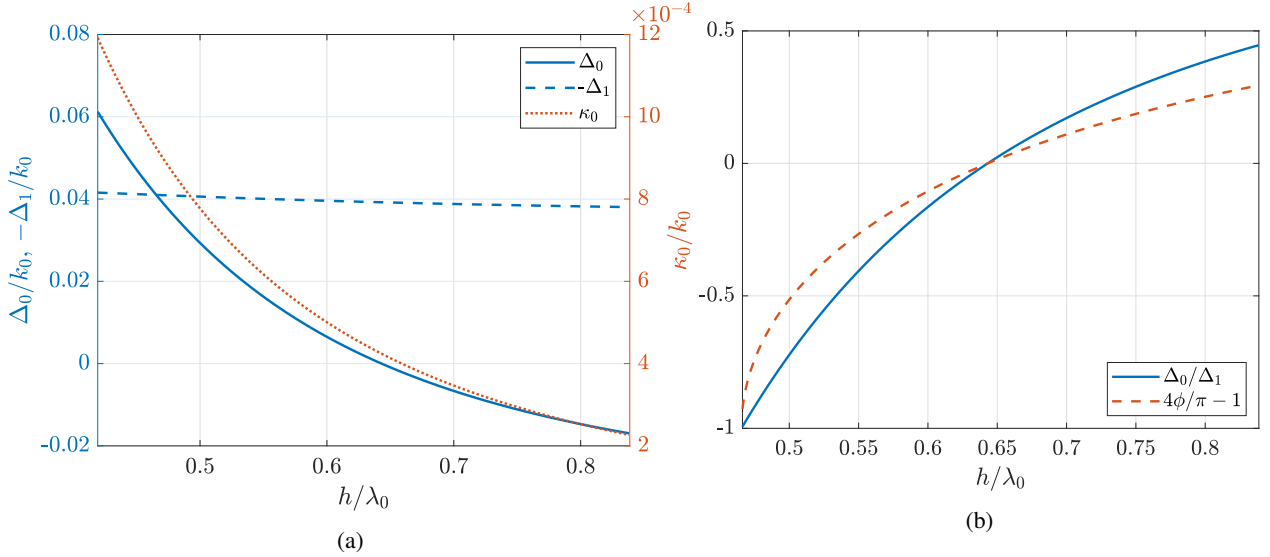


Figure 5.2: (a) Polarization parameters Δ_0 , Δ_1 , and κ_0 as functions of optical thickness h/λ_0 . The negative of Δ_1 is plotted, rather than Δ_1 directly, so the point where $\Delta_0 = -\Delta_1$ is visually evident. (b) Ratio Δ_0/Δ_1 (solid) and the angle ϕ (dashed) as functions of optical thickness h/λ_0 .

appreciable sub-interval. The coupling coefficient κ_0/k_0 varies considerably (by a factor of 6) over this range. Δ_0/k_0 decreases monotonically with optical thickness, going from 0.06 to -0.02. In contrast to these two, Δ_1/k_0 remains relatively constant around the value of -0.04.

We find that, over the studied h/λ_0 interval, Condition (5.7) is satisfied if and only if $h > 0.4655\lambda_0$. This agrees with the previous observation [118] that, for a given thickness h , full mode-hybridization is possible for some waveguide orientation ϕ if and only if the wavelength λ_0 is below a threshold value. In this case, the threshold value would be that of $h/0.4655 = 2.148h$.

From the values of the polarization parameters in Fig. 5.2a, we evaluate the parameter ratio Δ_0/Δ_1 and the concomitant tilt angle ϕ for phase-matched polarization coupling, via Eq. (5.6). The results are plotted in Fig. 5.2b as a function of h/λ_0 , starting from the minimum value of $h/\lambda_0 = 0.4655$ necessary to satisfy Condition (5.7). As expected from Fig. 5.2a, the curve for Δ_0/Δ_1 follows closely the shape of $-\Delta_0/k_0$ because Δ_1/k_0 remains relatively constant and negative in the considered interval for h/λ_0 . As h/λ_0 increases, the monotonic increase of Δ_0/Δ_1 leads to a monotonic increment in ϕ , as follows from Eq. (5.6). As a consequence of the nonlinear relationship between Δ_0/Δ_1 and ϕ [Eq. (5.6)], the rapid increment in Δ_0/Δ_1 immediately after $h/\lambda_0 = 0.4687$ results in an even faster increase in ϕ with h/λ_0 . Then, the increase in ϕ slows down as it approaches $\phi = \pi/4$, since there the derivative of ϕ with respect to Δ_0/Δ_1 reaches its minimum.

5.2.2 Effective coupling coefficient and rotator bandwidth

From Eq. (5.8), $|\kappa_{\text{eff}}|$ is inversely proportional to the length of the tilted segment and, thus, to the associated propagation loss in decibels. Hence, a larger $|\kappa_{\text{eff}}|$ is more desirable, as it results in a device with smaller footprint and lower insertion loss. Figure 5.3a shows the variation of $|\kappa_{\text{eff}}|/k_0$ with h/λ_0 . It vanishes when $h = 0.4655\lambda_0$, where $\Delta_0 = -\Delta_1$, as a consequence of its definition, Eq. (5.8). Then, it rapidly increases with h/λ_0 and reaches a maximum of 5.7556×10^{-4} when $h = 0.5283\lambda_0$. Afterwards, $|\kappa_{\text{eff}}|/k_0$ decreases slowly with increasing h/λ_0 over the sampled interval. The presence of a maximum in $|\kappa_{\text{eff}}|$ can be understood from Eq. (5.8) as a consequence of the interplay in the dependence on h/λ_0 of its two factors: $|\kappa|$, which decreases monotonically with increasing h/λ_0 ; and $\sqrt{1 - (\Delta_0/\Delta_1)^2}$, which increases from zero at $h = 0.4655\lambda_0$, where $\Delta_0 = -\Delta_1$, as found in Fig. 5.2b.

Because $|\kappa_{\text{eff}}|$ is maximized at $h = 0.5283\lambda_0$ for a given wavelength, this thickness h results in the minimum rotator length L . For example, at $\lambda_0 = 1550$ nm, the minimum-length thickness is 819 nm. From Figs. 5.2b and 5.3a, the corresponding tilt angle ϕ and waveguide length L are 0.5045 radians (29 degrees) and 673 μm , respectively.

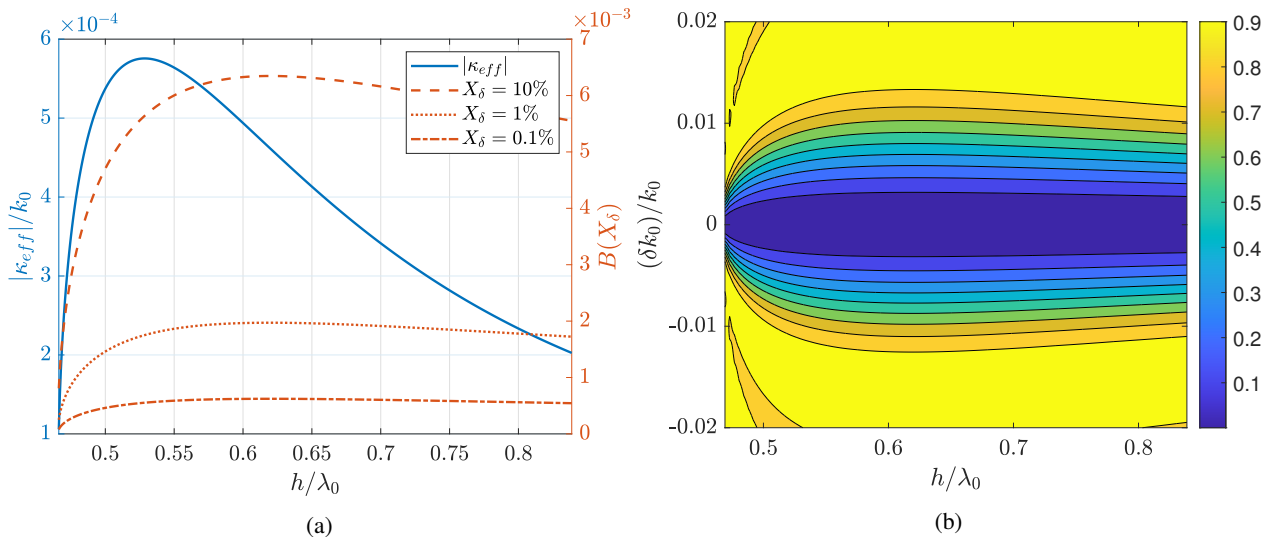


Figure 5.3: (a) Effective coupling coefficient $|\kappa_{eff}|$ and normalized rotator bandwidth $B(X_\delta)$ ($X_\delta = 10\%, 1\%, 0.1\%$) as functions of optical thickness h/λ_0 . (b) Contours of constant detuning-induced crosstalk X_δ as function of waveguide's thickness h/λ_0 and relative detuning $\delta k_0/k_0$.

LNOI waveguides with losses of 0.1 dB/cm or less can be reliably fabricated through dry-etching [11]. For a 673 μm -long polarization rotator, losses are thus estimated to be 6×10^{-3} dB or less. Even if this loss value increases to 10^{-2} dB when the waveguide thickness and other parameters do not have their optimum values, losses for our proposed polarization rotator are low enough to be acceptable for practical application.

For practical use, the bandwidth of the polarization rotator is of interest. Full polarization rotation (100% power transfer) occurs only for a target wavenumber, k_0 , even when residual crosstalk X_r from Eq. (5.9) is negligible. When k_0 deviates from this target value, a fraction X_δ of the input power is left in the input polarization. This results in polarization crosstalk and thus limits the device's bandwidth.

To evaluate the ideal rotator's bandwidth, we evaluate X_δ directly from Eq. (5.1) and study it as a function of wavenumber shift, δk_0 , for various rotator thicknesses. To isolate the effect of wavelength detuning, we assume r is large enough so X_r in Eq. (5.9) can be safely neglected. Thus, in Fig. 5.3b, we report a contour-plot of X_δ as a function of h/λ_0 and the normalized wavenumber shift, $\delta k_0/k_0$. For a given optical thickness, the dependence of X_δ on detuning is easy to describe. Naturally, X_δ vanishes for $\delta k_0 = 0$. For small $|\delta k_0|/k_0$ (e.g., $|\delta k_0|/k_0 < 5 \times 10^{-3}$ for $h > 0.5\lambda_0$), X_δ increases quadratically with δk_0 . For larger $|\delta k_0|/k_0$, X_δ begins to saturate and tends towards its maximum $X_\delta = 1$.

Next, we examine the shape of the lines of constant X_δ in Fig. 5.3b. We note that they all converge at the point $h/\lambda_0 = 0.4655$, $\delta k_0 = 0$. Clearly, a polarization rotator with thickness $h = 0.4655\lambda_0$ has vanishing bandwidth. As h/λ_0 increases beyond this value, the contours of constant X_δ spread out rapidly until $h = 0.6196\lambda_0$, where they all reach their respective maxima in $|\delta k_0|$. Thereafter, the constant-crosstalk lines seemingly converge slowly towards a point located to the right of the sampled parameter space (large $h \gg \lambda_0$) with $\delta k_0 = 0$.

The behavior of X_δ in Fig. 5.3b suggests that any measure of the rotator's bandwidth displays a maximum around $h = 0.6196\lambda_0$. To confirm this statement, we evaluate the normalized bandwidth $B(X_\delta)$, defined as a dimensionless quotient. Its numerator is the absolute difference between the detunings δk_0 of smallest magnitude resulting in a crosstalk of X_δ ; its denominator, the device's nominal wavenumber k_0 . We compute $B(X_\delta)$ for $X_\delta = 10\%, 1\%$, and 0.1% as a function of h/λ_0 using a numerical nonlinear-equation solver. The results are shown in Fig. 5.3a with the y-scale on the right side. As expected, all three curves for $B(X_\delta)$ vanish at $h = 0.4655\lambda_0$ and peak at $h = 0.6196\lambda_0$. After the maximum, all curves feature the slow descent observed in the lines of constant X_δ of Fig. 5.3b.

Analysis of the $B(X_\delta)$ curves in Fig. 5.3a allows the determination of the required rotator geometry for a given bandwidth specification. For example, if the acceptable crosstalk is -20 dB ($X_\delta = 1\%$), $B(X_\delta)$ is close to 0.2% for $h > 0.55\lambda_0$. At the telecom wavelength of 1550 nm, this translates to a detuning of up to 1.5 nm on each side. If we are willing to accept a larger crosstalk of up to -10 dB ($X_\delta = 10\%$), the detuning can be as large as 4.5 nm.

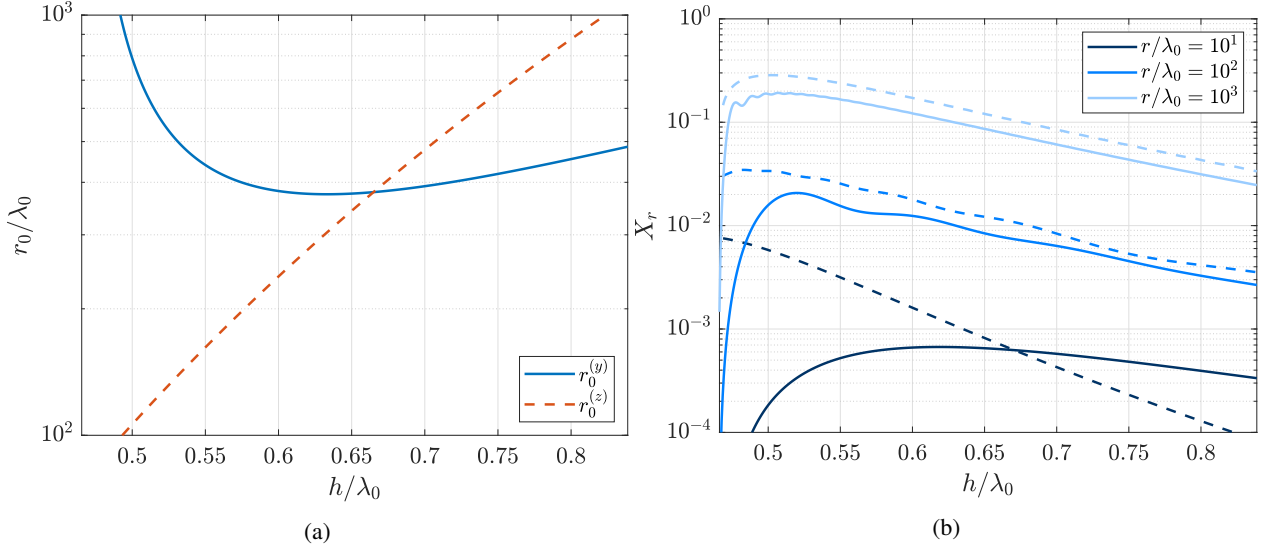


Figure 5.4: (a) Bound r_0 on the bending radius r as a function of optical thickness h/λ_0 . r_0 is such that $r \ll r_0$ ensures negligible polarization coupling along the curved joints. $r_0^{(y)}$ ($r_0^{(z)}$) is r_0 for Configuration Y (Configuration Z). (b) Residual crosstalk X_r as a function of optical thickness h/λ_0 , calculated for different bending radii ($r/\lambda_0 = 10^1, 10^2, 10^3$). Solid lines correspond to Configuration Y; dashed lines, to Configuration Z.

5.2.3 Residual crosstalk due to finite curvature at the joints

Next, we evaluate the residual crosstalk X_r due to polarization coupling along the curved joints for the LNOI rotator. As discussed in Sec. 5.1.3, this is governed by Eqs. (5.9) and (5.10). First, we evaluate r_0 , the upper bound on the bending radii r , defined in Eq. (5.10). Thus, in Fig. 5.4a we plot r_0 on a logarithmic scale as a function of h/λ_0 for both configurations, Y and Z; and label them $r_0^{(y)}$ and $r_0^{(z)}$, respectively. From Fig. 5.4a, two features are most prominent. First, $r_0^{(y)}$ diverges as h/λ_0 approaches 0.4655 from the right. Second, $r_0^{(y)} > r_0^{(z)}$ if $h < 0.6667\lambda_0$ and $r_0^{(y)} < r_0^{(z)}$ if $h > 0.6667\lambda_0$.

These two features can be understood from the definition of r_0 , Eq. (5.10). The divergence of $r_0^{(y)}$ is a consequence of the facts that r_0 is inversely proportional to $\sin^2 \phi$ and that ϕ vanishes at $h = 0.4655\lambda_0$, as seen in Fig. 5.2b. Meanwhile, the crossing of $r_0^{(y)}$ and $r_0^{(z)}$ at $h = 0.6667\lambda_0$ occurs because, in this neighborhood of h/λ_0 , Δ_0 vanishes, as seen in Fig. 5.2a. Consequently, $\phi = \pi/4$ for both configurations, according to Eqs. (5.6) and (5.11). Because $|\kappa|$ is (approximately) invariant between configurations, Eq. (5.10) then yields identical expressions for r_0 for both configurations when $\phi = \pi/4$. We acknowledge that this argument is not exact, as $r_0^{(o)}$ and $r_0^{(e)}$ in Fig. 5.4a intersect at $h = 0.6667\lambda_0$, but Δ_0 vanishes for Configuration Y at $h = 0.6427\lambda_0$, as seen in Fig. 5.2a. However, we attribute this slight discrepancy to the approximate (rather than exact) nature of SCMT, as discussed in Sec. 5.1.4.

These features of Fig. 5.4a suggest that, to minimize X_r , one should use Configuration Y if $h < 0.6667\lambda_0$ and Configuration Z if $h > 0.6667\lambda_0$, regardless of r . However, to achieve a stronger conclusion, we must examine the transcendental expression for X_r in Eq. (5.9), rather than just its simpler bound, Eq. (5.10). Thus, we evaluate X_r from Eq. (5.9) numerically for both configurations, for a continuum of values of h/λ_0 , and for discrete values of r/λ_0 ; specifically, $r/\lambda_0 = 10^1, 10^2, 10^3$. The results are plotted on a logarithmic scale in Fig. 5.4b.

For $r/\lambda_0 = 10$, the curve for X_r in Fig. 5.4b is well described as that of r_0/λ_0 in Fig. 5.4a, albeit subjected to a vertical stretch and a reflection over the y -axis. This implies that X_r is well approximated by the upper bound 5.10. This is expected, because for sufficiently small r (lower than or of the order of $|\Delta_1|^{-1}$), the phase factor in the integrand of Eq. (5.9) approximates unity, and Eq. (5.10) becomes an equality for X_r .

For larger values of r ($r \gg |\Delta_1|^{-1}$), however, the phase factor in Eq. (5.9) oscillates rapidly with the integrand. Consequently, X_r becomes much smaller than its upper bound of r/r_0 . Of course, the effect is more noticeable for larger ϕ , as then the phase of the integrand in Eq. (5.9) oscillates more over the integration domain. To see this, compare the curves for $r/\lambda_0 = 10^2$ and $r/\lambda_0 = 10^3$ with those for $r/\lambda_0 = 10^1$. If the integrand still oscillated slowly in

phase, the $r/\lambda_0 = 10^2$ and $r/\lambda_0 = 10^3$ would be identical to those for $r/\lambda_0 = 10^1$, merely shifted along the logarithmic y -axis by factors of 10^2 and 10^4 , respectively. However, the $r/\lambda_0 = 10^2$ and $r/\lambda_0 = 10^3$ curves are noticeably below those predicted through these shifts to the $r/\lambda_0 = 10^1$ lines, as expected.

Additionally, we observe that the $r/\lambda_0 = 10^2$ and $r/\lambda_0 = 10^3$ curves get closer to their corresponding $r/\lambda_0 = 10^1$ lines, the larger tilt angle ϕ is. Specifically, for Configuration Y, the $r/\lambda_0 = 10^2$ and $r/\lambda_0 = 10^3$ lines grow closer to the $r/\lambda_0 = 10^1$ line as h/λ_0 increases, because ϕ increases with h/λ_0 , as seen in Fig. 5.2b. For Configuration Z, the $r/\lambda_0 = 10^2$ and $r/\lambda_0 = 10^3$ curves grow closer to $r/\lambda_0 = 10^1$ curve as h/λ_0 decreases. This is because ϕ increases with decreasing h/λ_0 in this configuration, by applying the arguments of Sec. 5.1.4 to ϕ in Fig. 5.2b. This agrees with our claim that larger ϕ leads to larger inhibition of X_r due to phase-mismatch.

The net effect is that Configuration Y yields a smaller residual crosstalk X_r at any waveguide thickness, for $r/\lambda_0 = 10^2$ and $r/\lambda_0 = 10^3$. This is because, at small h/λ_0 , its upper bound of r/r_0 tends to zero as $\phi \rightarrow 0$; and, for large h/λ_0 , the larger ϕ leads to a larger accumulated phase-mismatch. Only for small r ($r/\lambda_0 \approx 10^1$), phase-mismatch is small overall and the conclusion from Fig. 5.4a holds, which recommends Configuration Z for large h/λ_0 ($h > 0.6667\lambda_0$).

5.3 Conclusion

We utilized our spatial couple-mode theory to design a passive polarization rotator, coupling fundamental polarization modes. It consists of a LNOI waveguide tilted at an optimum angle, such that material anisotropy induces phase-matched polarization coupling. We discussed how the device's tilt angle and length depend on the core's thickness h and the incident wavelength λ_0 through the optical thickness h/λ_0 . We discussed two sources of crosstalk: the finite curvature of the waveguide joints, and wavelength detuning from the device's nominal wavelength. From this discussion, we showed that joint-curvature crosstalk is negligible for experimentally feasible bending radii, and we characterized the crosstalk-limited bandwidth of the device. Our results suggest that compact (length < 1 mm), low-loss, passive polarization rotators can be fabricated with our proposed design.

Chapter 6

AFC in an all-pass resonator

As explained in Chapter 1, adiabatic frequency conversion (AFC) is a promising alternative for integrated, tunable, electro-optical frequency shifting, unconstrained by the limitations of nonlinear wave mixing. Nonetheless, theoretical work on AFC so far has focused either on its modeling and description [22–24, 46, 47], or on its proposal for novel applications [18, 24, 49, 50]. Discussion of the AFC efficiency has attracted less attention. It was found in Ref. [48] that AFC in an all-pass (i.e. Gires–Tournois) resonator can yield an energy efficiency of 74%. However, a comprehensive theoretical study of AFC efficiency is still lacking, that analyzes all its limitations and determines the conditions for optimal efficiency. Thus, the objective of this chapter is to perform such analysis for its simplest resonator-based configuration, i.e., in a single all-pass resonator, with a ring resonator coupled to a bus waveguide as a typical example. We hope that our study will help move the investigation of AFC from proof-of-principle demonstrations to engineering practical devices for diverse applications.

AFC has been analyzed through two semi-analytic approaches. One approach is based on heuristic traveling-wave models [45–47]. In these, an intuitive ansatz is proposed for optical wave propagation in a dynamic medium, inferred from generalizing wave propagation in static cavities. Although this approach is intuitive by construction, it is unclear how to derive their ansatz from Maxwell’s equations. As a result, its accuracy cannot be judged without comparing directly with experiments or an independent analysis.

The other approach employs temporal coupled-mode theory (TCMT), as presented in Chapter 3 [18, 23, 27, 48, 49]. The main advantage of this approach is the simplicity of the resulting equations, which reduce the electromagnetic field to a finite number of degrees of freedom. Moreover, this approach can be derived directly from Maxwell’s equations, as in Chapter 3 and in References [23, 27]. Hence, conditions sufficient for its validity can be obtained, and its accuracy can be assessed a priori. For these reasons, we analyze AFC in this paper utilizing TCMT.

The remainder of the chapter is organized as follows. In Section 6.1, we describe the system under analysis, write the governing TCMT equations, and find a general expression for the AFC energy efficiency in the high-modulation limit. In Section 6.2, we use the Cauchy-Schwarz inequality to examine the theoretical limit of energy efficiency for AFC, and to analyze the dependence of energy efficiency on input pulse shape. We also explain how the ideal input pulse shape to excite AFC emerges directly from energy conservation and reversibility in time. In Section 6.3, we consider a fixed, single-lobe input pulse shape, and analyze how the energy efficiency of AFC varies as we change the various timescales of the process. We obtain simple formulas to maximize the energy efficiency of AFC for any given pulse duration. In Section 6.4, we consider a continuous-wave input of fixed power and analyze the energy of the resulting AFC output. We compare the results with those of Section 6.3 and explain the similarities and differences. In Section 6.5, we present the paper’s conclusions. In Section 6.6, we mathematically justify Eq. (6.8), used in Section 6.1.

6.1 Analysis of the governing equations

We consider the configuration depicted in Figure 6.1. It consists of an optical all-pass resonator (i.e., a resonating structure with a single input port and a single output port [48, 133, 134]) under temporal modulation of its refractive index. Typical examples of all-pass resonators are a Gires–Tournois etalon, a microring resonator directionally coupled to a waveguide, and a photonic-crystal cavity butt-coupled to a photonic crystal waveguide. An optical pulse is

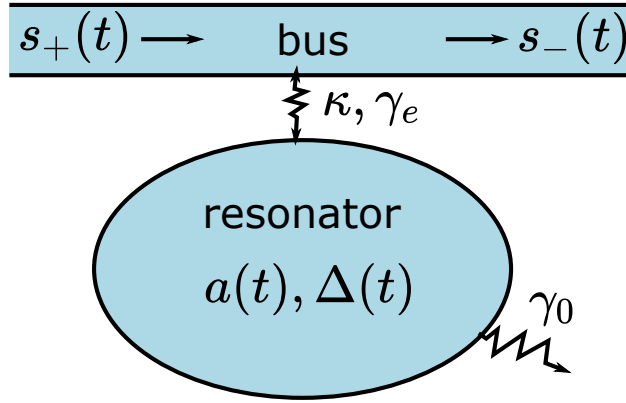


Figure 6.1: Schematic the bus-resonator system used for adiabatic frequency conversion

injected into the input port with a carrier frequency ω equal to that of a specific resonance ω_c of the resonator before modulation. As a result, a large fraction of the input pulse's energy is coupled into the resonator. The amplitude a of the excited resonator mode is normalized so that $|a|^2$ represents the mode's energy before modulation. Modulation of the resonator changes the refractive index, which in turn changes the mode's instantaneous frequency $\omega_c(t)$. As discussed in Section 3.5, the evolution of the mode's amplitude is governed by the TCMT equation [18, 49, 50]

$$\frac{da}{dt} = -i\Delta(t)a - \gamma a + \kappa s_{\text{in}}(t). \quad (6.1)$$

Here, $\Delta(t) = \omega_c(t) - \omega$ is the detuning from the resonance; $s_{\text{in}}(t)$ is the input amplitude, normalized such that $|s_{\text{in}}(t)|^2$ is its instantaneous power; κ is a coupling coefficient; and γ is the mode's decay rate, inversely proportional to the cavity's Q parameter. In general, γ consists of two contributions: an intrinsic decay rate γ_0 , independent of output coupling; and the extrinsic decay rate γ_e , resulting from coupling of the resonator to the output port [75, 77]. Thus we have the relation

$$\gamma = \gamma_0 + \gamma_e. \quad (6.2)$$

In an AFC experiment, the cavity's resonance frequency is modulated monotonically. For simplicity, we assume that the modulation occurs in a step-like fashion over a timescale shorter than the half photon-lifetime γ^{-1} and the duration of $s_{\text{in}}(t)$. In this case, $\Delta(t)$ can be modeled as

$$\Delta(t) = \Delta_0 H(t - t_0). \quad (6.3)$$

Here t_0 is the time at which modulation starts; $H(t)$, the Heaviside function; and Δ_0 , the post-modulation detuning of the cavity with respect to its original resonance.

To complete the description of AFC in an all-pass resonator, we must also consider the output wave $s_{\text{out}}(t)$ leaving the resonator. It is given by [77]

$$s_{\text{out}}(t) = \exp(i\phi) [s_{\text{in}}(t) - \kappa a(t)], \quad (6.4)$$

where ϕ is a constant phase that depends on the planes where $s_{\text{in}}(t)$ and $s_{\text{out}}(t)$ are defined. From energy conservation and time-reversibility considerations, it can be shown [75] that κ in Eq. (6.1) and κ in Eq. (6.4) must indeed be identical and that the sign between $s_{\text{in}}(t)$ and $\kappa a(t)$ in Eq. (6.4) must be negative, so the output energy equals the input energy in the absence of intrinsic loss. The form of Eq. (6.4) is also consistent with the results of our Weisskopf-Wigner analysis in Section 3.5. Increasing the coupling between the resonator and the bus increases both κ and γ_e . Hence, it is critical to model the relation between these two parameters to model and optimize AFC. This is accomplished via energy-conservation arguments and results in the relation [75]

$$\kappa = \sqrt{2\gamma_e}. \quad (6.5)$$

After the cavity undergoes modulation, we expect two things to happen. First, we expect the light contained therein to follow the new frequency. Second, we expect the coupling of the input $s_{\text{in}}(t)$, oscillating at the original resonance frequency, into the mode amplitude $a(t)$ to become inefficient. To verify these two expectations, it is convenient to

introduce a change of variable for $t > t_0$, from the rapidly oscillating $a(t)$ to the slowly oscillating $\tilde{a}(t)$, defined through

$$a(t) = \tilde{a}(t) \exp[-(i\Delta_0 + \gamma)(t - t_0)]. \quad (6.6)$$

Substituting Eq. (6.6) into Eq. (6.1), and integrating the resulting differential equation, we obtain

$$\tilde{a}(t) = a(t_0) + \int_{t_0}^t dt' \kappa s_{\text{in}}(t') \exp[(i\Delta_0 + \gamma)(t' - t_0)]. \quad (6.7)$$

If the second term on the right-hand side of Eq. (6.7) can be neglected, then both of our expectations would be correct. In that case, $\tilde{a}(t)$ would be a constant, and $a(t)$ would oscillate at the frequency Δ_0 , as indicated in Eq. (6.6). Also, $s_{\text{in}}(t)$ would have no effect, as it would not couple appreciably to $a(t)$. In Section 6.6, we show that neglect of the integral in Eq. (6.7) is justified if

$$8\gamma_e \ll T_s \Delta_0^2, \quad (6.8)$$

where T_s be the duration of the input pulse $s_{\text{in}}(t)$.

When Eq. (6.8) holds, Eq. (6.6) shows that $a(t)$ oscillates at the frequency Δ_0 and decays exponentially for $t > t_0$. Given the output relation in Eq. (6.4), $s_{\text{out}}(t)$ will lead to interference between $a(t)$ and the input $s_{\text{in}}(t)$ at the original frequency. Let us assume the original frequency is filtered out from $s_{\text{out}}(t)$. Then the output energy U_c at the converted frequency is a function of the modulation time t_0 and can be evaluated as

$$U_c = \int_{t_0}^{\infty} dt |s_{\text{out}}(t)|^2 = \frac{\gamma_e}{\gamma} |a(t_0)|^2. \quad (6.9)$$

Thus, we can maximize U_c if we maximize the product $(\gamma_e/\gamma)|a(t_0)|^2$. Because Eq. (6.1) is linear in $a(t)$, it proves convenient to consider the auxiliary variable

$$a_c(t_0) = \sqrt{\frac{\gamma_e}{\gamma}} a(t_0), \quad (6.10)$$

As $U_c = |a_c(t_0)|^2$, the output energy $U_c(t_0)$ is maximum whenever $|a_c(t_0)|$ is. Therefore, $a_c(t_0)$ can be interpreted as a converted-energy amplitude, just as $a(t)$ is the instantaneous energy amplitude of the resonator mode. We rewrite Eq. (6.1) as a differential equation for $a_c(t_0)$ and obtain

$$\frac{da_c}{dt_0} = -\gamma a_c + \sqrt{\frac{2\gamma_e^2}{\gamma}} s_{\text{in}}(t_0). \quad (6.11)$$

Eq. (6.11) is the main result of this section, and its solutions are the subject of interest in the following sections. We emphasize that the modulation time t_0 is the independent variable in this equation.

6.2 Upper limit on the Energy Efficiency

Usually, the cavity undergoing AFC is unexcited before the incident pulse $s_{\text{in}}(t)$ starts driving it. Let T be the time during which the input pulse $s_{\text{in}}(t)$ couples with the cavity before AFC is induced. By this definition, cavity excitation starts at $t_0 - T$. Then $a_c(t) = 0$ for $t \leq (t_0 - T)$, and Eq. (6.11) can be integrated to yield

$$a_c(t_0) = \int_{-\infty}^{\infty} dt h(t_0, t) s_{\text{in}}(t), \quad (6.12)$$

where $h(t_0, t)$ is the impulse response of Eq. (6.11) and is given by

$$h(t_0, t) = \sqrt{\frac{2\gamma_e^2}{\gamma}} \exp[-\gamma(t_0 - t)] \times [H(t + T - t_0) - H(t - t_0)]. \quad (6.13)$$

Recalling that the input $s_{\text{in}}(t)$ is normalized so that $|s_{\text{in}}(t)|^2$ is its instantaneous power, the input's total energy U_s is evaluated as

$$\int_{-\infty}^{\infty} dt |s_{\text{in}}(t)|^2 = U_s. \quad (6.14)$$

We are interested in maximizing the converted energy U_c , i.e., the square modulus of $a_c(t_0)$. To do so, we make two observations. First, Eq. (6.12) suggests that $a_c(t_0)$ can be interpreted as an inner product of two complex-valued functions: $h^*(t_0, t)$ and $s_{\text{in}}(t)$. Second, it follows from Eq. (6.13) and Eq. (6.14) that both $h^*(t_0, t)$ and $s_{\text{in}}(t)$ are square-integrable. From these two facts, we conclude that U_c is bounded from above by the Cauchy–Schwarz (CS) inequality for square-integrable functions [135].

$$\left| \int_{-\infty}^{\infty} dt h(t_0, t) s_{\text{in}}(t) \right|^2 \leq \int_{-\infty}^{\infty} dt |h(t_0, t)|^2 \int_{-\infty}^{\infty} dt |s_{\text{in}}(t)|^2. \quad (6.15)$$

From Eq. (6.14), the second integral in the right-hand side of Eq. (6.15) evaluates to U_s . On the other hand, the first integral can be evaluated by substituting Eq. (6.13) for $h(t_0, t)$. In this manner, one readily obtains

$$\int_{-\infty}^{\infty} dt |h(t_0, t)|^2 = (\gamma_e/\gamma)^2 [1 - \exp(-2\gamma T)], \quad (6.16)$$

In evaluating Eq. (6.16), we made use of Eq. (6.5), relating κ and γ_e .

Then, substituting Eq. (6.14) and Eq. (6.16) into the right-hand side of Eq. (6.15), and recalling that the left-hand side of Eq. (6.15) equals the converted energy U_c , we obtain the bound

$$U_c \leq U_s (\gamma_e/\gamma)^2 [1 - \exp(-2\gamma T)]. \quad (6.17)$$

Eq. (6.17) is an important result showing the upper bound on the maximum energy efficiency, $\eta = U_c/U_s$, for AFC in an all-pass resonator. Because both factors, $(\gamma_e/\gamma)^2$ and $[1 - \exp(-2\gamma T)]$ are bounded by unity, Eq. (6.17) is stricter than the intuitively evident condition that the output energy cannot exceed the input energy, i.e., $U_c \leq U_s$. Eq. (6.17) is imposed solely by the resonator and the modulation scheme; specifically, by the ratio of extrinsic to intrinsic decay rate, and the time T between the start of the pulse $s_{\text{in}}(t)$ and the start of the index modulation.

Even for an ideally shaped pulse (discussed below) and modulation satisfying $\gamma T \gg 1$, Eq. (6.17) restricts the energy efficiency η by $(\gamma_e/\gamma)^2$, rather than the intuitive limit of $\eta \leq 1$. Still, this additional factor of $(\gamma_e/\gamma)^2$ makes intuitive sense. One factor of (γ_e/γ) arises from Eq. (6.10). It reflects the fact that not all the energy in cavity at time of modulation exits into the bus, but only a fraction of (γ_e/γ) . The second factor of (γ_e/γ) accounts for the fact that intrinsic loss γ_0 causes coupling to be imperfect. Even for an ideally-shaped pulse, only a fraction (γ_e/γ) of the incident pulse's energy can be coupled into the resonator because energy continuously dissipates into the environment.

The bound in Eq. (6.17) increases with γT , where T is the delay between the start of the pulse and the start of index modulation. However, increasing γT for a fixed pulse shape does not always not increase efficiency of AFC. Such increase in energy efficiency needs only to hold for the ideal pulse shape, for which CS inequality becomes an equality.

A well-known corollary of the CS inequality, Eq. (6.15), is that it becomes an equality if and only if the two functions in the inner product, $s_{\text{in}}(t)$ and $h^*(t_0, t)$, are linearly dependent [135]. It follows from Eq. (6.13) that this can occur if and only if the input $s_{\text{in}}(t)$ has the form

$$s_{\text{in}}(t) = \sqrt{2\gamma U_s} [1 - \exp(-2\gamma T)]^{-1/2} \exp[-\gamma(t_0 - t)] \times [H(t + T - t_0) - H(t - t_0)], \quad (6.18)$$

where $s_{\text{in}}(t)$ has been normalized according to Eq. (6.14). This relation shows that, to achieve the maximum η allowed by Eq. (6.17), $s_{\text{in}}(t)$ must start at the time $(t_0 - T)$, increase exponentially with the rate γ , and terminate at the time t_0 of index modulation.

From Eq. (6.17) and the preceding discussion, we conclude that $U_c = U_s$ when $s_{\text{in}}(t)$ has the shape given in Eq. (6.18), $\gamma_e = \gamma$ (i.e., $\gamma_0 = 0$), and $\gamma T \rightarrow \infty$. In other words, one can transfer total energy U_s of the incident pulse into the frequency-converted output if and only if the cavity has no intrinsic loss, and the pulse exciting it is semi-infinite and exponentially increasing with rate γ_e . Both of these requirements are physically unattainable, so one always obtains $U_c < U_s$.

The interpretation of Eq. (6.12) as an inner product also gives us a prescription for maximizing the converted energy $U_c = |a_c(t_0)|^2$ over a restricted set of pulse shapes $s_{\text{in}}(t)$ of equal energy U_s . This prescription consists of maximizing the projection of $s_{\text{in}}(t)$ along $h(t_0, t)$. For instance, consider the set of exponentially increasing pulses $s_{\text{in}}(t)$ of the form Eq. (6.18), but with γ replaced by a free parameter μ . It is straightforward (albeit tedious) to verify that indeed $\mu = \gamma$ results in the largest possible U_c , equal to the right-hand side of Eq. (6.17).

However, the usefulness of the preceding guideline is limited. This is because it only allows comparison between pulses of equal energy U_s and equal pre-modulation time T . Also, it might not be evident which pulse among a set of possible choices yields the largest projection along $h(t_0, t)$, and numerical evaluation of Eq. (6.12) may be required. Such a calculation is equivalent to solving the original problem of integrating Eq. (6.11); so no insight is gained from the prescription in this case. Nonetheless, as discussed in Section 6.3.2, we show that this guideline is still useful to interpret the results of numerical optimization.

The requirements of no intrinsic loss and a semi-infinite, exponentially increasing $s_{\text{in}}(t)$ for 100% conversion efficiency can be understood via an argument based on the principles of energy conservation and reversibility. The argument is as follows. First, recall from Eq. (6.9) that the converted energy U_c is merely the energy in the cavity at the time of modulation, multiplied by a factor of (γ_e/γ) . But for $U_c = U_s$ to occur, we need $\gamma_e = \gamma$, so in this ideal case, the converted energy and the energy in the resonator are identical. Thus, we only need to argue that when the cavity has zero intrinsic loss and it is excited by a semi-infinite, exponentially increasing pulse, all of the pulse's energy couples to the resonator.

To do so, consider energy dissipation in an ideal cavity with no intrinsic loss. Such an ideal cavity dissipates all of its energy by emitting a semi-infinite exponential pulse into the output port. After an infinite period of time, all of the energy stored in the cavity is released into the output port. If we reverse this process in time, it becomes the injection of a semi-infinite, exponentially increasing pulse into the cavity. From the time-reversal symmetry of Maxwell's equations, this reversed process is also a valid solution to them [75, 136]. Thus, as required, we find that the energy in the exponentially increasing pulse must equal that deposited in the cavity, once the pulse is terminated.

Note that for this time-reversibility argument to agree with the purely mathematical Eq. (6.17), we required Eq. (6.5) to relate κ and γ_e . Therefore, Eq. (6.17) along with the same time-reversibility argument could be used conversely to establish Eq. (6.5). Indeed, such argument follows the same physical reasoning, based on energy conservation and time-reversibility, albeit slightly different mathematics, as the one originally employed by Haus [75] to derive Eq. (6.5).

6.3 Pulsed input of fixed shape

In this section, we examine AFC when the input pulse has a fixed shape and finite energy. Our objective is to analyze the effects of varying several relevant parameters such as relative values of the decay rates γ_0 and γ_e , the modulation time t_0 , and the input-pulse duration T_s .

Rather than working with the input signal $s_{\text{in}}(t)$ directly, it is more convenient to normalize $s_{\text{in}}(t)$ with respect to its duration T_s . Hence, we write $s_{\text{in}}(t)$ as

$$s_{\text{in}}(t) = \frac{1}{\sqrt{T_s}} \bar{s}_+(t/T_s), \quad (6.19)$$

where $\bar{s}_+(\tau)$ is the normalized input-pulse profile subject to two conditions. The first condition is that it obeys the normalization

$$\int_{-\infty}^{\infty} d\tau |\bar{s}_+(\tau)|^2 = U_s. \quad (6.20)$$

Evidently, Eq. (6.14) then follows from Eq. (6.19) and Eq. (6.20). The second condition is that $|\bar{s}_+(\tau)|^2$ is of the order of U_s only when $|\tau|$ is of the order of unity or lower. In other words, $|\bar{s}_+(\tau)|^2$ should be negligible, relative to U_s , for $|\tau| \gg 1$.

Substituting Eq. (6.19) into Eq. (6.11), we obtain

$$\frac{da_c}{d\tau} = -\tilde{\gamma}a_c + \bar{\kappa}\bar{s}_+(\tau), \quad (6.21)$$

where $\tau = t_0/T_s$ is the normalized modulation time; $\bar{\gamma}$, the normalized decay rate; and $\bar{\kappa}$, the normalized coupling constant. These last two are defined as

$$\bar{\gamma} \equiv \gamma_0 T_s + \gamma_e T_s, \quad \bar{\kappa} \equiv \sqrt{2} \gamma_e T_s / \sqrt{\bar{\gamma}}. \quad (6.22)$$

Thus, for a fixed pulse shape $\bar{s}_+(\tau)$, the converted energy amplitude a_c depends on three independent parameters: the normalized modulation time t_0/T_s , the normalized intrinsic decay rate $\gamma_0 T_s$, and the normalized external decay rate $\gamma_e T_s$.

To analyze the dependence of the converted-energy amplitude a_c on the modulation time, we consider input pulses of finite support such that $\bar{s}_+(\tau) = 0$ for $|\tau| > \tau_0$ and some τ_0 . For concreteness, we examine the case where the input pulse $\bar{s}_+(\tau)$ has the shape of a raised cosine, corresponding to

$$\begin{aligned} \bar{s}_+(\tau) &= \sqrt{2U_s/3} [1 + \cos(2\pi\tau)] \\ &\times [H(\tau + 1/2) - H(\tau - 1/2)]. \end{aligned} \quad (6.23)$$

The raised-cosine shape in Eq. (6.23) is also known as the Hann (or Hanning) window function in the context of numerical Fourier analysis [137, 138].

As desired, $\bar{s}_+(\tau)$ in Eq. (6.23) has a finite support: it is only nonzero for $|\tau| < 1/2$. In addition, the Hann pulse has the desirable features of being continuous and having continuous derivative for all real τ . Given Eq. (6.23) for $\bar{s}_+(\tau)$, both its full-width at half-maximum duration, T_{FWHM} , and root-mean-square duration T_{RMS} are straightforward to calculate. These are given by

$$\begin{aligned} T_{\text{FWHM}} &= T_s \arccos(\sqrt{2} - 1) / \pi \approx 0.364 T_s, \\ T_{\text{RMS}} &= \frac{T_s}{2} \sqrt{\frac{1}{3} - \frac{5}{2\pi^2}} \approx 0.141 T_s. \end{aligned} \quad (6.24)$$

Eq. (6.24) can be used to evaluate T_s in terms of experimentally measurable quantities.

In the remainder of this section, we study numerically the dependence of the energy efficiency η on AFC's timescales. Our objective is to determine how choose these timescales to maximize η . To do this, we sweep the normalized timescales of the process and solve Eq. (6.21) for their corresponding values and for the raised-cosine input shape $\bar{s}_+(\tau)$ of Eq. (6.23). Note that the space spanned by the normalized parameters, t_0/T_s , $\gamma_0 T_s$, and $\gamma_e T_s$, is three-dimensional. Thus, we first perform partial parameter sweeps where only two of the three are swept, while the other one is fixed. This allows us to visualize and understand the dependence of η on this reduced two-dimensional parameter space. Then, we perform a global parameter sweep, where all three normalized parameters are swept simultaneously to identify optimum values for all parameters. To enable visualization and because we are mostly interested in optimization, we reduce the dimensionality of the parameter space in this global parameter sweep by considering only the optimum η over the normalized modulation time, t_0/T_s .

6.3.1 Partial parameter sweeps

Having set Eq. (6.23) for $\bar{s}_+(\tau)$, we perform partial parameter sweeps of the solutions $a_c(\tau)$ to Eq. (6.11) and evaluate the corresponding energy efficiency $\eta = U_c/U_s$. The results are depicted in the two plots of Figure 6.2. Because we are interested in sweeping orders of magnitude of the parameter ratios, rather than in examining the effect of small changes, we label them with logarithmic scales. Furthermore, because we are mostly interested in the maxima of U_c ($|a_c(\tau)|^2$), we need only consider $\tau = t_0/T_s \in [-1/2, 1/2]$, as $\bar{s}_+(\tau)$ vanishes outside this range.

Figure 6.2 (top) shows the results of our first parameter sweep. In it, we set the resonator to critical coupling ($\gamma_e = \gamma_0$ [75]) and sweep t_0/T_s and $\gamma_0 T_s$. This figure can be interpreted as a visualization of η for different modulation times t_0 and pulse widths T_s , with fixed γ_0 and γ_e . The most prominent feature of Fig. 6.2 (top) is the maximum in η occurring at $\gamma_0 T_s = 1.1768$ and $t_0/T_s = 0.2172$, where η reaches a value of 0.1987. This indicates that, for a critically coupled resonator, one should set pulse duration T_s equal to $1.1768\gamma_0^{-1}$ and modulation time $t_0 = 0.2172T_s$ to achieve the maximum efficiency under critical coupling. This relatively low value suggests that, although critical coupling maximizes the resonator's energy for continuous-wave input [75], it is not the optimal choice to optimize the energy efficiency of AFC. We demonstrate this inference to be correct in Subsection 6.3.2.

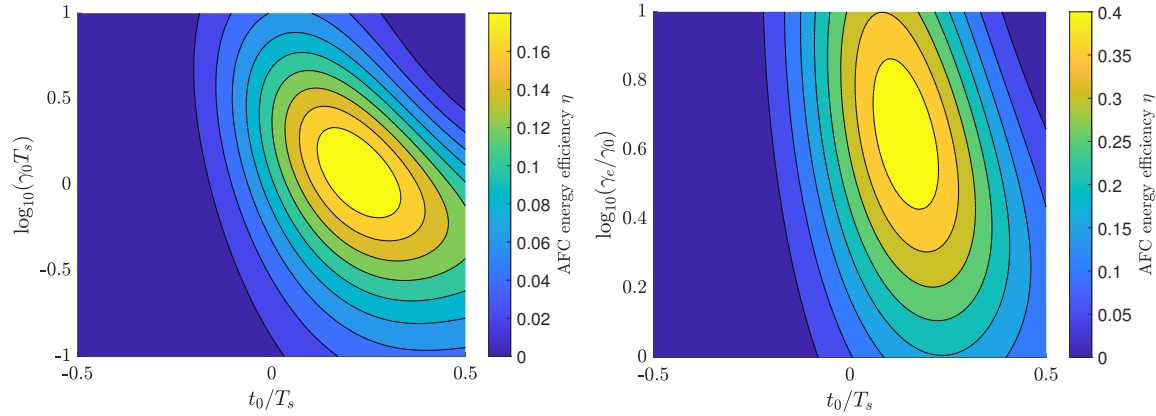


Figure 6.2: Contour plots of the AFC energy efficiency η in the high-modulation limit for a Hann-shape input pulse. Left: AFC energy efficiency η in the case of critical coupling ($\gamma_e/\gamma_0 = 1$). Right: AFC energy efficiency η for a fixed value of the normalized pulse duration ($\gamma_0 T_s = 1$).

We highlight another feature of Fig. 6.2 (top). This is that, for a given value of $\gamma_0 T_s$, the modulation time t_0 for maximum η decreases monotonically with increasing $\gamma_0 T_s$. To explain this feature, we note that $a_c(\tau)$ acts as the output of a first-order low-pass filter with a time constant $\bar{\gamma}^{-1}$. Moreover, because γ_e/γ_0 is fixed, the normalized decay $\bar{\gamma}$ scales linearly with $\gamma_0 T_s$, as a consequence of Eq. (6.22). If $\gamma_0 T_s \ll 1$, the shape of $a_c(\tau)$ resembles the integral of $\bar{s}_+(\tau)$, and its maximum lies close to $t_0 = T_s/2$. On the other hand, as $\gamma_0 T_s$ increases, $\bar{\gamma}^{-1}$ decreases, and the shape $a_c(\tau)$ gradually resembles that of $\bar{s}_+(\tau)$, which has its maximum at $\tau = 0$.

In Figure 6.2 (bottom), we set $\gamma_0 T_s = 1$, while sweeping t_0/T_s and γ_e/γ_0 . This can be interpreted as fixing the intrinsic decay γ_0 and the pulse duration T_s , while varying the modulation time t_0 and the extrinsic decay γ_e . Again, we find a choice of parameters where the AFC efficiency peaks at a value $\eta = 0.4373$. The peak occurs at $\gamma_e = 4.4306\gamma_0$ and $t_0 = 0.1364T_s$. Thus, when the pulse duration T_s is of the order of γ_0^{-1} (twice the intrinsic photon lifetime), one should design the resonator to be slightly overcoupled ($\gamma_e > \gamma_0$) to achieve the maximum AFC efficiency. We observe that the modulation time t_0 for best efficiency decreases with increasing γ_e/γ_0 . Again, this can be understood by interpreting $a_c(\tau)$ as the output of a low-pass filter with the time constant $\bar{\gamma}^{-1}$.

6.3.2 Global parameter sweep

Now, we perform a global parameter sweep, where we sweep the full parameter space by simultaneously varying all normalized parameters: the normalized modulation time t_0/T_s , the normalized pulse duration $\gamma_0 T_s$, and the normalized external decay γ_e/γ_0 . Once again, our objective is to identify the set of parameters which yield maximum AFC energy efficiency $\eta = U_c/U_s$. To allow visualization of the results, we collapse the dependence of η on t_0 by plotting only the maximum of η over t_0/T_s in the range $[-1/2, 1/2]$ for each pair of values for $\gamma_0 T_s$ and γ_e/γ_0 . The result is shown in Figure 6.3 (top). Again, we use logarithmic scales $\gamma_0 T_s$ and γ_e/γ_0 . As is clear from Fig. 6.3 (top), a necessary condition for maximizing η is to minimize $\gamma_0 T_s$. Moreover, as $\gamma_0 T_s \rightarrow 0$, the optimal γ_e that maximizes η for a given $\gamma_0 T_s$ converges to the asymptote

$$\gamma_e T_s = 2.3780, \quad \gamma_0 T_s \ll 1. \quad (6.25)$$

In Fig. 6.3 (top), Eq. (6.25) corresponds to the straight line, $\log_{10}(\gamma_e/\gamma_0) = \log_{10}(2.3780) - \log_{10}(\gamma_0 T_s)$, depicted graphically as a dashed green line. Eq. (6.25) implies that, for $\gamma_0 T_s \ll 1$, a resonator needs to be significantly overcoupled to maximize the converted energy U_c , as also observed in Ref. [48]. To see this, note that if $\gamma_0 T_s \ll 1$, then $(\gamma_e/\gamma_0) \gg \gamma_e T_s$, and $\gamma_e \gg \gamma_0$. This is also graphically evident from Fig. 6.3 (top), where the line for Eq. (6.25) lies noticeably upward from the horizontal level $\log_{10}(\gamma_e/\gamma_0) = 0$.

To understand how Eq. (6.25) emerges, we consider the idealized case of a resonator with no intrinsic loss ($\gamma_0 = 0$). It follows from Eq. (6.22) that $\bar{\gamma} = \gamma_e T_s$ and $\bar{\kappa} = \sqrt{2\gamma_e T_s}$. As a result, η depends only on t_0/T_s and $\gamma_e T_s$. In this idealized case, we determine via numerical optimization that, for an input $\bar{s}_+(\tau)$ with a Hann pulse shape (Eq. (6.23)), η is maximized at $t_0/T_s = 0.2194$ and $\gamma_e T_s = 2.3780$ (matching Eq. (6.25)), attaining the value of $\eta = 0.7951$. From

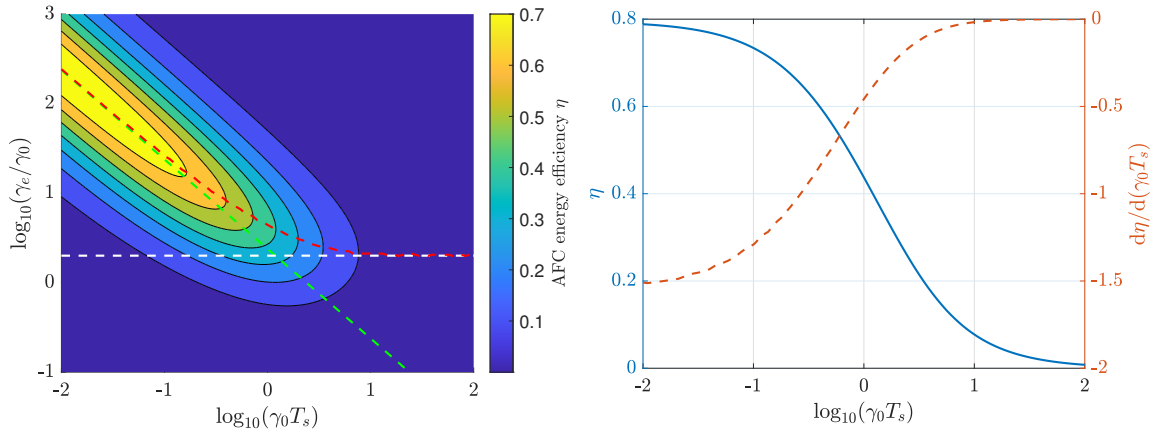


Figure 6.3: Global parameter sweep of the AFC energy efficiency η over both the normalized pulse duration $\gamma_0 T_s$ and the normalized external decay γ_e/γ_0 , optimized over the modulation time t_0 , for an input Hann pulse in the high-modulation limit. Left: Contour plot of AFC energy efficiency η . The red dashed line depicts the locus of optimum γ_e for a given value of $\gamma_0 T_s$. The dashed line indicates its asymptote for $\gamma_0 T_s \ll 1$ and the dashed white line for $\gamma_0 T_s \gg 1$. Right: Plot of the AFC energy efficiency η for a given normalized pulse duration $\gamma_0 T_s$ and maximized over the modulation time t_0 and external decay γ_e (solid blue line). Plot of the derivative of the the AFC efficiency η (optimized with respect to t_0 and γ_e) as a function of $\gamma_0 T_s$ (dashed orange line).

Section 6.2, we recall that maximization of η can be understood geometrically as the maximization of the magnitude of inner product in Eq. (6.12). As γ_0 increases from zero, it only slightly shifts the conditions and decreases the value of the maximum η , as long as it satisfies $\gamma_0 T_s \ll 1$ and $\gamma_0/\gamma_e \ll 1$. Specifically, an increasing, but still small, γ_0 slightly decreases the maximum attainable efficiency η and slightly shifts it towards larger values of γ_e .

Of course, the exact value of 2.3780 in Eq. (6.25) is particular to the Hann shape of the pulse in Eq. (6.23). Nonetheless, the Hann shape is generic in the sense that it represents a typical single-lobe pulse. Hence, an asymptote of the form,

$$\gamma_e T_s = k, \quad k \sim 1, \quad \gamma_0 T_s \ll 1, \quad (6.26)$$

must exist for any single-lobe pulse shape. Furthermore, k can be determined by setting $\gamma_0 = 0$ and optimizing η over t_0/T_s and $\gamma_e T_s$, just as we did for the Hann pulse. As discussed in Section 6.2, this value of k maximizes the magnitude of the inner product between the impulse response $h(t_0, t)$ and the input signal $s_{\text{in}}(t)$.

It follows from Eq. (6.26) that, when the energy efficiency η is maximized, the duration of output pulse is comparable to that of the input pulse. To see this, we recall from Eq. (6.11) that the frequency-shifted pulse is an exponentially decaying pulse with time constant of γ^{-1} . If Eq. (6.26) is satisfied, $\gamma^{-1} \approx \gamma_e^{-1} = T_s/k \sim T_s$. This result was first identified by Daniel et al. [48].

Although Eq. (6.26) maximizes the inner product, one cannot claim that it maximizes the projection of $s_{\text{in}}(t)$ over $h(t_0, t)$, or vice versa. This is because both $s_{\text{in}}(t)$ and $h(t_0, t)$ change as the ratios t_0/T_s , $\gamma_0 T_s$, and γ_e/γ_0 vary. Although $\bar{s}_+(\tau)$ does remain fixed, saying that Eq. (6.26) maximizes the projection of a renormalized $h(t_0, t)$ over $\bar{s}_+(\tau)$ is also misleading. This is because, as the parameter ratios are swept, the renormalized $h(t_0, t)$ changes its norm, rather than just its “direction” in the Hilbert space of square-integrable functions.

As $\gamma_0 T_s$ approaches unity, the external coupling γ_e required for maximum η progressively increases away from Eq. (6.25). When $\gamma_0 T_s$ increases beyond unity, the γ_e required to maximize η is no longer well described by Eq. (6.25). In fact, the optimum γ_e is converges to the asymptote

$$\gamma_e = 2\gamma_0, \quad \gamma_0 T_s \gg 1. \quad (6.27)$$

In Fig. 6.3 (top), Eq. (6.27) corresponds to the horizontal line shown as a dashed white line. It implies that, even for $\gamma_0 T_s \gg 1$, the resonator needs to be overcoupled for efficient AFC, as observed in Subsection 6.3.1.

To understand the origin of Eq. (6.27), we again examine Eq. (6.11) as a low-pass filter. When $\gamma_0 T_s \gg 1$, it follows from Eq. (6.22) that $\bar{\gamma}^{-1} \ll 1$; i.e., the response time $\bar{\gamma}^{-1}$ of $a_c(\tau)$ to $\bar{s}_+(\tau)$ becomes short. Consequently, the differential equation Eq. (6.11) approximates the algebraic relation

$$a_c(\tau) = \bar{\kappa} \bar{s}_+(\tau) / \bar{\gamma}. \quad (6.28)$$

To maximize the converted energy $U_c = |a_c(\tau)|^2$ with respect to γ_e , the coefficient $\bar{\kappa}\bar{\gamma}^{-1}$ should take its maximum value. Eq. (6.27) then results from maximizing $\bar{\kappa}\bar{\gamma}^{-1}$ with respect to γ_e . As implied by this argument, Eq. (6.27) does not depend on the shape of input pulses. This is in contrast to Eq. (6.26), where the precise value of k depends on the specific input pulse shape.

In Figure 6.3 (bottom), we consider a range of values of $\gamma_0 T_s$ and plot with a solid blue line the maximum AFC efficiency η attainable by tuning γ_e . Equivalently, these are the values of η along the dashed red line in Fig. 6.3 (top), plotted as a function of their corresponding $\gamma_0 T_s$. The maximum possible η decreases monotonically with increasing $\gamma_0 T_s$. This verifies the intuitive notion that, for efficient AFC, one should have $\gamma_0 \ll T_s^{-1}$ and $\gamma_0 \ll \gamma_e$, i.e., the intrinsic decay should be small. Also, the efficiency is limited by the upper bound $\eta = 0.7951$. This value corresponds to $\gamma_0 = 0$ for a Hann pulse.

Figure 6.3 (bottom) indicates that one must make $\gamma_0 T_s$ as small as possible to obtain the largest AFC efficiency. However, inspection of the plot for η in Fig. 6.3 (bottom) by itself seemingly implies that decreasing $\gamma_0 T_s$ below unity results in diminishing returns. Specifically, decreasing $\gamma_0 T_s$ to $\gamma_0 T_s - \delta$ ($\delta > 0$) increases η to $\eta + \delta |d\eta/d(\gamma_0 T_s)|$, for small δ ; and $|d\eta/d(\gamma_0 T_s)|$ appears to be maximized at $\gamma_0 T_s = 1$, according to the plot for η in Fig. 6.3 (bottom). However, one must keep in mind that the horizontal axis in Fig. 6.3 (bottom) employs a logarithmic scale. Thus, the local slope of the plot for η does not equal $d\eta/d(\gamma_0 T_s)$. For this reason, we numerically evaluate the derivative $d\eta/d(\gamma_0 T_s)$ and plot it as a dashed orange line in Fig. 6.3 (bottom). This way, we realize that $|d\eta/d(\gamma_0 T_s)|$ increases monotonically with decreasing $\gamma_0 T_s$. Therefore, decreasing of $\gamma_0 T_s$ to increase η actually never incurs diminishing returns, as one might have expected from inspection of only the solid blue curve in Fig. 6.3 (bottom).

6.4 Continuous-wave input

In this section, we consider AFC with a continuous-wave (CW) input of fixed power P_0 . Without loss of generality, we suppose that this CW input is turned on at $t = 0$. We also assume that the rise-time of $s_{\text{in}}(t)$ is negligible compared to the resonator's decay rates γ_0 and γ_e . In this case, we can write the input field $s_{\text{in}}(t)$ in Eq. (6.11) as

$$s_{\text{in}}(t) = \sqrt{P_0} H(t). \quad (6.29)$$

With this expression for $s_{\text{in}}(t)$, Eq. (6.11) can be solved for $a_c(t_0)$ in closed form. The solution corresponds to the step response of a first-order differential equation, well-known from the theory of first-order electric circuits, i.e., RC and RL circuits [139]. From it, we may immediately evaluate the converted energy U_c as

$$U_c = \frac{27}{4} \frac{\gamma_e^2 \gamma_0}{\gamma^3} U_c^{(\text{max})} [1 - \exp(-\gamma t_0)]^2, \quad (6.30)$$

where we have defined

$$U_c^{(\text{max})} = \frac{8}{27} \frac{P_0}{\gamma_0} \approx 0.296 \frac{P_0}{\gamma_0}. \quad (6.31)$$

When both P_0 and γ_0 are fixed, it follows from Eq. (6.30) that the maximum possible converted energy is indeed given by $U_c^{(\text{max})}$ in Eq. (6.31).

Because the CW input of Eq. (6.29) carries infinite energy U_s , we cannot normalize U_c with respect to U_s as in Section 6.3. Nonetheless, normalization of U_c is still useful, as it will allow us to perform a general parameter sweep, depending only on the ratios of the resonator's and modulation timescales, rather than their absolute magnitude. Hence, we take both the input power P_0 and the intrinsic decay rate γ_0 as fixed, normalize U_c with respect to the ratio $U_c^{(\text{max})}$ from Eq. (6.31), and examine the CW efficiency $\eta_{\text{CW}} \equiv U_c/U_c^{(\text{max})}$.

From Eq. (6.30), it is straightforward to verify that $\eta_{\text{CW}} < 1$. Furthermore, η_{CW} converges to unity when Eq. (6.27) is satisfied, with the pulse duration T_s replaced with the modulation time t_0 . Additionally, we note that, when Eq. (6.27) (with the substitution $T_s \rightarrow t_0$) is satisfied, the output pulse's duration γ^{-1} is necessarily much shorter than the modulation time because $\gamma^{-1} \sim \gamma_0^{-1} \ll t_0$.

Given Eq. (6.29) for $s_{\text{in}}(t)$, the CW efficiency η_{CW} depends only on the normalized modulation time $\gamma_0 t_0$ and the normalized decay rate γ_e/γ_0 . Therefore, we may visualize a global parameter sweep of η_{CW} with a simple contour plot. In Figure 6.4 (top) we present such a contour plot of η_{CW} as a function of $\gamma_0 t_0$ and γ_e/γ_0 . We only consider

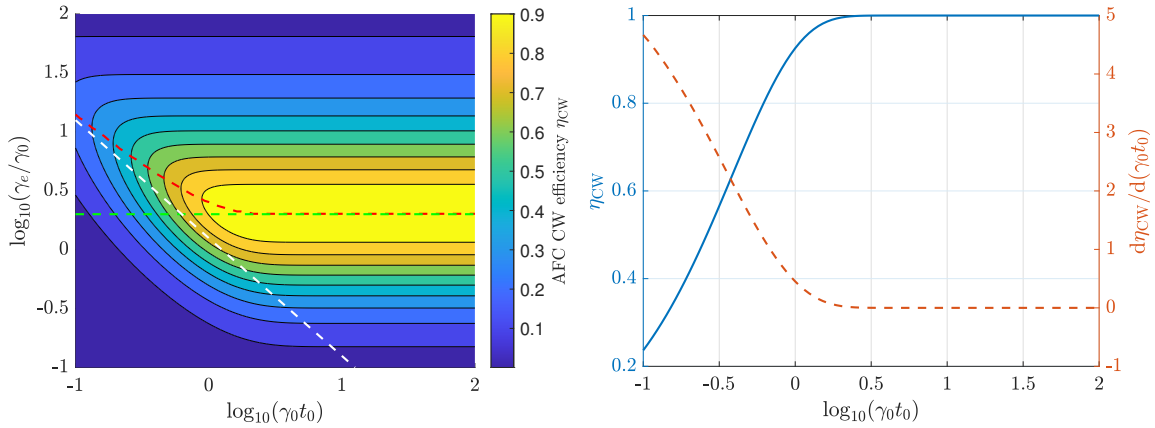


Figure 6.4: Global parameter sweep for the optimization of the AFC energy efficiency η_{CW} for a CW input. Left: Contour plot of the AFC energy efficiency η_{CW} for a CW input. The red dashed line depicts the locus of optimum γ_e for a given value of $\gamma_0 t_0$. The dashed green line indicates its asymptote for $\gamma_0 t_0 \ll 1$; the dashed white line shows the asymptote for $\gamma_0 t_0 \gg 1$. Right: Optimized η_{CW} as a function of $\gamma_0 t_0$ for a given $\gamma_0 t_0$ and maximized over γ_e (solid blue line). Plot of its derivative as a function of $\gamma_0 t_0$ (dashed orange line).

values $\gamma_0 t_0 > 0$, because γ_0 can only be positive, and because $t_0 < 0$ results in $\eta_{\text{CW}} = 0$ in the high-modulation limit, as a consequence of Eq. (6.29).

Figure 6.4 (top) corroborates that η_{CW} is maximized, if and only if Eq. (6.27) is satisfied after the substitution $T_s \rightarrow t_0$. As in Figure 6.3 (top), we show with a dashed red line the curve corresponding to the locus of γ_e that optimize η for a fixed $\gamma_0 t_0$ in Fig. 6.4 (top). As identified above, for $\gamma_0 t_0 \gg 1$, this curve has Eq. (6.27) as an asymptote (with $T_s \rightarrow t_0$). This asymptote is shown as a dashed green line in Fig. 6.4 (top). Similarly to Section 6.3, there exists a different asymptote for $\gamma_0 t_0 \ll 1$ given by the curve

$$\gamma_e t_0 = 1.2564, \quad \gamma_0 t_0 \ll 1. \quad (6.32)$$

To determine the value of 1.2564 in Eq. (6.32), we consider Eq. (6.30) for $\gamma_0 = 0$ and numerically optimize the resulting expression for U_c with respect to $\gamma_e t_0$. The straight line corresponding to Eq. (6.32) is shown as a dashed white line in Fig. 6.4 (top).

As expected, Eq. (6.32) is of the form of Eq. (6.26), albeit with the pulse duration T_s replaced with the modulation time t_0 . Furthermore, we have already shown that the asymptote for $\gamma_0 t_0 \gg 1$ has of the form of Eq. (6.27). Thus, both asymptotes in Figure 6.4 (top) are analogous to those in Figure 6.3 (top). Nonetheless, there is a clear difference between Figure 6.3 (top) for pulsed input and Figure 6.4 (top) for CW input. In Fig. 6.3 (top), the optimum η is achieved when $\gamma_0 T_s \ll 1$, while in Fig. 6.4 (top), the optimum η_{CW} is attained when $\gamma_0 t_0 \gg 1$.

We explain these similarities and differences between η and η_{CW} through the following argument. It is intuitively clear that the frequency-shifted energy U_c achieved with the CW input from Eq. (6.29) should be the same as that achieved with a rectangular input pulse that starts at $t = 0$ and ends at $t = t_0$ (duration $T_s = t_0$) and has total energy $U_s = P_0 t_0$. In evaluating η_{CW} , we normalize U_c with respect to $U_c^{(\max)}$, proportional to $P_0/\gamma_0 = U_s/(\gamma_0 t_0)$, rather than with respect to $U_s = P_0 t_0$. Therefore, η_{CW} in Figure 6.4 (top) can be understood as η for a square input pulse of duration $T_s = t_0$, albeit multiplied by a factor of $27\gamma_0 t_0/8$, as a consequence of normalization with respect to $U_c^{(\max)}$ in Eq. (6.31). The additional factor of $\gamma_0 t_0$ displaces the optimum normalized modulation time $\gamma_0 t_0$ from $\gamma_0 t_0 \ll 1$, as in red Fig. 6.3 (top) to $\gamma_0 t_0 \gg 1$, as in Fig. 6.4 (top). The additional factor of $\gamma_0 t_0$ does not change the optimal γ_e for a given value of $\gamma_0 t_0$. Consequently, the curves of optimal γ_e for a pulsed, square input and a CW input are the same. Recall that the asymptote in Eq. (6.26) is applicable for any single-lobe pulse, with only the value of k varying with the precise pulse shape, as argued in Section 6.3. Thus, the γ_e asymptotes for the Hann pulse are analogous to those for a square pulse. This explains why the asymptotes in Fig. 6.4 (top) resemble those in Fig. 6.3 (top).

As in Section 6.3, we also examine how the maximum attainable η_{CW} varies with the normalized modulation time, $\gamma_0 t_0$. This is equivalent to plotting the value of η_{CW} along the optimal γ_e curve of Fig. 6.4 (top). The result is shown as the solid blue line in Figure 6.4 (bottom). Notice that, as $\gamma_0 t_0$ increases beyond unity, η_{CW} rapidly converges to 1. From Eq. (6.31), we verify that, since the maximum with respect to γ_e converges to $\gamma_e = 2\gamma_0$, the maximum η_{CW} for

a fixed $\gamma_0 t_0$ converges to unity almost exponentially as $\gamma_0 t_0$ tends to infinity. In turn, this causes the derivative of η_{CW} (optimized with respect to γ_e) with respect to $\gamma_0 t_0$ to decay exponentially, as verified by inspection of the dashed orange line in Fig. 6.4 (bottom). Therefore, increasing the modulation time $\gamma_0 t_0$ to increase η_{CW} incurs diminishing returns. To see this, we note as in Section 6.3.2 that increasing $\gamma_0 t_0$ to $\gamma_0 t_0 + \delta(\gamma_0 t_0)$ increases η_{CW} by $\delta(\gamma_0 t_0) d\eta_{\text{CW}}/d(\gamma_0 t_0)$ for small $\delta(\gamma_0 t_0)$. As $d\eta_{\text{CW}}/d(\gamma_0 t_0)$ decreases monotonically with $\gamma_0 t_0$, so does the gain in increasing $\gamma_0 t_0$. This situation contrasts with that for a pulsed input of Section 6.3.2, where the increase in U_c due to a small decrease in $\gamma_0 T_s$ never results in diminishing returns.

6.5 Conclusion

In this paper, we presented a comprehensive theoretical analysis of the attainable energy efficiency of adiabatic frequency conversion (AFC). We invoked the Cauchy-Schwarz inequality, and used it to obtain a theoretical bound for AFC efficiency, determine the optimal pulse shape to excite AFC, and analyze how the pulse shape determines AFC efficiency. Next, we considered a fixed, single-lobe input pulse shape, and analyzed how the AFC efficiency depends on its various timescales. We showed that optimal AFC efficiency always requires resonator overcoupling, albeit with a degree varying with the input pulse duration. Then, we examined the case where AFC is excited by a continuous-wave (CW) optical input. We again found that maximum output energy is achieved when the resonator is overcoupled. Additionally, we interpreted the conditions for optimal AFC under CW input in terms of the results of AFC for a pulsed input. Our results are useful to optimize any realization of AFC in an all-pass resonator. This will enable shifting work on AFC from proof-of-principle experiments to engineering for applications.

6.6 Justification for the condition in Eq. (6.8)

Let $\tilde{a}_1(t)$ stand for the second term in the right side of Eq. (6.7):

$$\tilde{a}_1(t) \equiv \int_{t_0}^t dt' \kappa s_{\text{in}}(t') \exp[(i\Delta_0 + \gamma)(t' - t_0)] \quad (6.33)$$

In this section, we discuss the condition when $\tilde{a}_1(t)$ is negligible compared to $a(t_0)$, so $\tilde{a}(t)$ in Eq. (6.7) can be treated as a constant.

The integral in Eq. (6.33) cannot be performed analytically for an arbitrary pulse shape $s_{\text{in}}(t)$. Because our goal is to find a rule-of-thumb, rather than an exact formula, we choose a pulse shape suitable for analysis. Thus, for simplicity, we take $s_{\text{in}}(t)$ as a rectangular pulse. Then

$$s_{\text{in}}(t) = \sqrt{\frac{U_s}{T_s}} [H(t + T_s/2) - H(t - T_s/2)], \quad (6.34)$$

where U_s is the pulse's energy, and T_s its duration.

Substituting Eq. (6.5) and Eq. (6.34) into Eq. (6.33) and performing the integral, we obtain

$$|\tilde{a}_1(t)|^2 = \frac{4\gamma_e U_s}{(\Delta_0^2 + \gamma^2) T_s} \exp(\gamma t_m) \times [\cosh(\gamma t_m) - \cos(\Delta_0 t_m)], \quad (6.35)$$

where

$$t_m \equiv \min(T_s/2 - t_0, t - t_0). \quad (6.36)$$

As $a(t_0)$ in Eq. (6.7) is independent of Δ_0 , it follows from Eq. (6.35) that for sufficiently large detuning Δ_0 , one must have $|\tilde{a}(t)|^2 \ll |a(t_0)|^2$. In this case, neglect of the second term in the right-hand side of Eq. (6.7) is justified. However, Eq. (6.35) is a transcendental function of both Δ_0 and γ . Hence, it is useful to simplify it, even at the cost of generality. To do so, we consider the high-quality limit, in which $\gamma t_m \ll 1$. Then, $\exp(\gamma t_m) \approx 1$, and $|\tilde{a}_1(t)|^2$ becomes bounded by

$$|\tilde{a}_1(t)|^2 \leq \frac{8\gamma_e U_s}{(\Delta_0^2 + \gamma^2) T_s}. \quad (6.37)$$

If we assume that the ring cavity has been excited efficiently, $|a(t_0)|^2 \sim U_s$. It follows that $|a(t_0)|^2 \ll |\tilde{a}_1(t)|^2$ if

$$8\gamma_e \ll (\Delta_0^2 + \gamma^2) T_s. \quad (6.38)$$

Usually in the case of AFC, we have $|\Delta_0| \gg \gamma$ so the post-modulation output can be resolved from the pre-modulation output. Using this feature, Eq. (6.38) can be simplified to Eq. (6.8).

Chapter 7

Simultaneous AFC in coupled rings

In Chapter 6, we investigated the fundamental limits of AFC efficiency in an all-pass resonator employing temporal coupled-mode theory (TCMT) [74–77, 134]. There, we demonstrated that the process's efficiency is limited by a Schwarz inequality. Consequently, near-unity efficiency can only be attained when two conditions are satisfied. First, the intrinsic loss of the resonator must be small compared to the input pulse's bandwidth and the bus-resonator coupling rate. Second, in accordance with the matched-filter principle [51, 52], the incident pulse must resemble the ring's time-reversed impulse response; in this case, a truncated increasing exponential. Hence, for a symmetric single-lobe pulse (such as a Gaussian pulse), the maximum AFC efficiency is limited to less than 80% [48, 140]. It is desirable to increase the efficiency of AFC for such optical pulses because they are employed in optical communications [1, 141].

In this chapter, we utilize TCMT to demonstrate that the AFC of symmetric single-lobe pulses can achieve a considerably higher efficiency of 97% when it is induced over two coupled microrings, rather than over a single ring. To explain the increased efficiency in this coupled-ring system, we examine AFC as a linear operator of rank two in the Hilbert space of finite-energy pulses (i.e., square-integrable functions). We show that this operator can be understood as the composition of two linear maps: the first one representing the pre-modulation loading of the input into the rings' modal amplitudes, and the second one representing their post-modulation unloading into the frequency-shifted output. Then, we project the AFC operator's image and co-image onto orthonormal bases to represent the loading map, the unloading map, and the AFC operator as 2×2 matrices. We study these matrices' singular value decomposition and show how these decompositions govern the AFC process's efficiency. We evaluate our analytical results numerically in terms of the rings' TCMT parameters. We note that TCMT has been used before to describe accurately the response of time-varying resonators [18, 23, 49]. Thus, its use in this chapter is appropriate.

The rest of the chapter is organized as follows. In Section 7.1, we introduce the two-ring photonic circuit we propose for high-efficiency AFC and we describe its operation. We present the TCMT equations governing it, and write their analytical solution in the limit of strong and fast temporal modulations. In Section 7.2, we examine the solution of Sec. 7.1 as an operator in the vector space of finite-energy pulses, given by the composition of the loading and an unloading maps. We characterize the image and co-image of each of these maps. In Section 7.3, we project the AFC's linear operator into distinct orthonormal bases for its image and co-image to obtain a 2×2 matrix representation for it. Then, we propose a singular value decomposition (SVD) of this matrix representation and discuss its use to examine the AFC efficiency. In Section 7.4, we study the dependence of the rings' impulse response on the device parameters. This study aids the interpretation of the numerical results in subsequent sections. In Section 7.5, we investigate numerically the SVD of the ring loading and ring unloading maps which combine to form the complete two-ring AFC process. In Section 7.6, we analyze the SVD of the full AFC process using the results of the prior sections. In Section 7.7, we examine the AFC of a symmetric, single-lobe pulse in our proposed two-ring network and compare our results with AFC in a single-ring resonator. We interpret our results based on the SVD analysis of the preceding sections. In Section 7.8, we review the chapter's conclusions.

7.1 Description of the photonic circuit and the AFC linear operator

Figure 7.1 shows the proposed photonic circuit for high-efficiency AFC. It consists of two identical evanescently-coupled ring resonators (Ring 1 and Ring 2), one of them (Ring 1) coupled to a bus waveguide. An optical pulse

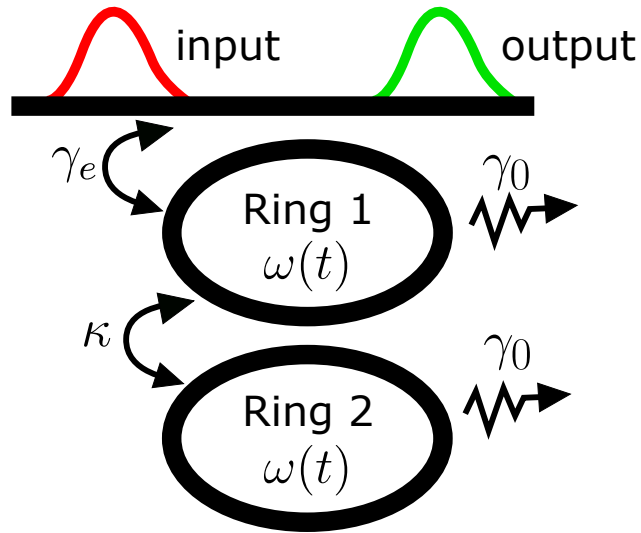


Figure 7.1: Schematic diagram of the photonic circuit for two-ring adiabatic frequency conversion

with carrier frequency equal to the rings' original resonance frequency ω_0 is injected through the bus. Afterwards, the rings' resonance frequency is modulated to induce AFC on the stored light. The frequency-shifted output exits through the bus waveguide. We note that the circuit in Fig. 7.1 is identical to one proposed in Ref. [19]. However, the ring modulation in Ref. [19] is sinusoidal, and the one in this work is monotonic. Hence, the mechanisms for frequency conversion are fundamentally different [22], and so is their corresponding analysis and optimization.

Let $a_j(t)$ ($j = 1, 2$) denote the amplitude of the field in the ring resonators at time t . As conventional in TCMT [74–77, 134] and in agreement with Chapter 3, these are normalized so that $|a_j(t)|^2$ equals the energy in Ring j at time t . Similarly, let $s_{\text{in}}(t)$ and $s_{\text{out}}(t)$ denote the amplitude of the pulse coming into and out of Ring 1. In agreement with Chapter 3, these are normalized so that $|s_{\text{in}}(t)|^2$ is the instantaneous incoming power at time t ; and $|s_{\text{out}}(t)|^2$, the instantaneous outgoing power at time t . Of course, as pointed out in Chapter 3 and Ref. [74], this normalization of $s_{\text{in}}(t)$ and $s_{\text{out}}(t)$ is only accurate when $s_{\text{in}}(t)$ and $s_{\text{out}}(t)$ are sufficiently narrowband for the variation of the waveguide's modal profile to be negligible.

Employing TCMT [74–77, 134] as in Chapter 3, we find that the temporal evolution of the column vector $a(t) = (a_1(t), a_2(t))^T$ is governed by the ordinary differential equation

$$\frac{da}{dt} = H(t)a(t) + ks_{\text{in}}(t). \quad (7.1)$$

Here k a constant column vector, and $H(t)$ a time-dependent square matrix, both given by

$$k = (\sqrt{2\gamma_e}, 0)^T, \quad (7.2)$$

$$H(t) = \begin{pmatrix} -i\omega(t) - \gamma_1 & i\kappa \\ i\kappa^* & -i\omega(t) - \gamma_2 \end{pmatrix}. \quad (7.3)$$

In Eq. (7.2), γ_e is the coupling rate between Ring 1 and the bus waveguide. In Eq. (8.2), $\omega(t)$ is the rings' instantaneous frequency; κ , the complex-valued coupling rate from Ring 2 to Ring 1; γ_1 , the decay rate of Ring 1; and γ_2 , the decay rate of Ring 2.

In accordance to Fig. 7.1, we assume that only Ring 1 is coupled to the bus. Hence, we write the decay rates γ_1 and γ_2 as

$$\begin{aligned} \gamma_1 &= \gamma_e + \gamma_0, \\ \gamma_2 &= \gamma_0. \end{aligned} \quad (7.4)$$

where γ_0 is the intrinsic decay rate of each ring, assumed to be the same for the two identical rings.

From TCMT, we also obtain an expression for the output $s_{\text{out}}(t)$ in terms of the input $s_{\text{in}}(t)$ and the rings' amplitude $a(t)$. As derived in Chapter 3, this is given by

$$s_{\text{out}}(t) = \exp(i\phi) [s_{\text{in}}(t) - k^\dagger a(t)], \quad (7.5)$$

where ϕ is a constant phase that depends on the locations where $s_{\text{in}}(t)$ and $s_{\text{out}}(t)$ are defined [77]. The negative sign before $k^\dagger a(t)$ is necessary to ensure the output energy equals the input energy when the ring frequencies are constant and there is zero intrinsic ring loss (i.e., when $\gamma_0 = 0$). This can be verified by writing the TCMT equations in the frequency domain and invoking Parseval's theorem. This negative sign is also consistent with perturbative treatment of TCMT in Ref. [77] and our Weisskopf-Wigner analysis of Chapter 3. We take $\exp(i\phi) = -1$ for convenience and without loss of generality.

To examine AFC, we consider the case in which $\omega(t)$ changes monotonically. For simplicity, and in the interest of studying fast, efficient AFC, we assume the modulation of $\omega(t)$ takes place rapidly compared to any other relevant timescale except the carrier optical frequency. Thus, as in Chapter 6, we write $\omega(t)$ as

$$\omega(t) = \omega_0 + \Delta\Theta(t - t_m). \quad (7.6)$$

Here, ω_0 is the value of $\omega(t)$ pre-modulation; $(\omega_0 + \Delta)$, its value post-modulation; t_m , the time at which modulation is applied; and $\Theta(t)$, the Heaviside unit-step function. Substituting Eq. (7.6) into Eq. (8.2), the coefficient matrix $H(t)$ may then be written in the analogous form

$$H(t) = H_0 + (H_m - H_0)\Theta(t - t_m). \quad (7.7)$$

Naturally, H_0 is the value of $H(t)$ before modulation, with $\omega(t)$ in Eq. (8.2) replaced by ω_0 ; and H_m , the value of $H(t)$ after modulation, with $\omega(t)$ replaced by $(\omega_0 + \Delta)$.

Using Eq. (7.7) for $H(t)$, it is straightforward to integrate Eq. (8.1). For investigating the AFC efficiency, we need only consider $a(t)$ for $t \geq t_m$. For $t < t_m$, $a(t)$ oscillates at the original frequency ω_0 , which we assume is filtered out after AFC. The solution of Eq. (8.1) for $t \geq t_m$ is given by

$$a(t) = \exp[H_m(t - t_m)]a(t_m) + \int_{t_m}^t dt' \exp[H_m(t - t')]ks_{\text{in}}(t'), \quad \text{for } t \geq t_m, \quad (7.8)$$

where $a(t_m)$, the rings' amplitude at the time of modulation t_m , is given by

$$a(t_m) = \int_{-\infty}^{t_m} dt \exp[H_0(t_m - t)]ks_{\text{in}}(t). \quad (7.9)$$

Henceforth, we assume that the ring modulation is such that the frequency-shift magnitude $|\Delta|$ is large compared to the bandwidth of the input $s_{\text{in}}(t)$. In this case, we may accurately neglect the second term in the right-hand side of Eq. (7.8), as in Chapter 6. This neglect is akin to the rotating-wave approximation in the theory of optical resonance in two-level atoms [20].

Because of this assumed large modulation, we may also neglect the first term in Eq. (7.5), by supposing that any output $s_{\text{out}}(t)$ oscillating at the original frequency is filtered out. Therefore, under this approximation, we may substitute Eq. (7.8) into Eq. (7.5) to obtain

$$s_{\text{out}}(t) = k^\dagger\Theta(t - t_m)\exp[H_m(t - t_m)]a(t_m). \quad (7.10)$$

Together, Eqs. (7.9) and (7.10) provide a linear operator transforming the input $s_{\text{in}}(t)$ into the frequency-shifted output $s_{\text{out}}(t)$. Eq. (7.9) describes the loading of $s_{\text{in}}(t)$ into the ring amplitude $a(t_m)$ at time t_m . And Eq. (7.10) describes the unloading of the ring amplitudes $a(t_m)$ into the output pulse $s_{\text{out}}(t)$ in the bus waveguide.

To close this section, we discuss sufficient conditions on the refractive-index modulation for coupled-ring AFC to be accurately described by Eqs. (8.1) and (7.6), and thus achieve high net efficiency. These conditions are for modulation to be both homogeneous in space (over the coupled rings) and fast in time (compared to the other TCMT timescales). If the modulation is spatially inhomogeneous and occurs with a speed comparable to or faster than the rings' free spectral range, it may induce energy leakage into the rings' neighboring longitudinal modes [22, 23, 27]. Usually, only the output spectrum within a free spectral range is useful, so the spectral broadening due to the excitation

of a ring's other longitudinal modes results in a reduction of the AFC efficiency. However, if either the modulation is spatially homogeneous or slow compared to the rings' free spectral range, dynamic mode coupling is inhibited [22, 23, 27], and we need only consider a single mode per ring (and per polarization) in Eq. (8.1). Nonetheless, for efficient AFC, index modulation must be fast compared to the other TCMT timescales, so long as the ring modulation is spatially homogeneous enough to avoid dynamical mode coupling. This is because, as modulation is induced, the rings' energy continuously decays in time due to coupling to the bus waveguide, and due to intrinsic loss. Thus, a slower index modulation results in a decrease in AFC efficiency, and we may restrict attention to the fast ring modulation described in Eq. (7.6).

7.2 Inner-product analysis of the AFC linear operator and its efficiencies

For the following analysis, we identify the input and output pulses, $s_{\text{in}}(t)$ and $s_{\text{out}}(t)$, as vectors in the vector space of finite-energy pulses; mathematically, the Hilbert space of square-integrable functions of time, L^2 . Thus, we employ Dirac notation and identify them with the kets $|s_{\text{in}}(t)\rangle$ and $|s_{\text{out}}(t)\rangle$, respectively. This vector space has a natural inner product, $\langle f(t)|g(t)\rangle$, defined as

$$\langle f(t)|g(t)\rangle \equiv \int_{-\infty}^{\infty} dt f^*(t)g(t). \quad (7.11)$$

In this notation, the energy E_{in} of the input pulse, and the energy E_{out} of the output pulse are given by

$$E_{\text{in}} = \langle s_{\text{in}}(t)|s_{\text{in}}(t)\rangle, \quad (7.12)$$

$$E_{\text{out}} = \langle s_{\text{out}}(t)|s_{\text{out}}(t)\rangle. \quad (7.13)$$

Of course, E_{out} depends on the energy E_r of the rings at the time of modulation t_m . Correspondingly, E_r given by

$$E_r = a^\dagger(t_m)a(t_m). \quad (7.14)$$

In this Dirac notation, we may rewrite Eqs. (7.9) and (7.10) which govern AFC. These become the abstract equations

$$a(t_m) = \hat{T}_{\text{in}} |s_{\text{in}}(t)\rangle, \quad (7.15)$$

$$|s_{\text{out}}(t)\rangle = \hat{T}_{\text{out}} a(t_m). \quad (7.16)$$

Here, \hat{T}_{in} and \hat{T}_{out} are linear maps. Specifically, \hat{T}_{in} is a linear map from L^2 to the vector space of two-dimensional, complex-valued vectors, \mathbb{C}^2 ; and \hat{T}_{out} is a linear map from \mathbb{C}^2 to L^2 .

For subsequent analysis, we wish to write explicit expressions for \hat{T}_{in} and \hat{T}_{out} in this Dirac notation. To do so, it is convenient to introduce some auxiliary functions. Let $[A]_{nm}$ be the m, n element of the matrix A . Then, we define the functions $u_{nm}(t, 0)$ and $u_{nm}(t, \Delta)$ as

$$\begin{aligned} u_{nm}(t, 0) &= [\exp(H_0 t)]_{nm}, \\ u_{nm}(t, \Delta) &= [\exp(H_m t)]_{nm}. \end{aligned} \quad (7.17)$$

Here, Δ stands for the post-modulation frequency shift, as in Eq. (7.6). Physically, $u_{nm}(t, 0)$ and $u_{nm}(t, \Delta)$ represent the impulse-response functions of the two rings before and after the index modulation. In Appendix ??, we provide explicit expressions for them and examine their properties that are relevant to our study. In terms of these impulse response functions, we can write \hat{T}_{in} and \hat{T}_{out} as

$$\hat{T}_{\text{in}} = \sqrt{2\gamma_e} \begin{pmatrix} \langle u_{11}^*(t_m - t, 0) | \\ \langle u_{21}^*(t_m - t, 0) | \end{pmatrix}, \quad (7.18)$$

$$\hat{T}_{\text{out}} = \sqrt{2\gamma_e} (|u_{11}(t - t_m, \Delta)\rangle, |u_{12}(t - t_m, \Delta)\rangle), \quad (7.19)$$

where the conjugation of the bra vectors results from the definition of the inner product in Eq. (7.11).

An immediate corollary of Eqs. (7.15) and (7.16) is that they constitute a linear map of $|s_{\text{in}}(t)\rangle$ to $|s_{\text{out}}(t)\rangle$ through their composition. Let us denote this map by \hat{T} . Then, we have

$$|s_{\text{out}}(t)\rangle = \hat{T} |s_{\text{in}}(t)\rangle. \quad (7.20)$$

It follows that \hat{T} is a linear map from L^2 to L^2 , i.e., a linear operator in L^2 . Comparing Eq. (7.20) to Eqs. (7.15) and (7.16), we find that

$$\hat{T} = \hat{T}_{\text{out}} \hat{T}_{\text{in}}. \quad (7.21)$$

Substituting Eq. (7.18) for \hat{T}_{in} and Eq. (7.19) for \hat{T}_{out} into (7.21), we get the explicit expression for \hat{T} ,

$$\hat{T} = 2\gamma_e \sum_{j=1}^2 u_{1j}(t-t_m, \Delta) u_{j1}^*(t_m-t, 0). \quad (7.22)$$

The preceding reformulation of AFC in Dirac notation allows us to write succinct expressions for the AFC process's efficiencies. In turn, we show below that these succinct expressions lend themselves to further analysis. We define the AFC's efficiency η as the ratio of the energy E_{out} in the frequency-shifted output to the energy of the input E_{in} . Substituting Eqs. (7.12) and (7.13), it follows that η is given by

$$\begin{aligned} \eta &= \frac{\langle s_{\text{out}}(t) | s_{\text{out}}(t) \rangle}{\langle s_{\text{in}}(t) | s_{\text{in}}(t) \rangle}, \\ &= \frac{\langle s_{\text{in}}(t) | \hat{T}^\dagger \hat{T} | s_{\text{in}}(t) \rangle}{\langle s_{\text{in}}(t) | s_{\text{in}}(t) \rangle}, \end{aligned} \quad (7.23)$$

where we used Eq. (7.20) for $|s_{\text{out}}(t)\rangle$.

As discussed above, the AFC process can be understood as a succession of two constituent processes: the loading \hat{T}_{in} of the input pulse until the modulation time t_m ; and the unloading \hat{T}_{out} of the output pulse after t_m . Hence, it is useful and physically significant to define efficiencies for each of these processes. Let η_{in} be the efficiency of the loading process, with map \hat{T}_{in} ; and η_{out} , the efficiency of the unloading process, with map \hat{T}_{out} . From Eqs. (7.12), (7.14), and (7.18), it follows that

$$\begin{aligned} \eta_{\text{in}} &= \frac{a^\dagger(t_m) a(t_m)}{\langle s_{\text{in}}(t) | s_{\text{in}}(t) \rangle}, \\ &= \frac{\langle s_{\text{in}}(t) | \hat{T}_{\text{in}}^\dagger \hat{T}_{\text{in}} | s_{\text{in}}(t) \rangle}{\langle s_{\text{in}}(t) | s_{\text{in}}(t) \rangle}, \end{aligned} \quad (7.24)$$

and from Eqs. (7.13), (7.14), and (7.19), it follows that

$$\begin{aligned} \eta_{\text{out}} &= \frac{\langle s_{\text{out}}(t) | s_{\text{out}}(t) \rangle}{a^\dagger(t_m) a(t_m)}, \\ &= \frac{a^\dagger(t_m) \hat{T}_{\text{out}}^\dagger \hat{T}_{\text{out}} a(t_m)}{a^\dagger(t_m) a(t_m)}. \end{aligned} \quad (7.25)$$

Intuitively, the efficiency of the complete AFC process is the product of the efficiency of each process. Thus, provided $E_r > 0$, we have

$$\eta = \eta_{\text{in}} \eta_{\text{out}}. \quad (7.26)$$

As a consequence of its expression in Eq. (7.18), \hat{T}_{in} is non-zero over vector components in the subspace of L^2 spanned by $|u_{11}^*(t_m-t, 0)\rangle$ and $|u_{21}^*(t_m-t, 0)\rangle$. Let us denote this subspace as \mathcal{V}_{in} , and let \hat{P}_{in} be the projection operator into \mathcal{V}_{in} . Because \hat{T}_{in} is non-zero only \mathcal{V}_{in} , we may write

$$\hat{T}_{\text{in}} = \hat{T}_{\text{in}} \hat{P}_{\text{in}}. \quad (7.27)$$

Then, substituting Eq. (7.27) into Eq. (7.24), and supposing that $\hat{P}_{\text{in}} |s_{\text{in}}(t)\rangle \neq 0$, we may factor the loading efficiency η_{in} as

$$\eta_{\text{in}} = \eta_{\text{in}}^{(p)} \eta_p. \quad (7.28)$$

In Eq. (7.28), η_p is the projection efficiency, defined as the ratio

$$\begin{aligned} \eta_p &= \frac{\langle s_{\text{in}}(t) | \hat{P}_{\text{in}}^\dagger \hat{P}_{\text{in}} | s_{\text{in}}(t) \rangle}{\langle s_{\text{in}}(t) | s_{\text{in}}(t) \rangle}, \\ &= \frac{\langle s_{\text{in}}^{(p)}(t) | s_{\text{in}}^{(p)}(t) \rangle}{\langle s_{\text{in}}^{(p)}(t) | s_{\text{in}}^{(p)}(t) \rangle + \langle s_{\text{in}}^{(o)}(t) | s_{\text{in}}^{(o)}(t) \rangle}. \end{aligned} \quad (7.29)$$

Here, $|s_{\text{in}}^{(p)}(t)\rangle$ and $|s_{\text{in}}^{(o)}(t)\rangle$ are the components of $|s_{\text{in}}(t)\rangle$ parallel and orthogonal to \mathcal{V}_{in} . In terms of the projector \hat{P}_{in} , these can be expressed as

$$\begin{aligned} |s_{\text{in}}^{(p)}(t)\rangle &= \hat{P}_{\text{in}} |s_{\text{in}}(t)\rangle, \\ |s_{\text{in}}^{(o)}(t)\rangle &= (1 - \hat{P}_{\text{in}}) |s_{\text{in}}(t)\rangle. \end{aligned} \quad (7.30)$$

In Eq. (7.28), $\eta_{\text{in}}^{(p)}$ is the projected loading efficiency, defined as the ratio

$$\eta_{\text{in}}^{(p)} = \frac{\langle s_{\text{in}}^{(p)}(t) | \hat{T}_{\text{in}}^\dagger \hat{T}_{\text{in}} | s_{\text{in}}^{(p)}(t) \rangle}{\langle s_{\text{in}}^{(p)}(t) | s_{\text{in}}^{(p)}(t) \rangle}. \quad (7.31)$$

Given Eqs. (7.27) and (7.28), it is useful to interpret the loading \hat{T}_{in} as a composition of two other maps. From Eq. (7.27), the first map is the projection \hat{P}_{in} of the input $|s_{\text{in}}(t)\rangle$ into the two-dimensional vector space $\mathcal{V}_{\text{in}} \in L^2$. From Eq. (7.29), the energy lost in this process is that in the component $|s_{\text{in}}^{(o)}(t)\rangle$, orthogonal to \mathcal{V}_{in} . The second map is the action of \hat{T}_{in} on the projected input $|s_{\text{in}}^{(p)}(t)\rangle \in \mathcal{V}_{\text{in}}$. The efficiency of this process is $\eta_{\text{in}}^{(p)}$, given by Eq. (7.31).

Given the second line in Eq. (7.29), the projection efficiency η_p can be interpreted as a function of the ratio of $\langle s_{\text{in}}^{(o)}(t) | s_{\text{in}}^{(o)}(t) \rangle$ to $\langle s_{\text{in}}^{(p)}(t) | s_{\text{in}}^{(p)}(t) \rangle$. The quantity $\langle s_{\text{in}}^{(o)}(t) | s_{\text{in}}^{(o)}(t) \rangle$ is non-negative, so η_p is maximized with respect to it when $\langle s_{\text{in}}^{(o)}(t) | s_{\text{in}}^{(o)}(t) \rangle$ vanishes, and η_p equals unity.

Furthermore, η_{in} depends on $\langle s_{\text{in}}^{(o)}(t) | s_{\text{in}}^{(o)}(t) \rangle$ only through the factor of η_p in Eq. (7.28). This has two consequences on the maximization of η_{in} . First, η_{in} is also maximized with respect to $\langle s_{\text{in}}^{(o)}(t) | s_{\text{in}}^{(o)}(t) \rangle$ when it equals zero. Second, the maximum loading efficiency η_{in} over any input non-zero $|s_{\text{in}}(t)\rangle \in L^2$ equals the maximum of the projected loading efficiency $\eta_{\text{in}}^{(p)}$ over any non-zero projected input $|s_{\text{in}}^{(p)}(t)\rangle \in \mathcal{V}_{\text{in}}$. Written mathematically,

$$\max_{|s_{\text{in}}(t)\rangle \neq 0} \eta_{\text{in}} = \max_{|s_{\text{in}}^{(p)}(t)\rangle \neq 0} \eta_{\text{in}}^{(p)}. \quad (7.32)$$

This result is significant because the right-hand side of Eq. (7.32) can be maximized via techniques of finite-dimensional linear algebra, as we discuss below in Section 7.3.

Having analyzed the implications of Eq. (7.27) in the properties of the loading efficiency η_{in} , we next do the same for the overall AFC efficiency η . Substituting Eq. (7.27) into Eq. (7.21), it follows directly that

$$\hat{T} = \hat{T} \hat{P}_{\text{in}}. \quad (7.33)$$

Then, just as for η_{in} in Eq. (7.28) and again assuming $|s_{\text{in}}^{(p)}(t)\rangle \neq 0$, the overall efficiency η can be factored as

$$\eta = \eta^{(p)} \eta_p, \quad (7.34)$$

where $\eta^{(p)}$ is the projected AFC efficiency and is given by the ratio

$$\eta^{(p)} = \frac{\langle s_{\text{in}}^{(p)}(t) | \hat{T}^\dagger \hat{T} | s_{\text{in}}^{(p)}(t) \rangle}{\langle s_{\text{in}}^{(p)}(t) | s_{\text{in}}^{(p)}(t) \rangle}, \quad (7.35)$$

and η_p is again the projection efficiency in Eq. (7.29).

Naturally, substituting Eq. (7.28) into Eq. (7.26) and comparing with Eq. (7.34) yields

$$\eta^{(p)} = \eta_{\text{in}}^{(p)} \eta_{\text{out}}, \quad (7.36)$$

which has the intuitive meaning that the overall projected efficiency $\eta^{(p)}$ is that of the projected loading followed by ring unloading.

Again, we note that the net efficiency η depends on the energy $\langle s_{\text{in}}^{(o)}(t) | s_{\text{in}}^{(o)}(t) \rangle$ only through η_p , as indicated in Eq. (7.34). Thus, just as η_{in} , η is maximized with respect to the non-negative $\langle s_{\text{in}}^{(o)}(t) | s_{\text{in}}^{(o)}(t) \rangle$ when the latter vanishes. In addition, we have

$$\max_{|s_{\text{in}}(t)| \neq 0} \eta = \max_{|s_{\text{in}}^{(p)}(t)| \neq 0} \eta^{(p)}, \quad (7.37)$$

just as η_{in} in Eq. (7.32). Once more, Eq. (7.37) is significant because the maximization of its right-hand side can be performed via methods of finite-dimensional linear algebra, which we do in Sec. 7.3.

We conclude this section with a few remarks on the interpretation of the AFC efficiency η . Within the phenomenological framework of TCMT, we defined η in Eq. (7.23) as the ratio of the output energy at the target output frequency, to the input energy. It follows from Eq. (7.23) that η is independent of the frequency shift Δ , so long as it is sufficiently large compared to the other TCMT time-rates, that filtering of the output results in negligible loss. Moreover, we show in Section 7.6 that η has a tight upper bound of unity. These properties of the AFC energy efficiency η seemingly contradict the intuition that the input light consists of a stream of photons, with energy proportional to their frequency; so the output AFC energy should depend on the frequency shift and have no upper limit, at least in the limit of negligible intrinsic ring loss.

Nonetheless, this photon-stream intuition is indeed compatible with our analysis's results because TCMT is known to be accurate only for narrowband optical excitations [74]. Thus, if the induced frequency shift is small compared to the input pulse's carrier frequency, TCMT is accurate and one may safely neglect the change in the photon energy due to the frequency shift. This is usually the case in AFC of telecom and optical signals, where the ratio of the frequency shift to the carrier frequency is on the order of 10^{-5} to 10^{-3} [10, 33, 34, 43].

Furthermore, we show in Appendix D, via a quantum-optical analysis of the AFC process, that the photon-stream intuition is correct: in the absence of intrinsic loss, AFC in a set of coupled resonators preserves the system's photon-number statistics, but not its energy statistics. Additionally, we show that, to the accuracy of the input-output formalism, popular in quantum optics [81–84], the energy efficiency η of Eq. (7.23), obtained via TCMT, can be interpreted as a mean photon-number efficiency, when the rings-waveguide system is initially in a coherent waveguide state. With this interpretation, the fact that η is independent of the the frequency shift and bounded by unity is intuitive. Additionally, with this interpretation as a photon-number efficiency, Eq. (7.23) for η can be extended beyond the accuracy of TCMT. Nonetheless, the input-output formalism itself is still only applicable to optical excitations with a bandwidth smaller than that of the ring-waveguide coupling, as explained Appendix D.

7.3 AFC matrix representation and singular value decomposition

We aim to fully dissect the AFC efficiency η , determine its upper bounds and examine its dependence on the rings' TCMT parameter and the input pulse shape. To do so, we next introduce orthonormal bases for the image and coimage of the AFC operator \hat{T} . This way, we can represent and analyze it as a matrix.

The coimage of \hat{T} is the orthogonal complement to its nullspace. Hence, it is the subspace of L^2 spanned by $\{|u_{11}^*(t_m - t, 0)\rangle, |u_{21}^*(t_m - t, 0)\rangle\}$, denoted by \mathcal{Y}_{in} in Section 7.2. From Eq. (7.22), the image of \hat{T} is the subspace of L^2 spanned by $\{|u_{11}(t - t_m, \Delta)\rangle, |u_{12}(t - t_m, \Delta)\rangle\}$. We denote this subspace by \mathcal{Y}_{out} .

As shown in Section C.1, $|u_{11}^*(t_m - t, 0)\rangle$ and $|u_{21}^*(t_m - t, 0)\rangle$ are not mutually orthogonal unless $\gamma_0 = 0$. Therefore, in general they do not form an orthonormal basis of \mathcal{Y}_{in} . Nonetheless, we generate an orthonormal basis $\{|n_1^{(\text{in})}\rangle, |n_2^{(\text{in})}\rangle\}$ from them through Gram-Schmidt orthonormalization [109, 135]. We define these unit vectors of \mathcal{Y}_{in} so they satisfy

$$\begin{aligned} \langle n_l^{(\text{in})} | n_m^{(\text{in})} \rangle &= \delta_{lm}, \\ |n_2^{(\text{in})}\rangle &\propto |u_{21}^*(t_m - t, 0)\rangle, \\ |n_1^{(\text{in})}\rangle &\in \mathcal{Y}_{\text{in}}, \\ \langle n_1^{(\text{in})} | u_{11}^*(t_m - t, 0) \rangle &> 0, \\ \langle n_2^{(\text{in})} | u_{21}^*(t_m - t, 0) \rangle &> 0. \end{aligned} \quad (7.38)$$

Here, δ_{lm} is the Kronecker delta. Explicit expressions for $|n_1^{(\text{in})}\rangle$ and $|n_2^{(\text{in})}\rangle$ which satisfy Eq. (7.38) are given in Section C.2. In Eq. (7.38), we choose $|n_2^{(\text{in})}\rangle$ to be proportional to $|u_{21}^*(t_m - t, 0)\rangle$, rather than have $|n_1^{(\text{in})}\rangle$ proportional to $|u_{11}^*(t_m - t, 0)\rangle$. We find that this choice in Eq. (7.38) simplifies the interpretation of the results in Section 7.7.

Analogously, we apply Gram-Schmidt orthonormalization to $|u_{11}(t - t_m, \Delta)\rangle$ and $|u_{12}(t - t_m, \Delta)\rangle$ to obtain an orthonormal basis $\{|n_1^{(\text{out})}\rangle, |n_2^{(\text{out})}\rangle\}$ for the image \mathcal{V}_{out} . This output basis satisfies relations analogous to those in Eq. (7.38), with $|u_{11}^*(t_m - t, 0)\rangle$ replaced by $|u_{11}(t - t_m, \Delta)\rangle$, $|u_{21}^*(t_m - t, 0)\rangle$ by $|u_{12}(t - t_m, \Delta)\rangle$, and \mathcal{V}_{in} by \mathcal{V}_{out} . This is shown in Section C.2, where explicit expressions for $|n_1^{(\text{out})}\rangle$ and $|n_2^{(\text{out})}\rangle$ are provided as well.

With these orthonormal bases for \mathcal{V}_{in} and \mathcal{V}_{out} , we next follow orthonormal representation theory [135] (popular in quantum mechanics [21, 70]) to represent the projected input vector $|s_{\text{in}}^{(p)}(t)\rangle$, and the output vector $|s_{\text{out}}(t)\rangle$ with column vectors, x_{in} and x_{out} ; and the linear maps \hat{T}_{in} , \hat{T}_{out} , and \hat{T} , with square matrices M_{in} , M_{out} , and M , respectively. In this way, we obtain

$$\begin{aligned} |s_{\text{in}}^{(p)}(t)\rangle &= \left(|n_1^{(\text{in})}\rangle, |n_2^{(\text{in})}\rangle \right) x_{\text{in}}, \\ |s_{\text{out}}(t)\rangle &= \left(|n_1^{(\text{out})}\rangle, |n_2^{(\text{out})}\rangle \right) x_{\text{out}}, \\ \hat{T}_{\text{in}} &= M_{\text{in}} \begin{pmatrix} \langle n_1^{(\text{in})} | \\ \langle n_2^{(\text{in})} | \end{pmatrix}, \\ \hat{T}_{\text{out}} &= \left(|n_1^{(\text{out})}\rangle, |n_2^{(\text{out})}\rangle \right) M_{\text{out}}, \\ \hat{T} &= \left(|n_1^{(\text{out})}\rangle, |n_2^{(\text{out})}\rangle \right) M \begin{pmatrix} \langle n_1^{(\text{in})} | \\ \langle n_2^{(\text{in})} | \end{pmatrix}. \end{aligned} \quad (7.39)$$

Here $x_{\text{in}}, x_{\text{out}} \in \mathbb{C}^2$, and $M_{\text{in}}, M_{\text{out}}, M \in \mathbb{C}^{2 \times 2}$, i.e., they are complex-valued two-dimensional vectors, and 2×2 matrices, respectively. Again, matrix multiplication in Eq. (7.39) is implied. Expressions for the matrices M_{in} , M_{out} , and M are given by

$$\begin{aligned} M_{\text{in}} &= \sqrt{2\gamma_e} \begin{pmatrix} \langle u_{11}^*(t_m - t, 0) | n_1^{(\text{in})} \rangle & \langle u_{11}^*(t_m - t, 0) | n_2^{(\text{in})} \rangle \\ \langle u_{21}^*(t_m - t, 0) | n_1^{(\text{in})} \rangle & \langle u_{21}^*(t_m - t, 0) | n_2^{(\text{in})} \rangle \end{pmatrix}, \\ M_{\text{out}} &= \sqrt{2\gamma_e} \begin{pmatrix} \langle n_1^{(\text{out})} | u_{11}(t - t_m, \Delta) \rangle & \langle n_1^{(\text{out})} | u_{12}(t - t_m, \Delta) \rangle \\ \langle n_2^{(\text{out})} | u_{11}(t - t_m, \Delta) \rangle & \langle n_2^{(\text{out})} | u_{12}(t - t_m, \Delta) \rangle \end{pmatrix}, \\ M &= M_{\text{out}} M_{\text{in}}. \end{aligned} \quad (7.40)$$

More explicit expressions for M_{in} and M_{out} , amenable for numerical evaluation, are presented in Section C.2.

Next, we express the efficiencies $\eta_{\text{in}}^{(p)}$, η_{out} , and $\eta^{(p)}$ in the representation of Eq. (7.39). To do so, we substitute Eq. (7.39) into their corresponding expressions (Eqs. (7.31), (7.25), and (7.35), respectively) and leverage the orthonormality of the input and output bases. In this way, we write

$$\begin{aligned} \eta_{\text{in}}^{(p)} &= \frac{x_{\text{in}}^\dagger M_{\text{in}}^\dagger M_{\text{in}} x_{\text{in}}}{x_{\text{in}}^\dagger x_{\text{in}}}, \\ \eta_{\text{out}} &= \frac{a^\dagger(t_m) M_{\text{out}}^\dagger M_{\text{out}} a(t_m)}{a^\dagger(t_m) a(t_m)}, \\ \eta^{(p)} &= \frac{x_{\text{in}}^\dagger M^\dagger M x_{\text{in}}}{x_{\text{in}}^\dagger x_{\text{in}}}. \end{aligned} \quad (7.41)$$

The expression $(x^\dagger Ax)/(x^\dagger x)$ for a square matrix A and a column vector x is called their Rayleigh quotient in the context of linear algebra [142].

The advantage of introducing the representation Eq. (7.39) and writing the efficiencies $\eta_{\text{in}}^{(p)}$, η_{out} , and $\eta^{(p)}$ as Rayleigh quotients is that these are well-understood in finite-dimensional linear algebra [142, 143]. Thus we can investigate them with the robust analytical and numerical techniques of this area. In particular, to study Eq. (7.41) we find it useful to introduce the singular value decomposition (SVD) of the matrices M_{in} , M_{out} , and M . Let $A \in \mathbb{C}^{n \times n}$. Then the SVD of A is a matrix decomposition of the form [143, 144]

$$A = \sum_{j=1}^n \sigma_j w_j v_j^\dagger. \quad (7.42)$$

Here, $\sigma_j \geq 0$ are called the singular values of A ; w_j and v_j are two orthonormal sets of vectors, called the left singular vectors and right singular vectors of A . Every matrix A , even non-square ones, has a SVD. Moreover, the singular values σ_j are uniquely determined, and for square A , the vectors w_j and v_j are uniquely determined up to arbitrary phase factors, so long as the σ_j are distinct [144]. Also, a matrix's SVD is a step in many algorithms in numerical linear algebra, so its computation is a well-studied problem.

Substituting the SVD of the matrices M_{in} , M_{out} , and M into Eq. (7.41), we may write the efficiencies $\eta_{\text{in}}^{(p)}$, η_{out} , and $\eta^{(p)}$ as

$$\begin{aligned} \eta_{\text{in}}^{(p)} &= \sum_{j=1}^2 p_j(M_{\text{in}}, x_{\text{in}}) \sigma_j^2(M_{\text{in}}), \\ \eta_{\text{out}} &= \sum_{j=1}^2 p_j(M_{\text{out}}, a(t_m)) \sigma_j^2(M_{\text{out}}), \\ \eta^{(p)} &= \sum_{j=1}^2 p_j(M, x_{\text{in}}) \sigma_j^2(M). \end{aligned} \quad (7.43)$$

As the notation suggests, $\sigma_j(A)$ is the j th singular value of the matrix A . The factors $p_j(A, x)$ are relative weights satisfying $p_j(A, x) \geq 0$ and $\sum_{j=1}^2 p_j(A, x) = 1$ and are given by

$$p_j(A, x) = \frac{x^\dagger v_j(A) v_j^\dagger(A) x}{x^\dagger x}. \quad (7.44)$$

In accordance to Eq. (7.42), $v_j(A)$ is the j th right singular vector of A .

Eq. (7.43) is one of the main results of this chapter. It implies that the efficiencies $\eta_{\text{in}}^{(p)}$, η_{out} , and $\eta^{(p)}$ are weighted sums of the square of the singular values of their corresponding matrix. Moreover, according to Eq. (7.44), the weight for each σ_j^2 is given by the normalized squared projection of the input column vector (either x_{in} or $a(t_m)$) into the j th right singular vector, v_j .

A corollary of Eq. (7.43) is that the extrema for the efficiencies $\eta_{\text{in}}^{(p)}$, η_{out} , and $\eta^{(p)}$ over their corresponding input are given by

$$\begin{aligned} \max_{|s_{\text{in}}^{(p)}(t)\rangle \neq 0} \eta_{\text{in}}^{(p)} &= \sigma_{\text{max}}^2(M_{\text{in}}), \\ \max_{a(t_m) \neq 0} \eta_{\text{out}} &= \sigma_{\text{max}}^2(M_{\text{out}}), \\ \max_{|s_{\text{in}}^{(p)}(t)\rangle \neq 0} \eta^{(p)} &= \sigma_{\text{max}}^2(M) \end{aligned} \quad (7.45)$$

and

$$\begin{aligned} \min_{|s_{\text{in}}^{(p)}(t)\rangle \neq 0} \eta_{\text{in}}^{(p)} &= \sigma_{\text{min}}^2(M_{\text{in}}), \\ \min_{a(t_m) \neq 0} \eta_{\text{out}} &= \sigma_{\text{min}}^2(M_{\text{out}}), \\ \min_{|s_{\text{in}}^{(p)}(t)\rangle \neq 0} \eta^{(p)} &= \sigma_{\text{min}}^2(M). \end{aligned} \quad (7.46)$$

Here, $\sigma_{\max}(A)$ ($\sigma_{\min}(A)$) is the maximum (minimum) singular value of A .

Moreover, Eqs. (7.43) and (7.44) provide us with prescriptions for how to attain the extrema in Eqs. (7.45) and (7.46). The maxima (minima) for $\eta_{\text{in}}^{(p)}$ and $\eta^{(p)}$ occur when $|s_{\text{in}}^{(p)}(t)\rangle$ has components in the input basis $\left\{|n_1^{(\text{in})}\rangle, |n_2^{(\text{in})}\rangle\right\}$ proportional to the right singular vector v_j corresponding to $\sigma_{\max}(M_{\text{in}})$ and $\sigma_{\min}(M_{\text{in}})$ and $\sigma_{\max}(M)$ ($\sigma_{\min}(M)$), respectively. Similarly, the maximum (minimum) of η_{out} occurs when the amplitude vector $a(t_m)$ is proportional to the right singular vector v_j corresponding to $\sigma_{\max}(M_{\text{out}})$ ($\sigma_{\min}(M_{\text{out}})$).

Lastly, the SVD of M_{in} , M_{out} , and M also prescribes how the energy in the extrema of Eqs. (7.45) and (7.46) is distributed over the images of \hat{T}_{in} , \hat{T}_{out} , and \hat{T} , respectively. When the maximum (minimum) of $\eta_{\text{in}}^{(p)}$ occurs, the amplitude vector $a(t_m)$ at the time of modulation is proportional to the left singular vector w_j corresponding to $\sigma_{\max}(M_{\text{in}})$ ($\sigma_{\min}(M_{\text{in}})$). Similarly, when the maxima (minima) of η_{out} and $\eta^{(p)}$ occur, the frequency-shifted output $|s_{\text{out}}(t)\rangle$ has components in the output basis $\left\{|n_1^{(\text{out})}\rangle, |n_2^{(\text{out})}\rangle\right\}$ proportional to the left singular vector w_j corresponding to $\sigma_{\max}(M_{\text{out}})$ and $\sigma_{\max}(M)$ ($\sigma_{\min}(M_{\text{out}})$ and $\sigma_{\min}(M)$), respectively.

It is important to note that Eq. (7.45) not only gives us the maxima for the projected efficiencies $\eta_{\text{in}}^{(p)}$ and $\eta^{(p)}$, but also the maxima for the overall efficiencies η_{in} and η . Substituting Eq. (7.45) into Eqs. (7.32) and (7.37), we obtain

$$\begin{aligned} \max_{|s_{\text{in}}(t)\rangle \neq 0} \eta_{\text{in}} &= \sigma_{\max}^2(M_{\text{in}}), \\ \max_{|s_{\text{in}}(t)\rangle \neq 0} \eta &= \sigma_{\max}^2(M). \end{aligned} \tag{7.47}$$

Just as discussed after Eq. (7.45), the maxima in Eq. (7.47) are attained when $|s_{\text{in}}(t)\rangle = |s_{\text{in}}^{(p)}(t)\rangle$ and $|s_{\text{in}}^{(p)}(t)\rangle$ has components x_{in} (as in Eq. (7.39)) proportional to the right singular vector v_j corresponding to $\sigma_{\max}(M_{\text{in}})$ or $\sigma_{\max}(M)$. Again, then the output is proportional to the corresponding left singular vector w_j . Unlike $\eta_{\text{in}}^{(p)}$ and $\eta^{(p)}$, however, the minima of η_{in} and η are zero and not the minimum singular values in Eq. (7.46). These vanishing efficiencies appear when $|s_{\text{in}}^{(p)}(t)\rangle = 0$, i.e., when $|s_{\text{in}}(t)\rangle = |s_{\text{in}}^{(o)}(t)\rangle$. This is a consequence of Eqs. (7.27) and (7.33).

7.4 Numerical analysis of the two-ring impulse-response functions

In the following sections, we evaluate numerically the analytical results of Sections 7.2 to 7.3 to quantitatively characterize two-ring AFC and its efficiency. In this section, we start by examining the impulse-response functions $u_{nm}(t, \Delta)$, which govern the AFC process as discussed in Section 7.2.

Let $\bar{u}_{nm}(t) = u_{nm}(t, \Delta) \exp[i(\omega_0 + \Delta)t]$ be the envelopes of the impulse response functions $u_{nm}(t, \Delta)$. We plot the envelope functions $\bar{u}_{11}(t)$ and $\bar{u}_{21}(t)$ in Fig. 7.2 for $\gamma_0 = 0$ and for different values of $|\kappa|/\gamma_e$. Increasing values of γ_0 merely cause the envelopes $\bar{u}_{nm}(t)$ to decay more rapidly with t . As seen in Section C.1, $\bar{u}_{12}(t) = \bar{u}_{21}(t)(\kappa/\kappa^*)$, so plotting $\bar{u}_{12}(t)$ in addition to $\bar{u}_{21}(t)$ is redundant.

It is important to observe the general shape of the envelopes $\bar{u}_{nm}(t)$. This is because of two reasons. First, as discussed in Section 7.2, $u_{11}^*(t_m - t, 0)$ and $u_{21}^*(t_m - t, 0)$ span the vector space $\mathcal{V}_{\text{in}} \in L^2$ over which the input efficiency η_{in} and the overall AFC efficiency η are non-zero. Second, as discussed in Sections 7.2 and 7.3, $u_{11}(t - t_m, \Delta)$ and $u_{12}(t - t_m, \Delta)$ span the image $\mathcal{V}_{\text{out}} \in L^2$ of \hat{T}_{out} (and hence \hat{T}).

We first note the behavior of $\bar{u}_{11}(t)$ and $\bar{u}_{21}(t)$ at $t = 0$. In Fig. 7.2, we observe that we always have $\bar{u}_{11}(0) = 1$ and $\bar{u}_{21}(0) = 0$. Consequently, at $t = 0$, $\bar{u}_{11}(t)$ is discontinuous from the left, but $\bar{u}_{21}(t)$ is continuous. Furthermore, we show in Section C.1 that we always have $du_{11}(0)/dt = -\gamma_1$ and $du_{21}(0)/dt = i\kappa^*$.

In contrast, the qualitative behavior of $\bar{u}_{11}(t)$ and $\bar{u}_{21}(t)$ for $t > 0$ depends on the ratio between the inter-ring coupling and the waveguide-ring coupling, i.e., $|\kappa|/\gamma_e$. We show in Section C.1 that, depending on the value of this ratio, inter-ring coupling can be underdamped, critically damped, or overdamped, just as the motion of a damped harmonic oscillator [145, 146].

If $|\kappa|/\gamma_e > 1/2$, then inter-ring coupling is underdamped. In this case, $\bar{u}_{11}(t)$ and $\bar{u}_{21}(t)$ oscillate around zero with a frequency of $\sqrt{|\kappa|^2 - (\gamma_e/2)^2}$, but their oscillation amplitude decays exponentially at the ring-averaged decay rate of $\bar{\gamma} = (\gamma_1 + \gamma_2)/2$.

If $|\kappa|/\gamma_e = 1/2$, then inter-ring coupling is critically damped. In this case, $\bar{u}_{11}(t)$ and $\bar{u}_{21}(t)$ become the products of two factors. The first factor is still an exponentially decreasing envelope, decaying with the rate $\bar{\gamma}$. The second

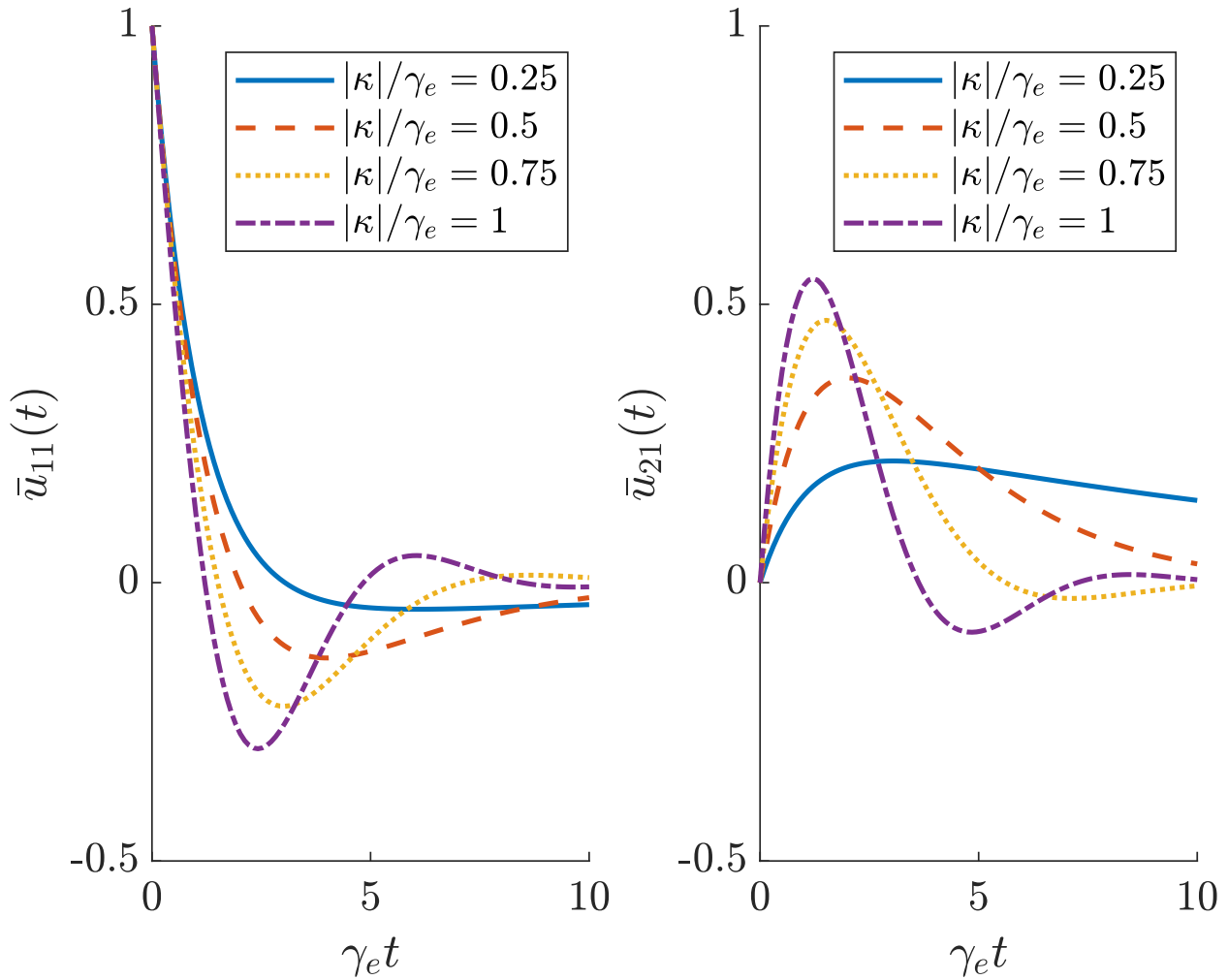


Figure 7.2: Plots of the envelopes $\bar{u}_{nm}(t)$ of the impulse-response functions $u_{nm}(t, \Delta)$ for $\gamma_0 = 0$ and for different values of $|\gamma|/\gamma_e$. For ease of visualization, we take $\text{Re}\{\kappa\} = 0$ and $\text{Im}\{\kappa\} \geq 0$

factor is an affine function of time. Hence, $\bar{u}_{11}(t)$ and $\bar{u}_{21}(t)$ still decay with the rate $\bar{\gamma}$ for $t \gg \gamma_e^{-1}$.

If $|\kappa|/\gamma_e < 1/2$, then inter-ring coupling is overdamped. In this case, $\bar{u}_{11}(t)$ and $\bar{u}_{21}(t)$ become the sum of two exponentially decaying terms: one decaying with a rate of $\bar{\gamma} + \sqrt{(\gamma_e/2)^2 - |\kappa|^2}$, and the other with a rate of $\bar{\gamma} - \sqrt{(\gamma_e/2)^2 - |\kappa|^2}$. Naturally, the latter term dominates for large t because it decays more slowly. In Section C.1, we show that, for overdamped inter-ring coupling, both envelopes $\bar{u}_{11}(t)$ and $\bar{u}_{21}(t)$ attain exactly one extremum. Moreover, $\bar{u}_{11}(t)$ always becomes negative for sufficiently large t ; but $\bar{u}_{21}(t)$ has the same phase for any t .

Next, we examine the inner products of the impulse-response functions $u_{nm}(t, \Delta)$ with each other and with themselves, i.e., their squared norms. These quantities are relevant to our analysis of AFC because they determine the matrices M_{in} and M_{out} (as seen in Sections 7.3 and C.2), and thus govern the projected efficiencies $\eta_{\text{in}}^{(p)}$, η_{out} , and $\eta^{(p)}$ through Eq. (7.43). Specifically, we analyze three dimensionless quantities. Two of these are the normalized squared norms $2\gamma_e \langle u_{11}|u_{11} \rangle = 2\gamma_e \langle u_{11}(t, \Delta)|u_{11}(t, \Delta) \rangle$ and $2\gamma_e \langle u_{21}|u_{21} \rangle = 2\gamma_e \langle u_{21}(t, \Delta)|u_{21}(t, \Delta) \rangle$. The third of these is the effective cosine $\cos \theta_{12}$ between $|u_{11}\rangle$ and $|u_{21}\rangle$, defined as

$$\cos \theta_{12} \equiv \frac{|\langle u_{11}|u_{21} \rangle|}{\sqrt{\langle u_{11}|u_{11} \rangle \langle u_{21}|u_{21} \rangle}}. \quad (7.48)$$

Clearly $\cos \theta_{12} \geq 0$, and $\cos \theta_{12} = 0$ if and only if $|u_{11}\rangle$ and $|u_{21}\rangle$ are orthogonal. Furthermore, as a consequence of the Schwarz inequality, $\cos \theta_{12} \leq 1$ and $\cos \theta_{12} = 1$ if and only if $|u_{11}\rangle \propto |u_{21}\rangle$. Therefore, $\cos \theta_{12}$ can be interpreted as a measure of the collinearity of $|u_{11}\rangle$ and $|u_{21}\rangle$. Below, we show that these three quantities govern the SVD of M_{in} and M_{out} .

To study the quantities $2\gamma_e \langle u_{11}|u_{11} \rangle$, $2\gamma_e \langle u_{21}|u_{21} \rangle$, and $\cos \theta_{12}$, we note that they depend only on the rings' TCMT parameters: the waveguide-ring coupling γ_e , the intrinsic decay rate γ_0 , and the inter-ring coupling κ . Additionally, we find in Section C.1 that they depend only on the magnitude of κ , rather than on both its magnitude and phase. So we need only investigate $2\gamma_e \langle u_{11}|u_{11} \rangle$, $2\gamma_e \langle u_{21}|u_{21} \rangle$, and $\cos \theta_{12}$ as functions of the two dimensionless ratios $|\kappa|/\gamma_e$ and γ_0/γ_e to understand their general behavior for non-zero γ_e .

Figure 7.3 shows contour plots of $2\gamma_e \langle u_{11}|u_{11} \rangle$, $2\gamma_e \langle u_{21}|u_{21} \rangle$, and $\cos \theta_{12}$ as functions of $|\kappa|/\gamma_e$ and γ_0/γ_e . We examine first their values for the ideal case of $\gamma_0 = 0$. As seen readily in Fig. 7.3 and shown analytically in Section C.1, for $\gamma_0 = 0$, $2\gamma_e \langle u_{11}|u_{11} \rangle = 2\gamma_e \langle u_{11}|u_{11} \rangle = 1$, and $\cos \theta_{12} = 0$, independently of the value of $|\kappa|/\gamma_e$. Then, as γ_0/γ_e increases from zero, both $2\gamma_e \langle u_{11}|u_{11} \rangle$ and $2\gamma_e \langle u_{21}|u_{21} \rangle$ decrease monotonically, while $\cos \theta_{12}$ increases monotonically. From the formulas for $\langle u_{11}|u_{11} \rangle$, $\langle u_{21}|u_{21} \rangle$, and $\langle u_{11}|u_{21} \rangle$ in Section C.1, it follows that $\langle u_{11}|u_{11} \rangle$ and $\langle u_{21}|u_{21} \rangle$ converge to 0; and that $\cos \theta_{12}$ converges to $1/\sqrt{2}$ in such a way that

$$\cos \theta_{12} < 1/\sqrt{2}, \quad (7.49)$$

for non-zero γ_e and $|\kappa|$. In other words, $\cos \theta_{12}$ converges to $1/\sqrt{2}$ from below as γ_0/γ_e tends to infinity and $|\kappa|/\gamma_e$ remains finite.

Although both $2\gamma_e \langle u_{11}|u_{11} \rangle$ and $2\gamma_e \langle u_{21}|u_{21} \rangle$ decrease with increasing γ_0/γ_e , we always have

$$\langle u_{11}|u_{11} \rangle \geq \langle u_{21}|u_{21} \rangle, \quad (7.50)$$

and equality is achieved if and only if $\gamma_0 = 0$, as shown in Section C.1, though their difference decreases with increasing $|\kappa|$.

Additionally, the rates at which the squared norms decrease and the effective cosine increases with γ_0/γ_e evidently depends on $|\kappa|/\gamma_e$. Increasing $|\kappa|/\gamma_e$ causes $2\gamma_e \langle u_{11}|u_{11} \rangle$ to decrease more rapidly with γ_0/γ_e , but it causes $2\gamma_e \langle u_{21}|u_{21} \rangle$ to decrease more slowly with γ_0/γ_e . On the other hand, $\cos \theta_{12}$ increases with γ_0/γ_e more rapidly with smaller $|\kappa|/\gamma_e$.

The dependence of the squared norms on $|\kappa|/\gamma_e$ makes intuitive sense. This is because, as depicted in Fig. 7.1, Ring 1 is directly coupled to the bus waveguide, but Ring 2 is not. Therefore, if $|\kappa| \ll \gamma_0$, energy coupled from Ring 1 into Ring 2 is quickly dissipated, causing $2\gamma_e \langle u_{21}|u_{21} \rangle$ to be small. But if $|\kappa|$ increases beyond γ_0 , energy can accumulate in $u_{21}(t, \Delta)$, and energy in $u_{11}(t, \Delta)$ leaks into Ring 2. This also explains why we always have $\langle u_{11}|u_{11} \rangle \geq \langle u_{21}|u_{21} \rangle$ for $\gamma_0 > 0$, and why their difference decreases with $|\kappa|$.

To understand the increase of $\cos \theta_{12}$ with γ_0/γ_e , we note that increasing γ_0 enhances damping in the impulse-responses $u_{11}(t, \Delta)$ and $u_{21}(t, \Delta)$ common to both rings. This pushes the behavior of both impulse-response functions towards exponential decay, thus increasing their collinearity, as measured by $\cos \theta_{12}$. However, this increase in their rate of exponential decay cannot make $u_{11}(t, \Delta)$ and $u_{21}(t, \Delta)$ fully collinear (i.e., linearly dependent), due to their

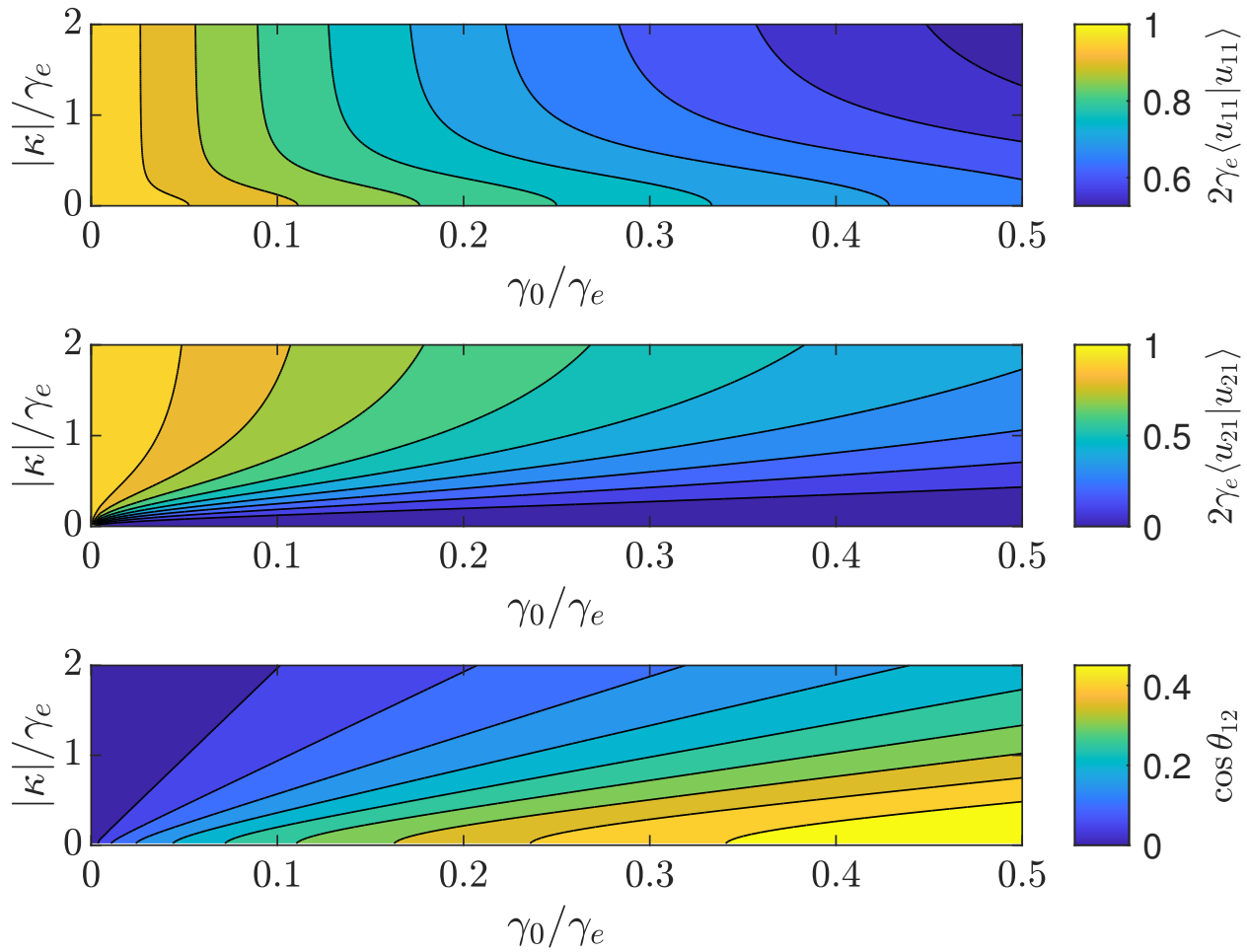


Figure 7.3: Contour plots of the normalized squared norms $2\gamma_e \langle u_{11}|u_{11} \rangle$ and $2\gamma_e \langle u_{21}|u_{21} \rangle$, and of the effective cosine $\cos \theta_{12}$ as functions of the normalized coupling magnitude $|\kappa|/\gamma_e$ and the normalized intrinsic loss γ_0/γ_e .

difference in initial conditions, as pointed out in the discussion of Fig. 7.2. As a result, $\cos \theta_{12}$ converges to $1/\sqrt{2}$ for large γ_0 rather than unity. As seen in Fig. 7.3, the increase in collinearity between $u_{11}(t, \Delta)$ and $u_{21}(t, \Delta)$ is inhibited by an increase in $|\kappa|$ as well. This is because larger $|\kappa|$ either inhibits exponential decay (if inter-ring coupling is overdamped), or keeps the amplitude oscillations of $u_{11}(t, \Delta)$ and $u_{21}(t, \Delta)$ out of phase (if inter-ring coupling is underdamped).

To conclude this section, we add a remark on the critical damping condition, $|\kappa| = \gamma_e/2$. It is that this condition corresponds to a so-called exceptional point of the rings' parameter space [147, 148], where the matrix $H(t)$ of Eq. (8.1) becomes non-diagonalizable. At this exceptional point, the eigenvalues of $H(t)$ are no longer holomorphic functions of the TCMT parameters and acquire a branch-cut topology [147, 148]. This singular behavior has recently been leveraged to design novel high-sensitivity photonic sensors and adiabatic mode converters, among other devices [148–150]. Nonetheless, at the exceptional point $|\kappa| = \gamma_e/2$, the exponential matrices $\exp(H_0 t)$ and $\exp(H_m t)$ in Eq. (7.17) remain well defined and continuous [151] with respect to the TCMT parameters. Furthermore, these matrices are expressible as Neumann series [109] in terms of perturbations to the TCMT parameters, as in quantum-mechanical time-dependent perturbation theory [70]. Thus, these matrices are holomorphic in the TCMT parameters, and so are their elements, the impulse responses $u_{nm}(t, 0)$ and $u_{nm}(t, \Delta)$. Hence, the AFC dynamics and efficiency exhibit no extraordinary behavior at the exceptional point $|\kappa| = \gamma_e/2$.

7.5 Numerical SVD of the loading and unloading maps

With the results of the previous section, we now study numerically the SVD of AFC in the two-ring system of Fig. 7.1. First, for this section, we study the SVD of the individual loading and unloading matrices, M_{in} and M_{out} . We then use these results to investigate the SVD of the full AFC process, with matrix representation $M = M_{\text{out}} M_{\text{in}}$ in Section 7.6.

In Section C.3, we perform a partial analytical SVD of both M_{in} and M_{out} . There, we obtain the left singular vectors of M_{in} , the right singular vectors of M_{out} , and the singular values of both matrices. First, we examine the singular values, but we also examine the singular vectors later in this section. As we demonstrate in Section C.3, M_{in} and M_{out} have identical singular values, i.e., we have

$$\sigma_j(M_{\text{in}}) = \sigma_j(M_{\text{out}}), \quad (7.51)$$

assuming these are ordered either in ascending or descending order. Thus we need only consider those of M_{in} , $\sigma_j(M_{\text{in}})$. In Section C.3, we show that these may be written in terms of the inner products of the impulse-response functions $u_{nm}(t, \Delta)$ as

$$\begin{aligned} \frac{\sigma_{\text{max}}^2(M_{\text{in}})}{2\gamma_e} &= \frac{\langle u_{11}|u_{11}\rangle + \langle u_{21}|u_{21}\rangle}{2} \\ &\quad + \sqrt{\left(\frac{\langle u_{11}|u_{11}\rangle - \langle u_{21}|u_{21}\rangle}{2}\right)^2 + |\langle u_{11}|u_{21}\rangle|^2}, \\ \frac{\sigma_{\text{min}}^2(M_{\text{in}})}{2\gamma_e} &= \frac{\langle u_{11}|u_{11}\rangle + \langle u_{21}|u_{21}\rangle}{2} \\ &\quad - \sqrt{\left(\frac{\langle u_{11}|u_{11}\rangle - \langle u_{21}|u_{21}\rangle}{2}\right)^2 + |\langle u_{11}|u_{21}\rangle|^2}. \end{aligned} \quad (7.52)$$

We note how these singular values depend on the inner product $\langle u_{11}|u_{21}\rangle$. If $\langle u_{11}|u_{21}\rangle = 0$, then, as a consequence of Eq. (7.50), $\sigma_{\text{max}}(M_{\text{in}}) = 2\gamma_e \langle u_{11}|u_{11}\rangle$, and $\sigma_{\text{min}}(M_{\text{in}}) = 2\gamma_e \langle u_{21}|u_{21}\rangle$. Nonetheless, $\langle u_{11}|u_{21}\rangle = 0$ happens if and only if $\gamma_0 = 0$, as seen in Fig. 7.3. Nonzero $\langle u_{11}|u_{21}\rangle$ then increases $\sigma_{\text{max}}^2(M_{\text{in}})$ above $2\gamma_e \langle u_{11}|u_{11}\rangle$, and decreases $\sigma_{\text{min}}^2(M_{\text{in}})$ below $2\gamma_e \langle u_{21}|u_{21}\rangle$. Therefore, non-orthogonality of $u_{11}(t, \Delta)$ and $u_{21}(t, \Delta)$ further splits the singular values $\sigma_j(M_{\text{in}})$. In particular, the splitting of the squares of the singular values is analogous to the eigenvalue splitting of a quantum-mechanical two-level system when interaction between its original eigenstates is introduced. This mathematical similarity arises because the squared singular values σ_j^2 of M_{in} and M_{out} are the eigenvalues of the Hermitian matrices $M_{\text{in}}^\dagger M_{\text{in}}$ and $M_{\text{out}}^\dagger M_{\text{out}}$, as is well-known in linear algebra [143, 144] and as we leverage in Section C.3.

Naturally, the Schwarz inequality limits the maximum singular-value splitting due to non-orthogonality of the impulse responses. Specifically, the Schwarz inequality bounds $|\langle u_{11}|u_{21}\rangle|^2$ from above by $\langle u_{11}|u_{11}\rangle \langle u_{21}|u_{21}\rangle$, when

$\cos \theta_{12} = 1$. Not only that, but the effective cosine $\cos \theta_{12}$ between the impulse-response functions is further restricted below $1/\sqrt{2}$ by Eq. (7.49). Correspondingly, this imposes an upper bound on $\sigma_{\max}(M_{\text{in}})$ and a lower bound on $\sigma_{\min}(M_{\text{in}})$ for fixed values of $2\gamma_e \langle u_{11}|u_{11} \rangle$ and $2\gamma_e \langle u_{21}|u_{21} \rangle$. Then, we conclude that the singular values $\sigma_j(M_{\text{in}})$ are bounded as

$$\begin{aligned} 2\gamma_e \langle u_{11}|u_{11} \rangle &\leq \sigma_{\max}^2(M_{\text{in}}) \leq \rho_+^2, \\ \rho_-^2 &\leq \sigma_{\min}^2(M_{\text{in}}) \leq 2\gamma_e \langle u_{21}|u_{21} \rangle. \end{aligned} \quad (7.53)$$

Here, the outer bounds ρ_+ and ρ_- , are given by

$$\frac{\rho_{\pm}^2}{\gamma_e} = \langle u_{11}|u_{11} \rangle + \langle u_{21}|u_{21} \rangle \pm \sqrt{\langle u_{11}|u_{11} \rangle^2 + \langle u_{21}|u_{21} \rangle^2}. \quad (7.54)$$

In accordance with the previous argument, these are given by substituting $|\langle u_{11}|u_{21} \rangle|^2 = \langle u_{11}|u_{11} \rangle \langle u_{21}|u_{21} \rangle / 2$ in the right-hand side of Eq. (7.52).

We evaluate the singular values $\sigma_j(M_{\text{in}})$ of M_{in} and their bounds from Eq. (7.53) as a function of the normalized intrinsic loss γ_0/γ_e and for different values of the normalized coupling $|\kappa|/\gamma_e$. Our results are shown in Fig. 7.4. We plot the square of the singular values rather than the singular values directly because, as discussed in Sec. 7.3, the latter can be interpreted immediately as the extrema of energy efficiencies.

Several features of Fig. 7.4 are noteworthy. First, we note that both singular values are exactly equal to unity when $\gamma_0 = 0$, for all values of $|\kappa|/\gamma_e$. This follows because, when $\gamma_0 = 0$, then $2\gamma_e \langle u_{11}|u_{11} \rangle = 2\gamma_e \langle u_{21}|u_{21} \rangle = 1$ and $\langle u_{11}|u_{21} \rangle = 0$, as seen in Fig. 7.3. Thus, substituting these values into Eq. (7.52), we get $\sigma_{\max}(M_{\text{in}}) = \sigma_{\min}(M_{\text{in}}) = 1$. This observation is significant because, as shown in Eqs. (7.45) and (7.46), $\sigma_{\max}^2(M_{\text{in}})$ and $\sigma_{\min}^2(M_{\text{in}})$ are the maximum and minimum of the projected efficiency $\eta_{\text{in}}^{(p)}$ over the projected input $|s_{\text{in}}^{(p)}(t)\rangle$. Hence, because both are equal to unity when $\gamma_0 = 0$, then $\eta_{\text{in}}^{(p)}$ equals unity too for any $|s_{\text{in}}^{(p)}(t)\rangle$. Consequently, the input efficiency $\eta_{\text{in}} = \eta_{\text{in}}^{(p)} \eta_p$ equals the projection efficiency η_p . In other words, when $\gamma_0 = 0$, energy is only lost in the loading process with map \hat{T}_{in} through the projection of the input $|s_{\text{in}}(t)\rangle$ into the vector space \mathcal{V}_{in} spanned by $|u_{11}^*(t_m - t)\rangle$ and $|u_{21}^*(t_m - t)\rangle$.

Analogously, because M_{in} and M_{out} have identical singular values (as stated in Eq. (7.51)), it follows too from Eqs. (7.45) and (7.46) that $\eta_{\text{out}} = 1$ for $\gamma_0 = 0$, independently of the ring-amplitude vector $a(t_m)$ at the time of modulation. Therefore, no energy is lost in the unloading process with map \hat{T}_{out} in this idealized case.

As γ_0/γ_e increases, both singular values decrease from unity, for all values of $|\kappa|/\gamma_e$ in Fig. 7.4. Naturally, this reflects that, for nonzero γ_0 , it becomes impossible to couple all the input energy into the two-ring system, regardless of input pulse shape. Because of the equality of singular values in Eq. (7.51), this means too that extraction of the energy from the rings into the bus after AFC becomes increasingly lossy, regardless of the form of $a(t_m)$.

In Fig. 7.4, the squared singular values remain closer to their inner bounds, $2\gamma_e \langle u_{11}|u_{11} \rangle$ and $2\gamma_e \langle u_{21}|u_{21} \rangle$, than to the outer bounds, ρ_{\pm}^2 . Based on Eq. (7.52) and this section's discussion, this is because the effective cosine $\cos \theta_{12}$ between $u_{11}(t, \Delta)$ and $u_{21}(t, \Delta)$ is small compared to its limit of $1/\sqrt{2}$ over the considered values of γ_0/γ_e and $|\kappa|/\gamma_e$. Note that, according to Fig. 7.3, $\cos \theta_{12}$ increases faster with γ_0/γ_e for lower $|\kappa|/\gamma_e$. Hence, the singular values in Fig. 7.4 should deviate from their inner bounds more rapidly with decreasing $|\kappa|/\gamma_e$. However, this is hard to appreciate in Fig. 7.4, because in this case, the inner and outer bounds grow closer together as well.

Next, we examine the dependence the singular vectors of M_{in} and M_{out} on the rings' TCMT parameters. However, rather than analyzing the components of the singular vectors directly, we analyze the components of their associated Bloch vectors, i.e., their pseudo-spin vectors [20, 152] (or their normalized Stokes parameters, in the context of polarization optics [106, 107, 153]). This Bloch vector representation is valid because, for our two-ring AFC, right and left singular vectors are represented by normalized column vectors in \mathbb{C}^2 ; a vector space isomorphic to the state space of a quantum-mechanical two-level system.

Two general advantages of this representation are that the Bloch vector components (or Bloch components for short) are real-valued quantities and that they have an intuitive geometrical interpretation. Additionally, for our particular analysis, we find below that some Bloch components have simple dependences on the impulse-response inner products and the ring parameters. There is a disadvantage of the representation of singular vectors through their Bloch components. This is that the value of the phase between a matrix's right singular vector and its corresponding left singular vector is lost [106, 153]. This phase could be measured by interferometry of the output signal $s_{\text{out}}(t)$, but it does not impact our investigation of AFC efficiency.

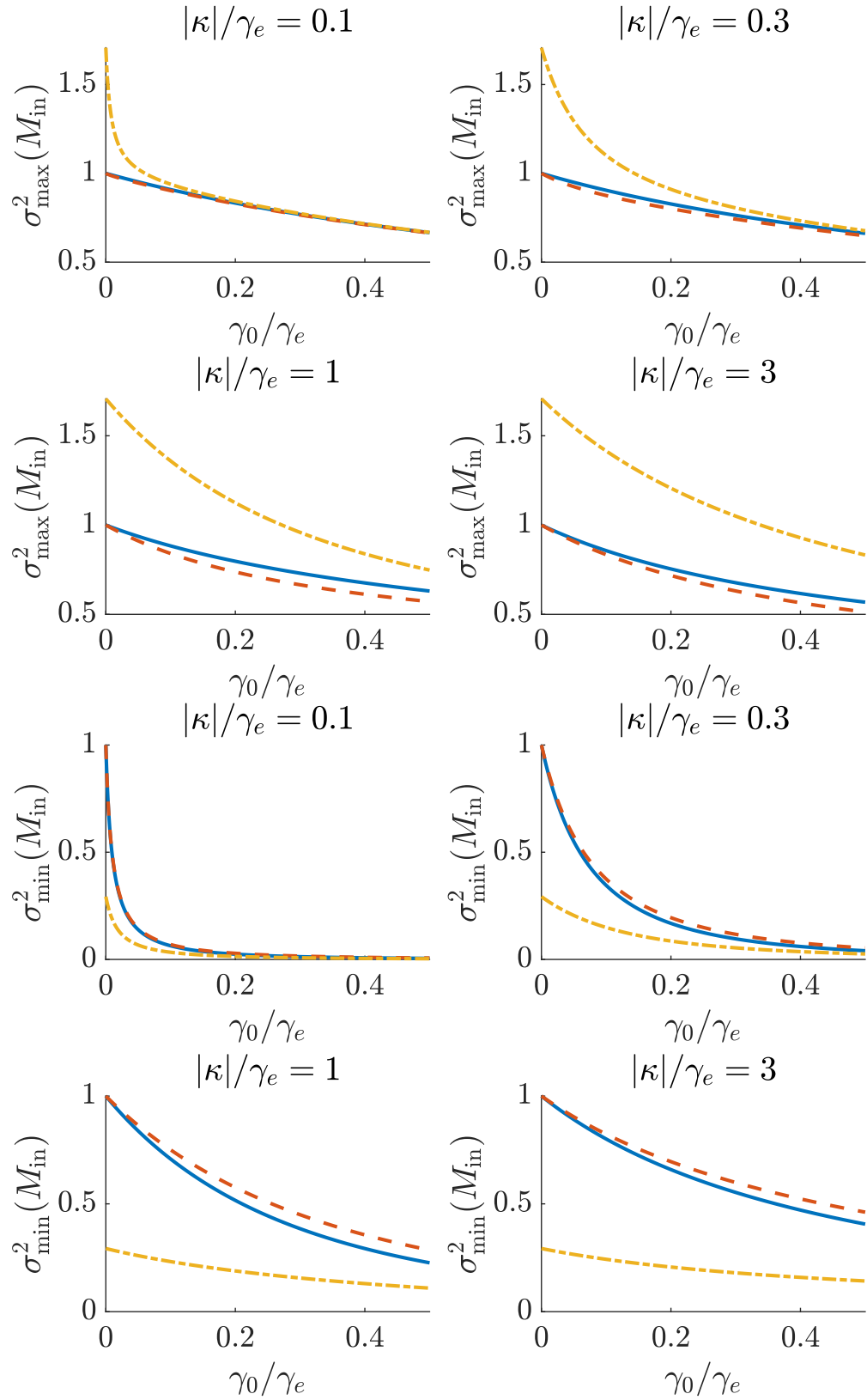


Figure 7.4: Plots of $\sigma_{\max}^2(M_{\text{in}})$ and its bounds (top), and $\sigma_{\min}^2(M_{\text{in}})$ and its bounds (bottom), as functions of γ_0/γ_e and for multiple values of $|\kappa|/\gamma_e$. The squared singular values are shown as solid blue lines; the inner bounds ($2\gamma_e \langle u_{11}|u_{11} \rangle$ and $2\gamma_e \langle u_{21}|u_{21} \rangle$), as a dashed orange lines; and the outer bounds (ρ_-^2 and ρ_+^2) as dotted yellow lines.

Let $S_j^{(r)}(M_{\text{in}})$ be the j th ($j = 1, 2, 3$) Bloch components of the right singular vector of M_{in} corresponding to $\sigma_{\text{max}}(M_{\text{in}})$. Analogously, $S_j^{(l)}(M_{\text{in}})$ is the j th Bloch component of the left singular vector of M_{out} corresponding to $\sigma_{\text{max}}(M_{\text{in}})$; $S_j^{(r)}(M_{\text{out}})$, that of the right singular vector corresponding to $\sigma_{\text{max}}(M_{\text{out}})$; and $S_j^{(l)}(M_{\text{out}})$, that of the left singular vector corresponding to $\sigma_{\text{max}}(M_{\text{out}})$. We need only consider the Bloch components of the singular vectors corresponding to one singular value, because the right singular vectors and left singular vectors are orthogonal sets. Therefore, the Bloch components of the ignored left or right singular vector are the negative of the other left or right singular vector.

With these definitions, the Bloch components $S_j^{(r)}(M_{\text{in}})$ are given by $S_j^{(r)}(M_{\text{in}}) = v_k^\dagger s_j v_k$. Here, v_k is the right singular vector of M_{in} associated with $\sigma_{\text{max}}(M_{\text{in}})$, and s_j are the Pauli matrices

$$s_1 = \begin{pmatrix} 0 & 1 \\ 1 & 0 \end{pmatrix}, \quad s_2 = \begin{pmatrix} 0 & -i \\ i & 0 \end{pmatrix}, \quad s_3 = \begin{pmatrix} 1 & 0 \\ 0 & -1 \end{pmatrix}. \quad (7.55)$$

In Section C.3, we show that $S_j^{(l)}(M_{\text{in}})$ and $S_j^{(r)}(M_{\text{out}})$ have particularly simple expressions in terms of the impulse-response inner products and of the ring parameters. Specifically, these are

$$\begin{aligned} S_1^{(l)}(M_{\text{in}}) &= F \operatorname{Re}\{\langle u_{11}|u_{21}\rangle\} = \operatorname{Im}\{\kappa\}/\sqrt{|\kappa|^2 + \bar{\gamma}^2}, \\ S_2^{(l)}(M_{\text{in}}) &= F \operatorname{Im}\{\langle u_{11}|u_{21}\rangle\} = \operatorname{Re}\{\kappa\}/\sqrt{|\kappa|^2 + \bar{\gamma}^2}, \\ S_3^{(l)}(M_{\text{in}}) &= F (\langle u_{11}|u_{11}\rangle - \langle u_{21}|u_{21}\rangle)/2, \\ &= \bar{\gamma}/\sqrt{|\kappa|^2 + \bar{\gamma}^2} \end{aligned} \quad (7.56)$$

and by

$$\begin{aligned} S_1^{(r)}(M_{\text{out}}) &= F \operatorname{Re}\{\langle u_{12}|u_{11}\rangle\} = -\operatorname{Im}\{\kappa\}/\sqrt{|\kappa|^2 + \bar{\gamma}^2}, \\ S_2^{(r)}(M_{\text{out}}) &= F \operatorname{Im}\{\langle u_{12}|u_{11}\rangle\} = -\operatorname{Re}\{\kappa\}/\sqrt{|\kappa|^2 + \bar{\gamma}^2}, \\ S_3^{(r)}(M_{\text{out}}) &= F (\langle u_{11}|u_{11}\rangle - \langle u_{12}|u_{12}\rangle)/2, \\ &= \bar{\gamma}/\sqrt{|\kappa|^2 + \bar{\gamma}^2}. \end{aligned} \quad (7.57)$$

In Eqs. (7.56) and (7.57), F is a normalization factor that ensures the magnitude of the Bloch vector is unity. Thus, it defined so $F^{-2} = (\langle u_{11}|u_{11}\rangle - \langle u_{21}|u_{21}\rangle)^2/4 + |\langle u_{11}|u_{21}\rangle|^2$. As in Section C.1, $\bar{\gamma} = (\gamma_1 + \gamma_2)/2$ is the ring-averaged decay rate. Eqs. (7.56) and (7.57) hold only if γ_0 is nonzero. Otherwise, $\langle u_{11}|u_{11}\rangle = \langle u_{12}|u_{12}\rangle$ and $\langle u_{11}|u_{12}\rangle = 0$. So the singular values are no longer distinct, according to Eq. (7.52), and the singular vectors are no longer uniquely defined (up to phase factors), as discussed in Section 7.3.

From Eqs. (7.56) and (7.57), we make some key observations. For the first of these, we focus on $S_j^{(l)}(M_{\text{in}})$, but analogous conclusions follow for $S_j^{(r)}(M_{\text{out}})$. First, $S_1^{(l)}(M_{\text{in}})$ and $S_2^{(l)}(M_{\text{in}})$ are non-zero only as a consequence of non-orthogonality of the impulse responses $u_{11}(t, \Delta)$ and $u_{21}(t, \Delta)$. Similarly, $S_3^{(l)}(M_{\text{in}})$ is nonzero due to the disparity between $\langle u_{11}|u_{11}\rangle$ and $\langle u_{21}|u_{21}\rangle$. Moreover, as a consequence of Eq. (7.50), $S_3^{(l)}(M_{\text{in}}) > 0$. Thus, the quantity $\sqrt{[S_1^{(l)}(M_{\text{in}})]^2 + [S_2^{(l)}(M_{\text{in}})]^2}$ compared to $S_3^{(l)}(M_{\text{in}})$ is a measure of the impulse-response non-orthogonality relative to the squared-norm difference $(\langle u_{11}|u_{11}\rangle - \langle u_{21}|u_{21}\rangle)$. Although decreasing $|\kappa|$ for fixed γ_e and γ_0 increases the non-orthogonality, as measured by $\cos \theta_{12}$ in Fig. 7.3, this also increases the difference $(\langle u_{11}|u_{11}\rangle - \langle u_{21}|u_{21}\rangle)$, yielding an overall increase in $S_3^{(l)}(M_{\text{in}})$ and a decrease in magnitude of $S_1^{(l)}(M_{\text{in}})$ and $S_2^{(l)}(M_{\text{in}})$, as indicated by the rightmost side of Eqs. (7.56) and (7.57).

The second observation is that, for any set of ring parameters excluding $\gamma_0 = 0$,

$$\begin{aligned} S_1^{(l)}(M_{\text{in}}) &= -S_1^{(r)}(M_{\text{out}}), \\ S_2^{(l)}(M_{\text{in}}) &= -S_2^{(r)}(M_{\text{out}}), \\ S_3^{(l)}(M_{\text{in}}) &= S_3^{(r)}(M_{\text{out}}). \end{aligned} \quad (7.58)$$

Consequently, the left singular vectors of M_{in} approximate the right singular vectors of M_{out} if and only if $S_1^{(l)}(M_{\text{in}})$ and $S_2^{(l)}(M_{\text{in}})$ are close to zero. From Eqs. (7.56) and (7.57), this occurs if and only if

$$|\kappa| \ll \bar{\gamma}. \quad (7.59)$$

This observation is significant because the similarity between the left singular vectors of M_{in} and the right singular vectors of M_{out} influences the singular values of their product, M , the matrix representing the overall AFC process. This is discussed below in Sec. 7.6 and in Section C.4.

The analogs of Eqs. (7.56) and (7.57) for $S_j^{(r)}(M_{\text{in}})$ and $S_j^{(l)}(M_{\text{out}})$ are generally complicated and yield little insight. Thus, we omit their general discussion and mostly investigate $S_j^{(r)}(M_{\text{in}})$ and $S_j^{(l)}(M_{\text{out}})$ numerically. This discrepancy in the complexity of $S_j^{(r)}(M_{\text{in}})$ and $S_j^{(l)}(M_{\text{out}})$ compared to that of $S_j^{(l)}(M_{\text{in}})$ and $S_j^{(r)}(M_{\text{out}})$ arises because the components of the right singular vectors of M_{in} and the left singular vectors of M_{out} depend on the orthonormal basis chosen for \mathcal{V}_{in} and \mathcal{V}_{out} . In contrast, the left singular vectors of M_{in} and the right singular vectors of M_{out} have a natural basis as column vectors of energy amplitudes in Ring 1 and Ring 2.

There is one analytical property of the Bloch components $S_j^{(r)}(M_{\text{in}})$ and $S_j^{(l)}(M_{\text{out}})$ that we derive in Section C.3 and that is useful to point out. This is that, just as $S_j^{(l)}(M_{\text{in}})$ and $S_j^{(r)}(M_{\text{out}})$ satisfy Eq. (7.58), $S_j^{(r)}(M_{\text{in}})$ and $S_j^{(l)}(M_{\text{out}})$ obey the relation

$$\begin{aligned} S_1^{(r)}(M_{\text{in}}) &= -S_1^{(l)}(M_{\text{out}}), \\ S_2^{(r)}(M_{\text{in}}) &= -S_2^{(l)}(M_{\text{out}}), \\ S_3^{(r)}(M_{\text{in}}) &= S_3^{(l)}(M_{\text{out}}), \end{aligned} \quad (7.60)$$

valid for any set of ring parameters, except for $\gamma_0 = 0$ when the singular values M_{in} and M_{out} become degenerate. Unlike Eq. (7.58), Eq. (7.60) holds only for our choice of bases $\left\{ \left| n_1^{(\text{in})} \right\rangle, \left| n_2^{(\text{in})} \right\rangle \right\}$ for \mathcal{V}_{in} , and $\left\{ \left| n_1^{(\text{out})} \right\rangle, \left| n_2^{(\text{out})} \right\rangle \right\}$ for \mathcal{V}_{out} that satisfy Eq. (7.38). If either of these were changed, Eq. (7.58) would still hold, but Eq. (7.60) would not in general.

Next, we study numerically the dependence of the complete SVD, both singular values and singular vectors, of M_{in} on the ring parameters. As a consequence of Eqs. (7.51), (7.58) and (7.60), this analysis covers the SVD of M_{out} as well. In Fig. 7.5, we plot as functions of γ_0/γ_e and for various different $|\kappa|/\gamma_e$ the squared singular values $\sigma_{\text{max}}^2(M_{\text{in}})$ and $\sigma_{\text{min}}^2(M_{\text{in}})$, along with the Bloch components $S_2^{(r)}(M_{\text{in}})$, $S_3^{(l)}(M_{\text{in}})$, $S_2^{(r)}(M_{\text{in}})$ and $S_3^{(l)}(M_{\text{in}})$. The components $S_1^{(r)}(M_{\text{in}})$ and $S_1^{(l)}(M_{\text{in}})$ are omitted because they are always zero. This is a consequence of our choice of taking the inter-ring coupling coefficient κ to be real and positive.

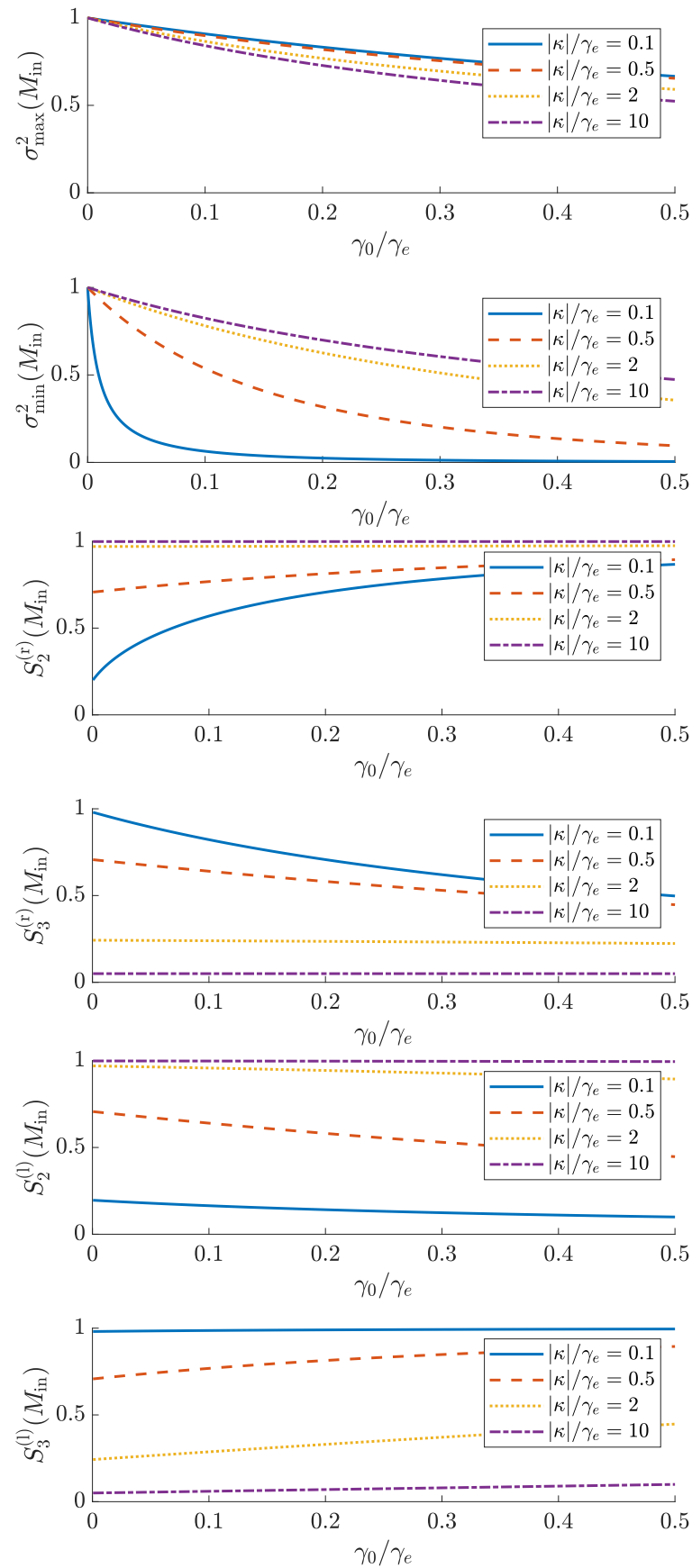
From Fig. 7.5, we first examine the behavior of the singular values $\sigma_{\text{max}}(M_{\text{in}})$ and $\sigma_{\text{min}}(M_{\text{in}})$. As seen in Fig. 7.4, they both start at unity for $\gamma_0 = 0$ and then decrease with increasing γ_0/γ_e for all values of $|\kappa|/\gamma_e$. In contrast to Fig. 7.4, in Fig. 7.5 the effect on $\sigma_{\text{max}}(M_{\text{in}})$ and $\sigma_{\text{min}}(M_{\text{in}})$ of varying $|\kappa|/\gamma_e$ is more transparent. For fixed γ_0/γ_e , increasing $|\kappa|/\gamma_e$ simultaneously decreases $\sigma_{\text{max}}(M_{\text{in}})$ and increases $\sigma_{\text{min}}(M_{\text{in}})$. Furthermore, this increment and this decrement are such that, in the limit of $|\kappa| \rightarrow \infty$ and for fixed γ_0/γ_e , $\sigma_{\text{max}}(M_{\text{in}})$ and $\sigma_{\text{min}}(M_{\text{in}})$ converge to a common value. As seen in Fig. 7.3, increasing $|\kappa|/\gamma_e$ inhibits impulse-response non-orthogonality, i.e., $\cos \theta_{12}$. So this convergence of $\sigma_{\text{max}}(M_{\text{in}})$ and $\sigma_{\text{min}}(M_{\text{in}})$ for increasing $|\kappa|/\gamma_e$ can be understood as a convergence of $2\gamma_e \langle u_{11}|u_{11} \rangle$ and $2\gamma_e \langle u_{21}|u_{21} \rangle$ to a common value. By manipulation of the formulas in Section C.1 for $\langle u_{11}|u_{11} \rangle$ and $\langle u_{21}|u_{21} \rangle$, it is straightforward to verify that this common asymptote is given by

$$\lim_{|\kappa| \rightarrow \infty} \sigma_{\text{max}}^2(M_{\text{in}}) = \lim_{|\kappa| \rightarrow \infty} \sigma_{\text{min}}^2(M_{\text{in}}) = \frac{\gamma_e}{\gamma_1 + \gamma_2}, \quad (7.61)$$

assuming that both γ_0 and γ_e remain finite in this limit. Likewise, it is easy to verify that, for vanishing $|\kappa|$,

$$\begin{aligned} \sigma_{\text{max}}^2(M_{\text{in}}) &= \gamma_e/\gamma_1, \\ \sigma_{\text{min}}^2(M_{\text{out}}) &= 0. \end{aligned} \quad (7.62)$$

This value of $\sigma_{\text{max}}^2(M_{\text{in}})$ for $|\kappa| = 0$ then equals the Schwarz limit for the loading of a single ring resonator (see Chapter 6), as one might expect. Similarly, it is intuitively clear that for zero inter-ring coupling, the minimum singular value corresponds to the efficiency of loading the now-uncoupled Ring 2 and thus equals zero.

Figure 7.5: Singular value decomposition of M_{in} as a function of γ_0/γ_e and for different values of $|\kappa|/\gamma_e$

Next, we inspect the plots for the Bloch components $S_2^{(l)}(M_{\text{in}})$ and $S_3^{(l)}(M_{\text{in}})$ of the left singular vectors of M_{in} . In Fig. 7.5, we see that their behavior is well-described by the expressions in the rightmost side of Eq. (7.56). $S_2^{(l)}(M_{\text{in}})$ increases with $|\kappa|/\gamma_e$ and decreases with γ_0/γ_e ; while $S_3^{(l)}(M_{\text{in}})$ decreases with $|\kappa|/\gamma_e$ and increases with γ_0/γ_e , ensuring that the Bloch vector remains normalized.

The behavior of $S_2^{(r)}(M_{\text{in}})$ and $S_3^{(r)}(M_{\text{in}})$, corresponding to the right singular vectors of M_{in} , is slightly different. For fixed γ_0/γ_e and increasing $|\kappa|/\gamma_e$, $S_2^{(r)}(M_{\text{in}})$ increases and $S_3^{(r)}(M_{\text{in}})$ decreases, just like $S_2^{(l)}(M_{\text{in}})$ and $S_3^{(l)}(M_{\text{in}})$, respectively. However, $S_2(M_{\text{in}})$ increases and $S_3(M_{\text{in}})$ decreases for increasing γ_0/γ_e and fixed $|\kappa|/\gamma_e$. In contrast, $S_2^{(l)}(M_{\text{in}})$ and $S_3^{(l)}(M_{\text{in}})$ exhibit the opposite behavior in this case.

7.6 Numerical SVD of the AFC operator

Having studied in detail the SVD of M_{in} and M_{out} in Sec. 7.5, we now examine the SVD of their product, M , the matrix representing the full AFC linear operator. Because the expression for M is given by the product of those for M_{in} and M_{out} , it is complicated. Hence, an explicit analytical SVD of M yields unwieldy mathematical expressions and little physical insight. Thus, we investigate the SVD of M mostly numerically.

Still, we show in Section C.4 that the fact that M equals the product of M_{in} and M_{out} allows us to bound its singular values in terms of those of M_{in} and M_{out} . Thus, we obtain

$$\begin{aligned}\sigma_{\max}(M) &\leq \sigma_{\max}(M_{\text{in}})\sigma_{\max}(M_{\text{out}}), \\ \sigma_{\min}(M) &\geq \sigma_{\min}(M_{\text{in}})\sigma_{\min}(M_{\text{out}}).\end{aligned}\tag{7.63}$$

Because the singular values of M_{in} equal those of M_{out} , as established in Section C.3, the terms on the right-hand side of Eq. (7.63) can also be written as $\sigma_{\max}^2(M_{\text{in}})$ and $\sigma_{\min}^2(M_{\text{in}})$ or as $\sigma_{\max}^2(M_{\text{out}})$ and $\sigma_{\min}^2(M_{\text{out}})$. Additionally, we show in Section C.4 that a sufficient condition to achieve equality in both lines of Eq. (7.63) is for the left singular vectors of M_{in} to equal the right singular vectors of M_{out} . Accordingly, we expect that differences between these sets of singular vectors will cause $\sigma_{\max}(M)$ to decrease below its upper bound of $\sigma_{\max}(M_{\text{in}})\sigma_{\max}(M_{\text{out}})$, and $\sigma_{\min}(M)$ to increase above its lower bound of $\sigma_{\min}(M_{\text{in}})\sigma_{\min}(M_{\text{out}})$.

To verify Eq. (7.63) and determine its implications, we compute the squared singular values of M_{in} and plot them alongside their corresponding bounds for different values of the ring parameters. The resulting plots are shown in Fig. 7.6. Two features of these plots are noteworthy. First, both $\sigma_{\max}^2(M)$ and $\sigma_{\min}^2(M)$ indeed lie below the upper bound $\sigma_{\max}^2(M_{\text{in}})\sigma_{\max}^2(M_{\text{out}})$ and above the lower bound $\sigma_{\min}^2(M_{\text{in}})\sigma_{\min}^2(M_{\text{out}})$ for all considered values of γ_0/γ_e and $|\kappa|/\gamma_e$. This confirms the validity of the analytically derived Eq. (7.63). Second, as $|\kappa|/\gamma_e$ is increased, the singular values $\sigma_{\max}(M)$ and $\sigma_{\min}(M)$ grow closer to each other, as do their lower and upper bounds. Of course, in the case of the upper and lower bounds, this follows from the fact that $\sigma_{\max}(M_{\text{in}})$ and $\sigma_{\min}(M_{\text{in}})$ exhibit this same behavior in Fig. 7.5.

Moreover, we observe that for small $|\kappa|/\gamma_e$, $\sigma_{\max}(M)$ and $\sigma_{\min}(M)$ lie close to their outer bounds. Then, as $|\kappa|/\gamma_e$ is increased, they grow apart from them. But then, this separation is inhibited by the outer bounds growing closer themselves. As stated above and discussed in Section C.4, the decrease of $\sigma_{\max}(M)$ below $\sigma_{\max}(M_{\text{in}})\sigma_{\max}(M_{\text{out}})$ (and the increase of $\sigma_{\min}(M)$ above $\sigma_{\min}(M_{\text{in}})\sigma_{\min}(M_{\text{out}})$) is a consequence of the mismatch between the left singular vectors of M_{in} and the right singular vectors of M_{out} . From Eqs. (7.56) and (7.57), we find that this mismatch increases with $|\kappa|/\gamma_e$ for fixed γ_0/γ_e . This explains the increasing deviation of the $\sigma_{\max}(M)$ and $\sigma_{\min}(M)$ from their bounds, as $|\kappa|/\gamma_e$ increments.

As in Sec. 7.5, both singular values of M are equal to unity when γ_0 vanishes, regardless of the value of $|\kappa|/\gamma_e$. This implies that for $\gamma_0 = 0$ the projected AFC efficiency, $\eta^{(p)}$, equals unity for any form of the projected input $|s_{\text{in}}^{(p)}(t)\rangle$. In this case, it follows from Eq. (7.34) that $\eta = \eta_p$. In other words, the AFC efficiency equals the projection efficiency. Hence, in this ideal case, energy is only lost in AFC through the projection of $|s_{\text{in}}(t)\rangle$ into \mathcal{V}_{in} spanned by $|u_{11}^*(t_m - t)\rangle$ and $|u_{21}^*(t_m - t)\rangle$. As γ_0 increases from zero, $\sigma_{\max}(M)$ and $\sigma_{\min}(M)$ decrease below unity, so the map from the projected input $|s_{\text{in}}^{(p)}(t)\rangle$ to $|s_{\text{out}}(t)\rangle$ becomes lossy.

Next, we investigate numerically the full SVD of the AFC matrix M as a function of the ring parameters. Thus, as in Fig. 7.5, we plot $\sigma_{\max}^2(M)$, $\sigma_{\min}^2(M)$, $S_2^{(r)}(M)$, $S_3^{(r)}(M)$, $S_2^{(l)}(M)$, and $S_3^{(l)}(M)$ as functions of γ_0/γ_e and for different

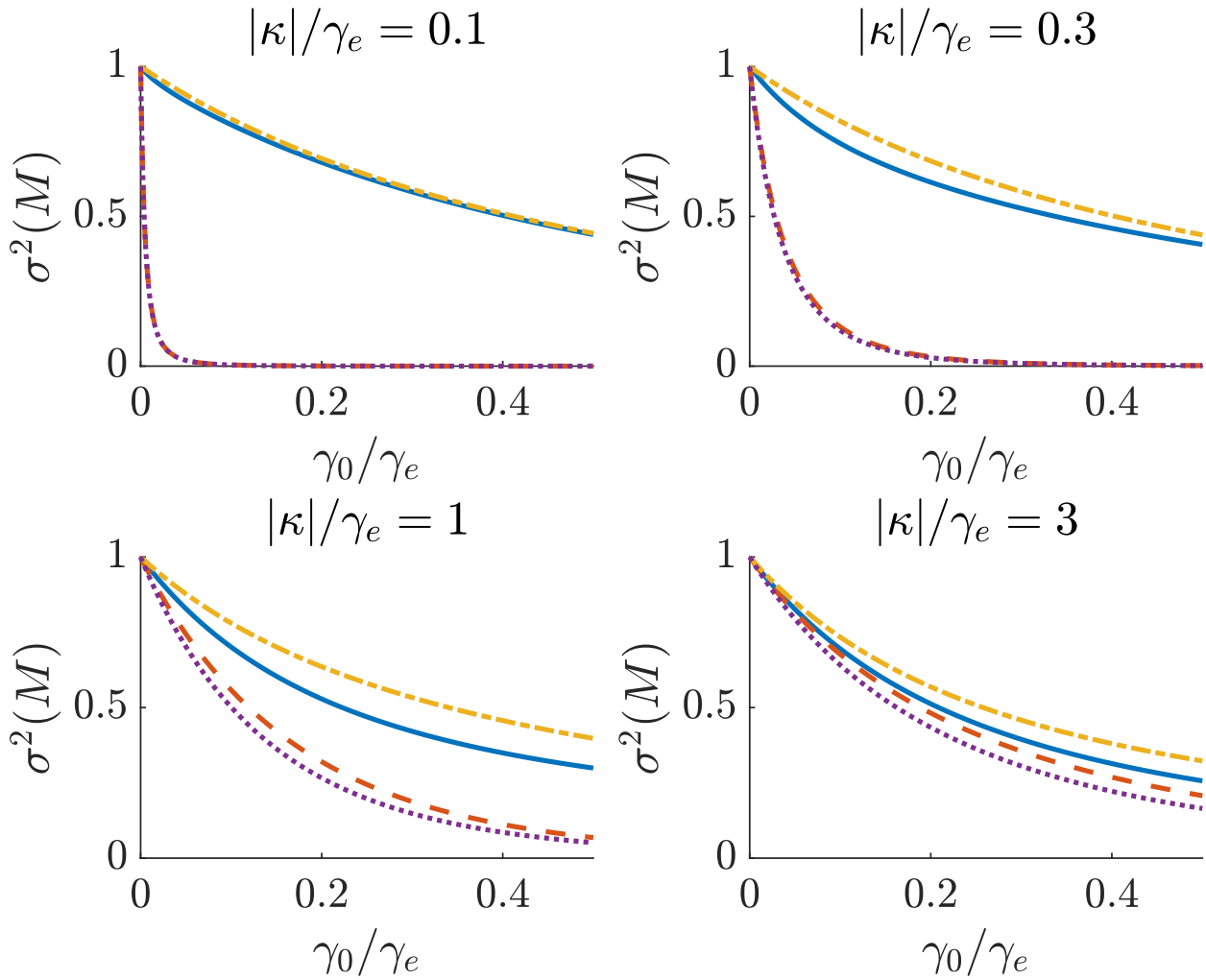


Figure 7.6: The squared singular values of M and their bounds as functions of γ_e/γ_0 and for various values of $|\kappa|/\gamma_e$. $\sigma_{\max}^2(M)$ is shown as a solid blue line; $\sigma_{\min}^2(M)$, as a dashed orange line; the upper bound $\sigma_{\max}^2(M_{\text{in}})\sigma_{\max}^2(M_{\text{out}})$, as a dotted yellow line; and the lower bound $\sigma_{\min}^2(M_{\text{in}})\sigma_{\min}^2(M_{\text{out}})$, as a dashed-dotted purple line.

values of $|\kappa|/\gamma_e$ in Fig. 7.7. As in Fig. 7.5, we omit the Bloch components $S_1^{(r)}(M)$ and $S_1^{(l)}(M)$ because they vanish for all ring parameters as a consequence of setting κ as real-valued.

Just like $\sigma_{\max}(M_{\text{in}})$ and $\sigma_{\min}(M_{\text{in}})$ in Fig. 7.5, it is evident in Fig. 7.7 that $\sigma_{\max}(M)$ and $\sigma_{\min}(M)$ grow closer as $|\kappa|/\gamma_e$ is increased. This occurs because their outer bounds from Eq. (7.63) themselves grow closer, as discussed in Sec. 7.5; thus forcing $\sigma_{\max}(M)$ and $\sigma_{\min}(M)$ to converge to a common value. From this argument and from Eq. (7.61), it follows that the common asymptote for $\sigma_{\max}^2(M)$ and $\sigma_{\min}^2(M)$ is given by

$$\lim_{|\kappa| \rightarrow \infty} \sigma_{\max}^2(M) = \lim_{|\kappa| \rightarrow \infty} \sigma_{\min}^2(M) = \left(\frac{\gamma_e}{\gamma_1 + \gamma_2} \right)^2. \quad (7.64)$$

As for Eq. (7.61), we assume for Eq. (7.64) that both γ_e and γ_0 remain finite.

From Fig. 7.7, it is also apparent that $\sigma_{\max}(M)$ and $\sigma_{\min}(M)$ each converge to distinct curves as $|\kappa|$ tends to zero. To determine their values for $|\kappa| = 0$, we recall that the inequalities in Eq. (7.63) become equalities when the left singular vectors of M_{in} equal the right singular vectors of M_{out} . And from Eqs. (7.56), (7.57), this is the case when $|\kappa| = 0$. Then, we may substitute Eq. (7.62) into Eq. (7.63), now equalities, to obtain

$$\begin{aligned} \sigma_{\max}^2(M) &= (\gamma_e/\gamma_1)^2, \\ \sigma_{\min}^2(M) &= 0, \end{aligned} \quad (7.65)$$

for $|\kappa| = 0$. As in Eq. (7.62), Eq. (7.65) has an intuitive interpretation. The first line of Eq. (7.65) means that for zero inter-ring coupling, AFC in the two-ring system is just as efficient as AFC in a single ring (Ring 1), analyzed in Chapter 6. The second line means that for zero inter-ring coupling, the efficiency of AFC in Ring 2 equals zero.

Next, we discuss the Bloch components in Fig. 7.7. Their dependence on the ring parameters is noticeably different from those in Fig. 7.5. For decreasing γ_0/γ_e , $S_2^{(r)}(M)$ and $S_2^{(l)}(M)$ always converge to zero and $S_3^{(r)}(M)$ and $S_3^{(l)}(M)$ always converge to unity. In contrast, in Fig. 7.5 they can take any value between 0 and 1 as γ_0/γ_e converges to zero, depending on the value of $|\kappa|/\gamma_e$. Additionally, the rate at which $S_3^{(r)}(M)$ and $S_3^{(l)}(M)$ decrease from unity as γ_0/γ_e increases from zero in Fig. 7.7 clearly decreases with increasing $|\kappa|/\gamma_e$. Correspondingly, the rate at which $S_2^{(r)}(M)$ and $S_2^{(l)}(M)$ grow in magnitude with increasing γ_0/γ_e decreases with $|\kappa|/\gamma_0$ as well. This is required for the Bloch vectors to remain normalized. Finally, for the range of ring parameters in Fig. 7.7, the Bloch components appear to satisfy

$$\begin{aligned} S_2^{(r)}(M) &= -S_2^{(l)}(M), \\ S_3^{(r)}(M) &= S_3^{(l)}(M), \end{aligned} \quad (7.66)$$

analogous to Eqs. (7.58) and (7.60). However, the validity of Eq. (7.66) is harder to verify analytically due to the explicit expression for M being considerably more unwieldy than that of M_{in} .

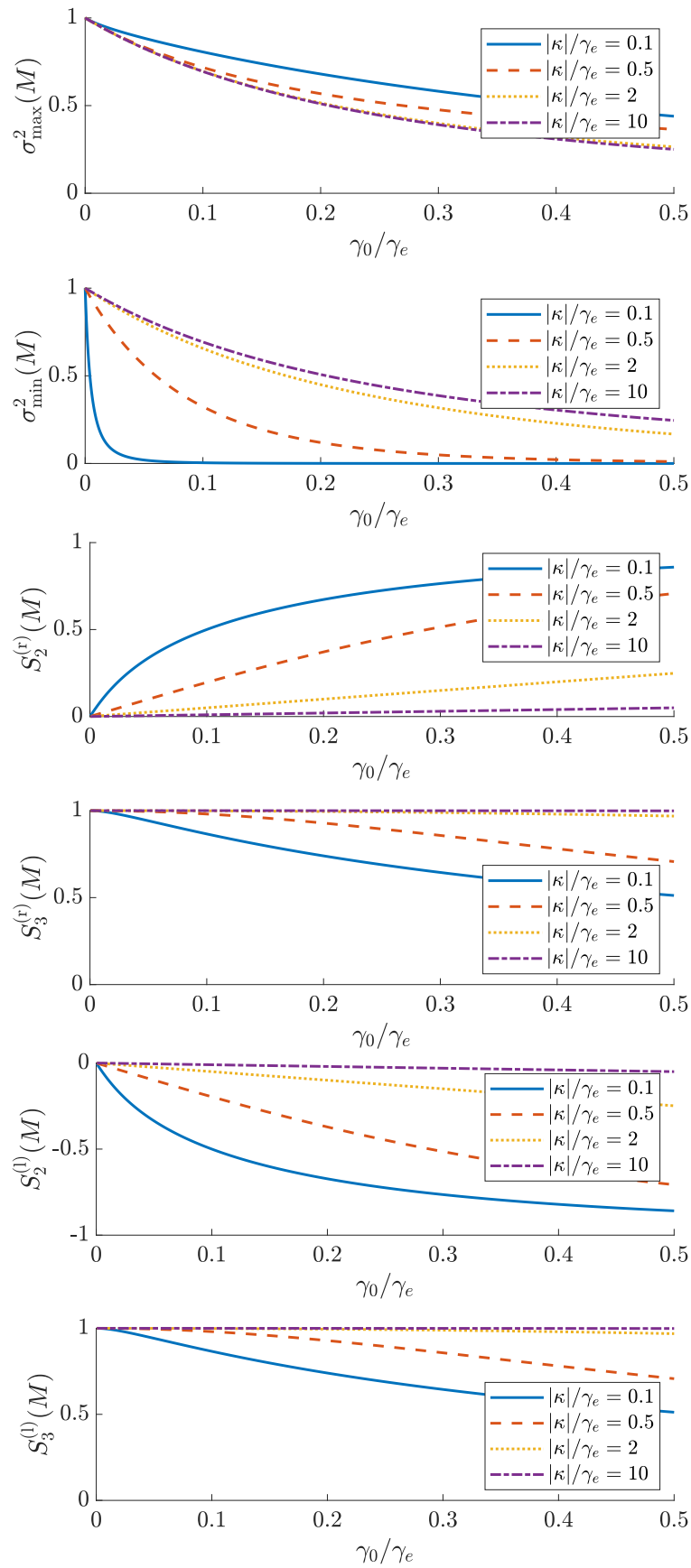
7.7 Efficiency analysis of AFC of a symmetric single-lobe pulse

In this section, we examine the AFC of an input pulse of fixed shape and duration in the two-ring system of Fig. 7.1. We investigate and optimize this process's efficiency with respect to the rings' TCMT parameters. We use the formalism developed in Sections 7.2 to 7.6 to interpret our results.

For the pulse shape of the AFC input $s_{\text{in}}(t)$, we follow Chapter 6 and consider a raised-cosine pulse, also known as a Hann function in numerical Fourier analysis [137, 138]. Thus, $s_{\text{in}}(t)$ is given by

$$\begin{aligned} s_{\text{in}}(t) &= \sqrt{\frac{2E_{\text{in}}}{3\tau}} [1 + \cos(2\pi t/\tau)] \exp(-i\omega_0 t) \\ &\quad \times [\Theta(t + \tau/2) - \Theta(t - \tau/2)] \end{aligned} \quad (7.67)$$

Here $E_{\text{in}} = \langle s_{\text{in}}(t) | s_{\text{in}}(t) \rangle$ is the input energy; and τ , the input pulse duration. As in Sec. 7.1, ω_0 is the rings' original bare resonance frequency, and $\Theta(t)$, the Heaviside step function. The total duration τ is related to the pulse's root mean square duration τ_{RMS} via $\tau_{\text{RMS}} \approx 0.141\tau$ [140]. We choose the raised-cosine pulse shape because it is a symmetric,

Figure 7.7: Singular value decomposition of M as a function of γ_0/γ_e and for different values of $|\kappa|/\gamma_e$

single-lobe shape, which is usually of interest in optical telecommunications [1, 154]. Additionally, this shape has a finite support, i.e., it is non-zero only over a finite time interval, unlike the typically analyzed Gaussian envelope. This latter feature simplifies the numerical analysis and optimization of its AFC. Moreover, as we show later in this section, the AFC efficiency of this raised-cosine input is mostly determined by the symmetry and single-lobe nature of the pulse. Hence, the analysis for the AFC optimization of a raised-cosine input applies qualitatively and yields similar results for other symmetric, single-lobe pulse shapes, e.g., Gaussian, super-Gaussian, and hyperbolic secant.

We aim to determine the upper limit to the AFC efficiency of the raised-cosine pulse and to observe how this efficiency decreases with increasing intrinsic ring loss γ_0 . To do so, we first solve numerically the TCMT equations for the ring amplitudes at the time of modulation $a(t_m)$ and compute the corresponding AFC efficiency for $\gamma_0 = 0$ and a broad range of ring parameters and modulation times. Then, we compare the obtained AFC efficiencies to estimate the ring parameters for global maximum efficiency. Subsequently, we refine this estimate via numerical local optimization.

In this way, we find that the maximum AFC efficiency η of a raised-cosine pulse for $\gamma_0 = 0$ is of 0.9683. This maximum is achieved when $t_m = 0.3280\tau$, $\gamma_e = 5.5324\tau^{-1}$, and $|\kappa| = 4.4027\tau^{-1}$. Qualitatively, then the conditions for optimal AFC of the raised-cosine pulse are as follows. The intrinsic decay rate γ_0 must be small compared to the extrinsic decay rate γ_0 , and the input pulse's bandwidth $\sim \tau^{-1}$. The external decay rate γ_e must be moderately large compared to the input bandwidth $\sim \tau^{-1}$. The inter-ring coupling must be slightly underdamped by the extrinsic decay. Finally, the ring modulation must be applied at a time t_m slightly after the input's maximum relative to the pulse's root mean square duration. The maximum AFC efficiency of 0.9683 in our two-ring system is appreciably larger than the single-ring maximum AFC efficiency of 0.7951 found in Chapter 6 for the same raised-cosine envelope.

To explain this difference in efficiencies, we recall from Sec. 7.6 and Chapter 3, that for $\gamma_0 = 0$, the overall AFC efficiency η equals the projection efficiency η_p , for both the two-ring system and for a single-ring system. From Eq. (7.29), we recall that the projection efficiency is simply the ratio of the energy in the projected input $|s_{\text{in}}^{(p)}(t)\rangle$ to that in the overall input $|s_{\text{in}}(t)\rangle$. Therefore, a larger AFC efficiency in the two-ring system than in the single-ring system means that the $s_{\text{in}}(t)$ in Eq. (7.67) achieves a larger projection in the input space \mathcal{V}'_{in} of the two-ring system than that of the single-ring system.

The main reason why the raised-cosine input $s_{\text{in}}(t)$ achieves a greater projection into \mathcal{V}'_{in} of the two-ring system than that of the single-ring system is the shape of the Ring 2's impulse response envelope, $\bar{u}_{21}(t)$, shown in Fig. 7.2. As discussed in Sec. 7.4, $\bar{u}_{21}(t)$ is continuous at $t = 0$, and, if $\gamma_e \gtrsim |\kappa|$, most of the squared norm $\langle \bar{u}_{21}(t) | \bar{u}_{21}(t) \rangle$ is accumulated under the first peak after $t = 0$. Thus, the time-reversed impulse response $u_{21}^*(t_m - t, 0)$ can match closely the raised-cosine input $s_{\text{in}}(t)$. This contrasts with the single-ring case, where its impulse response is a discontinuous, truncated, decaying exponential. Hence, the maximum overlap between the raised-cosine $s_{\text{in}}(t)$ and the single-ring time-reversed impulse response is poor, which limits the AFC efficiency to the aforementioned value of 0.7951.

To illustrate this interpretation, we examine Fig. 7.8. In it, we display two plots. The first pertains to the optimized single-ring AFC of the raised-cosine input $s_{\text{in}}(t)$ for $\gamma_0 = 0$. This first plot shows the envelopes of: $s_{\text{in}}(t)$, its projection $s_{\text{in}}^{(p)}(t)$ into the ring's impulse response for optimal AFC, and the corresponding AFC output $s_{\text{out}}(t)$. Analogously, the second plot pertains to the optimized two-ring AFC of the same input $s_{\text{in}}(t)$. It shows the envelopes of: $s_{\text{in}}(t)$, its projection $s_{\text{in}}^{(p)}(t)$ into \mathcal{V}'_{in} , and the corresponding AFC output $s_{\text{out}}(t)$. By comparing these two plots, it is clear that $s_{\text{in}}^{(p)}(t)$ of the two-ring system matches more closely $s_{\text{in}}(t)$ than that of the single-ring system. Consequently, it is expected that the two-ring system conserves more of the energy of $s_{\text{in}}(t)$ upon projection into $s_{\text{in}}^{(p)}(t)$.

For both the single-ring and two-ring system, the envelope of the output $s_{\text{out}}(t)$ seems proportional to the time-reversed envelope of $s_{\text{in}}^{(p)}(t)$ in Fig. 7.8. For the single-ring system, this apparent time-reversal is exact for $\gamma_0 = 0$ and for any form of $s_{\text{in}}(t)$ and any choice of ring parameters and t_m . However, for the two-ring system, this is only approximately true for $\gamma_0 = 0$ if $s_{\text{in}}^{(p)}(t)$ is mostly proportional to either $u_{11}^*(t_m - t, 0)$ or $u_{21}^*(t_m - t, 0)$. This is because the envelope's projection onto $u_{11}^*(t_m - t, 0)$ is only time-reversed when multiplied by $u_{11}(t - t_m, \Delta)$ at the AFC output; but its projection onto $u_{21}^*(t_m - t, 0)$ is time-reversed and multiplied by -1 when multiplied by $u_{12}(t - t_m, \Delta)$.

We observe one last feature of Fig. 7.8. This is that the frequency-shifted output $s_{\text{out}}(t)$ is noticeably discontinuous at the modulation time t_m in single-ring AFC; but it is seemingly continuous at t_m in two-ring AFC. This occurs because, in two-ring AFC, most of the energy is stored in Ring 2 at t_m , so this energy is released via $u_{12}(t - t_m, \Delta)$, which is continuous at $t = t_m$, as discussed in Sec. 7.4. Similarly, in single-ring AFC, the energy in the single ring is released via the ring's impulse response. In contrast, however, this impulse response is a decaying exponential multiplied by a step function $\Theta(t - t_m)$, and is thus discontinuous at $t = t_m$.

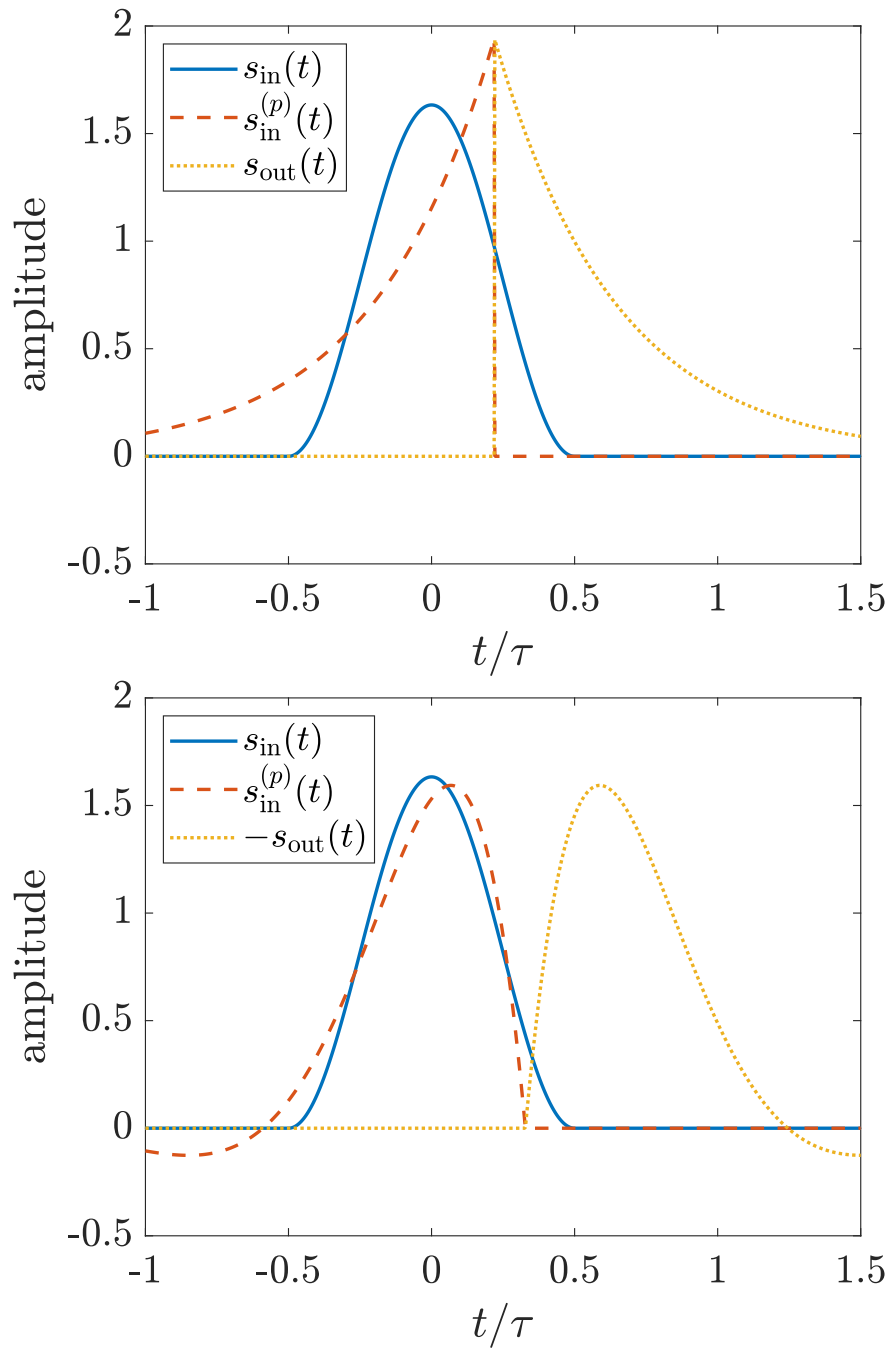


Figure 7.8: Envelopes of the raised-cosine input envelope $s_{in}(t)$, the associated projected input envelope $s_{in}^{(p)}(t)$, and the associated AFC output envelope $s_{out}(t)$. The top axis corresponds to single-ring AFC; the bottom axis corresponds to two-ring AFC. Amplitude units are arbitrary.

This observation on the continuity of $s_{\text{out}}(t)$ is important because the discontinuities of the AFC's outputs govern the asymptotic behavior of the output spectra and, hence, their robustness to dispersive phenomena (e.g., dispersive propagation and filtering). Let ω be the frequency variable for the spectrum of $s_{\text{out}}(t)$. According to Riemann's lemma [52, 91], the discontinuity of single-ring AFC output $s_{\text{out}}(t)$ at $t = t_m$ implies that its spectrum decays as ω^{-1} for $|\omega| \rightarrow \infty$. In contrast, for two-ring AFC $u_{12}(t, \Delta)$ is continuous, albeit with discontinuous derivative at $t = t_m$ (see Sec. 7.4). Hence, from Riemann's lemma, the spectrum of $u_{12}(t, \Delta)$ decays as ω^{-2} for $|\omega| \rightarrow \infty$. Therefore, the output spectrum of two-ring AFC decays more rapidly with ω than that of single-ring AFC, and is consequently more robust to dispersive effects.

Next, we compare how the maximum AFC efficiencies of the raised-cosine input in the single-ring and two-ring system vary as we increase the intrinsic ring loss γ_0 . To do this, we use a numerical local optimizer to find how the maximum AFC efficiency and the ring parameters required to attain this maximum are changed as γ_0 is increased. Naturally, the main assumption of this method is that increasing γ_0 only slightly perturbs the configuration for globally optimal AFC for both single-ring and two-ring networks. In Fig. 7.9, we present our numerical results on the optimization of AFC of the raised-cosine input in both the single-ring and two-ring networks and for increasing γ_0 . We report the attained AFC efficiencies in both configurations, along with the required modulation time t_m (referred to the input pulse's peak) and the required ring parameters γ_e and $|\kappa|$ for the two-ring system. The ring parameters and modulation time for optimal AFC in a single-ring system were studied in Chapter 3, so they are omitted for succinctness.

In Fig. 7.9, we observe that the maximum AFC efficiency of the raised-cosine input is larger in the two-ring system than in the single-ring system for all considered values of γ_0 . This is a remarkable result as it implies that the two-ring configuration generally offers a better choice for AFC of symmetric pulses. We explain this with two intuitive arguments. First, as we already noted for $\gamma_0 = 0$, the raised-cosine input achieves a larger projection into the input space \mathcal{V}_{in} of the two-ring system than that of the single-ring system. For $\gamma_0 = 0$, this immediately translates to a larger AFC efficiency. Accordingly, for sufficiently small γ_0 , we expect two-ring AFC to continue being more efficient than single-ring AFC. Second, if $|\kappa| = 0$ in two-ring AFC, it clearly acts as single-ring AFC. Therefore, two-ring AFC should, at worst, possess the same efficiency as single-ring AFC, and never lower.

Now, we interpret the variation in Fig. 7.9 of the modulation time t_m and ring parameters γ_e and $|\kappa|$ for optimal two-ring AFC with increasing γ_0 . In Fig. 7.9, we observe that t_m decreases from 0.3280τ at $\gamma_0 = 0$ to almost 0.15τ at $\gamma_0 = 0.7\tau^{-1}$; γ_e increases from $5.5324\tau^{-1}$ to almost $40\tau^{-1}$; and $|\kappa|$ increases from $4.4027\tau^{-1}$ to barely above $10\tau^{-1}$. This variation in the modulation time and ring parameters with γ_0 are similar to those of the single-ring case [140]. The coupling rate γ_e increases to inhibit energy loss to γ_0 during the loading and unloading processes. Meanwhile, t_m approaches the pulse peak at $t = 0$ to avoid energy leakage due to nonzero γ_0 .

Though both γ_e and $|\kappa|$ increase with γ_0 in Fig. 7.9, they do such that the ratio $\gamma_e/|\kappa|$ increases. This causes inter-ring coupling to transition from underdamped to overdamped. This transition removes the amplitude oscillations of $\bar{u}_{21}(t)$, characteristic of the underdamped regime, and makes $\bar{u}_{21}(t)$ have a common phase for all $t > 0$. This constant phase helps optimize the loading \hat{T}_{in} of the input pulse by ensuring the integrand determining $a_2(t_m)$ are in-phase for a long integration time t and thus interfere constructively.

To understand more deeply our results for optimal AFC of a raised-cosine pulse, we factorize the AFC efficiency η as the product of the projection efficiency η_p and the projection efficiency $\eta^{(p)}$, as in Eq. (7.34). To do this, we compute η_p from $a(t_m)$ and the ring parameters, as in Section C.2 and then evaluate $\eta^{(p)}$ as the quotient η/η_p . The results are shown in Fig. 7.10. As argued in the discussion of Fig. 7.8, when $\gamma_0 = 0$, $\eta^{(p)} = 1$ for both single-ring and two-ring AFC, so $\eta = \eta_p$. As γ_0 increases from zero, $\eta^{(p)}$ and η_p decrease for both ring networks, causing their product, η , to decrease accordingly. For both cases, the projected efficiency $\eta^{(p)}$ decrease similarly, starting at 1 for $\gamma_0 = 0$, and lying close to 0.7 for $\gamma_0 = 0.7\tau^{-1}$.

The main difference in Fig. 7.10 between single-ring and two-ring AFC clearly lies on their values for the projection efficiency η_p . For single-ring AFC, η_p starts at 0.7951 for $\gamma_0 = 0$ and always remains below $\eta^{(p)}$, even at $\gamma_0 = 0.7\tau^{-1}$. On the other hand, η_p for two-ring AFC starts at 0.9683 and becomes larger than $\eta^{(p)}$ just after $\gamma_0 = 0.0286\tau^{-1}$, where $\eta_p = \eta^{(p)} = 0.9676$. We note that the projection efficiency η_p decreases more slowly than the projected efficiency $\eta^{(p)}$ for both single-ring and two-ring AFC. But the initially larger value of 0.9683 for two-ring AFC allows η_p to overcome $\eta^{(p)}$ at just $\gamma_0 = 0.0286\tau^{-1}$.

Having computed the projected AFC efficiency $\eta^{(p)}$, it is interesting to compare it to its theoretical bounds, the squared singular values of M . This is what we do in the last plot of Fig. 7.10, where $\eta^{(p)}$, $\sigma_{\text{max}}^2(M)$ and $\sigma_{\text{min}}^2(M)$ for optimal two-ring AFC are plotted as functions of $\gamma_0\tau$ in a common axis. Indeed, we verify that $\eta^{(p)}$ lies within

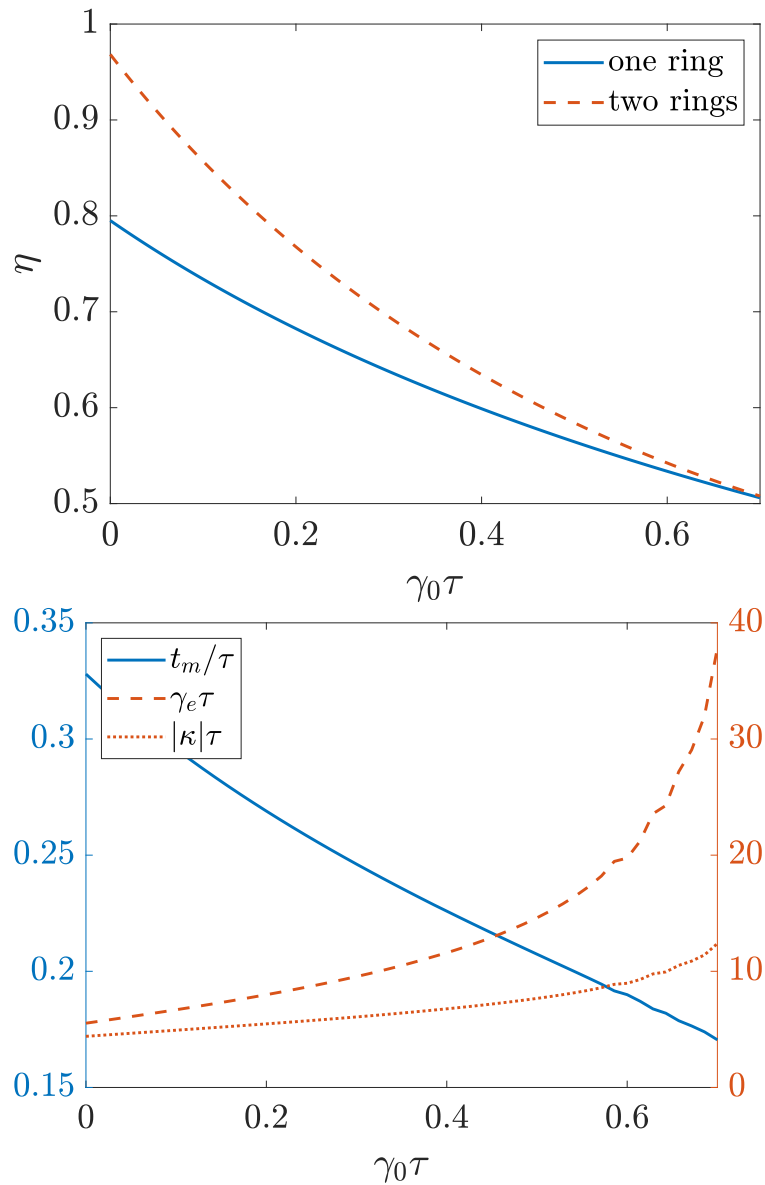


Figure 7.9: Maximum efficiency for a raised-cosine input of single-ring AFC and two-ring AFC as functions of intrinsic loss γ_0 (top). Modulation time t_m and ring parameters, γ_e and $|\kappa|$, for optimal two-ring AFC of a raised-cosine input as functions of γ_0 (bottom).

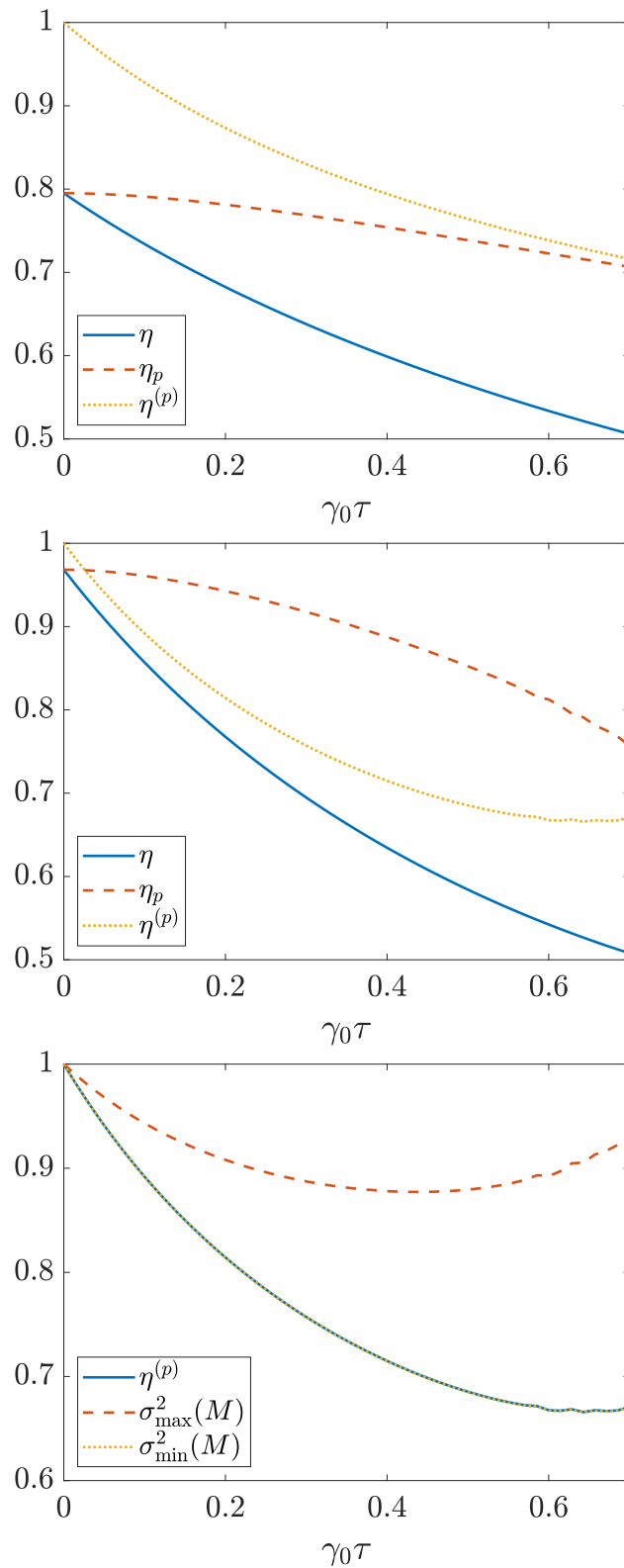


Figure 7.10: Maximum overall efficiency η , and its corresponding projection efficiency η_p , and projected efficiency $\eta^{(p)}$ for single-ring AFC (top) and two-ring AFC (middle) as functions of γ_0 . Comparison of the $\eta^{(p)}$ for a raised-cosine input, $\sigma_{\max}^2(M)$, and $\sigma_{\min}^2(M)$ as functions of γ_0 (bottom).

its theoretical bounds of $\sigma_{\min}^2(M)$ and $\sigma_{\max}^2(M)$. Moreover, $\eta^{(p)}$ follows closely $\sigma_{\max}^2(M)$. From Eq. (7.43), this implies that the projected input $|s_{\text{in}}^{(p)}(t)\rangle$ closely matches the right singular vector corresponding to $\sigma_{\min}(M)$. From Fig. 7.9, the rings' parameters are such that γ_0/γ_e is small compared to unity. From Fig. 7.7, we recall that the right singular vector corresponding to $\sigma_{\min}(M)$ for small γ_0/γ_e has Bloch components $-S_1^{(r)}(M) \approx 0$, $-S_2^{(r)}(M) \approx 0$, and $-S_3^{(r)}(M) \approx -1$. Recall that $S_j^{(r)}(M)$ were defined as the Bloch components of the right singular vector corresponding to $\sigma_{\max}(M)$, not $\sigma_{\min}(M)$. Thus, the right singular vector for $\sigma_{\min}(M)$ is approximately proportional to $|n_2^{(\text{in})}\rangle$. Hence, it is approximately proportional to $|u_{21}^*(t_m - t, 0)\rangle$, as follows from our basis definition in Eq. (7.38). Therefore, the close match between this right singular vector and $|s_{\text{in}}^{(p)}(t)\rangle$ agrees with our previous discussion of Fig. 7.8, where we observed that the raised-cosine input closely matches the time-reversed impulse response $u_{21}^*(t_m - t, 0)$.

Thus, we find that the AFC efficiency of the raised-cosine input is mostly determined by its close match to $u_{21}^*(t_m - t, 0)$ for $\gamma_e \gtrsim |\kappa_e|$, and $\gamma_e \gg \gamma_0$. This implies that any input pulse-shape that matches closely $u_{21}^*(t_m - t, 0)$ under these conditions also achieves similar optimal AFC efficiencies. From Fig. 7.2, we recall that $u_{21}(t, 0)$ for $\gamma_e \gtrsim |\kappa_e|$, and $\gamma_e \gg \gamma_0$ has an envelope continuous at $t = 0$, most of its energy in its first lobe, and small-amplitude oscillations (if underdamped) at its tail for $\gamma_e t \gtrsim 1$. Hence, symmetric, single-lobe pulses in general (e.g., Gaussian, super-Gaussian and hyperbolic secant), rather than just the raised-cosine pulse in particular, closely match the time-reversed impulse response $u_{21}^*(t_m - t, 0)$ and therefore may attain similar high AFC efficiencies under analogous conditions.

7.8 Conclusion

The efficiency of adiabatic frequency conversion (AFC) for a single-ring resonator is known to be limited to below 80% for input pulses with a symmetric single peak. This is a consequence of a relatively poor match between the pulse's shape and the ring's impulse response. To overcome this limitation, we propose inducing AFC simultaneously over two coupled rings, rather than a single one.

We analyze the efficiency of AFC in this two-ring system using temporal coupled mode theory. In this manner, we show that the AFC efficiency for symmetric, single-lobe pulses in two-ring devices has an upper limit of 97% when intrinsic ring losses are comparatively small; inter-ring coupling is slightly underdamped; extrinsic decay is comparable to the input bandwidth; and ring modulation occurs slightly after the input pulse's maximum. To explain this higher AFC efficiency, we analyze the AFC process as a linear operator in the vector space of finite-energy pulses. More specifically, we examine the AFC process as a composition of two linear maps: one representing loading of the input pulse's energy into the rings and another describing unloading of the rings's energy into a frequency-shifted output pulse. We use orthonormal representation theory to represent these maps as 2×2 matrices. This allows us examine each matrix's singular value decomposition, which we demonstrate to govern the AFC process's efficiency.

We expect that our results will stimulate experimental work on our proposed two-ring configuration. Moreover, the matrix analysis developed in this work can be extended to analyze more complicated, multi-ring networks for tunable frequency conversion with high-efficiency on integrated photonic chips.

Chapter 8

Cascaded AFC in coupled rings

In this chapter, we propose and analyze the energy efficiency of a new photonic circuit for AFC which increases the frequency shift possible in a given material platform. As is well known [10, 22, 23, 43], the magnitude of the frequency shift $\Delta\omega$ induced by AFC in a single optical resonator is given by $\Delta\omega = -\omega(\Delta n)/n$, where ω is the resonator's original resonance frequency; n , the resonator's original refractive index; and Δn , the change in the refractive index induced via modulation. Thus, the frequency shift $\Delta\omega$ attainable via AFC in a single ring is limited by the magnitude of the modulation Δn . To increase the frequency shift of the output signal, one could induce single-ring AFC twice in succession. This process, though, is fundamentally energy inefficient. This is a consequence of the mismatch between the shape of the output of the first single-ring AFC and that of the ideal input for the second single-ring AFC [140]. In this work, we propose to induce AFC in cascade over a chain of coupled, yet initially-detuned microrings; i.e., to induce cascaded AFC (CAFC). With this architecture, we can subject an optical pulse to AFC multiple times in succession, without unloading the pulse into a bus waveguide between modulations. Thus, we show that CAFC can achieve higher energy efficiency than simply inducing single-ring AFC twice in series. For concreteness, we examine thoroughly the simplest non-trivial case of a chain of two rings, and briefly discuss the generalization to a chain of an arbitrary number of rings.

In Chapter 7, we also proposed to induce AFC over two coupled rings. Nonetheless, in that scheme, AFC is induced simultaneously over two resonant rings, rather than in cascade over two initially-detuned rings. The objective of the scheme in Chapter 7 is to increase the energy efficiency of one instance of AFC. The objective of this chapter's scheme is to increase the net frequency-shift magnitude, without significantly compromising the process's net energy efficiency.

The rest of the chapter is organized as follows. In Section 8.1, we introduce the two-ring photonic circuit we propose to realize CAFC and we describe its operation. We present the TCMT equations governing it, and write their analytical solution for strong and fast temporal modulation. In Section 8.2, we discuss in detail a sample CAFC process for a symmetric, single-lobe optical pulse. There, we examine the temporal dynamics of the energy in each ring, and the power of the resulting frequency-shifted signal. In Section 8.3, we analyze the transformation of the input into the frequency-shifted output as a linear operator in the vector space of finite-energy pulses. We show that this operator is effectively of rank one, so the efficiency of CAFC is limited by a Schwarz inequality, similar to the case of simple, single-ring AFC [140]. In Section 8.4, we explain the numerical scheme we employ to practically optimize CAFC over the multiple timescales of the process. We discuss the physical processes which govern the optimal values of these timescales. In Section 8.5, we study how the CAFC efficiency converges to its theoretical maximum as it becomes progressively idealized, as measured by three distinct timescale ratios. We find that the CAFC of our scheme has an identical limit as that of single-ring AFC, e.g., of 0.7951 for a symmetric, single-lobe input pulse [140]. Thus, CAFC can become more efficient than multiple instances of single-ring AFC in series. We show that the CAFC efficiency has a polynomial dependence on these ratios. We explain this polynomial dependence as a consequence of the CAFC efficiency being a real-analytic function of the TCMT parameters. In Section 8.6, we leverage the polynomial convergence identified in Section 8.5 to model the CAFC efficiency as a polynomial function of the free timescale ratios. We utilize the simplicity of this polynomial model to optimize the CAFC efficiency over the remaining free TCMT parameters and to predict its rate of convergence with respect to the inter-ring detuning. In Section 8.7, we present the chapter's conclusions.

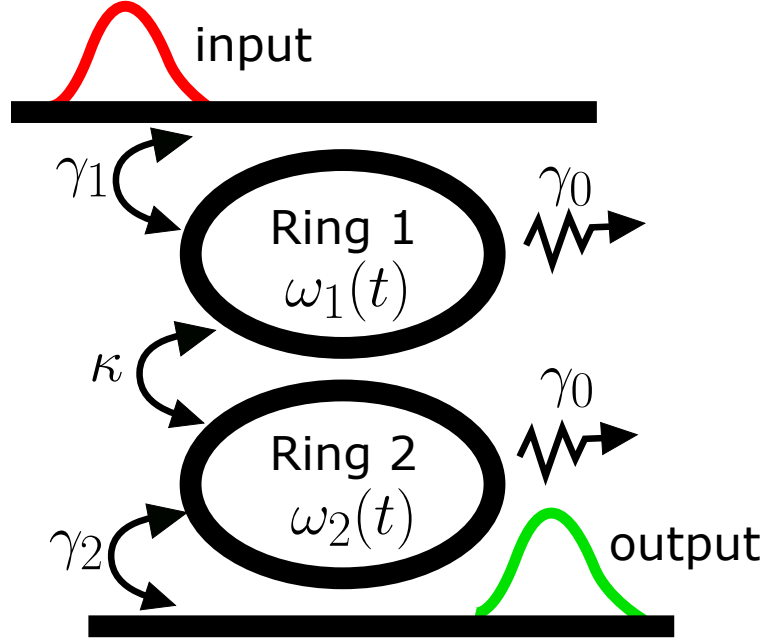


Figure 8.1: Schematic diagram of the photonic circuit proposed for cascaded adiabatic frequency conversion

8.1 Description of the photonic circuit and coupled-mode equations for CAFC

In Fig. 8.1, we present a schematic diagram of the photonic circuit we propose to realize CAFC. It consists of two microrings evanescently coupled to each other, and each coupled to a different bus waveguide. One of the bus waveguides carries the input optical pulse; the other, the output frequency-shifted pulse. The ring coupled to the input bus is labeled as Ring 1; and the ring coupled to the output bus, as Ring 2. The rings' refractive indices are modulated in time so that that Ring j has a time-dependent instantaneous resonance frequency $\omega_j(t)$ ($j = 1, 2$).

We assume that the input pulse is resonant with Ring 1 before frequency-modulation; and that the input's bandwidth, inter-ring coupling, bus-ring coupling, and the maximum frequency modulation are all small compared to the rings' free spectral range. Then, we may describe the temporal dynamics of the fields in this resonant system using TCMT [75–77, 134], as described in Chapter 3. Accordingly, the field in Ring j at time t is proportional to the amplitude $a_j(t)$ and the ring's energy equals $|a_j(t)|^2$. Analogously, the amplitude of the input (output) pulse at time t is proportional to $s_{\text{in}}(t)$ ($s_{\text{out}}(t)$) and its instantaneous power equals $|s_{\text{in}}(t)|^2$ ($|s_{\text{out}}(t)|^2$). In agreement with TCMT, the two-component column vector $a(t) = (a_1(t), a_2(t))^T$ and the output $s_{\text{out}}(t)$ evolve in time according to

$$\begin{aligned} \frac{da}{dt} &= -iH(t)a + k_{\text{in}}s_{\text{in}}(t), \\ s_{\text{out}}(t) &= k_{\text{out}}^\dagger a(t). \end{aligned} \quad (8.1)$$

Here, $H(t)$ is a time-dependent 2×2 matrix, while k_{in} and k_{out} are two-component column vectors. k_{out}^\dagger denotes the adjoint of k_{out} . Correspondingly, the matrix $H(t)$ and the vectors k_{in} and k_{out} are of the form

$$\begin{aligned} H(t) &= \begin{pmatrix} \omega_1(t) - i\gamma_1 & \kappa_{12} \\ \kappa_{21} & \omega_2(t) - i\gamma_2 \end{pmatrix}, \\ k_{\text{in}} &= (\sqrt{2\gamma_{1e}} \quad 0)^T, \\ k_{\text{out}} &= (0 \quad \sqrt{2\gamma_{2e}})^T. \end{aligned} \quad (8.2)$$

As stated above, $\omega_j(t)$ is the instantaneous frequency of Ring j . The rate γ_j is the total decay rate of Ring j ; and κ_{jk} , the complex-valued coupling from Ring k to Ring j . Naturally, coupling between a ring and a bus waveguide contributes to decay of the ring's energy. Thus, it follows from energy conservation and time-reversibility [75, 76] (see

also Chapter 3) that

$$\gamma_j = \gamma_0 + \gamma_{je}, \quad j = 1, 2. \quad (8.3)$$

Here, γ_0 is the rings' intrinsic decay rate. This rate is assumed equal for both rings for simplicity. Inter-ring coupling is assumed to conserve the rings' total energy. Then, as discussed in Chapter 3, it follows that κ_{12} and κ_{21} are related as [75, 76]

$$\kappa_{12} = \kappa_{21}^*. \quad (8.4)$$

Thus, for succinctness, we henceforth write κ_{12} as κ and κ_{21} as κ^* .

To induce CAFC on our two-ring system, we modulate the rings' resonance frequencies $\omega_j(t)$ in the following way. First, we let them be separated by a difference Δ_0 ($\Delta_0 = \omega_1(-\infty) - \omega_2(-\infty)$), sufficiently large in magnitude compared to the inter-ring coupling magnitude $|\kappa|$ to inhibit energy exchange between the rings. While the bare ring frequencies $\omega_j(t)$ remain separated in this way, the optical input (resonant with Ring 1) is launched into the input bus. Then, on a timescale short compared to the TCMT parameters and the ring duration, $\omega_1(t)$ is decreased by $\Delta_0/2$ and $\omega_2(t)$ increased by $\Delta_0/2$ to bring them in resonance with each other. As a result, energy exchange analogous to Rabi oscillation is induced between the rings [8]. This energy exchange is allowed until the energy in Ring 2 reaches its maximum and contains most of the coupled rings' energy. Then, the rings' resonance frequencies are restored to their initial values, separated by Δ_0 , again on a comparatively short timescale. In this way, the optical pulse, originally at resonance with Ring 1 at frequency $\bar{\omega} + \Delta_0/2$, is now in Ring 2, with frequency $\bar{\omega} - \Delta_0/2$. Thus, a frequency shift of Δ_0 is achieved even when only frequency modulations of $\pm\Delta_0/2$ are applied to each ring.

According to the preceding modulation protocol, we can write $\omega_j(t)$ in the form

$$\omega_j(t) = \bar{\omega} - (-1)^j(\Delta_0/2) [\Theta(t_1 - t) + \Theta(t - t_2)]. \quad (8.5)$$

In Eq. (8.5), t_1 and t_2 are the times at which frequency modulation is started and ended, respectively; and $\Theta(x)$, the Heaviside unit-step function. Of course, by substituting Eq. (8.5) into Eq. (8.2), we find that $H(t)$ has a form analogous to the right-hand side of Eq. (8.5), given by

$$H(t) = H_m + (H_0 - H_m) [\Theta(t_1 - t) + \Theta(t - t_2)]. \quad (8.6)$$

Here, H_0 is the value of $H(t)$ before and after ring modulation; and H_m is its value during modulation. Clearly, H_0 is given by Eq. (8.2) with $\omega_j(t) = \bar{\omega} - (-1)^j(\Delta_0/2)$; and H_m , by Eq. (8.2) with $\omega_j(t) = \bar{\omega}$.

Given Eqs. (8.5) and (8.6), we derive a closed-form expression for the CAFC output $s_{\text{out}}(t)$ Appendix E, under the assumption of large detuning $|\Delta_0|$ compared to the inter-ring coupling $|\kappa|$, the ring decay rates, γ_1 and γ_2 , and the input bandwidth. This assumption does not restrict the relevance of the subsequent analysis, because large detuning $|\Delta_0|$ is necessary for efficient CAFC, as we discuss below. This explicit solution for the frequency-shifted $s_{\text{out}}(t)$ is given by

$$\begin{aligned} s_{\text{out}}(t) &= k_{\text{out}}^\dagger U(t - t_2, \Delta_0) a(t_2), \\ a(t_2) &= U(t_2 - t_1, 0) a(t_1), \\ a(t_1) &= \int_{-\infty}^{\infty} dt U(t_1 - t, \Delta_0) k_{\text{in}} s_{\text{in}}(t). \end{aligned} \quad (8.7)$$

Here, $U(t, \Delta)$ is the impulse-response matrix of Eq. (8.1) for time-independent $H(t)$ with inter-ring detuning Δ . Explicit expressions for the matrix elements of $U(t, \Delta)$ are also given in Appendix E.

The proposed scheme for CAFC can be generalized to incorporate N initially-detuned, sequentially coupled rings, rather than just 2, with N being any integer greater than 2. In such a scheme, Ring 1 couples to the input waveguide; Ring N , to the output waveguide; and Ring j ($j = 2, \dots, N-1$), to Rings $(j-1)$ and $(j+1)$. Ring N is detuned Δ_0 from Ring 1; Ring 2 is detuned by $3\Delta_0/(2N)$ from Ring 1; and Ring j ($j = 1, 2, \dots, N-1$) is initially detuned by Δ_0/N from Ring $(j-1)$. In this scheme, light is coupled into the Ring 1 from the waveguide. Then, Ring 1 is modulated by Δ_0/N and Ring 2 by $-\Delta_0/(2N)$ so they are at resonance with each other and exchange energy. Then, Ring 2 is modulated by $\Delta_0/2$ and Ring 3 by $-\Delta_0/2$ and they exchange energy, and so on. Lastly, the excited Ring $(N-1)$ is modulated by $\Delta_0/(2N)$; and Ring N , by $-\Delta_0/N$, until Ring N reaches its maximum energy. Then, Ring N is returned to its original frequency, and releases its energy into the output waveguide. With this scheme, a net shift of Δ_0 is then achieved, when each ring was modulated by Δ_0/N .

Generalization of the derivation for Eq. (8.7) to the case of N coupled rings can be done via the same methods of Appendix E for two rings and is straightforward. One then obtains

$$\begin{aligned} s_{\text{out}}(t) &= k^{\text{out}} U_N(t - t_N) a(t_N), \\ a(t_{j+1}) &= U_j(t_{j+1} - t_j) a(t_j), \quad j = 1, \dots, N-1, \\ a(t_1) &= \int_{-\infty}^{\infty} dt U_0(t_1 - t) k_{\text{in}} s_{\text{in}}(t). \end{aligned} \quad (8.8)$$

Here, $U_0(t)$ is the impulse-response matrix before any modulation is applied; and $U_j(t)$, the impulse-response matrix after the N th modulation is applied. We note that, while the impulse-response matrix in Eq. (8.7) is 2×2 ; those in Eq. (8.8) are $N \times N$, as they describe the time-evolution of all N rings.

Though analytical study of the N -ring system is straightforward, its numerical analysis is generally challenging, as it increases the number of parameters with respect to which one must optimize the CAFC process. For this reason, we mostly restrict subsequent analysis to the two-ring system and briefly suggest generalizations to the N -ring system where appropriate.

8.2 Description of a sample CAFC process

To visualize the temporal dynamics of CAFC, we consider a specific example and numerically evaluate the corresponding temporal dependence of the input power $|s_{\text{out}}(t)|^2$, the output power $|s_{\text{out}}(t)|^2$, and the ring energies $|a_j(t)|^2$ ($j = 1, 2$).

As in Chapters 6 and 7, we consider an input $s_{\text{in}}(t)$ of the form of a raised-cosine pulse, i.e.,

$$\begin{aligned} s_{\text{in}}(t) &= \sqrt{2U_s/3T_s} [1 + \cos(2\pi t/T_s)] \\ &\quad [\Theta(t + T_s/2) - \Theta(t - T_s/2)] \\ &\quad \exp \left[-i \left(\bar{\omega} + s\Omega_0^{(r)}/2 \right) t \right]. \end{aligned} \quad (8.9)$$

Here, T_s is the pulse's duration; U_s , the pulse's total energy; and $\Theta(t)$, the Heaviside unit-step function. To match the resonance frequency of the rings' supermode with most energy in Ring 1, the input carrier frequency is set to $\bar{\omega} + s\Omega_0^{(r)}/2$. Here, $s \equiv \text{sgn}(\Delta_0)$ and $\Omega_0^{(r)} \equiv \text{Re}\{\Omega_0\}$, where Ω_0 is the ring supermodes' complex-valued frequency splitting in the absence of ring modulation. As discussed in Section F.1, Ω_0 is given in terms of the ring parameters by

$$\Omega_0 = \sqrt{(\Delta_0 - i\delta)^2 + 4|\kappa|^2}, \quad \text{Re}\{\Omega_0\} > 0. \quad (8.10)$$

Here, $\delta \equiv (\gamma_1 - \gamma_2)$ is the ring decay rate contrast.

The raised-cosine pulse of Eq. (8.9) is convenient for our analysis for two reasons. First, it is a symmetric, single-lobe pulse. Hence, it is comparatively robust to dispersive effects for a fixed pulse duration, and it is thus of interest for optical telecommunications [1, 141]. Second, it is non-zero only over a finite time interval, which simplifies the numerical evaluation of the TCMT equations (Eq. (8.1)) and the optimization of the modulation times t_1 and t_2 . As for simple (i.e., not cascaded) AFC in one ring (Chapter 6) and simultaneous AFC in two rings (Chapter 7), the CAFC of the raised-cosine pulse is mostly governed by the latter's symmetry and single-lobe nature. Thus, the analysis of CAFC of the raised-cosine input applies qualitatively and yields similar results for other symmetric, single-lobe pulse shapes such as Gaussian, super-Gaussian, and hyperbolic secant.

As we show in later sections, the efficiency of CAFC is limited by three distinct normalized timescales. These are the loss per pulse duration, $\gamma_0 T_s$; the inter-ring coupling per pulse duration, $|\kappa| T_s$; and the inter-ring coupling over the inter-ring detuning rate, $|\kappa/\Delta_0|$. The CAFC energy efficiency η increases monotonically as these ratios converge as $\gamma_0 T_s \rightarrow 0$, $|\kappa| T_s \rightarrow \infty$, and $|\kappa/\Delta_0| \rightarrow 0$. Of course, in practice all three dimensionless ratios have finite, non-zero values. For our sample numerical evaluation of CAFC, we fix the value of $\gamma_0 T_s$ and $|\kappa| T_s$, but sweep the value of $|\kappa/\Delta_0|$. For concreteness, we choose $\gamma_0 T_s = 0$ and $|\kappa| T_s = 10$. Although $\gamma_0 T_s = 0$ is clearly an idealization, we find that the resulting energy-transfer dynamics are representative, i.e., they do not change qualitatively as $\gamma_0 T_s$ increases

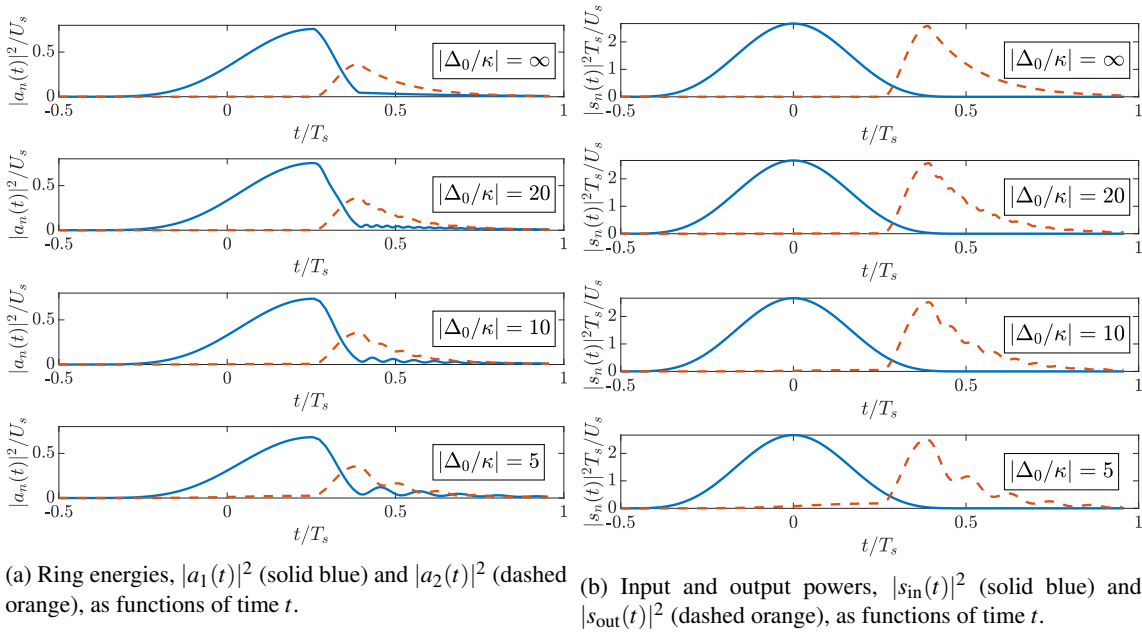


Figure 8.2: Plots of the instantaneous ring energies, $|a_1(t)|^2$ and $|a_2(t)|^2$, (left) and the instantaneous input and output powers, $|s_{\text{in}}(t)|^2$ and $|s_{\text{out}}(t)|^2$, (right) as functions of time t for a raised-cosine input, $\gamma_0 = 0$, $|\kappa|T_s = 10$, and various values of $|\Delta_0/\kappa|$. U_s is the input energy; and T_s , the input's duration.

beyond zero. Furthermore, setting $\gamma_0 = 0$ allows us to illustrate numerically that intrinsic ring loss is not the only physical mechanism limiting the CAFC efficiency, as discussed in Chapters 6 and 7.

Thus, we solve the TCMT equations, i.e., Eq. (8.1), numerically for the raised-cosine input $s_{\text{in}}(t)$ in Eq. (8.9), $\gamma_0 = 0$, $|\kappa|T_s = 10$, and various values of $|\Delta_0/\kappa|$, including the limit $|\Delta_0/\kappa| = \infty$. We choose the modulation times, t_1 and t_2 , and the bus-ring coupling rates, γ_{1e} and γ_{2e} to approximately optimize the CAFC efficiency, using the schemes explained below in Section 8.4. In Figure 8.2, we plot the resulting instantaneous energies, $|a_1(t)|^2$ and $|a_2(t)|^2$, and instantaneous powers, $|s_{\text{in}}(t)|^2$ and $|s_{\text{out}}(t)|^2$.

We first analyze the time-dependence of the instantaneous powers and energies in Fig. 8.2 for $|\Delta_0/\kappa| = \infty$. Then, we analyze the changes these quantities undergo as $|\Delta_0/\kappa|$ becomes finite and progressively decreases. For $|\Delta_0/\kappa| = \infty$, from the start of the pulse at $t = -T_s/2$ and until the start of ring modulation at $t = t_1$, $|a_1(t)|^2$ increases monotonically while $|a_2(t)|^2$ stays at zero. This is because, for $|\Delta_0/\kappa| = \infty$, the energy transferred from Ring 1 to Ring 2 cannot accumulate before the field amplitude in the rings grow out of phase with each other. Thus the energy in Ring 2 is effectively isolated from Ring 1, and the power injected through the input bus accumulates in Ring 1.

From $t = t_1$ to $t = t_2$, ring modulation is applied so that the inter-ring detuning Δ vanishes. Thus, the input $s_{\text{in}}(t)$ is no longer at resonance with a ring supermode. Consequently, loading of the input $s_{\text{in}}(t)$ into Ring 1 becomes inhibited; but inter-ring energy exchange is no longer so. Hence $|a_1(t)|^2$ decreases while $|a_2(t)|^2$ increases. The time-dependence of the ring energies in this time interval is approximately sinusoidal, in analogy to Rabi oscillation [8, 75]. Albeit the total energy in both rings decays exponentially with rate $(\gamma_1 + \gamma_2)$, which we show below must be of the order of the input bandwidth $\sim T_s^{-1}$ for efficient, bandwidth-preserving CAFC. Even if the rings' intrinsic decay rate γ_0 vanishes, the total decay rate $(\gamma_1 + \gamma_2) = (\gamma_{1e} + \gamma_{2e})$ is non-zero because we need non-vanishing γ_{1e} and γ_{2e} to couple the optical pulse from the input bus into Ring 1 and from Ring 2 into the output bus.

Ring modulation stops at $t = t_2$. The stopping time t_2 is chosen so that the energy transferred from Ring 1 to Ring 2 is approximately maximum. So to zeroth order in $\gamma_1/|\kappa|$ and $\gamma_2/|\kappa|$, t_2 is set so that $t_2 - t_1 = \pi/(2|\kappa|)$. From this statement and from last paragraph, it follows that efficient inter-ring energy transfer requires $(\gamma_1 + \gamma_2)(t_2 - t_1) \sim (|\kappa|T_s)^{-1} \ll 1$. Otherwise, a significant fraction of the rings' energy is leaked into the bus waveguides during inter-ring transfer. For the considered value of $|\kappa|T_s$, this energy leakage causes the maximum $|a_2(t_1)|^2$ in Fig. 8.2 to be appreciably smaller than the maximum for $|a_1(t_1)|^2$ at $|\Delta_0/\kappa| = \infty$. For $t > t_2$, inter-ring energy exchange is again inhibited by the large ratio $|\Delta_0/\kappa|$, so the energy in Ring 2 is isolated from Ring 1. From Ring 2, the energy leaks

continuously into the output bus with rate γ_{2e} , and its amplitude oscillates at frequency ω_2 (or $\bar{\omega} - s\Omega_0^{(r)}/2$, for finite $|\Delta_0/\kappa|$).

As a consequence of Eq. (8.1), $|s_{\text{out}}(t)|^2$ is proportional to $|a_2(t)|^2$. However, as we noted earlier, not all of the energy in the output $s_{\text{out}}(t)$ oscillates at the target output frequency ω_2 (or $\bar{\omega} - s\Omega_0/2$, for finite $|\Delta_0/\kappa|$). Only the energy in $s_{\text{out}}(t)$ for $t > t_2$ oscillates at this frequency. Therefore, only the segment of $s_{\text{in}}(t)$ for $t > t_2$ (mathematically given by $s_{\text{out}}(t)\Theta(t-t_2)$) corresponds to the frequency-shifted output. Thus, in the limit of $|\Delta_0/\kappa| \rightarrow \infty$, the frequency-shifted output equals exactly an exponentially decaying tail starting suddenly at $t = t_2$, decaying in power with rate $2\gamma_2$, and oscillating in amplitude at the target frequency $\omega_2 = \omega_1 - \Delta_0$. In the limit of large $|\Delta_0/\kappa|$, the total energy in this frequency-shifted output is $(\gamma_{2e}/\gamma_2)|a_2(t_2)|^2$. We choose $\gamma_{2e} = 1/(2T_{\text{RMS}})$ so that the input and frequency-shifted output power signals have the same root-mean-square duration in this limit. This choice of γ_{2e} and its implication on the CAFC efficiency are discussed in detail in Sections 8.4 and F.5.

As $|\Delta_0/\kappa|$ becomes finite, several new effects appear in the energy and power dynamics of CAFC. First, the maximum energy $|a_1(t_1)|^2$ loaded from the bus into Ring 1 decreases, as Ring 1 is continuously leaking energy into Ring 2. Second, the splitting in the rings' supermode resonance frequencies changes from Δ_0 to $\Omega_0^{(r)}$, as discussed for Eq. (8.9). Third, the decay rates of the supermodes also change. They are modified from their bare values of γ_j ($j = 1, 2$) to new values $\tilde{\gamma}_j$, defined as

$$\tilde{\gamma}_j = \bar{\gamma} + (-1)^j s \Omega_0^{(i)}/2. \quad (8.11)$$

Here, $\bar{\gamma} = (\gamma_1 + \gamma_2)/2$ is the ring-averaged decay rate, and $\Omega_0^{(i)} \equiv \text{Im}\{\Omega_0\}$. As a consequence of this alteration of the effective decay rates $\tilde{\gamma}_j$, both the optimal time t_1 to start modulation, and the optimal coupling between bus and Ring 1, γ_{1e} , are correspondingly modified. This modification of the optimal values for t_1 and γ_{1e} is studied below in Section 8.4.

Because $|a_1(t_1)|^2$ decreases, the maximum energy in Ring 2 at the end of modulation, $|a_2(t_2)|^2$, diminishes proportionally. Beyond that, the Rabi oscillation in ring energy from $t = t_1$ to $t = t_2$, remains unchanged, as it does not depend on $|\Delta_0|$. This is because we keep the modulation time $(t_2 - t_1)$ fixed for simplicity. In addition to the Rabi oscillation of the rings' energy, for finite $|\Delta_0/\kappa|$ energy from $s_{\text{in}}(t)$ can couple into the rings during ring modulation at $t \in [t_1, t_2]$. However, this effect is negligible as long as $|\Delta_0/\kappa|$ is large enough that the input bandwidth, $\sim T_s^{-1}$, is small compared to the shift in the supermode's resonance frequencies due to ring modulation, $\sim (|\Delta_0| - |\kappa|)$. This is the case for the TCMT parameters used for Fig. 8.2.

As $|\Delta_0/\kappa|$ becomes finite, the energy in Ring 2, $|a_2(t)|^2$, for $t > t_2$ no longer merely decays exponentially at the bare-ring rate γ_2 . Due to interference between the supermodes, $|a_2(t)|^2$ for $t > t_2$ becomes the sum of three terms: two decaying exponentially, one at rate $2\tilde{\gamma}_1$ and the other at rate $2\tilde{\gamma}_2$, and one oscillating with angular frequency $\Omega_0^{(r)}$ and with envelope decaying as $2\bar{\gamma} = (\gamma_1 + \gamma_2)$. For large $|\Delta_0/\kappa|$, the term decaying as $\tilde{\gamma}_2$ dominates. But as $|\Delta_0/\kappa|$ decreases, the other two terms become appreciable. This can be seen in Fig. 8.2, where the oscillating term causes a beat in Ring 2's energy, $|a_2(t_2)|^2$, which progressively increases in amplitude and decreases in frequency as $|\Delta_0/\kappa|$ decreases. The term decaying as $\tilde{\gamma}_1$ is not discernible in Fig. 8.2 as, in this case, $\tilde{\gamma}_1 \approx \tilde{\gamma}_2$. In theory, $|a_2(t)|^2$ for $t > t_2$ is also altered by the energy in $s_{\text{in}}(t)$ for $t > t_2$. However, the large detuning $|\Delta_0|$ compared to the input bandwidth T_s^{-1} again causes this effect to be negligible.

8.3 Inner-product analysis of the CAFC efficiency

To analyze the efficiency of CAFC, it is useful to identify the input $s_{\text{in}}(t)$ and the frequency-shifted output $s_{\text{out}}(t)$ as vectors in the vector space of finite-energy pulses (mathematically, the Hilbert space of square integrable functions of time, L^2) as in Chapter 7. Using Dirac notation, let $|f(t)\rangle$ and $|g(t)\rangle$ be vectors in this Hilbert space corresponding to the square-integrable functions of time t , $f(t)$ and $g(t)$, respectively. We define the inner product between these vectors as

$$\langle f(t)|g(t)\rangle \equiv \int_{-\infty}^{\infty} dt f^*(t)g(t). \quad (8.12)$$

Employing this Dirac notation, we rewrite Eq. (8.7) in the more abstract form

$$\begin{aligned} |s_{\text{out}}(t)\rangle &= \hat{T}_{\text{out}} a(t_2), \\ a(t_2) &= U(t_2 - t_1, 0) a(t_1), \\ a(t_1) &= \hat{T}_{\text{in}} |s_{\text{in}}(t)\rangle. \end{aligned} \quad (8.13)$$

In Eqs. (8.13), \hat{T}_{out} is a linear map from the vector space of two-dimensional, complex-valued vectors, \mathbb{C}^2 , to L^2 . Conversely, \hat{T}_{in} is a linear map from L^2 to \mathbb{C}^2 . Let $u_{jk}(t, \Delta)$ be the matrix element of $U(t, \Delta)$ from Eqs. (8.7) and (8.13) in its j th row and k th column. Then, we can write explicit expressions for the \hat{T}_{in} and \hat{T}_{out} maps as

$$\begin{aligned} \hat{T}_{\text{out}} &= \sqrt{2\gamma_2 e} (|u_{21}(t - t_2, \Delta_0)\rangle \quad |u_{22}(t - t_2, \Delta_0)\rangle), \\ \hat{T}_{\text{in}} &= \sqrt{2\gamma_1 e} \begin{pmatrix} \langle u_{11}^*(t - t_1, \Delta_0) | \\ \langle u_{21}^*(t - t_1, \Delta_0) | \end{pmatrix}. \end{aligned} \quad (8.14)$$

The conjugation of the impulse response functions $u_{j1}(t - t_1, \Delta_0)$ ($j = 1, 2$) in Eq. (8.14) results from the definition of the inner product, Eq. (8.12). As implied by their subindices, \hat{T}_{in} describes the loading of the input optical pulse into the coupled rings; and \hat{T}_{out} , the unloading of the ring energy into the frequency-shifted output. From Eq. (8.14), it follows that the net action of CAFC is that of a linear operator \hat{T} in L^2 , transforming $|s_{\text{in}}(t)\rangle$ into $|s_{\text{out}}(t)\rangle$. Furthermore, this operator is expressible as

$$\hat{T} = \hat{T}_{\text{out}} U(t_2 - t_1, 0) \hat{T}_{\text{in}}. \quad (8.15)$$

Eqs. (8.14) and (8.15) suggest that \hat{T}_{out} , \hat{T}_{in} , and \hat{T} are maps of rank 2, i.e., that their image is a two-dimensional vector space. In practice, this is inaccurate because, for CAFC, we consider only inputs $|s_{\text{in}}(t)\rangle$ nearly resonant with Ring 1's original frequency ($\omega_0 + \Delta_0/2$), and outputs $|s_{\text{out}}(t)\rangle$ resonant with Ring 2's final frequency ($\omega_0 - \Delta_0/2$), rather than over the complete frequency spectrum. Thus, the co-image of \hat{T}_{in} and the image of \hat{T}_{out} are practically restricted, which might reduce the rank of \hat{T}_{in} , \hat{T}_{out} and \hat{T} and impact the resulting efficiency of CAFC. To incorporate this restriction into our analysis, we introduce effective "filtered" maps $\hat{T}_{\text{in},F}$, $\hat{T}_{\text{out},F}$, and \hat{T}_F . Explicitly, the filtered loading map, $\hat{T}_{\text{in},F}$, is defined so that it models the effect of \hat{T}_{in} only over the vector space of inputs $|s_{\text{in}}(t)\rangle$ nearly resonant to Ring 1 before modulation. On the other hand, the filtered unloading map, $\hat{T}_{\text{out},F}$, is the restriction of \hat{T}_{out} to the preimage of outputs $|s_{\text{out}}(t)\rangle$ nearly resonant to Ring 2 after modulation. Finally, \hat{T}_F is defined, in analogy to Eq. (8.15), as

$$\hat{T}_F = \hat{T}_{\text{out},F} U(t_2 - t_1, 0) \hat{T}_{\text{in},F}. \quad (8.16)$$

As given in Eq. (8.16), \hat{T}_F describes the output of \hat{T} nearly resonant to Ring 2, restricted over inputs $|s_{\text{in}}(t)\rangle$ nearly resonant to Ring 1.

For subsequent analysis, we formulate abstract expressions for the filtered maps. To do so, we note from Appendix E that, before and after modulation, the ring supermodes oscillate at the frequencies $\bar{\omega} \pm \Omega_0^{(r)}/2$. Thus, we write

$$\begin{aligned} \hat{T}_{\text{in},F} &= \hat{T}_{\text{in}} \hat{F}(\bar{\omega} + s\Omega_0^{(r)}/2), \\ \hat{T}_{\text{out},F} &= \hat{F}(\bar{\omega} - s\Omega_0^{(r)}/2) \hat{T}_{\text{out}}. \end{aligned} \quad (8.17)$$

Here, $\hat{F}(\omega)$ is an ideal bandpass-filter operator, which retains only pulses near-resonant with ω . As in Section 8.2, $s = \text{sgn}(\Delta_0)$. Of course, the ideal bandpass-filter $\hat{F}(\omega)$ must have a given bandwidth. We assume that this bandwidth is large compared to typical bandwidths of the considered inputs $|s_{\text{in}}(t)\rangle$ and outputs $|s_{\text{out}}(t)\rangle$, albeit small compared to the ring detuning Δ_0 and leave it unspecified.

We take the ideal filter operator $\hat{F}(\omega)$ as self-adjoint. Thus, we may evaluate the right-hand sides of (8.17) by applying $\hat{F}(\omega)$ to the bras $\langle u_{j1}^*(t - t_1, \Delta_0) |$ and the kets $|u_{2j}(t - t_2, \Delta_0)\rangle$ ($j = 1, 2$) in Eq. (8.14). We do so by retaining only the terms in the matrix elements $u_{nm}(t, \Delta_0)$ oscillating at the frequency specified by the filtering operator $\hat{F}(\omega)$, either $(\bar{\omega} + s\Omega_0^{(r)}/2)$ or $(\bar{\omega} - s\Omega_0^{(r)}/2)$. In this way, we obtain the explicit expressions

$$\begin{aligned} \hat{T}_{\text{in},F} &= \sqrt{\frac{\gamma_1 e}{\tilde{\gamma}_1}} \begin{pmatrix} [1 + (|\Delta_0| - is\delta)/\Omega_0]/2 \\ s\kappa_{21}/\Omega_0 \end{pmatrix} \langle n_{\text{in}} |, \\ \hat{T}_{\text{out},F} &= \sqrt{\frac{\gamma_2 e}{\tilde{\gamma}_2}} |n_{\text{out}}\rangle (-s\kappa_{21}/\Omega_0 \quad [1 + (|\Delta_0| - is\delta)/\Omega_0]/2). \end{aligned} \quad (8.18)$$

In Eq. (8.18), $|n_{\text{in}}\rangle$ and $\langle n_{\text{out}}|$ are the ket and bra corresponding, respectively, to the normalized pulses

$$\begin{aligned} n_{\text{in}}(t) &= \sqrt{2\tilde{\gamma}_1} \Theta(t_1 - t) \exp[-(t_1 - t)(\tilde{\gamma} - i\tilde{\omega} - is\Omega_0^*/2)], \\ n_{\text{out}}(t) &= \sqrt{2\tilde{\gamma}_2} \Theta(t - t_2) \exp[-(t - t_2)(\tilde{\gamma} + i\tilde{\omega} - is\Omega_0/2)]. \end{aligned} \quad (8.19)$$

Again, $\Theta(t)$ is the Heaviside function; and $\tilde{\gamma}_j$, the modified decay rates of Eq. (8.11). The bra $\langle n_{\text{in}}|$ and the ket $|n_{\text{out}}\rangle$ in Eq. (8.18) are normalized so that $\langle n_{\text{in}}|n_{\text{in}}\rangle = \langle n_{\text{out}}|n_{\text{out}}\rangle = 1$. From Eqs. (8.16) and (8.18), it is clear that the filtered maps $\hat{T}_{\text{in},F}$, $\hat{T}_{\text{out},F}$, \hat{T}_F are of rank 1. This is in contrast to the unfiltered maps \hat{T}_{in} , \hat{T}_{out} , and \hat{T} in Eqs. (8.14) and (8.15), which are of rank 2. As we discuss next, consideration of this rank reduction is key to analyze CAFC efficiency's upper bounds and its dependence on the input pulse $s_{\text{in}}(t)$.

Leveraging Eqs. (8.16) and (8.18), it is now straightforward to write an explicit expression for the energy efficiency η of CAFC. Since the CAFC output is given by $\hat{T}_F |s_{\text{in}}(t)\rangle$, we substitute Eqs. (8.16) and (8.18) to obtain

$$\eta = \frac{\langle s_{\text{in}}(t) | \hat{T}_F^\dagger \hat{T}_F | s_{\text{in}}(t) \rangle}{\langle s_{\text{in}}(t) | s_{\text{in}}(t) \rangle} = \frac{\gamma_{1e} \gamma_{2e}}{\tilde{\gamma}_1 \tilde{\gamma}_2} |V|^2 \frac{|\langle n_{\text{in}} | s_{\text{in}}(t) \rangle|^2}{\langle s_{\text{in}}(t) | s_{\text{in}}(t) \rangle}. \quad (8.20)$$

Here, \dagger stands for the adjoint operation; and V , for the matrix product

$$\begin{aligned} V &= \begin{pmatrix} -s\kappa_{21}/\Omega_0 & [1 + (|\Delta_0| - is\delta)/\Omega_0]/2 \end{pmatrix} \\ U(t_2 - t_1, 0) &= \begin{pmatrix} [1 + (|\Delta_0| - is\delta)/\Omega_0]/2 \\ s\kappa_{21}/\Omega_0 \end{pmatrix}. \end{aligned} \quad (8.21)$$

Of course, the magnitude of the inner product $\langle n_{\text{in}} | s_{\text{in}}(t) \rangle$ is bounded by the Schwarz inequality [135, 140] as $|\langle n_{\text{in}} | s_{\text{in}}(t) \rangle|^2 \leq \langle n_{\text{in}} | n_{\text{in}} \rangle \langle s_{\text{in}}(t) | s_{\text{in}}(t) \rangle = \langle s_{\text{in}}(t) | s_{\text{in}}(t) \rangle$. Hence, the CAFC efficiency η is bounded from above as

$$\eta \leq \frac{\gamma_{1e} \gamma_{2e}}{\tilde{\gamma}_1 \tilde{\gamma}_2} |V|^2. \quad (8.22)$$

Furthermore, this bound is tight; as a well known corollary of the Schwarz inequality is that it becomes an equality if and only if the two vectors considered are linearly dependent [135]. Thus, Eq. (8.22) becomes an equality if and only if $|s_{\text{in}}(t)\rangle$ is proportional to $|n_{\text{in}}\rangle$. Additionally, increasing the projection of $|s_{\text{in}}(t)\rangle$ into $|n_{\text{in}}\rangle$ increases the ratio $|\langle n_{\text{in}} | s_{\text{in}}(t) \rangle|^2 / \langle s_{\text{in}}(t) | s_{\text{in}}(t) \rangle$, and thus increases the efficiency η , providing the remaining factors on the right-hand side of Eq. (8.20) remain fixed.

Generalization of the results of this section to the N -ring system is straightforward. The row vector of kets and the column vector of bras in Eq. (8.18) for \hat{T}_{out} now have entries $|u_{Nj}^{(N)}(t - t_N)\rangle$ and $\langle u_{j1}^{(0)*}(t - t_1)|$, respectively. Here $u_{kl}^j(t)$ is the kl entry of the impulse-response matrix $U_j(t)$, as defined in Eq. (8.8). Eqs. (8.15), (8.16), and (8.21), the matrix $U(t_2 - t_1, 0)$ is replaced by the matrix product

$$U(t_2 - t_1, 0) \rightarrow \prod_{j=1}^{N-1} U_j(t_{j+1} - t_j). \quad (8.23)$$

In the right-hand side of Eq. (8.23), the matrices $U_j(t_{j+1} - t_j)$ are multiplied in descending order for their index j .

In the N -ring system, the rings' supermodes no longer oscillate at the complex frequencies $\tilde{\omega} - i\tilde{\gamma} \pm \Omega_0/2$ before and after modulation. Rather, they oscillate at the complex frequencies is_j ($j = 1, \dots, N$). These s_j are the poles of the resolvent $(sI_N + iH_0)^{-1}$, where I_N is the $N \times N$ identity matrix, and H_0 , as in Eq. (8.6), is the frequency-coefficient matrix $H(t)$ before and after all ring modulations. Consequently, the filtering frequencies $\tilde{\omega} \pm \Omega_0^{(r)}/2$ in Eq. (8.17) must be changed to $-\text{Im}\{s_1\}$ and $-\text{Im}\{s_N\}$, respectively. Here, is_j is the complex supermode frequency with $-\text{Im}\{s_j\}$ closest to the bare resonance frequency of the j th Ring. Additionally, the input and output normalized pulses $n_{\text{in}}(t)$ and $n_{\text{out}}(t)$ in Eq. (8.19) retain the same form, with their central frequencies replaced by $-\text{Im}\{s_1\}$ and $-\text{Im}\{s_N\}$, and their decay rates by $-\text{Re}\{s_1\}$ and $-\text{Re}\{s_N\}$, respectively. Of course, the expressions for column and row vectors in Eq. (8.14) and (8.21) become altered for the N -ring system, and must be reevaluated for each value of N .

8.3.1 Limit of large inter-ring detuning

To aid the numerical optimization of the CAFC efficiency η and to develop an intuition of its behavior, it is useful to consider η in the limit of large inter-ring detuning $|\Delta_0|$ compared to the other time rates governing the CAFC process.

Expressly, this limit corresponds to that of $|\Delta_0|$ large compared to the inter-ring coupling $|\kappa|$, the ring decay rates γ_j ($j = 1, 2$), and the input pulse's bandwidth. Let us define η_0 as the CAFC efficiency in this limit, i.e., $\eta_0 = \lim_{|\Delta_0| \rightarrow \infty} \eta$. From Eq. (8.20) for η , we find that η_0 can be factored as

$$\eta_0 = \eta_{01} \eta_{12} \eta_{23}. \quad (8.24)$$

Here, the factors $\eta_{j,j+1}$ ($j = 0, 1, 2$) on the right-hand side of Eq. (8.24) can be interpreted as the efficiencies of the sub-processes composing CAFC. η_{01} is the efficiency of loading the input pulse from the input bus waveguide into Ring 1; η_{12} , the efficiency of transferring the energy from Ring 1 to Ring 2; and η_{23} , the efficiency of unloading the energy from Ring 2 into the output bus waveguide. The expressions for these partial efficiencies are

$$\begin{aligned} \eta_{01} &= \left(\frac{\gamma_e}{\gamma_1} \right) \frac{|\langle n_{\text{in}} | s_{\text{in}}(t) \rangle|^2}{\langle s_{\text{in}}(t) | s_{\text{in}}(t) \rangle}, \\ \eta_{12} &= |u_{21}(t_2 - t_1, 0)|^2, \\ \eta_{23} &= \gamma_e / \gamma_2. \end{aligned} \quad (8.25)$$

Clearly, the expressions in Eq. (8.25) agree with the previously described interpretations.

Let us briefly discuss the partial efficiencies η_{01} and η_{23} . In the limit $|\Delta_0| \rightarrow \infty$, the normalized input vector $|n_{\text{in}}\rangle$, given by Eq. (8.19), oscillates at frequency ω_1 and grows at a rate of γ_1 . Thus, as expected, η_{01} equals the efficiency of loading the input $s_{\text{in}}(t)$ into Ring 1 in the absence of Ring 2 and the output bus [140]. Similarly, the expression for η_{23} in Eq. (8.25) is identical to the efficiency of unloading the energy in Ring 2 into the bus waveguide in the absence of the input bus and Ring 1 [140].

Just as discussed for Eq. (8.22), η_{01} in Eq. (8.25) is bounded by the Schwarz inequality as $\eta_{01} \leq \gamma_e / \gamma_1$. Furthermore, from the Schwarz inequality's corollary, η_{01} increases as the projection of $|s_{\text{in}}(t)\rangle$ into $|n_{\text{in}}\rangle$ increments, if γ_e / γ_1 remains constant. Lastly, the maximum $\eta = \gamma_e / \gamma_1$ can be attained if and only if $|s_{\text{in}}(t)\rangle$ is proportional to $|n_{\text{in}}\rangle$.

Though it is difficult to obtain an explicit form for η for CAFC in the N -ring ($N > 2$) system for finite Δ_0 , the intuitive results of this subsection suggest it takes a simple form in the limit of infinite $|\Delta_0|$. Given the intuitive forms η_0 in Eq. (8.24) and of $\eta_{j,j+1}$ in Eq. (8.25), and the generalization rule Eq. (8.23), we surmise that, for the N -ring system, η_0 takes the form

$$\eta_0 = \prod_{j=0}^N \eta_{j,j+1}. \quad (8.26)$$

As in the two-ring system, $\eta_{j,j+1}$ ($j = 0, \dots, N$) are the partial efficiencies of the sub-processes constituting CAFC in the limit $|\Delta_0| \rightarrow \infty$. Just as in the two-ring system, η_{01} is the efficiency of loading the input from the input bus into Ring 1; and $\eta_{N,N+1}$, the efficiency of unloading the energy from Ring N into the output bus. These are still given by Eq. (8.25) for η_{01} and η_{23} , respectively. For $j \neq 0, N$, $\eta_{j,j+1}$ is the efficiency of transferring energy from Ring j to Ring $(j+1)$. As a consequence of Eq. (8.23), this is given by

$$\eta_{j,j+1} = |u_{j+1,j}^{(j)}(t_{j+1} - t_j)|^2, \quad j \neq 0, N. \quad (8.27)$$

As described above Eq. (8.23), $u_{j+1,j}^{(j)}(t)$ are off-diagonal entries of the impulse-response matrix $U_j(t)$.

8.4 Optimization of the CAFC timescales

As is clear from Sections 8.2 and 8.3, the two-ring CAFC process and its efficiency depend on the relation among various timescales and time rates. These are the pulse duration T_s , the initial t_1 and final t_2 times of modulation, the inter-ring detuning Δ_0 , the inter-ring coupling κ , the intrinsic decay rate γ_0 , the coupling rate γ_e between the input bus and Ring 2, and the coupling rate γ_2 between Ring 2 and the output bus. In this section, we describe our scheme for practical numerical optimization of the CAFC efficiency with respect to these variables. For concreteness, we suppose the input pulse is a simple, symmetric, single-lobe pulse as in Section 8.2.

Firstly, we discuss CAFC efficiency optimization with respect to the pulse duration T_s . In practice, the input pulse is usually fixed. Hence T_s is often not a free parameter to optimize the CAFC efficiency. For completeness, though, we briefly consider optimization of CAFC with respect to T_s . We see in Eq. (8.20) that T_s only appears in the expression

for the CAFC efficiency η through the inner product $\langle n_{\text{in}} | s_{\text{in}}(t) \rangle$. Thus, if all other TCMT parameters remain constant, optimal T_s is that which maximizes $|\langle n_{\text{in}} | s_{\text{in}}(t) \rangle|$. From Eq. (8.19), this implies that T_s must be of the order of the supermode decay rate $\tilde{\gamma}_1 \sim \gamma_1$. Furthermore, the derivation of the solution of Eqs. (8.1) in Appendix E assumes that the bandwidth of $s_{\text{in}}(t)$ is small compared to the modulation-induced change in the rings' supermode resonant frequency, which is of the order of $(|\Delta_0| - |\kappa|)$. This requirement is equivalent to the condition $(|\Delta_0| - |\kappa|)T_s \gg 1$. This condition is satisfied if $|\Delta_0| \gg |\kappa|$ and $|\kappa|T_s \gg 1$, which are necessary for efficient CAFC, as discussed in Sec. 8.2 and below in this section. Nonetheless, as discussed below in this section and Section 8.5, efficient CAFC under our scheme requires simultaneously $\gamma_0 T_s \ll 1$ and $|\kappa|T_s \gg 1$. The first condition arises because efficient CAFC requires both $\gamma_{1e} \gg \gamma_0$ and $\gamma_{1e} \sim T_s^{-1}$, as explained below in this section, which occurs only if $\gamma_0 T_s \ll 1$. Similarly, the second condition emerges because efficient CAFC requires $\gamma_{1e} \ll |\kappa|$ and $\gamma_{1e} \sim T_s^{-1}$, again explained below, which occurs only if $|\kappa|T_s \gg 1$.

Secondly, we consider CAFC optimization with respect to the modulation start time t_1 . From Eqs. (8.19) and (8.20), t_1 only appears in the expression for η through the bra vector $\langle n_{\text{in}} |$ in the inner product $\langle n_{\text{in}} | s_{\text{in}}(t) \rangle$. Specifically, t_1 is the time at which the normalized, truncated, increasing exponential $n_{\text{in}}(t)$ is terminated. Thus, the value of t_1 which optimizes η is the one which shifts $|n_{\text{in}}\rangle$ so that it achieves the largest overlap with $|s_{\text{in}}(t)\rangle$. For a large detuning ratio $|\Delta_0/\kappa|$, the CAFC optimization with respect to t_1 can be interpreted as an optimization of the loading of the input pulse into one of the rings' supermodes at time t_1 .

Thirdly, we examine CAFC optimization with respect to the modulation end time t_2 . For a high modulation ratio $|\Delta_0/\kappa|$ and small input bandwidth $|\kappa| \gg T_s^{-1}$, coupling of $s_{\text{in}}(t)$ into the rings is inhibited during ring modulation, from $t = t_1$ to $t = t_2$. Thus, the only effect of varying t_2 is to modify the duration $(t_2 - t_1)$ of Rabi oscillation of the rings' energies. This is seen from Eqs. (8.20) and (8.21). Thus, to optimize the CAFC efficiency η with respect to t_2 , we choose the t_2 which maximizes the modulus of V in Eq. (8.21). Nonetheless, direct maximization of $|V|^2$ for finite Δ_0 is a challenging problem, requiring numerical solution for each value of $|\Delta_0/\kappa|$. To simplify the problem, we note, as in Subsection 8.3.1, that $\lim_{\Delta_0 \rightarrow \infty} V = u_{21}(t_2 - t_1, 0)$. Furthermore, maximization of $\eta_{12} = |u_{21}(t_2 - t_1, 0)|^2$ with respect to t_2 can be performed analytically for arbitrary values of the other TCMT parameters. This analytical optimization is discussed in Section F.2. Thus, for simplicity of numerical implementation, we set t_2 to the value which maximizes η_{12} , and thus η in the limit of high $|\Delta_0|$. Of course, this value of t_2 also approximately maximizes $|V|^2$ (and thus the exact CAFC efficiency η) for large $|\Delta_0/\kappa|$, which itself is necessary for efficient CAFC.

Fourthly, we discuss the effect of the pre- and post-modulation inter-ring detuning Δ_0 on the CAFC efficiency. Mathematically, changing Δ_0 changes the pre- and post-modulation rings' supermodes and their complex-valued frequency splitting Ω_0 . Consequently, this changes the supermodes' modified decay rates $\tilde{\gamma}_j$ in Eq. (8.11), which modifies the input and output functions $n_{\text{in}}(t)$ and $n_{\text{out}}(t)$ in Eq. (8.19). Increasing $|\Delta_0|$ modifies the supermodes by causing them to concentrate each on one of the two rings. This energy concentration reduces the inter-ring energy leakage before and after ring modulation, and thus increases the CAFC efficiency. In particular, to inhibit inter-ring energy exchange before and after modulation, we must have $|\Delta_0/\kappa| \gg 1$.

Fifthly, we consider the effect of inter-ring coupling κ . Before and after ring modulation, we require $|\kappa|$ to be small compared to $|\Delta_0|$ to inhibit inter-ring energy leakage, as discussed above. During ring modulation, we require $|\kappa|$ to be large compared to the ring-averaged decay rate $\bar{\gamma}$ so that the energy in Ring 1 can be transferred to Ring 2 before the rings' total energy dissipates noticeably. Combining these two criteria, we deduce that there exists an value of $|\kappa|$ that optimizes η , satisfying $\bar{\gamma} \ll |\kappa| \ll |\Delta_0|$. Exact determination of this optimal $|\kappa|$ is a formidable numerical problem. In Section 8.6, we present an approximate numerical scheme to estimate this optimal $|\kappa|$.

Sixthly, we examine the effect of the intrinsic decay rate γ_0 on the CAFC efficiency. Physically, the effect of non-zero γ_0 is to introduce energy loss at all stages of CAFC. Thus, the CAFC efficiency is maximized with respect to γ_0 in the ideal case of $\gamma_0 = 0$. More specifically, efficient CAFC requires the intrinsic photon lifetime $(2\gamma_0)^{-1}$ large compared to all other timescales of CAFC. Among the remaining timescales, we show below that efficient CAFC requires T_s , $(2\gamma_{1e})^{-1}$, and $(2\gamma_{2e})^{-1}$ to be largest, with these three all being of similar order of magnitude. Thus, a concrete criterion for small intrinsic loss is $\gamma_0 T_s \ll 1$. In particular, $\gamma_0 T_s \sim \gamma_0/\gamma_{1e} \ll 1$ directly implies low intrinsic loss upon coupling of the input into Ring 1 before modulation. Similarly, $\gamma_0 T_s \sim \gamma_0/\gamma_{2e} \ll 1$ implies low intrinsic loss upon coupling the frequency-shifted output out of Ring 2 after modulation.

Seventhly, we analyze the net effect on the CAFC efficiency η of the coupling rate γ_{1e} between the input bus and Ring 1. From Eq. (8.20), η depends on γ_{1e} through three of its factors: $(\gamma_{1e}/\tilde{\gamma}_1)$, $|\langle n_{\text{in}} | s_{\text{in}}(t) \rangle|^2$, and $|V|^2$. In the limit of large $|\Delta_0|$, $(\gamma_{1e}/\tilde{\gamma}_1)$ converges to γ_{1e}/γ_1 . So for large $|\Delta_0|$, the ratio $(\gamma_{1e}/\tilde{\gamma}_1)$ increases monotonically with γ_{1e} . In particular, $(\gamma_{1e}/\tilde{\gamma}_1)$ becomes near unity when $\gamma_{1e} \gg \gamma_0$ for large $|\Delta_0|$. On the other hand, the magnitude of the inner product $\langle n_{\text{in}} | s_{\text{in}}(t) \rangle$ is optimized with respect to γ_{1e} when the duration $\tilde{\gamma}_1$ of $n_{\text{in}}(t)$ (in Eq. (8.19)) is of the

order of the input bandwidth $\sim T_s^{-1}$. Lastly, in the limit of large $|\Delta_0|$, V converges to $u_{21}(t_2 - t_1, 0)$. Consequently, large $|V|^2 \approx |u_{21}(t_2 - t_1, 0)|^2$ requires γ_{1e} small compared to $|\kappa|$ for large $|\Delta_0|$. Balancing all of these dependences to obtain the value of γ_{1e} which optimizes η is evidently a challenging numerical problem which also depends on the particular value of $|\Delta_0|$. To make the problem numerically amenable, we assume $|\Delta_0|$ large enough so we can optimize the factorized η of Subsection 8.3.1 instead of the general η to good accuracy.

To this approximation, we need only balance the dependences on γ_{1e} of the partial efficiencies η_{01} and η_{12} from Eq. (8.25). From Subsection 8.3.1, we recall that η_{01} can be interpreted as the efficiency of loading the input $s_{\text{in}}(t)$ into Ring 1 before index modulation is applied at time t_1 . Hence, from Ref. [140], η_{01} is maximized when $\gamma_{1e} \gg \gamma_0$ and $\gamma_{1e} = k/T_s$ for a constant k of the order of unity, depending on the input pulse shape, e.g., $k = 2.3780$ for the raised-cosine [140]. In contrast, η_{12} is maximized with respect to non-negative γ_{1e} when $\gamma_{1e} = 0$. Physically, this is because coupling between the input bus and Ring 1 results only in energy leakage during the energy transfer from Ring 1 to Ring 2. Thus, the partial efficiency $\eta_{02} = \eta_{01}\eta_{12}$ of energy transfer from the input bus to Ring 2 in the limit $|\Delta_0| \rightarrow \infty$ (and hence η in this same limit) is maximized with respect to γ_{1e} at some critical value between 0 and k/T_s .

To determine this value, we assume that the ratios $\gamma_j/|\kappa|$ ($j = 1, 2$) are small enough so that the value of γ_{1e} which maximizes η_{02} differs only slightly from k/T_s . Then, we may approximate through Taylor polynomials η_{01} as a function of $(\gamma_{1e}T_s - k)$; and η_{12} as a function of $\gamma_j/|\kappa|$. As a result, $\eta_{02} = \eta_{01}\eta_{12}$ can be approximated as a third-order polynomial in γ_{1e} , which optimum γ_{1e} we can determine analytically. We then use this approximate optimal γ_{1e} as the initial guess of a numerical routine for local optimization. We discuss the details of the polynomial model for η_{02} as a function of γ_{1e} in Section F.3.

We evaluate this approach for numerical optimization of η_{02} with respect to γ_{1e} . To do so, we first note that we consider the limit $|\Delta_0| \rightarrow \infty$, and that we optimize CAFC with respect to t_1 and t_2 as discussed above in this section. Then, we focus on the case of a raised-cosine input of duration T_s and the idealized case of $\gamma_0 = 0$. As in Sec. 8.2, $\gamma_0 = 0$ is chosen for simplicity and to illustrate the fundamental limits of the CAFC efficiency. We illustrate the following analysis of the dependence of η_{02} on γ_{1e} for non-vanishing γ_0 in Section F.3, though the qualitative behavior of all quantities is identical for small γ_0 . The value of γ_{2e} is set to tune the duration of the CAFC output, as described below in this section. Then, η_{02} depends only on two dimensionless products: $\gamma_{1e}T_s$ and $|\kappa|T_s$. Given this observation, we evaluate η_{02} for different values of $\gamma_{1e}T_s$ and $|\kappa|T_s$. We display the results as a contour plot in Fig. 8.3. In this contour plot, we also trace the curve corresponding to the values of $\gamma_{1e}T_s$ that maximize η_{02} for set values of $|\kappa|T_s$. To compare with this curve, we also highlight two estimates for it. The first estimate is the curve with values of $\gamma_{1e}T_s$ which optimize the aforementioned polynomial model for η_{02} for fixed $|\kappa|T_s$. The second estimate is the curve with values of $\gamma_{1e}T_s$ which optimize η_{01} [140], and are thus constant for all $|\kappa|T_s$, which influences only η_{12} .

We examine the lines of constant $\gamma_{1e}T_s$ and of constant $|\kappa|T_s$ in Fig. 8.3. For constant $\gamma_{1e}T_s$, η_{02} increases monotonically with $|\kappa|T_s$. This is because, to maximize η_{01} , from the input bus to Ring 1, γ_{1e} must be of the order of T_s^{-1} . Hence, large $|\kappa|T_s$ implies large $|\kappa|/\gamma_{1e}$, and thus small energy leakage during energy transfer from Ring 1 to Ring 2. In contrast, for constant $|\kappa|T_s$, there is always a finite value of $\gamma_{1e}T_s$ which maximizes η_{02} , in agreement with the aforementioned polynomial model for η_{02} and its discussion.

We compare the line of optimal values of $\gamma_{1e}T_s$ with its analytical estimates in Fig. 8.3. For this comparison, we make three observations. First, the exact optimum value of $\gamma_{1e}T_s$ lies between its two estimates for all of the considered values of $|\kappa|T_s$. This allows us to use these estimates as bounds for the optimum $\gamma_{1e}T_s$ for any $|\kappa|T_s$ for numerical optimization of η_{02} . Second, as $|\kappa|T_s$ increases, the exact optimum $\gamma_{1e}T_s$ converges to its polynomial estimate. This is because then, the inter-ring transfer efficiency η_{12} approaches unity, and its first-order polynomial in $\gamma_j/|\kappa|$ approximates it more accurately. Third, as $|\kappa|T_s$ increases, the polynomial estimate converges to the value which optimizes input loading from the input bus to Ring 1. Again, this is because then η_{01} approaches unity, so $\eta_{02} \approx \eta_{01}$. Then, because the exact optimum $\gamma_{1e}T_s$ is always between these two estimates, it also converges to the value for maximum η_{01} .

Eightly, we discuss the effect on the CAFC output of the coupling rate γ_{2e} between Ring 2 and the output bus, and we explain the scheme we use to set its value. In general, varying γ_{2e} has two effects in the CAFC output. First, a change in γ_{2e} alters the CAFC efficiency η . Mainly, this occurs via two competing mechanisms: it decreases the efficiency in energy transfer from Ring 1 to Ring 2 during ring modulation, as energy leaks from Ring 2 into the output bus while the energy in Ring 1 is coupled into Ring 2, which decreases η ; also, it increments the energy coupled from Ring 2 into the output bus after modulation, which increases η . Second, an increase in γ_{2e} decreases the duration of the frequency-shifted output pulse. This is because most of the energy of the output is in an exponentially decaying tail of characteristic timescale $1/(2\tilde{\gamma}_2)$ which decreases with increasing γ_{2e} .

We might consider setting γ_{2e} to the value which maximizes the η . Nonetheless, determining this optimal value

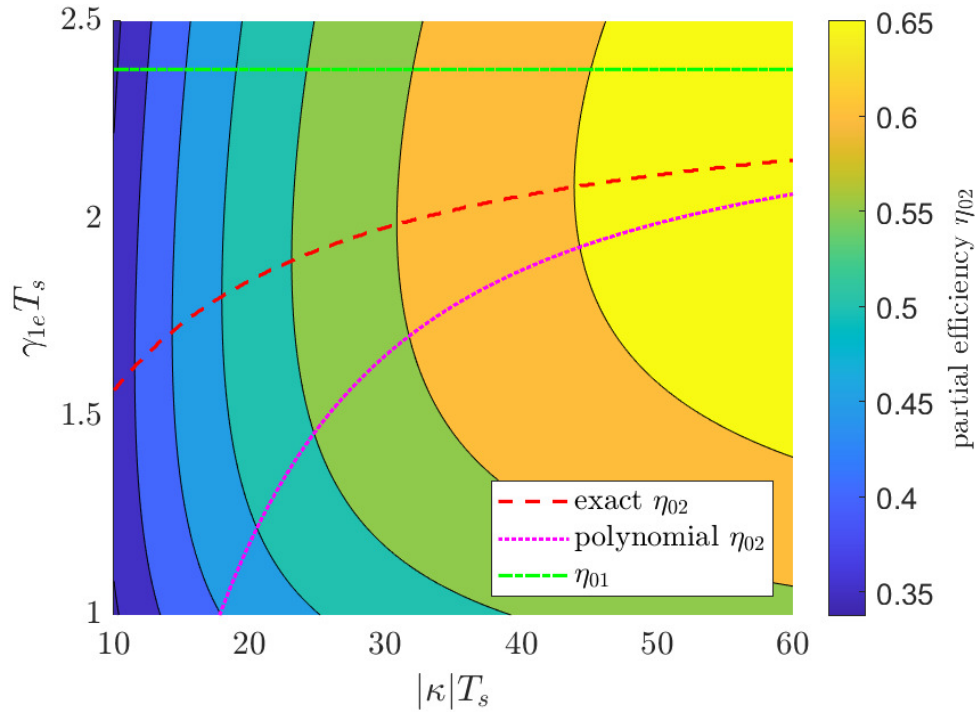


Figure 8.3: Contour plot of the maximum partial efficiency η_{02} for $\gamma_0 = 0$ for different values of $|\kappa|T_s$ and $\gamma_{1e}T_s$. Highlighted are also three curves. The first curve corresponds to the value of $\gamma_{1e}T_s$ which maximizes η_{02} for fixed $|\kappa|T_s$ (red). The second and third curves are estimates of the aforementioned optimal curve. One corresponds to the value of $\gamma_{1e}T_s$ which maximizes the polynomial model for η_{02} (purple); the other, to the value which maximizes the partial efficiency η_{01} (green).

of γ_{2e} is challenging. For simplicity, we may consider η in the limit $|\Delta_0| \rightarrow \infty$, where η becomes expressible as the product of the partial efficiencies $\eta_{j,j+1}$ ($j = 0, 1, 2$). Even then, the problem remains formidable. However, if we assume that the inter-ring coupling strength $|\kappa|$ is large compared to the ring decay rates γ_j ($j = 1, 2$), we may approximate the partial efficiency $\eta_{12} = |u_{21}(t_*, 0)|^2$ by a Taylor polynomial. Then, we may analytically optimize the partial efficiency $\eta_{13} = \eta_{12}\eta_{23}$. This is analogous to how we set γ_{1e} by optimizing $\eta_{02} = \eta_{01}\eta_{12}$.

Nonetheless, optimizing η with respect to γ_{2e} in the limits $|\Delta_0| \rightarrow \infty$ and $\gamma_j/|\kappa| \rightarrow 0$ yields a value of γ_{2e} that depends on γ_{1e} . Conversely, optimizing η similarly with respect to γ_{1e} yields a value of γ_{1e} that depends on γ_{2e} . Thus, the problem of optimizing η with respect to both rates simultaneously, even under these approximations, becomes a challenging set of simultaneous nonlinear equations, which requires numerical solution. Even obtaining initial estimates for the optimal γ_{1e} and γ_{2e} proves difficult.

To circumvent the formidable numerical problem of optimizing η with respect to γ_{2e} , we neglect the effect of γ_{2e} on η , and we rather engineer its effect on the output pulse duration. As we discuss in Sections F.2 and F.5, this neglect is accurate for small $\gamma_{2e}/|\kappa|$. Explicitly, we set γ_{2e} so that the frequency-shifted output $s_{\text{out}}(t)$ has a root-mean-square (RMS) duration T_{RMS} approximately equal to that of the input $s_{\text{in}}(t)$. Consequently, the frequency-shifted $s_{\text{out}}(t)$ shall have a bandwidth comparable to that of $s_{\text{in}}(t)$, in the order of $2\pi/T_{\text{RMS}}$. Our scheme used to accomplish this is discussed further in the Section F.5.

To close this section, we briefly discuss the extension of our optimization scheme for N -ring CAFC with $N > 2$. Most of the results of this section still hold for the N -ring system, albeit with the following small modifications. First, we note that the middle rings (with index j , such that $2 \leq j \leq (N-1)$), have no extrinsic loss γ_{je} , as they are not coupled to the input or output buses. They have only intrinsic loss γ_0 . Hence the inter-ring coupling $|\kappa|$ among them need only be large enough so $\gamma_0 \ll |\kappa|$ to inhibit loss during inter-ring energy exchange. In turn, this looser requirement on the inter-ring coupling allows inter-ring leakage due to finite $|\kappa/\Delta_0|$ to be smaller for a fixed value of $|\Delta_0|$. By adding additional rings to the system, one must optimize the efficiency η over the durations $(t_{j+1} - t_j)$ of the intermediate ring modulations. These must maximize inter-ring energy transfer, just as the single modulation duration $(t_2 - t_1)$ of the two-ring system. To zeroth order in γ_0 , the optimal durations $(t_{j+1} - t_j)$ equal $\pi/(2|\kappa|)$. For exact, and higher-order expressions, see the Section F.2. Lastly, we note that for $N > 2$, there is no first-neighbor coupling between Ring 1 and Ring N , the two rings coupled to waveguide buses and hence with non-zero extrinsic loss. Thus, independent optimization of η with respect to γ_{1e} and γ_{2e} is more accurate for finite inter-ring detuning $|\Delta_0|$, as they become increasingly decoupled as the number of rings, N , increases.

8.5 Convergence analysis of the CAFC efficiency

With the scheme of Section 8.4, we optimize CAFC with respect to most of the process's timescales. In particular, we explain in that section that the CAFC efficiency increases as $\gamma_0 T_s$ tends to zero, and as $|\kappa|T_s$ and $|\Delta_0/\kappa|$ tend to infinity. In practice, these three dimensionless parameters have finite, nonzero values; so it is important to analyze how quickly the CAFC efficiency η converges to its maximum with respect to them, and of course, the numerical value of this maximum. As we show in Section 8.6, this analysis allows us to develop an accurate, simple polynomial model of the dependence of η on these three dimensionless parameters. We may then use this polynomial model to estimate optimal values for the remaining free TCMT timescales (e.g., the inter-ring coupling rate $|\kappa|$, and possibly the pulse duration T_s) and the scaling of η with the inter-ring detuning $|\Delta_0|$. Furthermore, we show in this section that our CAFC scheme converges to the same maximum as single-ring AFC [140]. This is a key result because, as we discuss below, it directly implies there exist conditions under which CAFC can be more efficient than multiple instances of single-ring AFC in series.

We start by examining the convergence of η with respect to the normalized inter-ring detuning $|\Delta_0/\kappa|$. As stated previously, efficient CAFC requires this ratio to be large, so the input pulse $s_{\text{in}}(t)$ can be efficiently loaded from the input bus into Ring 1 without leaking into Ring 2, and so the frequency-shifted output $s_{\text{out}}(t)$ can efficiently exit from Ring 2 into the output bus without leaking into Ring 1. As stated in the previous paragraph, η depends on the three dimensionless parameters $|\Delta_0/\kappa|$, $|\kappa|T_s$, and $\gamma_0 T_s$. Hence, we analyze the rate of convergence of η with respect to $|\Delta_0/\kappa|$ as a function of two independent variables: $|\kappa|T_s$ and $\gamma_0 T_s$. First, we take $\gamma_0 T_s$ as constant, and examine the rate of convergence of η with respect to $|\Delta_0/\kappa|$ for different values of $|\kappa|T_s$. Then, we take $|\kappa|T_s$ as constant, and consider different values of $\gamma_0 T_s$. Lastly, we draw general conclusions by varying both $|\kappa|T_s$ and $\gamma_0 T_s$ simultaneously.

The numerical results of this convergence analysis are shown in Fig. 8.4. First, in Fig. 8.4a we study the con-

vergence of η with respect to $|\Delta_0/\kappa|$ for $\gamma_0 T_s = 0$ and different values of $|\kappa|T_s$. To aid visualization and subsequent discussion, Fig. 8.4a also shows $\eta_0 = \lim_{|\Delta_0| \rightarrow \infty} \eta$ (as introduced in Subsection 8.3.1) for $\gamma_0 T_s = 0$ and each value of $|\kappa|T_s$. We verify that, for all values of $|\kappa|T_s$, η indeed converges to η_0 as $|\Delta_0/\kappa|$ increases. Moreover, we observe in Fig. 8.4a that η converges to η_0 monotonically from below for all considered values of $|\Delta_0/\kappa|$. This observation suggests that η_0 is indeed an upper bound on η for large, finite $|\Delta_0/\kappa|$, provided the remaining TCMT parameters remain fixed. Of course, we expect this to be the case for sufficiently large $|\Delta_0/\kappa|$, based on the discussion of the role of $|\Delta_0|$ in Sec. 8.4. Furthermore, we observe in Fig. 8.4a that both η for finite $|\Delta_0|$ and its limit η_0 for infinite $|\Delta_0|$ increase monotonically with $|\kappa|T_s$. This monotonic increase with $|\kappa|T_s$ agrees with the discussion in Sec. 8.4. There, we explained that increasing $|\kappa|T_s$ enables larger ratios of $|\kappa|$ to the optimal bus-ring coupling rates γ_{1e} and γ_{2e} , reducing the energy dissipated in transferring energy from Ring 1 to Ring 2 during ring modulation.

We examine the convergence of η with respect to $|\Delta_0/\kappa|$. To do so, we evaluate the difference between η and its value in the limit of infinite inter-ring detuning, η_0 . We surmise that $(\eta_0 - \eta)$ scales approximately as a positive power of $|\kappa/\Delta_0|$ for sufficiently large $|\Delta_0/\kappa|$. To test this hypothesis, we plot the logarithm of $(\eta_0 - \eta)$ against that of $|\Delta_0/\kappa|$ for $\gamma_0 T_s = 0$ and different values of $|\kappa|T_s$ in Fig. 8.4b. From this figure, we observe that the relation between $\log_{10}(\eta_0 - \eta)$ and $\log_{10}|\Delta_0/\kappa|$ is approximately linear, with negative slope, for all values of $|\kappa|T_s$. This implies that $(\eta_0 - \eta)$ is indeed approximately proportional to a positive power of $|\kappa/\Delta_0|$, for large $|\Delta_0/\kappa|$. We note that the curves in Fig. 8.4b all have approximately the same slope, which implies $(\eta_0 - \eta)$ is approximately proportional to the same power of $|\kappa/\Delta_0|$, for all considered values of $|\kappa|T_s$.

Next, we analyze the convergence of η with respect to $|\Delta_0/\kappa|$ for different values of $\gamma_0 T_s$ and constant $|\kappa|T_s$. Thus, in analogy to Fig. 8.4a, we plot η and its limit η_0 as a function of $|\Delta_0/\kappa|$ for different values of $\gamma_0 T_s$ and large, fixed $|\kappa|T_s$, specifically, $|\kappa|T_s = 10$. The result is shown in Fig. 8.4c. The qualitative behavior of η in Fig. 8.4c is similar to that in Fig. 8.4a. Explicitly, η grows monotonically with $|\Delta_0/\kappa|$, converging to η_0 from below for each value of $\gamma_0 T_s$. As expected, as $\gamma_0 T_s$ increases, both η and η_0 decrease, as then more energy is dissipated into the environment during the CAFC process. Again, we surmise there is a power law relating $(\eta_0 - \eta)$ to $|\Delta_0/\kappa|$ for sufficiently large $|\Delta_0/\kappa|$. To test this claim, we again plot $(\eta_0 - \eta)$ against $|\Delta_0/\kappa|$ in a logarithmic scale. The result is in Fig. 8.4d. As Fig. 8.4b, Fig. 8.4d confirms an approximate linear relation between the logarithms of $(\eta_0 - \eta)$ and $|\Delta_0/\kappa|$ and thus a power law between them, now for all considered values of $\gamma_0 T_s$. Again, we note that the curves in the logarithmic plot of Fig. 8.4d have approximately the same slope. Hence, $(\eta_0 - \eta)$ is proportional to the same power of $|\Delta_0/\kappa|$, independently of $\gamma_0 T_s$.

Having confirmed numerically the existence of an approximate power law for $(\eta_0 - \eta)$ as a function of $|\Delta_0/\kappa|$, we next characterize it quantitatively. To do so, based on the observations of this section, we approximate η as a function of $|\Delta_0/\kappa|$ via

$$\eta \approx \eta_0 - k_1 \left| \frac{\kappa}{\Delta_0} \right|^{\alpha_1} \quad \text{for } |\Delta_0| \gg |\kappa|. \quad (8.28)$$

In Eq. (8.28), we introduce the convergence coefficient k_1 , and the convergence exponent α_1 . Because η depends on $|\Delta_0/\kappa|$, $|\kappa|T_s$, and $\gamma_0 T_s$, k_1 and α_1 generally depend on $|\kappa|T_s$ and $\gamma_0 T_s$. We then estimate k_1 and α_1 as functions of $|\kappa|T_s$ and $\gamma_0 T_s$. We estimate them via linear regression of $\log_{10}(\eta_0 - \eta)$ as a function of $\log_{10}|\Delta_0/\kappa|$ based on a least mean squares criterion, for different values of $|\kappa|T_s$ and $\gamma_0 T_s$.

In Figs. 8.4e and 8.4f, we show contour plots of the resulting estimates of k_1 and α_1 , respectively, as functions of $|\kappa|T_s$ and $\gamma_0 T_s$. In Fig. 8.4e, the convergence coefficient k_1 exhibits large relative change with these parameters, varying from 1 to 3. For small $|\kappa|T_s$ (less than 20), k_1 is approximately independent of $\gamma_0 T_s$. But as $|\kappa|T_s$ grows, k_1 increases and so does its susceptibility to $\gamma_0 T_s$. In contrast, the convergence exponent α_1 exhibits small relative change, in Fig. 8.4f varying from 1.85 to 1.93. In Fig. 8.4f, α_1 appears more sensitive to $|\kappa|T_s$ than to $\gamma_0 T_s$. Though the relative variation of α_1 with respect to $|\kappa|T_s$ is still appreciably small.

Next, we study the dependence of the value η_0 of the CAFC efficiency η in the limit of infinite inter-ring detuning $|\Delta_0|$. The limiting value η_0 itself depends on the dimensionless products $|\kappa|T_s$ and $\gamma_0 T_s$, converging to a finite maximum as $|\kappa|T_s \rightarrow \infty$, and $\gamma_0 T_s \rightarrow 0$. For simplicity of the subsequent analysis, we examine first the convergence of η_0 with respect to $|\kappa|T_s$, and then the convergence of the resulting limit with respect to $\gamma_0 T_s$. From Subsection 8.3.1, we recall that the limit η_0 is expressible as the product of three partial efficiencies $\eta_{j,j+1}$ ($j = 0, 1, 2$). Furthermore, the partial efficiency η_{23} (of the energy release from Ring 2 into the output bus) is independent of $|\kappa|T_s$ for our CAFC scheme. Thus, we need only consider the convergence of the partial efficiency $\eta_{02} = \eta_{01}\eta_{12}$ with respect to $|\kappa|T_s$ to analyze that of η_0 , i.e., the efficiency of the complete CAFC process.

Thus, we analyze numerically the convergence of η_{02} as $|\kappa|T_s$ diverges for several values of $\gamma_0 T_s$. To do this, we study the plots in Fig. 8.5. In Fig. 8.5a, in particular, we observe η_{02} converges with respect to $|\kappa|T_s$, similarly to

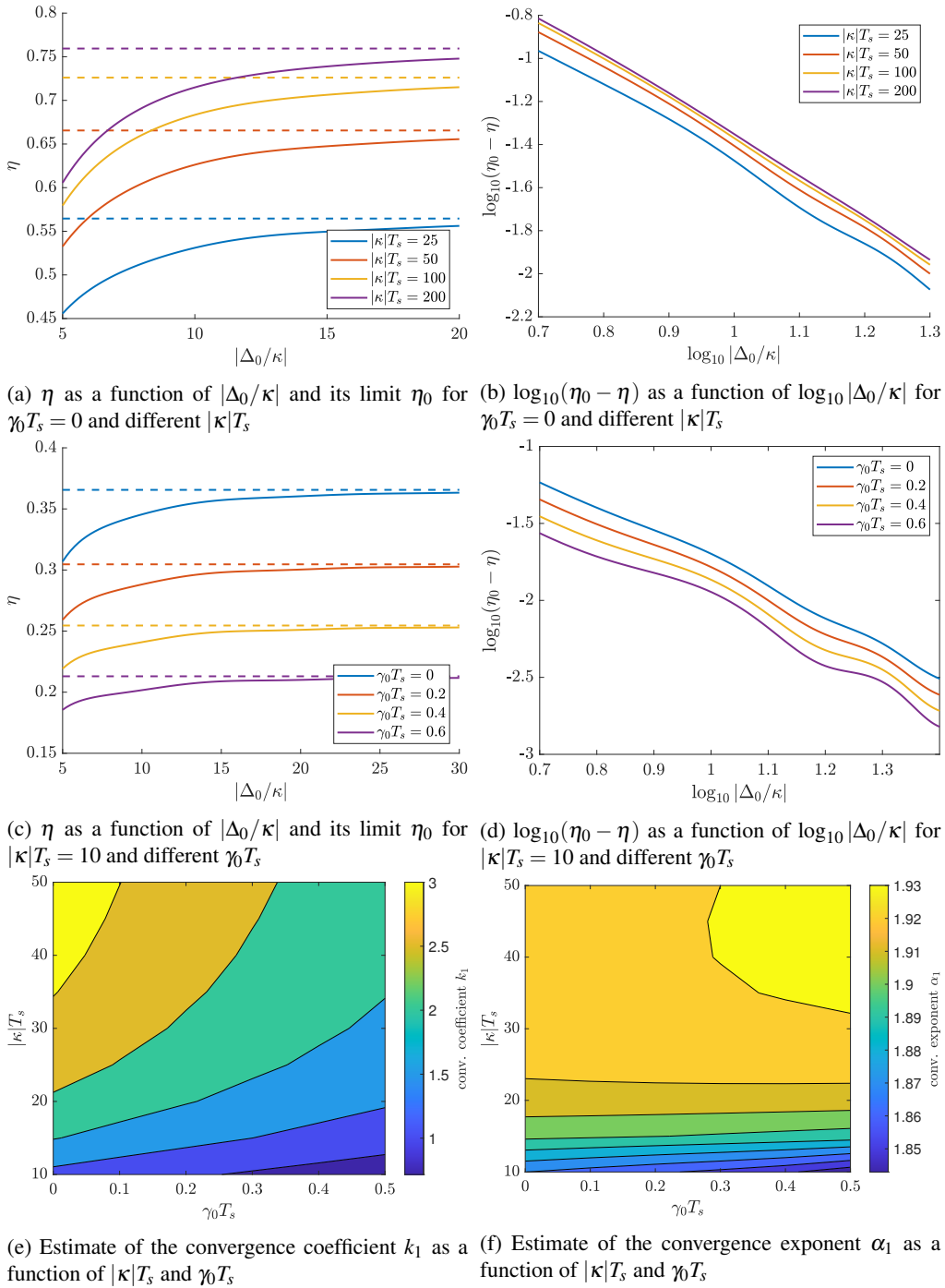


Figure 8.4: Numerical analysis of the rate of convergence of the CAFC efficiency η with respect to the normalized inter-ring detuning $|\Delta_0/\kappa|$ to its infinite-detuning value, η_0

how η converges with respect to $|\Delta_0/\kappa|$ in Figs. 8.4a and 8.4c. Explicitly, η_{02} increases monotonically with $|\kappa|T_s$, converging to a finite limit below unity, depending on the value of $\gamma_0 T_s$. In particular, we find that the limiting value of η_{02} for infinite $|\kappa|T_s$ equals the partial efficiency η_{01} , maximized over the input bus-Ring 1 coupling γ_{1e} and the modulation start time t_1 for the corresponding value of $\gamma_0 T_s$. This limiting value for η_{02} is intuitive. When $\gamma_0 T_s$ is small, and $|\kappa|$ is large compared to T_s^{-1} , $|\kappa|$ is large compared to γ_1 and γ_2 . Then the energy exchange between Ring 1 and Ring 2 is nearly lossless, so $\eta_{12} \approx 1$ and $\eta_{02} \approx \eta_{01}$.

As in our discussion of Fig. 8.4, we surmise that there might be a power law describing the convergence of η_{02} with respect to $|\kappa|T_s$ observed in Fig. 8.5a. To test this hypothesis, we consider the difference $(\eta_{01} - \eta_{02})$ between η_{02} and its limiting efficiency η_{01} and we again plot $\log_{10}(\eta_{01} - \eta_{02})$ against $\log_{10}(|\kappa|T_s)$ in Fig. 8.5b. Again, we confirm from Fig. 8.5b that the relation between these logarithms is approximately linear for all considered values of $\gamma_0 T_s$. Moreover, the relation between $(\eta_{01} - \eta_{02})$ and $|\kappa|T_s$ appears approximately equal for all values of $\gamma_0 T_s$. Thus, the most notable effect of $\gamma_0 T_s$ on η_{02} is to change η_{01} , i.e., its limit for infinite $|\kappa|T_s$.

Next, we leverage the apparent power law from Fig. 8.5b between $(\eta_{01} - \eta_{02})$ and $|\kappa|T_s$ to quantitatively characterize the rate of convergence of η_{02} with respect to $|\kappa|T_s$. Thus, we model the dependence of η_{02} on $|\kappa|T_s$ as

$$\eta_{02} \approx \eta_{01} - k_2 (|\kappa|T_s)^{-\alpha_2}, \quad \text{for } |\kappa| \gg T_s^{-1}, \quad (8.29)$$

for some convergence coefficient k_2 , and a convergence exponent α_2 . Because η_{02} is a function of $|\kappa|T_s$ and $\gamma_0 T_s$, k_2 and α_2 are functions of $\gamma_0 T_s$. As for k_1 and α_1 in Eq. (8.28), we estimate k_2 and α_2 through linear regression of $\log_{10}(\eta_{01} - \eta_{02})$ as a function of $\log_{10}(|\kappa|T_s)$ for different values of $\gamma_0 T_s$. The resulting estimates for k_2 and α_2 are shown in Fig. 8.5c. We confirm that both k_2 and α_2 exhibit small relative change for the considered values of $\gamma_0 T_s$, as expected from our discussion of Fig. 8.5b. The convergence coefficient k_2 goes from 4.95 at $\gamma_0 T_s = 0$ to 4.40 for $\gamma_0 T_s$. Conversely, the convergence exponent α_2 decreases from 0.946 at $\gamma_0 T_s = 0$ to 0.938 at $\gamma_0 T_s = 0.6$. Both parameters change approximately linearly with $\gamma_0 T_s$.

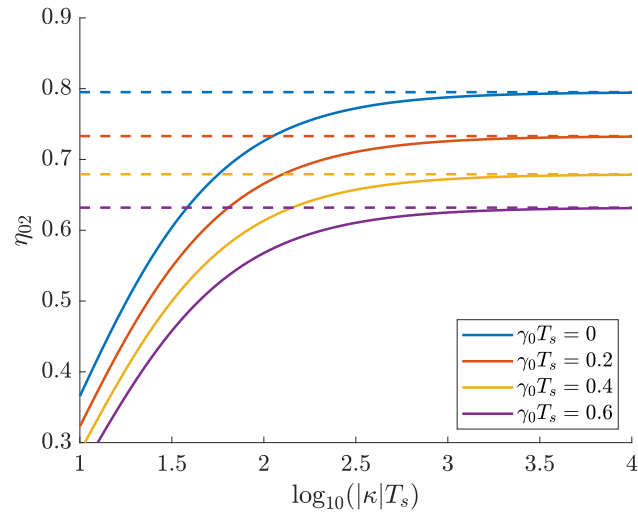
To complete our convergence analysis, we next examine how the partial efficiency η_{01} converges to its maximum as $\gamma_0 T_s$ tends to zero. As mentioned in this section, and as follows from Eq. (8.25) in Subsection 8.3.1, η_{01} is the efficiency with which the input pulse $s_{\text{in}}(t)$ in the input bus is loaded into Ring 1, isolated from Ring 2 due to the large inter-ring detuning. We recall that, for each value of $\gamma_0 T_s$, the input coupling γ_{1e} and the modulation time t_1 are chosen to maximize η_{01} . For $\gamma_0 = 0$, we have $\gamma_{1e} = \gamma_1$, and then η_{01} from Eq. (8.25) reduces to the squared modulus of the projection of $s_{\text{in}}(t)$ onto n_{in} (the time-reversed impulse response of Ring 1), normalized to the input energy $\langle s_{\text{in}}(t) | s_{\text{in}}(t) \rangle$. For $\gamma_0 = 0$, the loading efficiency η_{01} is then identical to the efficiency of single-ring AFC at time $t = t_1$ (also with vanishing intrinsic loss) [140]. In Ref. [140], we found that single-ring AFC efficiency for a raised-cosine input has a maximum of 0.7951 when the input-ring coupling γ_e equals $2.3780T_s^{-1}$, and modulation is induced at a time $0.2194T_s$ after the input's maximum. Hence, η_{01} has this same maximum of $\eta_{01}^{(0)} = 0.7951$ under the equivalent conditions $\gamma_{1e}T_s = 2.3780$ and $t_1 = 0.2194T_s$.

In Fig. 8.6, we analyze numerically the convergence of the partial efficiency η_{01} to its maximum with respect to $\gamma_0 T_s$. In this plot, we show η_{01} as a function of $\log_{10}(\gamma_0 T_s)$, along with its upper limit of $\eta_{01}^{(0)} = 0.7951$. We verify that η_{01} converges monotonically to $\eta_{01}^{(0)}$ as $\gamma_0 T_s$ decreases for $\log_{10}(\gamma_0 T_s) \leq -1$ ($\gamma_0 T_s \leq 0.1$). To characterize the rate of convergence, we also plot in Fig. 8.6 $\log_{10}(\eta_{01}^{(0)} - \eta_{01})$ as a function of $\log_{10}(\gamma_0 T_s)$. Again, we find that the relation between these logarithms is approximately linear. Hence, the convergence of η_{01} to $\eta_{01}^{(0)}$ is well described by a power law for sufficiently small $\gamma_0 T_s$. Then, in analogy to Eqs. (8.28) and (8.29), we approximate the dependence of η_{01} on $\gamma_0 T_s$ as

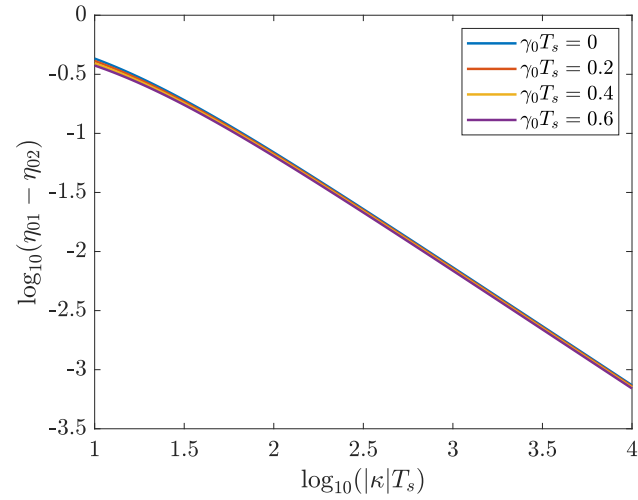
$$\eta_{01} \approx \eta_{01}^{(0)} - k_3 (\gamma_0 T_s)^{\alpha_3}, \quad \text{for } \gamma_0 \ll T_s^{-1}, \quad (8.30)$$

for some convergence coefficient k_3 and convergence exponent α_3 . Because η_{01} depends only on $\gamma_0 T_s$, k_3 and α_3 are constant dimensionless parameters. Applying linear regression to the numerical values in Fig. 8.6, we estimate $k_3 = 0.3259$ and $\alpha_3 = 0.9965$.

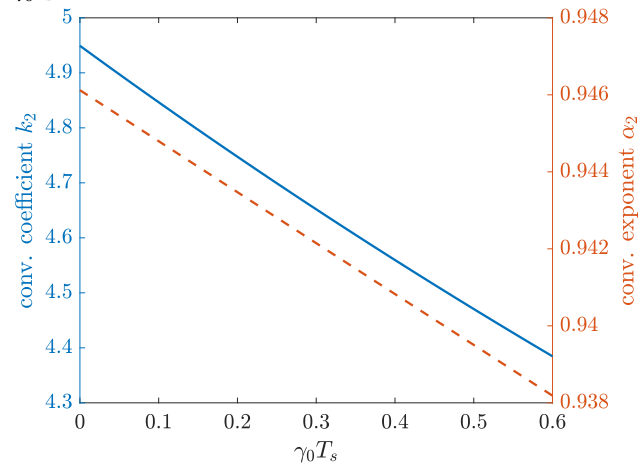
Throughout our numerical analysis of the rate of convergence of η with respect to the dimensionless smallness parameters $|\kappa/\Delta_0|$, $(|\kappa|T_s)^{-1}$, and $\gamma_0 T_s$, we identify four recurring features for sufficiently small values of these parameters. These are the following: convergence is always monotonically increasing; convergence is always well described by a power law; the convergence coefficient k_j ($j = 1, 2, 3$) may exhibit significant relative change with the remaining free TCMT parameters, but the convergence exponents α_j do not; and the convergence exponents α_j always take on values slightly smaller than specific integers (either 1 or 2). The fact that η or the corresponding partial efficiency



(a) η_{02} as a function of $\log_{10}(|\kappa|T_s)$ and its limit η_{01} for different $\gamma_0 T_s$



(b) $\log_{10}(\eta_{01} - \eta_{02})$ as a function of $\log_{10}(|\kappa|T_s)$ for different $\gamma_0 T_s$



(c) Estimates of the convergence coefficient k_2 and of the convergence exponent α_2 as functions of $\gamma_0 T_s$

Figure 8.5: Numerical analysis of the rate of convergence of the partial CAFC efficiency η_{02} with respect to the normalized inter-ring coupling $|\kappa|T_s$ to the partial efficiency η_{01}

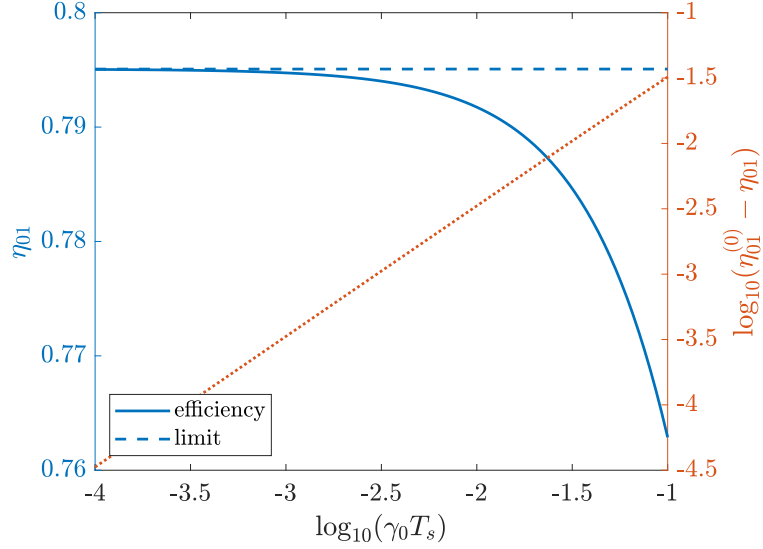


Figure 8.6: Numerical analysis of the rate of convergence of the partial CAFC efficiency η_{01} with respect to the normalized intrinsic loss $\gamma_0 T_s$ to its maximum $\eta_{01}^{(0)}$. Depicted are η_{01} (solid blue line), $\eta_{01}^{(0)}$ (dashed blue line), and $\log_{10}(\eta_{01}^{(0)} - \eta_{01})$ (dotted orange line).

converges monotonically for sufficiently small parameter values agrees with the discussion of Sec. 8.4. There, we provided intuitive, physical arguments explaining that we expect η to increase with increasing $|\Delta_0/\kappa|$, increasing $|\kappa|T_s$, and decreasing $\gamma_0 T_s$.

However, the other three observations are new results that cannot be predicted from our previous discussion of the CAFC efficiency η . We interpret these observations as indications that η for our scheme is a smooth function of the three smallness parameters: $|\kappa/\Delta_0|$, $(|\kappa|T_s)^{-1}$, and $\gamma_0 T_s$. Thus, for sufficiently small values of these parameters, η can be accurately approximated through a Taylor polynomial in the smallness parameters, and then this polynomial dependence dominates the variation of η . In this case, for a given smallness parameter, the corresponding convergence coefficient k_j approximates the coefficient of the Taylor polynomial's lowest-order non-vanishing term; and the corresponding convergence exponent α_j , the order of this term. In Appendix G, we provide a mathematical argument explaining that the CAFC efficiency of our scheme always is a real analytic (and hence smooth) function of the three smallness parameters, if the input $s_{\text{in}}(t)$ is a complex analytic function of the TCMT parameters.

Given this interpretation of the convergence exponents α_j ($j = 1, 2, 3$) as polynomial-term orders, it is interesting to compare them to each other. From Figs. 8.4f and 8.5c, and the value of $\alpha_3 = 0.9965$, the closest integer to α_1 is 2, but the closest integer to α_2 and α_3 is 1. This implies the lowest-order term in the Taylor expansion of η with respect to $(|\kappa|T_s)^{-1}$ and $\gamma_0 T_s$ is of first order; but that with respect to $|\kappa/\Delta_0|$ is of second order. Hence, the implication is that the dependence of η on $|\kappa/\Delta_0|$ vanishes to first order. This result is not obvious from our analysis in the prior sections. But it is consistent with the fact that, for sufficiently large $|\Delta_0|$, Ω_0 varies quadratically with $|\kappa|$, as discussed in Appendix G. In Section 8.6, we note that this second-order dependence of η on $|\kappa/\Delta_0|$ modifies the scaling of both the maximum CAFC efficiency η and the conditions required to attain this maximum.

To close this section, we make a key observation from our convergence analysis. This is that the CAFC efficiency η and that of single-ring AFC share the same fundamental tight upper limit, $\eta_{01}^{(0)}$ of Eq. (8.30). In other words, the efficiencies of CAFC and single-ring AFC converge towards the same value as they become progressively ideal. This result follows because, in the limit of infinite inter-ring detuning $|\Delta_0|$, η converges to η_0 , as implied by Eq. (8.28). Then, in the limit of infinite normalized inter-ring coupling $|\kappa|T_s$, η_0 converges to $\eta_{01}\eta_{23}$, as implied by Eq. (8.29). Finally, in the limit of vanishing normalized intrinsic loss, η_{01} converges to $\eta_{01}^{(0)}$, as implied by Eq. (8.30), and η_{23} converges to unity (see Section F.3); so $\eta_{01}\eta_{23}$ converges to $\eta_{01}^{(0)}$. In summary,

$$\lim_{\substack{|\Delta_0/\kappa| \rightarrow \infty \\ |\kappa|T_s \rightarrow \infty \\ \gamma_0 T_s \rightarrow 0}} \eta = \eta_{01}^{(0)}. \quad (8.31)$$

As stated in the discussion of Fig. 8.6, $\eta_{01}^{(0)}$ is also the value of single-ring AFC in the limit of zero intrinsic loss, i.e., its fundamental tight upper bound.

Eq. (8.31) is a key result of this chapter. It implies that, for sufficiently small values of the smallness parameters $|\kappa/\Delta_0|$, $(|\kappa|T_s)^{-1}$, and $\gamma_0 T_s$, the efficiency η of CAFC and that of single-ring AFC can be made arbitrarily close. In particular, it implies that CAFC can be made more efficient than two instances of single-ring AFC in series, which can also induce the same frequency shift of Δ_0 by modulating each ring by $\Delta_0/2$, just as CAFC. To prove that CAFC can become more efficient than serial AFC, we note that in serial AFC, there exists a fundamental mismatch between the output of the first single-ring AFC and the ideal input for the second single-ring AFC. This is because the former is a truncated decaying exponential; and the latter, a truncated increasing exponential [140]. Thus, even for an ideal choice of parameters for the second ring, the second instance of single-ring AFC only attains an energy efficiency of $4e^{-2} \approx 0.5413$ (see Appendix H). Then, so long as the CAFC efficiency is smaller than single-ring AFC efficiency by no more than this factor of $4e^{-2}$, CAFC is more efficient than two instances of single-ring AFC in series.

Though we do not prove it numerically, this result also applies for N -ring CAFC with $N > 2$. In this case, η must still converge polynomially to η_0 of Subsection 8.3.1, as it is still a real-analytic function of the TCMT parameters. Then, the N -ring η_0 converges to $\eta_{01}^{(0)}$, as in Eq. (8.31). This is because the values of η_0 for two-ring CAFC and N -ring CAFC differ only via the partial efficiencies $\eta_{j,j+1}$ (for $j = 1, \dots, (N-1)$) of the additional stages of inter-ring energy exchange and these all converge to unity as $\gamma_0/|\kappa|$ tends to zero (see Sections 8.4 and F.2). Then, the N -ring CAFC efficiency can become arbitrarily close to $\eta_{01}^{(0)}$, the upper limit for single-ring AFC. Consequently, N -ring CAFC can be more efficient than N instances of single-ring AFC in series, which, at best, have a net efficiency of $\eta_{01}^{(0)}(4e^{-2})^{N-1}$.

8.6 Modeling of the CAFC efficiency as a polynomial function

In Section 8.5, we analyze how the CAFC efficiency η converges monotonically to a maximum as the three normalized smallness parameters $|\kappa/\Delta_0|$, $(|\kappa|T_s)^{-1}$, and $\gamma_0 T_s$ tend to zero. There, we show that the convergence with respect to these parameters is approximately polynomial for sufficiently small values of these parameters. Thus, in this section, we leverage the results of Section 8.5 to model the efficiency η of our scheme as a polynomial function of the smallness parameters. Then, we leverage this polynomial model to estimate optimal values of the few remaining free TCMT parameters and to predict scaling laws for these optimal values and for the associated rate of convergence of η .

In Appendix G, we argue that the CAFC efficiency η is a smooth function of the smallness parameters. Then, we utilize the smoothness of η to approximate it as a Taylor polynomial in these parameters. For simplicity, we consider for this section a fixed normalized intrinsic loss $\gamma_0 T_s$, but variable normalized inter-ring detuning $|\Delta_0/\kappa|$ and normalized inter-ring coupling $|\kappa|T_s$. In practice, this occurs in the case of a fixed intrinsic loss γ_0 and pulse duration T_s , but tunable inter-ring detuning $|\Delta_0|$ and inter-ring coupling $|\kappa|$.

Hence, to lowest order in each of the variable smallness parameters, we write

$$\eta \approx \eta_{01}\eta_{23} - c_1 \left| \frac{\kappa}{\Delta_0} \right|^2 - \frac{c_2}{|\kappa|T_s} \quad |\Delta_0| \gg |\kappa|, \quad |\kappa|T_s \gg 1. \quad (8.32)$$

We recall that η in Eq. (8.32) is the value of the CAFC efficiency when the constrained TCMT parameters (γ_{1e} , γ_{2e} , t_1 and t_2) are chosen according to our scheme of Section 8.4. $\eta_{j,j+1}$ ($j = 0, 1, 2$) are partial CAFC efficiencies in the limit of infinite $|\Delta_0|$, as described in Subsection 8.3.1. Explicitly, η_{01} is the partial efficiency of loading the input $s_{\text{in}}(t)$ into Ring 1, optimized over γ_{1e} and t_1 . Conversely, η_{23} is the partial efficiency of loading the frequency-shifted output from Ring 2 into the output bus. For our scheme, η_{23} is given in Sections 8.4 and F.5. In Eq. (8.32), c_1 and c_2 are positive constant coefficients of the order of unity. These coefficients are related, yet not identical, to the convergence coefficients k_1 and k_2 of Sec. 8.5, as we discuss below. Because η depends on the normalized intrinsic loss $\gamma_0 T_s$, so do the coefficients c_1 and c_2 . In Eq. (8.32), we take the lowest-order term in $|\kappa/\Delta_0|$ as quadratic, and the one in $(|\kappa|T_s)^{-1}$ as linear. As discussed in Appendix G, this choice is made so that the polynomial model reproduces the numerical results of Section 8.5's convergence analysis, where η converges approximately quadratically with $|\kappa/\Delta_0|$ and approximately linearly with $(|\kappa|T_s)^{-1}$. According to the discussion in Appendix G, Eq. (8.32) is accurate only if $|\Delta_0/\kappa| \gg 1$, and $|\kappa|T_s \gg 1$.

Of course, for Eq. (8.32) to be useful, we need concrete estimates for the values of $\eta_{01}\eta_{23}$, c_1 , and c_2 . As noted above, η , and thus $\eta_{01}\eta_{23}$, c_1 , and c_2 depend on $\gamma_0 T_s$. So we fix its value to $\gamma_0 T_s = 0.1$ for the subsequent example

and the corresponding calculations. The product $\eta_{01}\eta_{23}$ is readily evaluated from the formulas in Subsection 8.3.1, yielding $\eta_{01}\eta_{23} = 0.7413$ for $\gamma_0 T_s = 0.1$. To estimate c_1 and c_2 , we evaluate Eq. (8.32) in the limits of infinite normalized inter-ring detuning $|\Delta_0/\kappa|$ and of infinite normalized inter-ring coupling $|\kappa|T_s$ as

$$\begin{aligned} \lim_{|\Delta_0/\kappa| \rightarrow \infty} \eta &\approx \eta_{01}\eta_{23} - \frac{c_2}{|\kappa|T_s}, \\ \lim_{|\kappa|T_s \rightarrow \infty} \eta &\approx \eta_{01}\eta_{23} - c_1 \left| \frac{\kappa}{\Delta_0} \right|^2. \end{aligned} \quad (8.33)$$

From Eqn. (8.33), c_1 (c_2) is the coefficient of convergence of η with respect to $|\Delta_0/\kappa|$ ($|\kappa|T_s$) in the limit of infinite $|\kappa|T_s$ ($|\Delta_0/\kappa|$). Then, we compare Eq. (8.33) to Eqs. (8.28) and (8.29), making the approximation $\alpha_1 = 2$ and $\alpha_2 = 1$. This is justified based on the closeness of the numerically estimated values of α_1 and α_2 to these integers, and on our argument in Sec. 8.5 that η must be a real-analytic function of the smallness parameters. In this way, we relate c_1 and c_2 of Eq. (8.32) to k_1 and k_2 of Eqs. (8.28) and (8.29) in Sec. 8.5 as

$$\begin{aligned} c_1(\gamma_0 T_s) &= \lim_{|\kappa|T_s \rightarrow \infty} k_1(|\kappa|T_s, \gamma_0 T_s), \\ c_2(\gamma_0 T_s) &= \eta_{23}(\gamma_0 T_s) k_2(\gamma_0 T_s). \end{aligned} \quad (8.34)$$

For clarity, in Eq. (8.34), we explicitly indicate that k_1 of Section 8.5 depends on both $|\kappa|T_s$ and $\gamma_0 T_s$, but the remaining quantities (including k_2) depend only on $\gamma_0 T_s$. Following Eq. (8.34), we immediately estimate c_2 from k_2 at $\gamma_0 T_s = 0.1$ of Sec. 8.5 as $c_2 = 4.7094$. In contrast, we lack an analytical formula to evaluate η in the limit of infinite $|\kappa|T_s$, but finite $|\Delta_0/\kappa|$. Thus, we estimate c_1 as the convergence coefficient k_1 for $\gamma_0 T_s = 0.1$, and the large, but finite, value of $|\kappa|T_s = 50$. In this way, we obtain $c_1 = 3.0050$.

Eq. (8.32) is useful due to its simple and explicit dependence on the smallness parameters $|\kappa/\Delta_0|$ and $(|\kappa|T_s)^{-1}$. This simplicity allows us to estimate optimal values of the remaining free TCMT parameters ($|\kappa|$ in this case of fixed $\gamma_0 T_s$), and predict scaling laws for these optimal values and their associated CAFC efficiency η . The objective of the remainder of this section is to showcase this utility.

First, we leverage Eq. (8.32) to estimate the optimal inter-ring coupling $|\kappa|$ which maximizes the CAFC efficiency η of our scheme and the corresponding maximum value. To do so, we need only extremize analytically the right-hand side of Eq. (8.32) with respect to $|\kappa|$, which is straightforward due to its simple polynomial dependence. In this way, we find that η is maximized with respect to $|\kappa|$ when

$$|\kappa| = \kappa_* \approx \left(\frac{c_2}{2c_1} \right)^{1/3} \frac{|\Delta_0|^{2/3}}{T_s^{1/3}}. \quad (8.35)$$

In Eq. (8.35), we introduce the critical inter-ring coupling κ_* . When Eq. (8.35) is satisfied, then Eq. (8.32) predicts η approximately equals

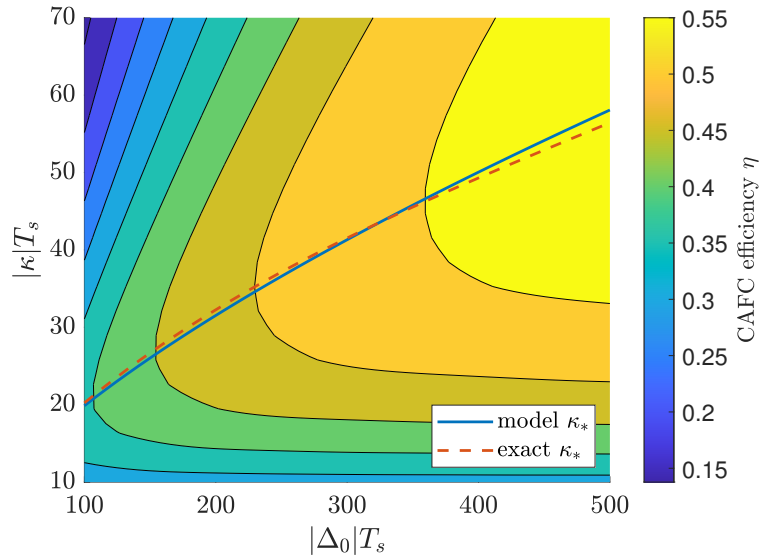
$$\eta \approx \eta_{01}\eta_{23} \left[1 - \left(\frac{\Delta_T}{|\Delta_0|} \right)^{2/3} \right]. \quad (8.36)$$

In Eq. (8.36), $\Delta_0 T$ is a threshold detuning, given by

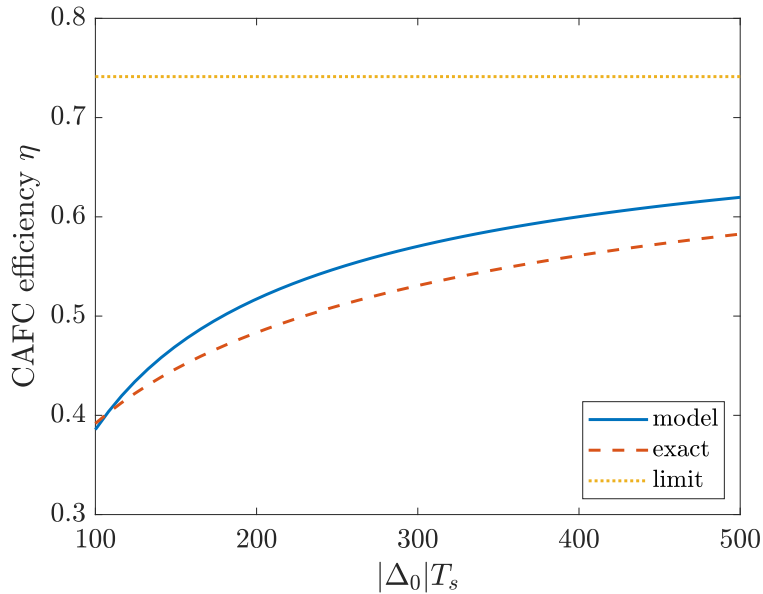
$$\Delta_T = \frac{3\sqrt{3}}{2} \frac{T_s^{-1} c_1^{1/2} c_2}{(\eta_{01}\eta_{23})^{3/2}}. \quad (8.37)$$

Of course, Eq. (8.36) is accurate only if $|\Delta_0| \gg \Delta_T$. Eqs. (8.36) and (8.37) predict that, as the product $|\Delta_0|T_s$ increases, then η (maximized with respect to $|\kappa|$) converges to its upper limit $\eta_{01}\eta_{23}$. This is because, as $|\Delta_0|T_s$ increases, the negative terms in Eq. (8.32) decrease after maximization with respect to $|\kappa|$.

Next, we validate the accuracy of the analytical estimates of Eqs. (8.35) and (8.36) by comparing them with numerical results in Fig. 8.7. First, in Fig. 8.7a we show a contour plot of η as a function of $|\Delta_0|T_s$ and $|\kappa|T_s$. In this contour plot, we also plot the analytical estimate for the optimal value $\kappa_* T$ of $|\kappa|T_s$ predicted by Eq. (8.35), and we compare it with the exact value of $\kappa_* T_s$, obtained via numerical optimization of η with respect to $|\kappa|T_s$. We verify that the analytical and numerical estimates for κ_* remain relatively close for all considered values of $|\Delta_0|T_s$. Furthermore, both the analytical and the numerical estimates for $\kappa_* T_s$ increase similarly with $|\Delta_0|T_s$, proportional to $(|\Delta_0|T_s)^{2/3}$, in agreement with Eq. (8.35).



(a) Contour plot of η as a function of $|\Delta_0|T_s$ and $|\kappa|T_s$. Also shown are estimates for the optimal value of $|\kappa|$, κ_* , obtained from Eq. (8.35) and from direct numerical optimization.



(b) Plot of the maximized CAFc efficiency η as a function of $|\Delta_0|T_s$, as estimated via the analytical model of Eq. (8.36) (solid blue line) and via numerical optimization (dashed orange line). Also depicted is the limit $\eta_{01}\eta_{23}$ of η for infinite $|\Delta_0|T_s$.

Figure 8.7: Comparison of the CAFc efficiency η for $\gamma_0 T_s = 0.1$ as estimated from the polynomial model of Eq. (8.32) and as obtained via numerical evaluation

Second, in Fig. 8.7b we plot as a function of $|\Delta_0|T_s$ both the analytical estimate from Eq. (8.36) and the numerical value for the maximum η after it is maximized with respect to $|\kappa|$. For comparison, we also show the value of η in the limit of infinite $|\Delta_0|T_s$, i.e., $\eta_{01}\eta_{23}$. Similarly to the behavior of κ_* in Fig. 8.7a, the analytical estimate for the maximized η accurately predicts the numerically exact value and its dependence on $|\Delta_0|T_s$ for all the considered values of $|\Delta_0|T_s$. Hence, we verify that the maximized η for a given value of $|\Delta_0|T_s$ converges to $\eta_{01}\eta_{23}$ approximately according to $(|\Delta_0|T_s)^{-2/3}$, as implied by Eqs. (8.36) and (8.37).

Having verified the accuracy of Eqs. (8.35) and (8.36), we next examine their predictions for the scaling of the optimal coupling ratio κ_* and the convergence rate of the optimized η , respectively. Eq (8.35) predicts the optimal inter-ring coupling κ_* scales as $|\Delta_0|^{2/3}/T_s^{1/3}$; and Eq. (8.36) predicts the maximized efficiency η converges to $\eta_{01}\eta_{23}$ at a rate proportional to $(|\Delta_0|T_s)^{2/3}$. These scaling behaviors are a direct consequence of Eq. (8.32); in particular, of the exponents therein for the smallness parameters $|\kappa/\Delta_0|$ and $(|\kappa|T_s)^{-1}$. Let us compare this to the hypothetical case where the term in Eq. (8.32) proportional to $|\kappa/\Delta_0|^2$ was instead directly proportional to $|\kappa/\Delta_0|$, i.e., to its first power, rather than the second. In this hypothetical case, it is straightforward to verify that κ_* would scale as $(|\Delta_0|T_s)^{1/2}$, and the maximized η would converge to $\eta_{01}\eta_{23}$ as $(|\Delta_0|T_s)^{-1/2}$. Then, the fact that η depends on $|\kappa/\Delta_0|$ only to second order in Eq. (8.32) qualitatively changes Eqs. (8.35) and (8.36). First, it causes the optimal κ_* to increase more rapidly with $|\Delta_0|$ and more slowly with T_s^{-1} . Second, and more importantly, it causes the maximized η to converge to $\eta_{01}\eta_{23}$ more quickly with $|\Delta_0|T_s$.

To highlight the significance of the scaling behavior of the maximized η with $|\Delta_0|T_s$, we provide a sample calculation. In Fig. 8.7b, we find that both the analytical and numerical estimates for the maximum η as a function of $|\Delta_0|T_s$ reach a value of approximately 0.6 for $|\Delta_0|T_s = 500$. We assume that the maximized η for fixed $|\Delta_0|T_s$ continues to converge to its maximum $\eta_{01}\eta_{23} = 0.7413$ for $\gamma_0 T_s = 0.1$ at a rate proportional to $(|\Delta_0|T_s)^{-2/3}$, as identified in the previous paragraph. Then, for instance, we immediately deduce from the scaling behavior that a product $|\Delta_0|T_s$ of the order of 3000 is required for η to reach a value of 0.70. Naturally, this assumption on convergence rate is expected to hold. This is because as $|\Delta_0|T_s$ increases, the concomitant optimal values of the smallness parameters $|\kappa/\Delta_0|$ and $(|\kappa|T_s)^{-1}$ decreases, and the polynomial model of κ Eq. (8.32) becomes more accurate, as indicated therein and following the discussion of Appendix G.

8.7 Conclusion

In this chapter, we proposed and analyzed the energy efficiency of a new photonic circuit and the corresponding modulation scheme for adiabatic frequency conversion (AFC). The circuit consists of a chain of coupled, yet initially detuned ring resonators, coupled at each of its ends to a bus waveguide. The scheme consists of injecting an optical pulse from a bus waveguide into the first ring of the chain; modulating the first pair of rings so they reach resonance and their energies undergo Rabi oscillation; and stopping ring modulation after the energy in the first ring is deposited into the second ring. Then the process is repeated between the second and third ring, and so on. This scheme then realizes cascaded AFC (CAFC), where the output pulse has a frequency shift of N times that applied to the resonance frequency of each ring, where N is the total number of rings in the chain. This CAFC scheme offers the advantage of inducing AFC multiple times in succession without the need to unload the optical pulse into a bus waveguide between modulations. For concreteness, we examined thoroughly the simplest non-trivial case of a chain of two rings, and briefly discuss the generalization to a chain of arbitrary number of rings.

In the chapter, we modeled the temporal dynamics of CAFC using temporal coupled mode theory (TCMT); and we proposed a scheme to optimize CAFC practically with respect to the process's timescales. To do so, we first presented the TCMT equations for CAFC and obtained their analytical solution for strong and fast temporal modulation. Then, we illustrated the CAFC scheme by discussing in detail a sample CAFC process of a symmetric, single-lobe optical pulse. We analyzed the transformation of the input pulse into the frequency-shifted output as a rank-one linear operator in the vector space of finite-energy pulses. In this way, we identified that the CAFC efficiency depends on the input pulse shape through a Schwarz inequality, just as in single-ring AFC. Then, we explained the numerical scheme we utilize to practically optimize CAFC process over its multiple timescales. We identified a tight upper bound for the CAFC efficiency under our scheme. We found that this upper bound is identical to that of single-ring AFC, specifically of 0.7951 for a symmetric, single-lobe input pulse. Consequently, we showed CAFC can become more energy efficient than multiple instances of single-ring AFC in series. We examined how the CAFC efficiency for our scheme converges to its theoretical upper bound as it becomes progressively idealized, as measured by three distinct timescale ratios. We

showed that this convergence is polynomial and explained this behavior based on the real-analyticity of the CAFC efficiency as a function of its timescales. We leveraged this polynomial convergence to model the CAFC efficiency of our scheme as a polynomial function of the remaining free TCMT parameters. We utilized this polynomial model to optimize our CAFC scheme with respect to the remaining free parameters and to predict its scaling with respect to inter-ring detuning post-optimization.

The CAFC scheme of this work represents then an energy-efficient strategy to extend the frequency shift induced by AFC beyond the limit imposed by the material platform. This broadens the utility of integrated AFC as an alternative for practical frequency-shifting of optical signals. This is of technological interest as AFC promises a route towards fully integrated, tunable frequency conversion in the optical regime.

Chapter 9

Conclusion and future work

This chapter presents the thesis's conclusions and directions for future work. The former are found in Section 9.1; and the latter, in Section 9.2.

9.1 Conclusion

Adiabatic frequency conversion (AFC) is the phenomenon in which light excites an optical cavity's resonant mode, the cavity's refractive index is modulated, and light follows the cavity's instantaneous resonance frequency. To realize electro-optical AFC, we proposed the material platform of lithium-niobate on insulator (LNOI), which enables high-quality, electro-optically tunable ring resonators. Thus, our objective was to analyze and optimize electro-optical AFC in LNOI ring resonators.

We analyzed the temporal dynamics of AFC using temporal coupled-mode theory (TCMT) and the polarization coupling in the resonant modes of LNOI rings using spatial coupled-mode theory (SCMT). Thus, we first derived and examined the equations governing spatial SCMT and TCMT from Maxwell's macroscopic equations and the constitutive relations. Most of this discussion of TCMT and SCMT consisted of review of previously published theory. However, we also provided an original derivation of the input-output description of coupling between a discrete resonant mode of a cavity and the continuum resonance modes of a waveguide. This derivation was useful, as we then generalized it to the case of temporally modulated resonances to model AFC.

Then, we utilized SCMT to study polarization coupling in a LNOI ring resonator, induced by lithium niobate's material birefringence. We show that the SCMT equations are isomorphic to the Schrödinger equation describing a two-level atom modulated sinusoidally in frequency and driven by a classical optical field. Thus, we examined polarization coupling along the ring using techniques popular in the context of two-level atoms under resonant optical excitation. In this manner, we identified and characterized three parameter regimes where the polarization-coupling dynamics are approximately integrable: a perturbative regime, a resonant regime, and an adiabatic regime. Then, we utilized this general SCMT formalism to examine the material system of interest to this thesis of a LNOI ring resonator.

Subsequently, we took a brief detour and we leveraged our SCMT-based polarization-coupling analysis to design a LNOI waveguide as a passive fundamental-mode polarization rotator. This polarization rotator consisted of an X-cut LNOI waveguide with a propagation axis at an oblique angle with the lithium niobate core's optic axis. We set this oblique angle so that the core's material anisotropy compensates for the waveguide's geometrical anisotropy and induces phase-matched polarization rotation. We discussed the rotator's ideal-device length, crosstalk, and bandwidth. We demonstrated that our proposed design can yield compact (shorter than 1 mm), low-loss, passive polarization rotators for telecom wavelengths.

Afterwards, we examined the optimization of AFC in ring resonators employing TCMT. First, we analyzed AFC in a single ring resonator coupled to a single bus waveguide. In particular, we studied comprehensively the energy efficiency of the AFC process. We demonstrated that this efficiency is proportional to the squared modulus of the inner product of two squared-integrable functions. The first is the input pulse. The second is the resonator's impulse response, reversed in time at the instant when index modulation is applied to induce AFC. Thus, we invoked Schwarz's inequality to show that the AFC efficiency increases with respect to the input pulse when its projection along the time-reversed impulse response increases. We discussed the AFC efficiency's dependence on the process's timescales for

a symmetric, single-lobe pulse of fixed shape. We showed that, for such a shape, the maximum AFC efficiency attainable is of 80%, limited by the mismatch between the input pulse shape, and the ideal input shape for 100% AFC efficiency. Furthermore, we demonstrated that maximum AFC efficiency requires overcoupling of the resonator to a degree dependent on the input pulse's duration. We compared and contrasted the requirements for optimal AFC for pulsed and continuous-wave inputs.

We proposed and analyzed inducing AFC simultaneously over two coupled rings to overcome the fundamental efficiency limit of 80% for a symmetric, single-lobe input pulse. We showed that simultaneous AFC over two rings can attain an energy efficiency of 97% in the limit of negligible intrinsic ring loss. To explain this higher AFC efficiency, we analyzed two-ring AFC as a linear operator of rank two in the vector space of finite-energy optical pulses. We represented this AFC operator as a 2×2 matrix using orthonormal representation theory. Then, we studied the matrix's (and hence, the operator's) singular value decomposition (SVD). We showed that this SVD governs the efficiency of AFC in the two-ring system. With this analysis, we explained the dependence of the two-ring AFC efficiency on the input pulse shape and the system's TCMT timescales.

Lastly, we proposed and examined a scheme to induce cascaded AFC (CAFC) along a chain of coupled, yet initially detuned rings, without unloading the optical signal into a bus waveguide between successive modulations. In this way, we accomplish multiple instances of AFC, without compromising the process's energy efficiency. For concreteness, we studied thoroughly the simplest non-trivial case of a chain of two rings, and briefly discussed the generalization to a chain of an arbitrary number of rings. We analyzed the transformation of the input into the frequency-shifted output as a rank-one linear operator in the vector space of finite-energy pulses. In this way, we showed that the energy efficiency of CAFC depends on the input pulse shape through a Schwarz inequality, just as in single-ring AFC. We proposed a numerical scheme to maximize the CAFC efficiency with respect to the process's timescales and explained the physics involved. We showed that the resulting CAFC efficiency converges in a polynomial manner to a maximum as the process becomes progressively idealized. Furthermore, we demonstrated that this maximum efficiency is identical to that for single-ring AFC, e.g., 80% for a symmetric, single-lobe input pulse. Thus, we showed that CAFC can become more efficient than multiple instances of single-ring AFC in series. We explained the polynomial convergence of the CAFC efficiency as a consequence of its real-analyticity as a function of the process's timescales under our scheme. We utilized this polynomial convergence to model the CAFC efficiency as a simple polynomial in few normalized timescales. We then leveraged this polynomial model to predict optimal values for the remaining free parameters, and the scaling of the CAFC with the inter-ring detuning.

9.2 Future work

In Sections 2.4 and 3.1, we showed that the propagation modes of a dielectric waveguide and the resonant modes of a dielectric resonator each obey an orthogonality relation when they are modes of a single, common waveguide or resonator, respectively. In practice, one might be interested in the coupling between modes of different waveguides or resonators when they are in proximity to each other, as in the design of directional waveguide couplers. In this case, it is desirable to approximate the modes of the system of waveguides (or resonators) as a coherent superposition of the modes of the waveguides (or resonators) which compose the system. This is because the modes of a single waveguide (or resonator) are usually easier to calculate either analytically or numerically. However, the modes of one waveguide (or resonator) are generally not orthogonal to those of another waveguide (or resonator). Thus, the modes of all waveguides (or resonators) generally constitute a non-orthogonal set. If one pursues a coupled-mode description of the system, it has been shown that this mode non-orthogonality leads to non-negligible effects such as crosstalk between waveguides [155, 156]. In general, the effect of mode non-orthogonality in coupled-mode theory has been investigated in spatial coupling between waveguides [53, 65, 157–162], and in temporal coupling between resonators [65]. Nonetheless, the effect of non-orthogonality in the temporal coupling between a resonator and a waveguide has not been studied. Thus, this could be the direction of future research.

To study this effect, we propose to model the waveguide in a coupled resonator-waveguide system as a dielectric resonator of finite length L as we did in Section 3.4. Then, we may model this system utilizing non-orthogonal TCMT between resonators of Ref. [65]. Afterwards, we may employ the continuum approximation of the non-orthogonal TCMT equations, as in Section 3.4, and modify the Weisskopf-Wigner analysis of Section 3.5 to obtain input-output relations which account for the non-orthogonality between the resonator and waveguide modes. In particular, it would be of interest to compare the predictions of orthogonal and non-orthogonal theories for the coupling rate between

waveguide and resonator and for the resonator mode's resonance frequency's shift due to coupling to the waveguide continuum.

In Chapter 4, we investigated the polarization dynamics in a ring resonator etched with a uniaxial core such as lithium niobate. We showed that significant polarization coupling can occur if the polarization dynamics lie in its resonant regime. Nonetheless, we only examined the ring resonator on isolation. To couple light into and out of it, we should consider its side-coupling to a bus waveguide. Then, it would be interesting to examine the polarization-transmission properties of the resulting waveguide-resonator system. An intriguing question to answer is whether the waveguide-coupled resonator can be used as a resonant polarization rotator. Heuristically, we would expect the polarization coupling to accumulate as light does multiple round trips along the resonator. Perhaps when light of resonant polarization and frequency impinges upon the resonator, the polarization rotation after each round trip can accumulate to yield a larger net polarization rotation. It would be of interest to investigate analytically and numerically this possibility. A possible issue to address in this system is the impact of the anisotropy of the directional coupling between resonator and waveguide [163].

In Chapter 5, we designed a LNOI waveguide as a polarization rotator, which converts transverse-electric (TE) light into transverse-magnetic (TM) light and viceversa. With this same design, but with half the waveguide length, the polarization rotator becomes a 3 dB polarization beamsplitter, which transforms either TE or TM light into a coherent superposition of the two modes, each with half of the incident power. Thus, one can construct a polarization Mach-Zehnder interferometer (MZI) using only LNOI waveguides. As any MZI, this polarization MZI would consist of three components in sequence: a first 3 dB beamsplitter, a relative phase difference between the two paths, and second 3 dB beamsplitter. Both 3 dB beamsplitters would be realized as these oblique, polarization-rotating LNOI waveguides. The relative phase-difference component would then be a LNOI waveguide oriented parallel (or perpendicular) to lithium niobate's optical axis. The phase-difference itself would be provided by the difference in effective indices of each polarization mode. Furthermore, this polarization MZI could be made electrically tunable by modulating the core of the parallel waveguide electro-optically. Thus, the resulting device would be an electrically-tunable polarization MZI, where the output polarization can be tuned between fully TE and fully TM.

In Chapters 6 to 8, we analyzed the efficiency of three schemes for AFC in optical resonators. In Chapter 6, we proved that, for single-ring AFC, the AFC efficiency is maximized with respect to the input pulse when the latter equals the resonator's time-reversed impulse response. Then, in Chapter 7, we proved that simultaneous AFC in coupled resonators, the AFC efficiency is maximized with respect to the input pulse when it is a linear combination of the rings' impulse responses. We explained that this results agree with the matched-filter principle [51, 52], known in the context of signal analysis.

In the absence of intrinsic resonator loss, we found that AFC in a single resonator and simultaneous AFC in coupled resonators can both achieve unit efficiency when the matched-filter principle is satisfied. This implies that all input energy is mapped to the frequency-shifted output. This implies that there is zero transmission before the resonator system is modulated, even though there is non-zero power impinging on the resonant system. This phenomenon of zero transient transmission has been termed coherent virtual absorption [164, 165] and has recently attracted attention for efficient storage and release of radiation. In particular, the condition required for coherent virtual absorption in single-port resonators has been termed virtual critical coupling (VCC) [166, 167]. So far, VCC has only been proposed and achieved through the injection of exponentially increasing pulses which excite the complex-valued zeros of the transmission's transfer function, which are hard to engineer. However, our results from Chapter 7 suggest that, in a coupled-ring system, VCC does not necessarily require an exponentially increasing pulse, but it can be approximately satisfied with a symmetric, single-lobe pulse. Thus a possible direction for future research consists of studying whether VCC can be satisfied (and thus, coherent virtual absorption be observed) with symmetric, single-lobe pulses in coupled-resonator systems. This would be of interest to elucidate our results for efficient AFC of Chapters 6 to 8, and, more generally, to realize efficient storage and release of light in integrated photonic systems.

In Chapter 7, we proposed to induce AFC simultaneously over several coupled rings to increase the AFC efficiency. Then, in Chapter 8, we proposed to induce AFC in cascade over a chain of initially detuned rings to increase the net output frequency shift. Thus, a natural direction for future work is to design a scheme to induce AFC over a chain or coupled rings that combines both of these two approaches, and thus simultaneously accomplishes larger AFC efficiency and larger net frequency shift. A simple system which combines these approaches consists of a chain of four rings. In this chain, Rings 1 and 2 are initially at resonance with each other, and so are Rings 3 and 4. Meanwhile, Rings 2 and 3 are initially detuned. Ring 1 is coupled to the input bus waveguide, and Ring 4 to the output bus waveguide. The symmetric, single-lobe pulse input is efficiently loaded into Ring 2, as in the scheme of Chapter 7. Then, once Ring 2 is maximally excited, Ring 2 and Ring 3 are brought in resonance, until the energy in Ring 2 is

transferred to Ring 3. Then, Ring 3 is brought back to resonance with Ring 4, and the output is extracted via the output bus coupled to Ring 4. Though the scheme can be accomplished without Ring 4, the presence of Ring 4 causes the envelope of the output to be always continuous, as for simultaneous AFC in Chapter 7. Consequently, due to Riemann's lemma [52, 91], the resulting output spectrum decays more rapidly with increasing frequency magnitude. Thus, it is less adversely affected by subsequent dispersive phenomena like filtering and propagation in dispersive media.

Appendix A

Guided modes and coupling coefficients of the uniaxial slab

In Chapter 4, we aim to investigate via spatial coupled-mode theory (SCMT) the polarization dynamics along a microring etched with a uniaxial core like lithium niobate. To evaluate the parameters in the resulting SCMT equations, we require two set of calculations. First, we must obtain the mode profiles of the unperturbed uniaxial waveguide, i.e., with a constant permittivity dyadic along its propagation axis. This is the objective of Section A.1. Second, we must calculate the matrix elements of the perturbation operator inducing the polarization modulation and coupling. This is the objective of Section A.2. As explained in Chapter 4, we model the waveguide cross-section as a one-dimensional birefringent slab, rather than as fully two-dimensional. This allows us to retain the physics of the problem, while keeping the mathematical analysis tractable before utilizing commercial numerical software.

A.1 Guided modes along principal axes of the asymmetric birefringent slab

In this section we derive the mode profiles and eigenvalue equation for the guided modes of an asymmetric dielectric slab whose all three layers (the core, substrate, and cladding) are made with biaxial anisotropic materials. We restrict our attention to the simplified case where the principal axes of all three media are aligned with the direction of propagation (the z axis), the direction normal to the material interfaces (x), and the direction perpendicular to these two axes (y).

In this thesis, we only need consider uniaxial materials. The guided modes of uniaxial slabs can be found for an arbitrary orientation of the optic axis [95, 98]. However, restricting the optic-axis orientation to the x , y , or z direction greatly simplifies the form of the guided modes because then TE and TM modes are uncoupled and can be considered separately. We note in passing that the TE and TM modes can also be labeled as s and p polarization modes, respectively.

A.1.1 Transverse-electric modes

By definition, normal modes of electromagnetic propagation are time-harmonic solutions to Maxwell's equations where all fields $\mathbf{F}(\mathbf{x})$ have a spatial dependence of the form

$$\mathbf{F}(\mathbf{x}) = \mathbf{F}_0(x) \exp(i\beta z) \quad (\text{A.1})$$

for a yet-undetermined propagation constant β . As stated in the paragraphs above, z is the direction of propagation of the mode. x is the direction normal to the material interfaces. As is conventional, we have assumed no y -dependence.

Substituting the spatial dependence (A.1) into Maxwell's curl equations, and assuming the permittivity dyadic has principal values $\epsilon_x, \epsilon_y, \epsilon_z$ along the indicated principal axes, Maxwell's equations decouple into two sets: one for TE

and one for TM modes, just as in the isotropic case. The equations describing TE waves are

$$\begin{aligned} -i\beta E_y &= i\omega\mu_0 H_x, \\ \frac{dE_y}{dx} &= i\omega\mu_0 H_z, \\ i\beta H_x - \frac{dH_z}{dx} &= -i\omega\epsilon_0\epsilon_y E_y, \end{aligned} \quad (\text{A.2})$$

which, of course, can be used to derive the Helmholtz equation

$$\frac{d^2 E_y}{dx^2} + (k_0^2 \epsilon_y - \beta^2) E_y = 0. \quad (\text{A.3})$$

Note that Eq. (A.2) are the same set of equations as those for TE modes of an isotropic slab with index of refraction $n = \sqrt{\epsilon_y}$. Thus, the results of this subsection are identical to those of that well-known [168] problem and are included only to serve as a point of reference for the analysis of TM modes and to introduce notation used in Section A.2.

The boundary conditions at each interface are the continuity of E_y and H_z . From Eq. (A.2), the continuity of H_z is equivalent to continuity of dE_y/dx .

For the mode to be guided, it needs to decay towards zero as $|x| \rightarrow \infty$. This is compatible with Eq. (A.3) if it decays exponentially in the substrate and cladding. Furthermore, for the mode to satisfy the continuity of the transverse fields at the boundaries, it needs to be oscillate harmonically with x in the core. Hence, the transverse envelope $E_y(x)$ needs to be of the form

$$E_y(x) = \begin{cases} E_{y,0} \cos(\kappa_{s,f}x + \phi_s), & |x| < d, \\ E_{y,0} \cos(\kappa_{s,f}d + \phi_s) \exp[-\gamma_{s,c}(x-d)], & x > d, \\ E_{y,0} \cos(\kappa_{s,f}d - \phi_s) \exp[\gamma_{s,s}(x+d)], & x < -d, \end{cases} \quad (\text{A.4})$$

where d is the half-width of the slab. It immediately follows that the magnetic field envelopes $H_z(x)$ and $H_x(x)$ are given by

$$\begin{aligned} H_z(x) &= -\frac{i}{\omega\mu_0} \frac{dE_y}{dx}, \\ &= \begin{cases} i\kappa_{s,f}E_{y,0} \sin(\kappa_{s,f}x + \phi_s)/(\omega\mu_0), & |x| < d, \\ i\gamma_{s,c}E_{y,0} \cos(\kappa_{s,f}d + \phi_s) \exp[-\gamma_{s,c}(x-d)]/(\omega\mu_0), & x > d, \\ -i\gamma_{s,s}E_{y,0} \cos(\kappa_{s,f}d - \phi_s) \exp[\gamma_{s,s}(x+d)]/(\omega\mu_0), & x < -d, \end{cases} \end{aligned} \quad (\text{A.5})$$

and

$$H_x(x) = -\frac{\beta}{\omega\mu_0} E_y(x). \quad (\text{A.6})$$

So Eq. (A.4) satisfies the Helmholtz equation, Eq. (A.3), one imposes the dispersion relations

$$\begin{aligned} \kappa_{s,f} &= \sqrt{\epsilon_{f,y}k_0^2 - \beta^2}, \\ \gamma_{s,c} &= \sqrt{\beta^2 - \epsilon_{c,y}k_0^2}, \\ \gamma_{s,s} &= \sqrt{\beta^2 - \epsilon_{s,y}k_0^2}. \end{aligned} \quad (\text{A.7})$$

For the mode to actually be guided, all quantities in Eq. (A.7) need to be real. This bounds β as

$$\sqrt{\epsilon_{s,y}k_0} < \beta < \sqrt{\epsilon_{f,y}k_0}. \quad (\text{A.8})$$

As is conventional, we assume $\epsilon_{s,y} > \epsilon_{c,y}$ for concreteness.

Eq. (A.4) automatically ensures continuity of $E_y(x)$ at the boundaries. Imposing continuity of $H_z(x)$ yields the eigenvalue equations

$$\begin{aligned} \tan(\kappa_{s,f}d + \phi_s) &= \frac{\gamma_{s,c}}{\kappa_{s,f}}, \\ \tan(\kappa_{s,f}d - \phi_s) &= \frac{\gamma_{s,s}}{\kappa_{s,f}}, \end{aligned} \quad (\text{A.9})$$

which can be more conveniently rewritten as [168]

$$\begin{aligned}\kappa_{s,f}d &= \frac{1}{2}m\pi + \frac{1}{2}\arctan\left(\frac{\gamma_{s,c}}{\kappa_{s,f}}\right) + \frac{1}{2}\arctan\left(\frac{\gamma_{s,s}}{\kappa_{s,f}}\right), \\ \phi_s &= \frac{1}{2}m\pi + \frac{1}{2}\arctan\left(\frac{\gamma_{s,c}}{\kappa_{s,f}}\right) - \frac{1}{2}\arctan\left(\frac{\gamma_{s,s}}{\kappa_{s,f}}\right),\end{aligned}\quad (\text{A.10})$$

where $m = 0, 1, 2, \dots$ is the order of the guided mode.

As explained in Chapter 2, we find it useful for the development of spatial coupled mode theory to normalize the modes of structures with two-dimensional cross-sections so they carry unit power normal to z . For the case of modes with one transversal dimension, a more convenient requirement for them to carry unit power per unit length (along the uniform direction y). Imposing this condition to the mode profile of Eq. (A.4), fixes the amplitude $E_{y,0}$ to the value

$$E_{y,0} = \sqrt{\frac{2\omega\mu_0}{\beta d_s}}, \quad (\text{A.11})$$

where

$$d_s \equiv d + \frac{1}{2}\gamma_{s,c}^{-1} + \frac{1}{2}\gamma_{s,s}^{-1} \quad (\text{A.12})$$

For the numerical solution of the eigenvalue equations (A.10), it is more convenient to work with dimensionless variables. Define $\bar{\kappa}_{s,f} \equiv \kappa_{s,f}d$ and so on. Then, it is easy to verify that the eigenvalue problem is equivalent to the solution of the normalized set of equations

$$\begin{aligned}\bar{\kappa}_{s,f} &= \frac{1}{2}m\pi + \frac{1}{2}\arctan\left(\frac{\bar{\gamma}_{s,c}}{\bar{\kappa}_{s,f}}\right) + \frac{1}{2}\arctan\left(\frac{\bar{\gamma}_{s,s}}{\bar{\kappa}_{s,f}}\right), \\ V_s^2 &= \bar{\kappa}_{s,f}^2 + \bar{\gamma}_{s,s}^2, \\ V_s^2\delta_s &= \bar{\gamma}_{s,c}^2 - \bar{\gamma}_{s,s}^2,\end{aligned}\quad (\text{A.13})$$

where we introduced the normalized frequency V_s and the asymmetry parameter δ_s , defined through

$$\begin{aligned}V_s &\equiv k_0d\sqrt{\varepsilon_{f,y} - \varepsilon_{s,y}}, \\ \delta_s &\equiv \frac{\varepsilon_{s,y} - \varepsilon_{c,y}}{\varepsilon_{f,y} - \varepsilon_{s,y}}\end{aligned}\quad (\text{A.14})$$

Lastly, it can be shown [168] that, given V_s and δ_s , one may readily calculate the mode-index of the highest-order TE mode supported by the slab waveguide, M_s , using the formula

$$M_s = \text{floor}\left(\frac{2V_s - \arctan(\sqrt{\delta_s})}{\pi}\right). \quad (\text{A.15})$$

A.1.2 Transverse-magnetic modes

Next, we discuss the transverse-magnetic (TM) modes of the biaxial slab waveguide. From Maxwell's curl equations, we find that the equations governing them are

$$\begin{aligned}i\beta E_x - \frac{dE_z}{dx} &= i\omega\mu_0 H_y, \\ -i\beta H_y &= -i\omega\varepsilon_0\varepsilon_x E_x, \\ \frac{dH_y}{dx} &= -i\omega\varepsilon_0\varepsilon_z E_z.\end{aligned}\quad (\text{A.16})$$

As with the TE modes, Eq. (A.16) leads to a Helmholtz equation for the transverse field, H_y in this case. This is given by

$$\frac{d^2 H_y}{dx^2} + \left(k_0^2\varepsilon_z - \frac{\varepsilon_z}{\varepsilon_x}\beta^2\right)H_y = 0. \quad (\text{A.17})$$

The boundary conditions at each dielectric interface are the continuity of H_y and E_z . From Eq. (A.16), it follows that the latter is equivalent to the continuity of $\epsilon_z^{-1} dH_y/dx$.

As in the TE-mode analysis, we look for guided modes that satisfy the Helmholtz equation, Eq. (A.17). For these two requirements to be met simultaneously, the field must decay exponentially for $|x| \rightarrow \infty$. Furthermore, to satisfy the Helmholtz equation in the core and the boundary conditions at the dielectric interfaces, the fields must oscillate harmonically inside the core. Thus, $H_y(x)$ must be of the form

$$H_y(x) = \begin{cases} H_{y,0} \cos(\kappa_{p,f}x + \phi_p), & |x| < d, \\ H_{y,0} \cos(\kappa_{p,f}d + \phi_p) \exp[-\gamma_{p,c}(x-d)], & x > d, \\ H_{y,0} \cos(\kappa_{p,f}d - \phi_p) \exp[\gamma_{p,s}(x+d)], & x < -d. \end{cases} \quad (\text{A.18})$$

Again, d denotes the half-length of the core.

From Maxwell's equations, (A.16), it follows that the electric field components must be given by

$$E_z(x) = \frac{i}{\omega \epsilon_0 \epsilon_z} \frac{dH_y}{dx} = \begin{cases} -i\kappa_{p,f} H_{y,0} \sin(\kappa_{p,f}x + \phi_p) / (\omega \epsilon_0 \epsilon_{f,z}), & |x| < d, \\ -i\gamma_{p,c} H_{y,0} \cos(\kappa_{p,f}d + \phi_p) \exp[-\gamma_{p,c}(x-d)] / (\omega \epsilon_0 \epsilon_{c,z}), & x > d, \\ i\gamma_{p,s} H_{y,0} \cos(\kappa_{p,f}d - \phi_p) \exp[\gamma_{p,s}(x+d)] / (\omega \epsilon_0 \epsilon_{s,z}), & x < -d \end{cases} \quad (\text{A.19})$$

and

$$E_x(x) = \frac{\beta}{\omega \epsilon_0 \epsilon_x} H_y(x). \quad (\text{A.20})$$

To satisfy the Helmholtz equation, (A.17), the parameters $\kappa_{p,f}$, $\gamma_{p,c}$ and $\gamma_{p,s}$ must satisfy the dispersion relations

$$\begin{aligned} \kappa_{p,f} &= \sqrt{\epsilon_{f,z} k_0^2 - \epsilon_{f,z} \beta^2 / \epsilon_{f,x}}, \\ \gamma_{p,c} &= \sqrt{\epsilon_{c,z} \beta^2 / \epsilon_{c,x} - \epsilon_{c,z} k_0^2}, \\ \gamma_{p,s} &= \sqrt{\epsilon_{s,z} \beta^2 / \epsilon_{s,x} - \epsilon_{s,z} k_0^2}. \end{aligned} \quad (\text{A.21})$$

For the mode to be truly guided, all parameters in Eq. (A.21) must be real-valued. This restricts the propagation constant β to the interval

$$\sqrt{\epsilon_{c,x} k_0} < \beta < \sqrt{\epsilon_{f,x} k_0}. \quad (\text{A.22})$$

Eq. (A.18) automatically satisfies continuity of $H_y(x)$ at the material boundaries. Imposing continuity of $E_z(x)$ leads to the set of eigenvalue equations

$$\begin{aligned} \tan(\kappa_{p,f}d + \phi_p) &= \frac{\epsilon_{f,z} \gamma_{p,c}}{\epsilon_{c,z} \kappa_{p,f}}, \\ \tan(\kappa_{p,f}d - \phi_p) &= \frac{\epsilon_{f,z} \gamma_{p,s}}{\epsilon_{s,z} \kappa_{p,f}}, \end{aligned} \quad (\text{A.23})$$

which, similarly to Eq. (A.10), can be recast in the more convenient form

$$\begin{aligned} \kappa_{p,f}d &= \frac{1}{2}m\pi + \frac{1}{2} \arctan\left(\frac{\epsilon_{f,z} \gamma_{p,c}}{\epsilon_{c,z} \kappa_{p,f}}\right) + \frac{1}{2} \arctan\left(\frac{\epsilon_{f,z} \gamma_{p,s}}{\epsilon_{s,z} \kappa_{p,f}}\right), \\ \phi_p &= \frac{1}{2}m\pi + \frac{1}{2} \arctan\left(\frac{\epsilon_{f,z} \gamma_{p,c}}{\epsilon_{c,z} \kappa_{p,f}}\right) - \frac{1}{2} \arctan\left(\frac{\epsilon_{f,z} \gamma_{p,s}}{\epsilon_{s,z} \kappa_{p,f}}\right). \end{aligned} \quad (\text{A.24})$$

To ensure the mode carries unit power linear-density normal to z , we must have

$$H_{y,0} = \sqrt{\frac{2\omega \epsilon_0}{\beta d_p}}, \quad (\text{A.25})$$

where we have introduced the characteristic distance d_p , defined by

$$d_p := \frac{d}{\epsilon_{f,x}} + \frac{\epsilon_{c,z}}{2\gamma_{p,c}} \left[\left(\frac{\epsilon_{f,z}}{\epsilon_{f,x}} \right) \gamma_{p,c}^2 + \left(\frac{\epsilon_{c,z}}{\epsilon_{c,x}} \right) \kappa_{p,f}^2 \right] [(\epsilon_{f,z}\gamma_{p,c})^2 + (\epsilon_{c,z}\kappa_{p,f})^2]^{-1} \\ + \frac{\epsilon_{s,z}}{2\gamma_{p,s}} \left[\left(\frac{\epsilon_{f,z}}{\epsilon_{f,x}} \right) \gamma_{p,s}^2 + \left(\frac{\epsilon_{s,z}}{\epsilon_{s,x}} \right) \kappa_{p,f}^2 \right] [(\epsilon_{f,z}\gamma_{p,s})^2 + (\epsilon_{s,z}\kappa_{p,f})^2]^{-1}. \quad (\text{A.26})$$

For numerical evaluation, we again normalize the transversal variables as $\bar{\kappa}_{p,f} := \kappa_{p,f}d$ and so on. Then, in analogy to Eq. (A.13), we may pose the eigenvalue problem as finding solution to the set of simultaneous equations

$$\bar{\kappa}_{p,f} = \frac{1}{2}m\pi + \frac{1}{2} \arctan \left(\frac{\epsilon_{f,z}}{\epsilon_{c,z}} \frac{\bar{\gamma}_{p,c}}{\bar{\kappa}_{p,f}} \right) + \frac{1}{2} \arctan \left(\frac{\epsilon_{f,z}}{\epsilon_{s,z}} \frac{\bar{\gamma}_{p,s}}{\bar{\kappa}_{p,f}} \right), \\ V_p^2 = \frac{\epsilon_{f,x}}{\epsilon_{f,z}} \bar{\kappa}_{p,f}^2 + \frac{\epsilon_{s,x}}{\epsilon_{s,z}} \bar{\gamma}_{p,s}^2, \\ V_p^2 \delta_p = \frac{\epsilon_{c,x}}{\epsilon_{c,z}} \bar{\gamma}_{p,c}^2 - \frac{\epsilon_{s,x}}{\epsilon_{s,z}} \bar{\gamma}_{p,s}^2, \quad (\text{A.27})$$

where the normalized frequency V_p and the asymmetry parameter δ_p are now given by

$$V_p := k_0 d \sqrt{\epsilon_{f,x} - \epsilon_{s,x}}, \\ \delta_p := \frac{\epsilon_{s,x} - \epsilon_{c,x}}{\epsilon_{f,x} - \epsilon_{s,x}} \quad (\text{A.28})$$

As in the TE case, we may find a closed-form formula for M_p , the index of the highest-order TM mode supported by the birefringent slab. This is given by

$$M_p = \text{floor} \left(\frac{2V_p \sqrt{\epsilon_{f,z}/\epsilon_{f,x}} - \arctan(\sqrt{\delta_p \epsilon_{f,x} \epsilon_{f,z} / \epsilon_{c,x} \epsilon_{c,z}})}{\pi} \right). \quad (\text{A.29})$$

A.2 Matrix elements of perturbation for the uniaxial dielectric slab

In this section, we calculate the matrix elements of the perturbation operators $\hat{D}^{(n)}$ (defined in Chapter 2) for the modes of an asymmetric slab waveguide. There are two slab configurations of practical interest: the out-of-plane (OOP) slab homogeneous along the y axis and the in-plane (IP) slab homogeneous along the x axis.

Before considering these two configurations, we note that expressions for $\hat{D}^{(n)}$ contain spatial derivatives with respect to the generalized function $C(x, y)$, defined as unity inside the ring-waveguide cross-section and zero everywhere else in the xy -plane. To obtain formulas suitable for numerical computation, we recognize the spatial derivatives of $C(x, y)$ as generalized derivatives and evaluate them accordingly [69] (formally, by applying integration by parts). In this way, the matrix element of $\hat{D}^{(n)}$ for two states $|\psi_a\rangle$ and $|\psi_b\rangle$ can be written as

$$\langle \psi_a | \hat{D}^{(1)} | \psi_b \rangle = \frac{\omega \epsilon_0 \bar{\epsilon}}{4} \iint dx dy C(x, y) E_{xa}^* E_{xb}, \\ \langle \psi_a | \hat{D}^{(2)} | \psi_b \rangle = \frac{i}{4} \iint dx dy C(x, y) [\hat{\mathbf{z}} \cdot (\nabla_t \times \mathbf{H}_{ta}^*) E_{xb} - E_{xa}^* \hat{\mathbf{z}} \cdot (\nabla_t \times \mathbf{H}_{tb})], \\ \langle \psi_a | \hat{D}^{(3)} | \psi_b \rangle = \frac{1}{4\omega \epsilon_0 \bar{\epsilon}} \iint dx dy C(x, y) (\nabla_t \times \mathbf{H}_{ta}^*) \cdot (\nabla_t \times \mathbf{H}_{tb}). \quad (\text{A.30})$$

Eq. (A.30) is suitable for numerical evaluation as it contains no spatial derivatives of $C(x, y)$ inside the integrals. From the definition of $C(x, y)$, its presence in the integrands of Eq. (A.30) can now be ignored if the integrals are taken over only the ring-waveguide cross-section. The formulas in Eq. (A.30) have the additional benefit of making evident the Hermiticity of the perturbations $\hat{D}^{(n)}$.

As pointed out in Chapter 2, $\nabla_t \times \mathbf{H}_t$ is just the longitudinal part (z -component) of the curl of \mathbf{H} . So, if $|\psi_a\rangle$ and $|\psi_b\rangle$ are solutions to the Maxwell's equations for the unperturbed system, we may rewrite the last two matrix elements in Eq. (A.30) as

$$\begin{aligned}\langle \psi_a | \hat{D}^{(2)} | \psi_b \rangle &= -\frac{\omega}{4} \iint dx dy C(x, y) (D_{za}^* E_{xb} + E_{xa}^* D_{zb}), \\ \langle \psi_a | \hat{D}^{(3)} | \psi_b \rangle &= \frac{\omega}{4\epsilon_0 \bar{\epsilon}} \iint dx dy C(x, y) D_{za}^* D_{zb},\end{aligned}\tag{A.31}$$

where D_{za} (D_{zb}) is the longitudinal displacement field induced by the field $|\psi_a\rangle$ ($|\psi_b\rangle$) on the unperturbed medium. Note that the displacements D_z are determined from Maxwell's equations that the modes $|\psi\rangle$ satisfy. If $|\psi_a\rangle$ is a normal mode of the unperturbed dielectric waveguide, the permittivity that should be used to evaluate D_{za} would be the permittivity of the unperturbed waveguide.

A.2.1 Out-of-plane slab

By definition, the OOP slab is homogeneous along the y axis, normal to both the propagation direction and the optical axis. This homogeneity has three effects on the formulas in Eq. (A.30). First, $C(x, y)$ is now only a function of x , equal to unity if $|x| < d$. Second, the integrals in Eq. (A.30) over x and y become integrals over only x only. Third, spatial derivatives with respect to y vanish for all fields. Applying these observations, the integrals in Eq. (A.30) become

$$\begin{aligned}\langle \psi_a | \hat{D}^{(1)} | \psi_b \rangle &= \frac{\omega \epsilon_0 \bar{\epsilon}}{4} \int_{-d}^d dx E_{xa}^* E_{xb}, \\ \langle \psi_a | \hat{D}^{(2)} | \psi_b \rangle &= \frac{i}{4} \int_{-d}^d dx \left(\frac{dH_{ya}^*}{dx} E_{xb} - E_{xa}^* \frac{dH_{yb}}{dx} \right), \\ \langle \psi_a | \hat{D}^{(3)} | \psi_b \rangle &= \frac{1}{4\omega \epsilon_0 \bar{\epsilon}} \int_{-d}^d dx \frac{dH_{ya}^*}{dx} \frac{dH_{yb}}{dx}.\end{aligned}\tag{A.32}$$

Next, we apply Eq. (A.32) to the case where the state $|\psi\rangle$ correspond to the normal modes of the unperturbed waveguide, as described in Section A.1. Consider first the TE modes. for which both E_x and H_y vanish. Hence, all the integrands in Eq. (A.32) vanish and we find

$$\langle \beta_n | \hat{D}^{(m)} | \beta_{n'} \rangle = 0, \quad \text{if } n = s \text{ or } n' = s \text{ for any } m.\tag{A.33}$$

This makes physical sense because because the TE modes depend only on the principal value ϵ_y , which is unaltered by the rotation of the extraordinary axis in the xz -plan, for an OOP slab. This feature has been noted before in the literature [105].

Hence we only need to evaluate Eq. (A.32) for the diagonal matrix elements $\langle \beta_p | \Delta \hat{A}_n | \beta_p \rangle$ over the TM modes. In this case, $\langle \beta_p | \hat{D}^{(2)} | \beta_p \rangle$ vanishes because E_x and H_y are in-phase for all x , and the two terms in the integrand cancel each other out. Hence, out of the nine independent matrix elements $\langle \beta_l | \Delta \hat{A}_m | \beta_n \rangle$, only two can be non-zero for an OOP slab. Evaluating these with the mode-profile formulas of Section A.1, we obtain

$$\begin{aligned}\langle \beta_p | \hat{D}^{(1)} | \beta_p \rangle &= \frac{\beta_p \bar{\epsilon}}{2\epsilon_{fx}^2 \kappa_{pf} d_p} \left[\kappa_{pf} d + \frac{1}{2} \frac{\epsilon_{fz} \gamma_{pc} \epsilon_{cz} \kappa_{pf}}{(\epsilon_{cz} \kappa_{pf})^2 + (\epsilon_{fz} \gamma_{pc})^2} + \frac{1}{2} \frac{\epsilon_{fz} \gamma_{ps} \epsilon_{sz} \kappa_{pf}}{(\epsilon_{sz} \kappa_{pf})^2 + (\epsilon_{fz} \gamma_{ps})^2} \right], \\ \langle \beta_p | \hat{D}^{(3)} | \beta_p \rangle &= \frac{\kappa_{pf}}{2\bar{\epsilon} \beta_p d_p} \left[\kappa_{pf} d - \frac{1}{2} \frac{\epsilon_{fz} \gamma_{pc} \epsilon_{cz} \kappa_{pf}}{(\epsilon_{cz} \kappa_{pf})^2 + (\epsilon_{fz} \gamma_{pc})^2} - \frac{1}{2} \frac{\epsilon_{fz} \gamma_{ps} \epsilon_{sz} \kappa_{pf}}{(\epsilon_{sz} \kappa_{pf})^2 + (\epsilon_{fz} \gamma_{ps})^2} \right].\end{aligned}\tag{A.34}$$

A.2.2 In-plane slab

Next, we calculate the perturbation matrix elements for the IP slab. As for the OOP slab, the integrals to evaluate them simplify because there is a single relevant transverse direction. Thus, the expressions to evaluate become

$$\begin{aligned}\langle \psi_a | \hat{D}^{(1)} | \psi_b \rangle &= \frac{\omega \epsilon_0 \bar{\epsilon}}{4} \int_{-d}^d dy E_{xa}^* E_{xb}, \\ \langle \psi_a | \hat{D}^{(2)} | \psi_b \rangle &= \frac{i}{4} \int_{-d}^d dy \left(E_{xa}^* \frac{dH_{xb}}{dy} - \frac{dH_{xa}^*}{dy} E_{xb} \right), \\ \langle \psi_a | \hat{D}^{(3)} | \psi_b \rangle &= \frac{1}{4\omega \epsilon_0 \bar{\epsilon}} \int_{-d}^d dy \frac{dH_{xa}^*}{dy} \frac{dH_{xb}}{dy}.\end{aligned}\tag{A.35}$$

We wish to evaluate Eq. (A.35) using the mode-profiles obtained in Section A.1. However, the profiles there vary along the x axis and are homogeneous along the y axis. One might be tempted to just permute the x and y indices of the vector components in the formulas of Section A.1, but this changes the handedness of the coordinate system, so the resulting expressions no longer satisfy Maxwell's equations. Thus, we perform a 90° rotation of the coordinate axes because rotations do preserve handedness. Let (V'_x, V'_y) be the components in the new coordinate frame of the vector \mathbf{V} , with components (V_x, V_y) in our original coordinate frame. Because they are related through a 90° rotation, they are related by

$$V'_x = V_y, \quad V'_y = -V_x.\tag{A.36}$$

This coordinate transformation has the additional advantage that the y axis transforms to the x' axis with the same ordering. Thus, if substrate corresponded to negative y -coordinates and cladding to positive y -coordinates, they now correspond to negative and positive x' -coordinates, respectively.

Performing the coordinate rotation of Eq. (A.36), we find that the integrals in Eq. (A.35) transform as

$$\begin{aligned}\int_{-d}^d dy E_{xa}^* E_{xb} &= \int_{-d}^d dx' E'_{ya}{}^* E'_{yb}, \\ \int_{-d}^d dy \left(E_{xa}^* \frac{dH_{xb}}{dy} - \frac{dH_{xa}^*}{dy} E_{xb} \right) &= \int_{-d}^d dx' \left(E'_{ya}{}^* \frac{dH'_{yb}}{dx'} - \frac{dH'_{ya}{}^*}{dx'} E'_{yb} \right), \\ \int_{-d}^d dy \frac{dH_{xa}^*}{dy} \frac{dH_{xb}}{dy} &= \int_{-d}^d dx' \frac{dH'_{ya}{}^*}{dx'} \frac{dH'_{yb}}{dx'}.\end{aligned}\tag{A.37}$$

We can now evaluate the integrals in the right-hand sides of Eq. (A.37) using the mode-profiles of Section A.1.

From inspection of the field components in the integrands on the right side of Eq. (A.37), it is evident that only three of the nine independent matrix elements are non-vanishing, one for each perturbation operator $\hat{D}^{(n)}$. Substituting the mode-profiles of Section A.1, these non-vanishing elements are given by

$$\begin{aligned}\langle \beta_s | \hat{D}^{(1)} | \beta_s \rangle &= \frac{k_0^2 \bar{\epsilon}}{2\beta_s d_s} \left(d + \frac{1}{2} \frac{\gamma_{sc}}{\kappa_{sf}^2 + \gamma_{sc}^2} + \frac{1}{2} \frac{\gamma_{ss}}{\kappa_{sf}^2 + \gamma_{ss}^2} \right), \\ \langle \beta_s | \hat{D}^{(2)} | \beta_p \rangle &= -\frac{ik_0 \kappa_{pf} d_{ps}}{2\sqrt{\beta_s \beta_p} d_s d_p}, \\ \langle \beta_p | \hat{D}^{(3)} | \beta_p \rangle &= \frac{\kappa_{pf}}{2\bar{\epsilon} \beta_p d_p} \left[\kappa_{pf} d - \frac{1}{2} \frac{\epsilon_{fz} \gamma_{pc} \epsilon_{cz} \kappa_{pf}}{(\epsilon_{cz} \kappa_{pf})^2 + (\epsilon_{fz} \gamma_{pc})^2} - \frac{1}{2} \frac{\epsilon_{fz} \gamma_{ps} \epsilon_{sz} \kappa_{pf}}{(\epsilon_{sz} \kappa_{pf})^2 + (\epsilon_{fz} \gamma_{ps})^2} \right].\end{aligned}\tag{A.38}$$

From the Hermiticity of $\hat{D}^{(2)}$, $\langle \beta_p | \hat{D}^{(2)} | \beta_s \rangle$ is also non-vanishing and given by $\langle \beta_p | \hat{D}^{(2)} | \beta_s \rangle = \langle \beta_s | \hat{D}^{(2)} | \beta_p \rangle^*$.

In the matrix element $\langle \beta_s | \hat{D}^{(2)} | \beta_p \rangle$, we introduced the ‘‘interaction length’’ d_{ps} defined by the integral

$$d_{ps} \equiv \int_{-d}^d dx \sin(\kappa_{pf} x + \phi_p) \cos(\kappa_{sf} x + \phi_s).\tag{A.39}$$

This integral has two contributions,

$$d_{ps} = d_{ps}^{(+)} + d_{ps}^{(-)},\tag{A.40}$$

that are found to be

$$d_{ps}^{(+)} = (2K)^{-1} [\cos(Kd - \Phi) - \cos(Kd + \Phi)],$$

$$d_{ps}^{(-)} = \begin{cases} d \sin(\Delta\phi_{ps}), & \text{if } \kappa_{sf} = \kappa_{pf}, \\ (2\Delta\kappa_{ps})^{-1} [\cos(\Delta\kappa_{ps}d - \Delta\phi_{ps}) - \cos(\Delta\kappa_{ps}d + \Delta\phi_{ps})] & \text{if } \kappa_{sf} \neq \kappa_{pf}. \end{cases} \quad (\text{A.41})$$

where K , Φ , $\Delta\kappa_{ps}$ and $\Delta\phi_{ps}$ are abbreviations standing for

$$K \equiv \kappa_{sf} + \kappa_{pf}, \quad \Phi \equiv \phi_s + \phi_p,$$

$$\Delta\kappa_{ps} \equiv \kappa_{pf} - \kappa_{sf}, \quad \Delta\phi_{ps} \equiv \phi_p - \phi_s. \quad (\text{A.42})$$

Consider the particular case of a symmetric slab waveguide, for which the substrate and cladding are made of the same material. In this case, it follows from Eqs. (A.10) and (A.23) that $\phi_s = m_s\pi/2$ and $\phi_p = m_p\pi/2$ for integers m_s and m_p equal to the order of each mode. Of course, for the fundamental TE and TM modes, $\phi_s = \phi_p = 0$. In this case, the integral in Eq. (A.39) vanishes. Consequently, there is no coupling between the fundamental TE and TM modes of a symmetric IP slab within the accuracy of our coupled-mode formalism.

Appendix B

Quantum-inspired analyses of polarization coupling

As a consequence our power-preserving formulation of spatial coupled-mode theory (SCMT) in Chapter 2, our SCMT equations of polarization coupling are isomorphic to the Schrödinger equation of a system with two discrete quantum mechanical states. Thus, throughout Chapters 4 and 5, we leverage this isomorphism to approximately solve these SCMT equations using techniques popular in quantum mechanical time-dependent systems [21, 70, 110]. In this appendix, we collect some mathematical analyses we use to examine polarization coupling in Chapters 4 and 5 which employ techniques from quantum mechanics.

In Section B.1, we utilize the rotating-wave approximation [20, 21] to describe polarization coupling in an uniaxial ring in its resonant regime. In Section B.2, we evaluate the Berry phase [113] accumulated by the local guided modes of an uniaxial ring in its adiabatic regime. In Section B.3, we utilize time-dependent perturbation theory [21, 70] to approximate the polarization crosstalk acquired in a curved segment of a waveguide etched on a uniaxial film.

B.1 Resonant polarization coupling

In this section, we find an approximate expression for the unitary propagation operator $U(\phi, 0)$, as defined in Chapter 4, in the case of the in-plane uniaxial slab. As explained in the main text, the evolution of $U(\phi, 0)$ is governed by the Hamiltonian

$$H(\phi) = \frac{1}{2}(\Delta_0 + \Delta_1 \cos 2\phi) \sigma_1 + (\kappa \sin 2\phi) \sigma_3. \quad (\text{B.1})$$

Here, Δ_0 , Δ_1 , and κ are the real-valued polarization-coupling parameters, and σ_j ($j = 1, 2, 3$) are the Pauli matrices, as defined in Chapter 4.

As in the context of optical resonance [20], it proves useful to perform an unitary transformation on the polarization state $a(\phi)$ such that the σ_1 term vanishes in Eq. (B.1). This allows us to observe the effect of the coupling term (proportional to σ_3) in a “rotating frame,” while accounting for the evolution due to the phase-mismatch term proportional to σ_1 . This is accomplished through the transformation

$$\begin{aligned} a(\phi) &= \exp \left[i \frac{1}{2} \sigma_1 \int_0^\phi d\phi' (\Delta_0 + \Delta_1 \cos 2\phi') \right] a'(\phi), \\ &= \exp \left[i \frac{1}{2} \sigma_1 \left(\Delta_0 \phi + \frac{1}{2} \Delta_1 \sin 2\phi \right) \right] a'(\phi). \end{aligned} \quad (\text{B.2})$$

Now, we may substitute Eq. (B.2) into the coupled-mode equations for $a(\phi)$ (with Hamiltonian matrix $H(\phi)$). Additionally, we recall the Jacobi–Anger expansion [109]

$$\exp(iz \sin \theta) = \sum_{n=-\infty}^{\infty} J_n(z) \exp(in\theta), \quad (\text{B.3})$$

and take its derivative with respect to the variable z . Here $J_n(z)$ is the Bessel function of first kind and integer order n ,

evaluated at z . In this way, we find that $a'(\phi)$ evolves with a Hamiltonian matrix $H'(\phi)$ given by

$$\begin{aligned} H'(\phi) &= -i\kappa \sin(2\phi) \exp \left[-i \left(\Delta_0 \phi + \frac{1}{2} \Delta_1 \sin 2\phi \right) \right] \sigma_+ + \text{H. c.}, \\ &= \kappa \sum_n J'_n(\Delta_1/2) \exp[-i(\Delta_0 + 2n)\phi] \sigma_+ + \text{H. c.} \end{aligned} \quad (\text{B.4})$$

where $\sigma_{\pm} = (\sigma_2 \pm i\sigma_3)/2$ and H. c. stands for the Hermitian conjugate.

As discussed in the analysis of the perturbative regime of Chapter 4, we find again that the modulation due to nonzero Δ_1 of the level spacing Δ_0 leads to the emergence of an infinite series of resonance-terms in $H'(\phi)$. This has also been documented in the context of time-modulated quantum systems [108].

Next, generalizing the rotating-wave approximation (RWA) popular in optical resonance [20], we argue that when one of the terms in the infinite series on the right-hand-side of Eq. (B.4) is close to resonance (i.e., when $\Delta_0 + 2m \approx 0$ for some m), this term, and only this term, will exert an accumulative effect. If the coupling coefficient κ is small enough, only accumulative effects change the dynamics noticeably, so we may ignore all other terms in the Hamiltonian Eq. (B.4). This argument is valid only if the strength of the other terms is sufficiently small. Otherwise, the non-resonant terms in Eq. (B.4) will still alter the evolution of $a'(\phi)$ by rotating it sufficiently before it changes in phase, leading to effects such as Bloch-Siegert shifts [20, 108].

Hence we drop all terms from the infinite series for $H'(\phi)$ except for the term with slowest-varying phase. Explicitly, let m be the integer defined as

$$m \equiv -\text{round}(\Delta_0/2). \quad (\text{B.5})$$

Then our RWA consists of the approximation $H' \approx H'_{\text{RWA}}$, in the sense that they both induce the same dynamics, where

$$H'_{\text{RWA}}(\phi) \equiv \kappa J'_m(\Delta_1/2) [\cos(\delta_m \phi) \sigma_2 + \sin(\delta_m \phi) \sigma_3] \quad (\text{B.6})$$

and δ_m is the resonance detuning given by

$$\delta_m \equiv \Delta_0 + 2m. \quad (\text{B.7})$$

The main advantage of the RWA is that the dynamics governed by H'_{RWA} can be analytically integrated (contrary to those with the full Hamiltonian H'). To integrate the dynamics, we introduce one last change of variable, from $a'(\phi)$ to $a''(\phi)$ using

$$a'(\phi) = \exp \left(-i \frac{1}{2} \sigma_1 \delta_m \phi \right) a''(\phi). \quad (\text{B.8})$$

In the rotating-frame of $a''(\phi)$, the RWA Hamiltonian is given by

$$H''_{\text{RWA}} = \frac{1}{2} \delta_m \sigma_1 + \kappa J'_m(\Delta_1/2) \sigma_2. \quad (\text{B.9})$$

The effective Hamiltonian H''_{RWA} does not depend on the independent variable ϕ , so the differential equation for $a''(\phi)$ has constant coefficients and can be immediately integrated. Substituting the resulting expressions for $a''(\phi)$ and $a'(\phi)$ back into Eqs. (B.8) and (B.2) respectively, we get

$$a(\phi) \approx \exp \left[i \sigma_1 \left(-m\phi + \frac{1}{4} \Delta_1 \sin 2\phi \right) \right] \exp(i\phi H''_{\text{RWA}}) a(0), \quad (\text{B.10})$$

and correspondingly

$$U(\phi, 0) \approx \exp \left[i \sigma_1 \left(-m\phi + \frac{1}{4} \Delta_1 \sin 2\phi \right) \right] \exp(i\phi H''_{\text{RWA}}) \quad (\text{B.11})$$

as reported in Chapter 4.

B.1.1 Simplified case of constant detuning

Because of its simplicity, it is interesting to study the special case of constant detuning, i.e., $\Delta_1 = 0$. Mathematically, this simplification comes from the fact that each of the infinite sums in Eq. (B.4) reduce to a single term. This is a consequence of the recurrence relation $J'_n(z) = [J_{n-1}(z) - J_{n+1}(z)]/2$ and the property

$$J_m(0) = \begin{cases} 1, & \text{if } m = 0 \\ 0, & \text{if } m \neq 0, \end{cases} \quad (\text{B.12})$$

of the Bessel functions $J_n(z)$ of integer order [109]. In this case, only the terms with $n \pm 1$ may be non-zero, and we may reduce the formula for m , Eq. (B.5), to

$$m = -\text{sgn}(\Delta_0), \quad (\text{B.13})$$

where $\text{sgn}(x)$ is the signum function. Of course, the RWA is only accurate if $\Delta_0/2 \approx \pm 1$, since just the $n = \pm 1$ resonances persist.

Substituting Eqs. (B.12) and (B.13) into Eqs. (B.9) and (B.11), we find that, for $\Delta_1 = 0$, the RWA Hamiltonian H''_{RWA} and the resulting $U(\phi, 0)$ take the simplified forms

$$H''_{\text{RWA}} = \frac{1}{2} \text{sgn}(\Delta_0) [(|\Delta_0| - 2)\sigma_1 - \kappa\sigma_1]. \quad (\text{B.14})$$

and

$$U(\phi, 0) \approx \exp[i\sigma_1 \text{sgn}(\Delta_0)\phi] \exp(iH''_{\text{RWA}}\phi). \quad (\text{B.15})$$

Alternatively, Eqs. (B.14) and (B.15) can be obtained by evaluating separately the expression for Eq. (B.1) for constant detuning ($\Delta_1 = 0$) and directly applying the RWA to the polarization dynamics.

B.2 Berry phase for the in-plane slab ring

When the polarization state $a(\phi)$ starts as an eigenstate of $H(0)$ and undergoes adiabatic evolution, it follows the instantaneous eigenstate $a^{(\pm)}(\phi)$ and accumulates a phase. This phase is the sum of a dynamical phase and the geometrical phase $\gamma_{\pm}(\phi)$. In Chapter 4, we state that

$$\exp[i\gamma_{\pm}(\pi)] = \begin{cases} -1, & |\Delta_0| < |\Delta_1|, \\ +1, & |\Delta_0| > |\Delta_1|, \end{cases} \quad (\text{B.16})$$

and

$$\exp[i\gamma_{\pm}(2\pi)] = \exp[i2\gamma_{\pm}(\pi)] = 1, \quad \text{for } |\Delta_0| \neq |\Delta_1|. \quad (\text{B.17})$$

In Chapter 4, we mention this follows from Berry's analysis [113] of the geometrical phase of quantum-mechanical states evolving adiabatically in time under the Schrödinger equation. In this section, we provide the reasoning that supports these statements.

Berry's results for discrete quantum-mechanical systems are directly applicable to our problem because the polarization state $a(\phi)$ obeys a Schrödinger-like differential equation with Hamiltonian matrix $H(\phi)$ given by Eq. (B.1). Following Berry, we visualize that $H(\phi)$ changes with ϕ because it depends on scalar parameters h_l ($l = 1, 2, \dots$), which also vary with ϕ . If we arrange these h_l in a vector \mathbf{h} , we can write $H(\phi) = H[\mathbf{h}(\phi)]$. In our case, H is a 2×2 , Hermitian, traceless matrix, so we may take h_l as the expansion-coefficients for H in terms of the Pauli matrices, i.e.,

$$H[\mathbf{h}(\phi)] = \sum_{l=1}^3 h_l(\phi) \sigma_l = \begin{pmatrix} h_1(\phi) & h_2(\phi) - ih_3(\phi) \\ h_2(\phi) + ih_3(\phi) & -h_1(\phi) \end{pmatrix}. \quad (\text{B.18})$$

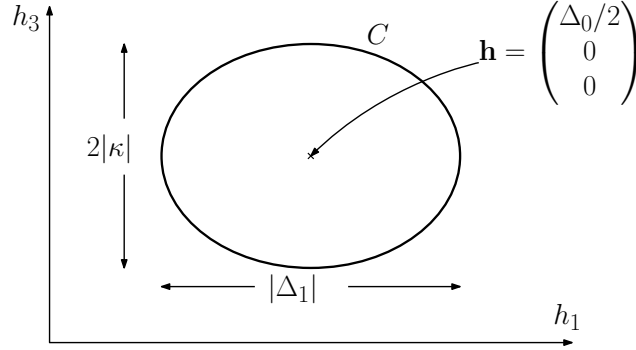
Comparing Eq. (B.18) with Eq. (B.1), it readily follows that

$$\begin{aligned} h_1(\phi) &= (\Delta_0 + \Delta_1 \cos 2\phi) / 2, \\ h_2(\phi) &= 0, \\ h_3(\phi) &= \kappa \sin 2\phi. \end{aligned} \quad (\text{B.19})$$

In his seminal paper [113], Berry analyzed the particular case when the parameters h_l , determining the Hamiltonian, trace a closed path C (or circuit) in the parameter space, causing the matrix H to return to its original value. For our problem, this occurs when $\phi = p\pi$, for integer p , as $H(p\pi) = H(0)$ in view of Eq. (B.1). Berry showed that, when the circuit C closes, the geometrical phase $\gamma(C)$ accumulated becomes independent of the local choice of phases for the eigenstates of $H[\mathbf{h}(\phi)]$.

For a two-state system, $\gamma(C)$ can be labeled with subindex \pm , as there are only two instantaneous eigenstates $a^{(\pm)}(\phi)$. Specifically if $H(\phi)$ is traceless, as in our case, Berry showed that $\gamma_{\pm}(C)$ becomes such that [113]

$$\exp[i\gamma_{\pm}(C)] = \exp[\mp i\Omega(C)/2]. \quad (\text{B.20})$$

Figure B.1: Parameter-space circuit C determining the Berry phase $\gamma_{\pm}(C)$

Here, $\Omega(C)$ is the solid angle that C subtends over the parameter-space origin, $\mathbf{h} = 0$ when the parameters h_l are chosen as the Pauli-matrix coefficients as in Eq. (B.18).

Given Eq. (B.20), we must then evaluate the solid angle $\Omega(C)$ projected by C over $\mathbf{h} = 0$ for our case. From Eq. (B.19), it is evident that C traces an ellipse in the $h_2 = 0$ plane of parameter space. This ellipse is centered at $\mathbf{h} = (\Delta_0/2, 0, 0)^T$ and has its principal axes along h_1 and h_3 . The length of each of these axes is given by $|\Delta_1|$ and $2|\kappa|$, respectively. For ease of visualization, C is depicted in Figure B.1.

Because C is confined to the $h_2 = 0$ plane, there are only two possible values $\Omega(C)$ can take (modulo 4π). If the circuit C encloses $\mathbf{h} = 0$, C projects a solid angle of $\Omega(C) = 2\pi$ over it. If $\mathbf{h} = 0$ lies outside of C , C projects then only as a line upon $\mathbf{h} = 0$, and thus projects a solid angle of zero, i.e., $\Omega(C) = 0$. Then, because $\Omega(C)$ is either 2π or 0 , $\exp[\mp i\Omega(C)/2]$ equals either -1 or $+1$. This special case of $\exp(i\gamma_{\pm}(C))$ being equal to either $+1$ or -1 because of C lying on a plane containing $\mathbf{h} = 0$ was explicitly studied in Berry's original manuscript [113].

The case where $\mathbf{h} = 0$ lies exactly on the circuit C (i.e., on the perimeter of an ellipse) does not need to be considered because the condition of adiabatic evolution is violated in that case. As mentioned in the main document, the adiabatic approximation requires the instantaneous level spacing $\Delta(\phi)$ to be large in comparison to the rate at which the Hamiltonian matrix $H(\phi)$ changes [70, 112]. This condition cannot be satisfied if $\mathbf{h} = 0$ lies on C because $\Delta(\phi)$ is proportional to the Euclidean norm of $\mathbf{h}(\phi)$.

From the geometry of C in Fig. B.1, it is then straightforward to see that C encloses the origin of the parameter space if and only if $|\Delta_0| < |\Delta_1|$. Similarly, the origin lies outside C if and only if $|\Delta_0| > |\Delta_1|$. Then, recalling that the ellipse C closes when $\phi = p\pi$ for integer p , we recover Eq. (B.16), as desired. To complete the discussion, we note that the adiabatic evolution from $\phi = 0$ to $\phi = 2\pi$ is equivalent to adiabatic evolution from $\phi = 0$ and $\phi = \pi$, followed by adiabatic evolution from $\phi = \pi$ to $\phi = 2\pi$. Therefore, $\exp[i\gamma_{\pm}(2\pi)] = \exp[i2\gamma_{\pm}(\pi)]$, as stated in Eq. (B.17).

B.3 Crosstalk due to polarization coupling along the curved joints

Consider the joints at the beginning and both ends of the tilted segment of the polarization rotator in Fig. 5.1. To minimize propagation losses, each consists of a circular arc of radius with a central angle equal to the tilt angle ϕ . In the polarization rotator design of Chapter 5, we assume these circular arcs are short enough so polarization coupling along them is negligible. Nonetheless, because of their finite size, polarization coupling does occur along them, resulting in a small fraction of power remaining in the original polarization, i.e., crosstalk. In this section, we derive a perturbative expression and bound for this crosstalk.

To do so, we first need a general relation between the propagation coordinate z (not to be confused with the crystallographic Z -axis of LN) and the local tilt angle χ of the waveguide, that accounts for the curved joints. The simplest relation of this sort is given by

$$\chi(z) = \begin{cases} (z - z_0)/r, & z_0 \leq z < z_1, \\ \phi, & z_1 \leq z < z_2, \\ (z_3 - z)/r, & z_2 \leq z \leq z_3, \end{cases} \quad (\text{B.21})$$

where r is the radius of curvature common to both joints and the discrete lengths points z_n are

$$z_0 = -r\phi, \quad z_1 = 0, \quad z_2 = L, \quad z_3 = L + r\phi, \quad (\text{B.22})$$

where, as in the main text, L and ϕ are the length and tilt angle of the oblique waveguide segment, respectively.

As stated in Section 5.2.3, we are mostly interested in the effect of nonzero bending radii, and not so much in the interference due to mismatch in their values. Hence, we take r as common to both joints in Eq. (B.21), for simplicity. It is straightforward to generalize the subsequent analysis to distinct bending radii.

Next, we consider the propagation matrix $U(z_3, z_0)$, defined as the 2×2 matrix relating the Jones vector $a(z_3)$ at the endpoint z_3 to $a(z_0)$ at the initial point z_0 . It is analogous to the time-evolution operator from quantum mechanics [70, 116]. Given its composition property [70], $U(z_3, z_0)$ can be evaluated as the product

$$U(z_3, z_0) = U(z_3, z_2)U(z_2, z_1)U(z_1, z_0). \quad (\text{B.23})$$

Next, we evaluate each propagation matrix in the right-hand side of Eq. (B.23) to find an explicit expression for the net propagation matrix $U(z_3, z_0)$.

We assume that the tilted segment is designed according to Sec. 5.1.2; i.e., with its tilt angle ϕ given by Eq. (5.6), and its length L given by Eq. (5.8). Then,

$$U(z_2, z_1) = \exp[iM(\phi)L] = i\text{sgn}(\kappa_{\text{eff}})\sigma_3 \quad (\text{B.24})$$

where $\text{sgn}(\cdot)$ is the signum function, and σ_n ($n = 1, 2, 3$) represent the Pauli matrices, defined as

$$\sigma_1 \equiv \begin{pmatrix} 1 & 0 \\ 0 & -1 \end{pmatrix}, \quad \sigma_2 \equiv \begin{pmatrix} 0 & 1 \\ 1 & 0 \end{pmatrix}, \quad \sigma_3 \equiv \begin{pmatrix} 0 & -i \\ i & 0 \end{pmatrix}. \quad (\text{B.25})$$

The Pauli matrices are labeled following optics convention [106, 116], so that the Stokes parameters S_n of the Jones vector a are given by $S_n = a^\dagger \sigma_n a$ ($n = 1-3$).

Next, we evaluate $U(z_1, z_0)$ and $U(z_3, z_2)$. They are solutions to the differential equation [116]

$$i \frac{d}{dz} U(z, z_n) = M[\chi(z)] U(z, z_n), \quad (n = 0, 2) \quad (\text{B.26})$$

for $z \in (z_n, z_{n+1})$, along with the initial condition

$$U(z_n, z_n) = I, \quad (\text{B.27})$$

where I is the 2×2 identity matrix.

Eqs. (B.26) and (B.27) do not admit general closed-form solutions, so we solve them approximately via perturbation theory. To do so, we express $M(\chi)$ as the sum of two parts: one modeling the χ -dependent effective-index detuning between the polarization modes, and one modeling the χ -dependent coupling strength. Thus, using the Pauli matrices σ_n , we write

$$M(\chi) = \frac{1}{2} \Delta(\chi) \sigma_1 + \kappa(\chi) \sigma_3. \quad (\text{B.28})$$

We assume

$$|\kappa_0|(z_{n+1} - z_n) \ll 1, \quad (n = 0, 2) \quad (\text{B.29})$$

so the second term in the right side of Eq. (B.28) makes only a perturbative contribution to the polarization dynamics along the curved joints. Then, the corresponding $U(z_{n+1}, z_n)$ matrices have a rapidly converging Dyson series in $\kappa(\chi)$ [70].

Thus, we truncate these series after their second term to obtain the approximations

$$U(z_{n+1}, z_n) \approx U^{(0)}(z_{n+1}, z_n) + U^{(1)}(z_{n+1}, z_n), \quad (n = 0, 2) \quad (\text{B.30})$$

where $U^{(0)}(z_{2n+1}, z_{2n})$ is the zeroth-order term

$$U^{(0)}(z_{n+1}, z_n) = \exp \left\{ \frac{1}{2} i \sigma_1 \int_{z_n}^{z_{n+1}} dz \Delta[\chi(z)] \right\}, \quad (\text{B.31})$$

and $U^{(1)}(z_{2n+1}, z_{2n})$ is the first-order correction

$$U^{(1)}(z_{n+1}, z_n) = i \int_{z_n}^{z_{n+1}} dz U^{(0)}(z_{n+1}, z) \kappa[\chi(z)] \sigma_3 U^{(0)}(z, z_n). \quad (\text{B.32})$$

We note that, although Condition (B.29) is sufficient for Eq. (B.30) to hold, it is not necessary, as the non-vanishing mismatch $\Delta(\chi)$ for $\chi \in (0, \phi)$ further inhibits coupling along the bends.

Given Eqs. (B.24) and (B.30) for the propagation matrices $U(z_{n+1}, z_n)$, we may directly evaluate Eq. (B.23) for $U(z_3, z_0)$ and thus the crosstalk X_r due to finite joint curvature. Let $a_s \equiv (1, 0)^T$, then one finds that X_r is given by

$$X_r = |a_s^\dagger U(z_3, z_0) a_s|^2 = 4r^2 \left| \int_0^\phi d\chi \kappa(\chi) \exp[i\theta_r(\chi)] \right|^2, \quad (\text{B.33})$$

where $\theta_r(\chi)$ is the accumulated phase-mismatch

$$\theta_r(\chi) \equiv r \int_0^\chi d\chi' \Delta(\chi'). \quad (\text{B.34})$$

Clearly, Eqs. (B.33) and (B.34) together are equivalent to Eq. (5.9).

Because of the dependence of $\theta_r(\chi)$ on r , the right-hand side of Eq. (B.33) is a transcendental function of r . For a given waveguide cross-section and bending radius, the right-hand side of Eq. (B.33) can be evaluated numerically for X_r . However, it is useful to have a simpler expression for a quick estimation of X_r . Such an expression can be obtained by noting that

$$\begin{aligned} \left| \int_0^\phi d\chi \kappa(\chi) \exp[i\theta_r(\chi)] \right| &\leq \text{sgn}(\phi) \int_0^\phi d\chi |\kappa(\chi) \exp[i\theta_r(\chi)]| \\ &= \text{sgn}(\phi) \int_0^\phi d\chi |\kappa(\chi)|. \end{aligned} \quad (\text{B.35})$$

The inequality in Eq. (B.35) is a well known property of complex-valued integrals [169]. Physically, the right-most side of Eq. (B.35) can be interpreted as the magnitude of the coupled amplitude to first-order perturbation, when phase-mismatch between the polarization modes is neglected.

To compute the integral in Eq. (B.35), we take ϕ to lie in either the first or fourth quadrant, so the bending segment spans the smallest possible arc. Then, combining Eqs. (B.33) and (B.35), we find the bound for X_r :

$$X_r \leq 4r^2 |\kappa_0|^2 \sin^4 \phi \quad (\text{B.36})$$

Evidently, Eq. (B.36) is equivalent to Eq. (5.10). As noted for Eq. (B.35), X_r approaches the right-hand side of Eq. (B.36) when the accumulated phase-mismatch $\theta_r(\chi)$ [Eq. (B.34)] is negligible (i.e., $|\theta_r(\chi)| \ll \pi$) for $\chi \in (0, \phi)$.

Appendix C

Mathematical expressions and analyses for the SVD of simultaneous AFC

In this appendix, we collect several mathematical expressions and analyses we utilize in Chapter 7 to evaluate and examine the singular value decomposition (SVD) of simultaneous adiabatic frequency conversion (AFC) of light over two coupled rings. In Section C.1, we study analytically the rings' impulse-response functions which govern the AFC efficiency. In Section C.2, we utilize the Gram-Schmidt orthonormalization process to obtain orthonormal bases for the image and coimage of two-ring AFC. In Section C.3, we examine analytically the SVD of the loading and unloading matrices. In Section C.4, we prove the submultiplicative property of the maximum and minimum singular values, used in Chapter 7 to relate the singular values of the net AFC operator with those of its constituent maps.

C.1 Characterization of the impulse-response functions

In this section, we examine analytically the impulse-response functions $u_{nm}(t, \Delta)$, defined by Eq. (7.17). Our objective is to describe their properties which are useful for our study of AFC. Specifically, we give explicit formulas to evaluate them in each inter-ring coupling regime; provide their initial values and those of their derivatives; characterize their continuity with respect to the TCMT parameters; examine their general behavior; and analyze their inner products and collinearity.

For succinctness, we first factorize these functions as

$$u_{nm}(t, \Delta) = \tilde{u}_{nm}(t) \exp[-i(\omega_0 + \Delta)t - \bar{\gamma}t] \Theta(t). \quad (\text{C.1})$$

Here, as in Eq. (7.6), ω_0 is the rings' original resonance frequency; $\Theta(t)$, the Heaviside step function; and $\bar{\gamma}$ the average ring decay rate

$$\bar{\gamma} = (\gamma_1 + \gamma_2)/2. \quad (\text{C.2})$$

The expressions for the factorized functions $\tilde{u}_{nm}(t)$ provided below can be obtained by solving the TCMT equations, Eq. (8.1), for constant $H(t)$ using the Laplace-transform method.

Similarly to a damped harmonic oscillator [145, 146], the inter-ring coupling (and thus, the impulse-response functions) can be underdamped, critically damped, or overdamped. Inter-ring coupling is underdamped when

$$|\kappa| > \gamma_e/2. \quad (\text{C.3})$$

In this case, the impulse-response functions exhibit oscillatory behavior and their expressions are given by

$$\begin{aligned} \tilde{u}_{11}(t) &= \cos(\Omega t/2) - (\gamma_e/\Omega) \sin(\Omega t/2), \\ \tilde{u}_{12}(t) &= (2i\kappa/\Omega) \sin(\Omega t/2), \\ \tilde{u}_{21}(t) &= (2i\kappa^*/\Omega) \sin(\Omega t/2), \\ \tilde{u}_{22}(t) &= \cos(\Omega t/2) + (\gamma_e/\Omega) \sin(\Omega t/2). \end{aligned} \quad (\text{C.4})$$

Here Ω is the frequency of energy exchange, analogous to the Rabi frequency in a quantum-mechanical two-level system. It is given by

$$\Omega = \sqrt{4|\kappa|^2 - \gamma_e^2}. \quad (\text{C.5})$$

Inter-ring coupling is critically damped when

$$|\kappa| = \gamma_e/2. \quad (\text{C.6})$$

In this case, the factor functions $\tilde{u}_{nm}(t)$ in Eq. (C.1) become affine functions of time, specifically

$$\begin{aligned} \tilde{u}_{11}(t) &= 1 - \gamma_e t/2, \\ \tilde{u}_{12}(t) &= i\kappa t, \\ \tilde{u}_{21}(t) &= i\kappa^* t, \\ \tilde{u}_{22}(t) &= 1 + \gamma_e t/2. \end{aligned} \quad (\text{C.7})$$

Inter-ring coupling is overdamped when

$$|\kappa| < \gamma_e/2. \quad (\text{C.8})$$

In this case, the factor functions $\tilde{u}_{nm}(t)$ become sums of hyperbolic functions of time; explicitly

$$\begin{aligned} \tilde{u}_{11}(t) &= \cosh(\xi t/2) - (\gamma_e/\xi) \sinh(\xi t/2), \\ \tilde{u}_{12}(t) &= (2i\kappa/\xi) \sinh(\xi t/2), \\ \tilde{u}_{21}(t) &= (2i\kappa^*/\xi) \sinh(\xi t/2), \\ \tilde{u}_{22}(t) &= \cosh(\xi t/2) + (\gamma_e/\xi) \sinh(\xi t/2). \end{aligned} \quad (\text{C.9})$$

Here, ξ is the positive rate

$$\xi = \sqrt{\gamma_e^2 - 4|\kappa|^2}. \quad (\text{C.10})$$

Regardless of the damping regime, the column vector $(u_{11}(t, \Delta), u_{21}(t, \Delta))^T$ ($(u_{12}(t, \Delta), u_{22}(t, \Delta))^T$) is a solution of the TCMT equations, i.e., Eq. (8.1), with $H(t) = H_m$, $s_+(t) = 0$ and initial condition $a(0) = (1, 0)^T$ ($a(0) = (0, 1)^T$). Consequently, they have the initial values

$$\begin{aligned} u_{11}(0) &= 1, & u_{12}(0) &= 0, \\ u_{21}(0) &= 0, & u_{22}(0) &= 1. \end{aligned} \quad (\text{C.11})$$

Additionally, the envelope functions $\bar{u}_{nm}(t) = u_{nm}(t, \Delta) \exp[i(\omega_0 + \Delta)t]$ have the initial values for their time derivatives given by

$$\begin{aligned} \frac{d\bar{u}_{11}(0)}{dt} &= -\gamma_1, & \frac{d\bar{u}_{12}(0)}{dt} &= i\kappa, \\ \frac{d\bar{u}_{21}(0)}{dt} &= i\kappa^*, & \frac{d\bar{u}_{22}(0)}{dt} &= -\gamma_2. \end{aligned} \quad (\text{C.12})$$

Although the expressions in Eqs. (C.4), (C.7), and (C.9) appear qualitatively different, they are continuous functions of the ring parameters (i.e., κ , γ_e and γ_0), even at the parameter transition between underdamped and overdamped coupling (i.e., in the neighborhood of Eq. (C.6)).

The behavior of the impulse-response functions $u_{nm}(t, \Delta)$ in the underdamped and critically damped regimes are straightforward to interpret. However, their behavior in the overdamped regime merits some discussion. Only the impulse-response functions $u_{11}(t, \Delta)$, $u_{12}(t, \Delta)$, and $u_{21}(t, \Delta)$ are relevant for our investigation of AFC. Furthermore, $u_{12}(t, \Delta)$ and $u_{21}(t, \Delta)$ are always proportional, so we only analyze $u_{11}(t, \Delta)$ and $u_{21}(t, \Delta)$. First, we consider the forms of these functions for large, positive values of t . Specifically, for $t \gg 2\xi^{-1}$, we may approximate the hyperbolic functions in Eq. (C.9) as $\sinh(x) \approx \cosh(x) \approx \exp(x)/2$. Then, to the accuracy of this approximation, the factor functions $\tilde{u}_{11}(t)$ and $\tilde{u}_{21}(t)$ become

$$\begin{aligned} \tilde{u}_{11}(t) &\approx \frac{1}{2} (1 - \gamma_e/\xi) \exp(\xi t/2), \\ \tilde{u}_{21}(t) &\approx (i\kappa^*/\xi) \exp(\xi t/2). \end{aligned} \quad (\text{C.13})$$

Consequently, for $t \gg 2\xi^{-1}$, $u_{11}(t)$ and $u_{21}(t)$ decay in magnitude as $\exp[-(\tilde{\gamma} - \xi/2)t]$. Moreover, we find that for large t , \bar{u}_{11} is always negative. This follows because the factor $(1 - \gamma_e/\xi)$ itself is negative as a consequence of the assumed overdamping condition, Eq. (C.8), and of the definition of ξ in Eq. (C.10).

We also point out that, in the overdamped regime, the envelopes $\bar{u}_{11}(t) = u_{11}(t, \Delta) \exp[i(\omega_0 + \Delta)t]$ and $\bar{u}_{21}(t) = u_{21}(t, \Delta) \exp[i(\omega_0 + \Delta)t]$ always have a single extremum each. In other words, for each envelope there exists one and only one positive time t such that $d\bar{u}_{1n}/dt = 0$ ($n = 1, 2$). We first prove this statement for $\bar{u}_{11}(t)$. By differentiation of Eq. (C.9), the condition $d\bar{u}_{11}/dt = 0$ in the overdamped regime is equivalent to

$$\tanh(\xi t/2) = \frac{\tilde{\gamma} + \gamma_e/2}{\gamma_e \tilde{\gamma}/\xi + \xi/2}. \quad (\text{C.14})$$

The left-hand side of Eq. (C.14) is a monotonically increasing function of t ; while its right-hand side is time-independent constant. Thus, there is, at most, one value of t for which the left-hand side of Eq. (C.14) equals its right-hand side. But $d\bar{u}_{11}/dt$ is negative when $t = 0$ and it converges to a positive value for $t \rightarrow \infty$, as can be seen from Eq. (C.13). So there must be at least one positive value of t for which $d\bar{u}_{11}/dt = 0$. Hence, there exists exactly one positive value of t for which $d\bar{u}_{11}/dt$ vanishes. By an analogous argument, we can prove that there is exactly one positive value of t for which $d\bar{u}_{21}/dt$ vanishes.

Next, we evaluate the inner products required for our AFC efficiency analysis in terms of the ring parameters. Given Eqs. (C.4), (C.7), and (C.9) for the factor functions $\bar{u}_{nm}(t)$, we next substitute them back into Eq. (C.1) and into the inner-product definition in Eq. (7.11). Then, employing elementary integration techniques, we obtain

$$\begin{aligned} \langle u_{11} | u_{11} \rangle &= \frac{\gamma_2(\gamma_1 + \gamma_2) + |\kappa|^2}{2(\gamma_1 + \gamma_2)(\gamma_1 \gamma_2 + |\kappa|^2)}, \\ \langle u_{11} | u_{12} \rangle &= \frac{i\kappa\gamma_2}{2(\gamma_1 + \gamma_2)(\gamma_1 \gamma_2 + |\kappa|^2)}, \\ \langle u_{12} | u_{12} \rangle &= \frac{|\kappa|^2}{2(\gamma_1 + \gamma_2)(\gamma_1 \gamma_2 + |\kappa|^2)}. \end{aligned} \quad (\text{C.15})$$

As in the Chapter 7, $\langle u_{nm} | u_{pq} \rangle$ is an abbreviation for $\langle u_{nm}(t, \Delta) | u_{pq}(t, \Delta) \rangle$. We note that, for our investigation of AFC, we only require the inner products of impulse-response functions $u_{nm}(t, \Delta)$ with equal frequency shift Δ . Because of the aforementioned continuity of the impulse-response functions with respect to the ring parameters, Eq. (C.15) holds regardless of the whether inter-ring coupling is underdamped, critically damped or overdamped.

As seen in Eqs. (C.4), (C.7), and (C.9), $u_{21}(t, \Delta)$ is always proportional to $u_{12}(t, \Delta)$. Therefore, we may evaluate the inner products of $u_{21}(t, \Delta)$ with other functions from those of $u_{12}(t, \Delta)$. In this way, we have

$$\begin{aligned} \langle u_{11} | u_{21} \rangle &= (\kappa^*/\kappa) \langle u_{11} | u_{12} \rangle, \\ \langle u_{21} | u_{21} \rangle &= \langle u_{12} | u_{12} \rangle. \end{aligned} \quad (\text{C.16})$$

In Eq. (C.16), we assume that $\kappa \neq 0$. Otherwise both $u_{12}(t, \Delta)$ and $u_{21}(t, \Delta)$ vanish, and so do their inner products with any function.

As a consequence of Eq. (C.15), for non-zero inter-ring coupling κ , $u_{11}(t, \Delta)$ and $u_{12}(t, \Delta)$ (and consequently $u_{11}(t, \Delta)$ and $u_{21}(t, \Delta)$) are mutually orthogonal if and only if $\gamma_2 = 0$. As a consequence of Eq. (7.4), $\gamma_2 = 0$ if and only if the intrinsic decay rate γ_0 vanishes. Furthermore, if $\gamma_0 = 0$, then Eq. (C.15) simplifies to

$$\begin{aligned} \langle u_{11} | u_{11} \rangle &= \frac{1}{2\gamma_1}, \\ \langle u_{11} | u_{12} \rangle &= 0, \\ \langle u_{12} | u_{12} \rangle &= \frac{1}{2\gamma_1}. \end{aligned} \quad (\text{C.17})$$

In Sections 7.4 and 7.5, we find it useful to introduce the effective cosine $\cos \theta_{12}$ in Eq. (7.48) as a normalized measure of the collinearity between $u_{11}(t, \Delta)$ and $u_{21}(t, \Delta)$. Here, we provide an explicit expression for it in terms of the ring parameters, we bound its value, and we investigate it in the limit of large intrinsic loss.

To obtain the expression for $\cos \theta_{12}$ in terms of the rings' TCMT parameters, we directly substitute the expressions for the inner products in Eq. (C.15) and (C.16) into the definition of Eq. (7.48). In this way we get

$$\cos^2 \theta_{12} = \frac{\gamma_2^2}{\gamma_2(\gamma_1 + \gamma_2) + |\kappa|^2}. \quad (\text{C.18})$$

As expected, $\cos \theta_{12} \in [0, 1]$. Furthermore, it increases monotonically with γ_2 for fixed γ_1 and $|\kappa|$, and with γ_0 for fixed γ_e and $|\kappa|$. Though it decreases with $|\kappa|$ for fixed γ_1 and γ_2 , or equivalently, fixed γ_0 and γ_e . This agrees with the behavior observed in Fig. 7.3.

Next, we utilize Eq. (C.18) to obtain an upper bound for $\cos \theta_{12}$ tighter than $\cos \theta_{12} \leq 1$, which follows from the Schwarz inequality. To do so, we first note that $\cos \theta_{12}$ is maximized with respect to $|\kappa|$ when $|\kappa| = 0$. Likewise, we note that $\cos \theta_{12}$ for $|\kappa| = 0$ is largest when $\gamma_e = 0$. In this way, we obtain

$$\cos^2 \theta_{12} \leq \frac{\gamma_2}{\gamma_1 + \gamma_2} = \frac{\gamma_0}{2\gamma_0 + \gamma_e} \leq \frac{1}{2}. \quad (\text{C.19})$$

Hence, we find that $\cos \theta_{12} \leq 1/\sqrt{2}$. Then, because Eq. (C.19) prohibits $\cos \theta_{12} = 1$, we conclude from the Schwarz inequality that $u_{11}(t, \Delta)$ and $u_{21}(t, \Delta)$ are never collinear, as then $\cos \theta_{12}$ would equal unity. This result is relevant because it implies that the AFC operator \hat{T} in a two-ring system always is of rank two.

Lastly, we note that it follows from Eq. (C.18) that

$$\lim_{\gamma_0 \rightarrow \infty} \cos \theta_{12} = 1/\sqrt{2}, \quad (\text{C.20})$$

assuming that, in this limit, γ_e and $|\kappa|$ remain finite. Combining Eqs. (C.19) and (C.20), we further conclude that $\cos \theta_{12}$ converges to $1/\sqrt{2}$ always from below in the limit $\gamma_0 \rightarrow \infty$.

C.2 Gram-Schmidt orthonormalization of AFC image and coimage

In this section, we use the Gram-Schmidt process [109, 135] to obtain orthonormal bases for both the image \mathcal{V}_{out} and the coimage \mathcal{V}_{in} of the AFC operator \hat{T} . Then, we use them to derive results useful to our discussion in Chapter 7. First, we find explicit expressions for the matrices M_{in} and M_{out} representing the maps \hat{T}_{in} and \hat{T}_{out} in these bases. Then, we obtain formulas for the projected input $|s_{\text{in}}^{(p)}(t)\rangle$ and its energy in terms of the ring amplitudes at the time of modulation and of the rings' parameters.

We first write expressions for the basis vectors $|n_1^{(\text{in})}\rangle$ and $|n_2^{(\text{in})}\rangle$ spanning \mathcal{V}_{in} . We recall from Section 7.3 that these are defined to satisfy the conditions in Eq. (7.38). These conditions uniquely determine $|n_1^{(\text{in})}\rangle$ and $|n_2^{(\text{in})}\rangle$ as

$$\begin{aligned} |n_2^{(\text{in})}\rangle &= \frac{|u_{21}^*(t_m - t, 0)\rangle}{\sqrt{\langle u_{21} | u_{21} \rangle}}, \\ |n_1^{(\text{in})}\rangle &= \frac{|N_1^{(\text{in})}\rangle}{\sqrt{\langle N_1^{(\text{in})} | N_1^{(\text{in})} \rangle}}, \end{aligned} \quad (\text{C.21})$$

where the auxiliary vector $|N_1^{(\text{in})}\rangle$ is defined as

$$\begin{aligned} |N_1^{(\text{in})}\rangle &= |u_{11}^*(t_m - t, 0)\rangle \\ &\quad - |u_{21}^*(t_m - t, 0)\rangle \frac{\langle u_{11} | u_{21} \rangle}{\langle u_{21} | u_{21} \rangle}. \end{aligned} \quad (\text{C.22})$$

From Eq. (C.22), it follows that the squared norm of $|N_1^{(\text{in})}\rangle$ is given by

$$\langle N_1^{(\text{in})} | N_1^{(\text{in})} \rangle = \langle u_{11} | u_{11} \rangle - \frac{|\langle u_{11} | u_{21} \rangle|^2}{\langle u_{21} | u_{21} \rangle} \quad (\text{C.23})$$

The inner products in Eqs. (C.21) to (C.23) can be evaluated in terms of the rings' TCMT parameters using Eqs. (C.15) and (C.16).

Note that in writing Eqs. (C.21) to (C.23), we repeatedly use the fact that

$$\langle f(t_m - t) | g(t_m - t) \rangle = \langle f(t) | g(t) \rangle \quad (\text{C.24})$$

for any real value of t_m ; as follows from the inner product definition, Eq. (7.11).

In an analogous way, we define the orthonormal basis vectors $|n_1^{(\text{out})}\rangle$ and $|n_2^{(\text{out})}\rangle$ spanning the image \mathcal{V}_{out} of \hat{T} . These are then given by

$$\begin{aligned} |n_2^{(\text{out})}\rangle &= \frac{|u_{12}(t - t_m, \Delta)\rangle}{\sqrt{\langle u_{12} | u_{12} \rangle}}, \\ |n_1^{(\text{out})}\rangle &= \frac{|N_1^{(\text{out})}\rangle}{\sqrt{\langle N_1^{(\text{out})} | N_1^{(\text{out})} \rangle}}, \end{aligned} \quad (\text{C.25})$$

with

$$\begin{aligned} |N_1^{(\text{out})}\rangle &= |u_{11}(t - t_m, \Delta)\rangle \\ &\quad - |u_{12}(t - t_m, \Delta)\rangle \frac{\langle u_{12} | u_{11} \rangle}{\langle u_{12} | u_{12} \rangle} \end{aligned} \quad (\text{C.26})$$

and

$$\langle N_1^{(\text{out})} | N_1^{(\text{out})} \rangle = \langle u_{11} | u_{11} \rangle - \frac{|\langle u_{11} | u_{12} \rangle|^2}{\langle u_{12} | u_{12} \rangle}. \quad (\text{C.27})$$

The inner products in Eqs. (C.25) to (C.27) can be evaluated in terms of the rings' TCMT parameters using Eq. (C.15).

With the explicit expressions for the orthonormal bases $\{|n_1^{(\text{in})}\rangle, |n_2^{(\text{in})}\rangle\}$ and $\{|n_1^{(\text{out})}\rangle, |n_2^{(\text{out})}\rangle\}$ in Eqs. (C.21) and (C.25), we may write corresponding expressions for the loading matrix M_{in} and the unloading matrix M_{out} . Substituting then Eqs. (C.21) and (C.25) into Eq. (7.40), we obtain

$$\begin{aligned} M_{\text{in}} &= \sqrt{2\gamma_e} \begin{pmatrix} \sqrt{\langle N_1^{(\text{in})} | N_1^{(\text{in})} \rangle} & \langle u_{21} | u_{11} \rangle / \sqrt{\langle u_{21} | u_{21} \rangle} \\ 0 & \sqrt{\langle u_{21} | u_{21} \rangle} \end{pmatrix}, \\ M_{\text{out}} &= \sqrt{2\gamma_e} \begin{pmatrix} \sqrt{\langle N_1^{(\text{out})} | N_1^{(\text{out})} \rangle} & 0 \\ \langle u_{12} | u_{11} \rangle / \sqrt{\langle u_{12} | u_{12} \rangle} & \sqrt{\langle u_{12} | u_{12} \rangle} \end{pmatrix}. \end{aligned} \quad (\text{C.28})$$

Next, we derive expressions for the projected input $|s_{\text{in}}^{(p)}(t)\rangle$ and its energy, $\langle s_{\text{in}}^{(p)}(t) | s_{\text{in}}^{(p)}(t) \rangle$ in terms of the rings' amplitude vector $a(t_m)$ at the time of modulation. To achieve this, we write the projector \hat{P}_{in} , introduced in Sec. 7.2, as [70]

$$\hat{P}_{\text{in}} = \sum_{j=1}^2 n_j^{(\text{in})} n_j^{(\text{in})}. \quad (\text{C.29})$$

Thus, we may write the projected input as

$$|s_{\text{in}}^{(p)}(t)\rangle = \sum_{j=1}^2 |n_j^{(\text{in})}\rangle \langle n_j^{(\text{in})} | s_{\text{in}}(t) \rangle, \quad (\text{C.30})$$

and its energy as

$$\langle s_{\text{in}}^{(p)}(t) | s_{\text{in}}^{(p)}(t) \rangle = \sum_{j=1}^2 |\langle n_j^{(\text{in})} | s_{\text{in}}(t) \rangle|^2. \quad (\text{C.31})$$

Given Eq. (C.21) for $|n_1^{(\text{in})}\rangle$ and $|n_2^{(\text{in})}\rangle$, we need only expressions for the inner products $\langle n_1^{(\text{in})} | s_{\text{in}}(t) \rangle$ and $\langle n_2^{(\text{in})} | s_{\text{in}}(t) \rangle$ to evaluate Eqs. (C.30) and (C.31). To do so, we recall from Eq. (7.18) that the ring amplitudes $a_j(t_m)$ may be written as

$$a_j(t_m) = \sqrt{2\gamma_e} \langle u_{j1}^* | s_{\text{in}}(t) \rangle \quad (\text{C.32})$$

for $j = 1, 2$. Then, we utilize the adjoint of Eq. (C.21) and Eq. (C.32) to obtain

$$\begin{aligned} \langle n_2^{(\text{in})} | s_{\text{in}}(t) \rangle &= \frac{a_2(t_m)}{\sqrt{2\gamma_e} \langle u_{21} | u_{21} \rangle}, \\ \langle n_1^{(\text{in})} | s_{\text{in}}(t) \rangle &= \frac{\langle N_1^{(\text{in})} | s_{\text{in}}(t) \rangle}{\sqrt{\langle N_1^{(\text{in})} | N_1^{(\text{in})} \rangle}}, \end{aligned} \quad (\text{C.33})$$

where $\langle N_1^{(\text{in})} | s_{\text{in}}(t) \rangle$ is evaluated through

$$\langle N_1^{(\text{in})} | s_{\text{in}}(t) \rangle = \frac{a_1(t_m)}{\sqrt{2\gamma_e}} - \frac{a_2(t_m) \langle u_{21} | u_{11} \rangle}{\sqrt{2\gamma_e} \langle u_{21} | u_{21} \rangle}. \quad (\text{C.34})$$

C.3 Partial analytical SVD of the loading and unloading matrices

In this section, we investigate analytically the SVD of the loading and unloading matrices, M_{in} and M_{out} . In particular, we derive the expressions for their singular values in Eqs. (7.51) and (7.52), and for the Bloch components $S_j^{(l)}(M_{\text{in}})$ and $S_j^{(r)}(M_{\text{out}})$; and we prove Eq. (7.60) relating the remaining Bloch components $S_j^{(r)}(M_{\text{in}})$ and $S_j^{(l)}(M_{\text{out}})$.

To start this analysis, we first define the auxiliary matrices

$$\begin{aligned} K_{\text{in}} &\equiv \hat{T}_{\text{in}} \hat{T}_{\text{in}}^\dagger = M_{\text{in}} M_{\text{in}}^\dagger, \\ &= 2\gamma_e \begin{pmatrix} \langle u_{11} | u_{11} \rangle & \langle u_{21} | u_{11} \rangle \\ \langle u_{11} | u_{21} \rangle & \langle u_{21} | u_{21} \rangle \end{pmatrix} \end{aligned} \quad (\text{C.35})$$

and

$$\begin{aligned} K_{\text{out}} &\equiv \hat{T}_{\text{out}}^\dagger \hat{T}_{\text{out}} = M_{\text{out}}^\dagger M_{\text{out}}, \\ &= 2\gamma_e \begin{pmatrix} \langle u_{11} | u_{11} \rangle & \langle u_{11} | u_{12} \rangle \\ \langle u_{12} | u_{11} \rangle & \langle u_{12} | u_{12} \rangle \end{pmatrix}. \end{aligned} \quad (\text{C.36})$$

By construction, the eigenvalues of K_{in} are the squared singular values of M_{in} , and its eigenvectors are the left singular vectors of M_{in} [143, 144]. Similarly, the eigenvalues of K_{out} are the squared singular values of M_{out} , and its eigenvectors are the right singular vectors of M_{out} .

Then, by finding the eigenvalues of K_{in} , we verify that the squared singular values of M_{in} are indeed given by Eq. (7.52). Moreover, finding the eigenvalues of K_{out} and recalling Eq. (C.16), we find that K_{in} and K_{out} have the same eigenvalues. Therefore, M_{in} and M_{out} have the same singular values, as stated in Eq. (7.51).

Next, we determine the Bloch components $S_j^{(l)}(M_{\text{in}})$ and $S_j^{(r)}(M_{\text{out}})$ of the left singular vector of M_{in} with largest singular value and of the right singular vector of M_{out} with largest singular value. To do this, we obtain the components of K_{in} and K_{out} in the basis of the Pauli matrices. Let $k_{\text{in}}^{(j)}$ be the components of K_{in} and $k_{\text{out}}^{(j)}$ be those of K_{out} ($j = 1, 2, 3$). These computed through the formula [106, 153]

$$\begin{aligned} k_{\text{in}}^{(j)} &= \frac{1}{2} \text{Tr}\{K_{\text{in}} s_j\}, \\ k_{\text{out}}^{(j)} &= \frac{1}{2} \text{Tr}\{K_{\text{out}} s_j\}. \end{aligned} \quad (\text{C.37})$$

Here $\text{Tr}\{A\}$ is the trace of A , and s_j are the Pauli matrices, as in Eq. (7.55). Thus, we substitute Eqs. (C.35) and (C.36) into Eq. (C.37) to find $k_{\text{in}}^{(j)}$ and $k_{\text{out}}^{(j)}$ in terms of the impulse-response inner products. Then, we substitute Eqs. (C.15) and (C.16) to find them in terms of the ring parameters. In this way, we obtain

$$\begin{aligned} k_{\text{in}}^{(1)} &= 2\gamma_e \text{Re}\{\langle u_{11}|u_{21}\rangle\} = \mu_k \text{Im}\{\kappa\}, \\ k_{\text{in}}^{(2)} &= 2\gamma_e \text{Im}\{\langle u_{11}|u_{21}\rangle\} = \mu_k \text{Re}\{\kappa\}, \\ k_{\text{in}}^{(3)} &= \gamma_e (\langle u_{11}|u_{11}\rangle - \langle u_{21}|u_{21}\rangle) = \mu_k \bar{\gamma}, \end{aligned} \quad (\text{C.38})$$

and

$$\begin{aligned} k_{\text{out}}^{(1)} &= 2\gamma_e \text{Re}\{\langle u_{12}|u_{11}\rangle\} = -\mu_k \text{Im}\{\kappa\}, \\ k_{\text{out}}^{(2)} &= 2\gamma_e \text{Im}\{\langle u_{12}|u_{11}\rangle\} = -\mu_k \text{Re}\{\kappa\}, \\ k_{\text{out}}^{(3)} &= \gamma_e (\langle u_{11}|u_{11}\rangle - \langle u_{12}|u_{12}\rangle) = \mu_k \bar{\gamma}. \end{aligned} \quad (\text{C.39})$$

where the factor μ_k is given by

$$\mu_k = \frac{\gamma_2 \gamma_e}{(\gamma_1 + \gamma_2)(\gamma_1 \gamma_2 + |\kappa|^2)}. \quad (\text{C.40})$$

Given Eqs. (C.38) and (C.39), we may now evaluate the Bloch components $S_j^{(l)}(M_{\text{in}})$ and $S_j^{(r)}(M_{\text{out}})$, as intended. To do so, we need only one result from spinor theory. This is that the Bloch components (i.e., the normalized Stokes parameters) of the eigenvectors of K_{in} and K_{out} with largest eigenvalue equal $k_{\text{in}}^{(j)}$ and $k_{\text{out}}^{(j)}$ after these are normalized so their squares add up to unity [106]. With this result, along with Eqs. (C.38) and (C.39), we confirm that $S_j^{(l)}(M_{\text{in}})$ and $S_j^{(r)}(M_{\text{out}})$ are given by Eqs. (7.56) and (7.57).

Lastly, we prove Eq. (7.60) relating the Bloch components $S_j^{(r)}(M_{\text{in}})$ and $S_j^{(l)}(M_{\text{out}})$. To do this, we evaluate the matrix products

$$\begin{aligned} M_{\text{in}}^\dagger M_{\text{in}} &= 2\gamma_e \begin{pmatrix} \langle N_1^{(\text{in})}|N_1^{(\text{in})}\rangle & \langle u_{21}|u_{11}\rangle \sqrt{\langle N_1^{(\text{in})}|N_1^{(\text{in})}\rangle / \langle u_{21}|u_{21}\rangle} \\ \langle u_{11}|u_{21}\rangle \sqrt{\langle N_1^{(\text{in})}|N_1^{(\text{in})}\rangle / \langle u_{21}|u_{21}\rangle} & \langle u_{21}|u_{21}\rangle + |\langle u_{11}|u_{21}\rangle|^2 / \langle u_{21}|u_{21}\rangle \end{pmatrix}, \\ M_{\text{out}} M_{\text{out}}^\dagger &= 2\gamma_e \begin{pmatrix} \langle N_1^{(\text{out})}|N_1^{(\text{out})}\rangle & \langle u_{11}|u_{12}\rangle \sqrt{\langle N_1^{(\text{out})}|N_1^{(\text{out})}\rangle / \langle u_{12}|u_{12}\rangle} \\ \langle u_{12}|u_{11}\rangle \sqrt{\langle N_1^{(\text{in})}|N_1^{(\text{in})}\rangle / \langle u_{21}|u_{21}\rangle} & \langle u_{12}|u_{12}\rangle + |\langle u_{11}|u_{12}\rangle|^2 / \langle u_{12}|u_{12}\rangle \end{pmatrix}. \end{aligned} \quad (\text{C.41})$$

We note that the right singular vectors of M_{in} are the eigenvectors of $M_{\text{in}}^\dagger M_{\text{in}}$; and the left singular vectors of M_{out} are the eigenvectors of $M_{\text{out}} M_{\text{out}}^\dagger$. Hence, the Bloch components $S_j^{(r)}(M_{\text{in}})$ and $S_j^{(l)}(M_{\text{out}})$ can be evaluated from Eq. (C.41), just as $S_j^{(l)}(M_{\text{in}})$ and $S_j^{(r)}(M_{\text{out}})$ were obtained from Eqs. (C.35) and (C.36) for K_{in} and K_{out} .

However, rather than obtaining explicit expressions for $S_j^{(r)}(M_{\text{in}})$ and $S_j^{(l)}(M_{\text{out}})$ and comparing them, we need only make two observations about the entries of $M_{\text{in}}^\dagger M_{\text{in}}$ and $M_{\text{out}} M_{\text{out}}^\dagger$ in Eq. (C.41) to establish the desired results, Eq. (7.60). First, we note that the value of these diagonal entries of $M_{\text{in}}^\dagger M_{\text{in}}$ and $M_{\text{out}} M_{\text{out}}^\dagger$ are identical, as a consequence of Eq. (C.16). Hence, we get $S_3^{(r)}(M_{\text{in}}) = S_3^{(l)}(M_{\text{out}})$. Second, the ratio between the first-row off-diagonal element of $M_{\text{in}}^\dagger M_{\text{in}}$ and that of $M_{\text{out}} M_{\text{out}}^\dagger$ equals $\langle u_{21}|u_{11}\rangle / \langle u_{11}|u_{12}\rangle$, again recalling Eq. (C.16). This is the same case as for K_{in} and K_{out} . Therefore, we obtain $S_1^{(r)}(M_{\text{in}}) = -S_1^{(l)}(M_{\text{out}})$ and $S_2^{(r)}(M_{\text{in}}) = -S_2^{(l)}(M_{\text{out}})$, just as in Eq. (7.58).

C.4 Proof of submultiplicative property of maximum and minimum singular values

In Sec. 7.6, we are interested in relating the minimum and maximum singular values of a matrix product to those of its factors. Let $\sigma_{\text{max}}(M)$ ($\sigma_{\text{min}}(M)$) be the maximum (minimum) singular value of some matrix M . In this section we

prove that, for any matrices A and B for which their product AB exists, $\sigma_{\max}(AB)$ ($\sigma_{\min}(AB)$) is bounded above (below) by

$$\sigma_{\max}(AB) \leq \sigma_{\max}(A)\sigma_{\max}(B). \quad (\text{C.42})$$

$$\sigma_{\min}(AB) \geq \sigma_{\min}(A)\sigma_{\min}(B). \quad (\text{C.43})$$

In the context of matrix norms (or operator norms), the maximum singular value is proven to be a matrix norm [143], and Eq. (C.42) is referred to as its sub-multiplicative property.

A similar proof of Eq. (C.42) for bounded operators in a Hilbert space is given in Ref. [135], Ch. 17. Though our proof is more detailed, including discussion of sufficient conditions for Eq. (C.42) to be an equality. Of course, we have also extended the proof of Eq. (C.42) to also prove Eq. (C.43).

We start with the proof of Eq. (C.42). From References [142, 143], $\sigma_{\max}(M)$ can be written as

$$\sigma_{\max}^2(M) = \max_{x \neq 0} \frac{x^\dagger M^\dagger M x}{x^\dagger x}. \quad (\text{C.44})$$

In other words, $\sigma_{\max}^2(M)$ is the maximum value of the quotient in the right-hand side of Eq. (C.44). As mentioned in Sec. 7.3, the right-hand side of Eq. (C.44) is a Rayleigh quotient.

Momentarily, we assume that the vector x which maximizes the right-hand side of Eq. (C.44) for $M = AB$ is such that $Bx \neq 0$, and consequently $x^\dagger B^\dagger B x = \|Bx\|^2 > 0$. Then, we may write

$$\begin{aligned} \sigma_{\max}^2(AB) &= \max_{x \neq 0} \frac{x^\dagger B^\dagger A^\dagger A B x}{x^\dagger B^\dagger B x} \frac{x^\dagger B^\dagger B x}{x^\dagger x}, \\ &\leq \max_{x \neq 0} \frac{x^\dagger B^\dagger A^\dagger A B x}{x^\dagger B^\dagger B x} \max_{x \neq 0} \frac{x^\dagger B^\dagger B x}{x^\dagger x}, \\ &= \max_{x \neq 0} \frac{x^\dagger B^\dagger A^\dagger A B x}{x^\dagger B^\dagger B x} \sigma_{\max}^2(B). \end{aligned} \quad (\text{C.45})$$

In Eq. (C.45), we made use of Eq. (C.44) for $M = B$.

Next, we bound from above the first factor in the last line of Eq. (C.45). Thus, we write

$$\max_{x \neq 0} \frac{x^\dagger B^\dagger A^\dagger A B x}{x^\dagger B^\dagger B x} \leq \max_{y \neq 0} \frac{y^\dagger A^\dagger A y}{y^\dagger y} = \sigma_{\max}^2(A) \quad (\text{C.46})$$

The inequality in Eq. (C.46) becomes an equality if and only if a right singular vector of A with its largest singular value is in the range of B . Of course, this is the case if B is a square matrix of full rank. Finally, substituting Eq. (C.46) into (C.45), we obtain the desired bound, Eq. (C.42).

Now, if the vector x maximizing the right-hand side of Eq. (C.44) for $M = AB$ is such that $Bx = 0$, then $\sigma_{\max}(AB) = 0$. Then, Eq. (C.42) is trivially satisfied, as the singular values are non-negative by definition.

Next, we show that if the left singular vector of B corresponding to $\sigma_{\max}(B)$ equals the right singular vector of A corresponding to $\sigma_{\max}(A)$, then Eq. (C.42) is an equality. In this case, let x be the right singular vector of B corresponding to $\sigma_{\max}(B)$. Then,

$$\begin{aligned} \sigma_{\max}^2(A)\sigma_{\max}^2(B) &= \frac{x^\dagger B^\dagger A^\dagger A B x}{x^\dagger B^\dagger B x} \frac{x^\dagger B^\dagger B x}{x^\dagger x}, \\ &= \frac{x^\dagger B^\dagger A^\dagger A B x}{x^\dagger x}, \\ &\leq \sigma_{\max}^2(AB). \end{aligned} \quad (\text{C.47})$$

Here, we used Eq. (C.44) with $M = AB$. But for Eq. (C.47) to be compatible with the Eq. (C.42), the inequality in the last line of Eq. (C.47) must be an equality. This completes the proof.

Now, we prove Eq. (C.43). Similarly to Eq. (C.44), the minimum singular value $\sigma_{\min}(M)$ of some matrix M satisfies the relation [142],

$$\sigma_{\min}^2(M) = \min_{x \neq 0} \frac{x^\dagger M^\dagger M x}{x^\dagger x}. \quad (\text{C.48})$$

Momentarily, we assume that $Bx = 0$ if and only if $x = 0$. Then, $x^\dagger B^\dagger Bx = \|Bx\|^2 > 0$ for $x \neq 0$. So we may substitute $M = AB$ in Eq. (C.48) to obtain

$$\begin{aligned} \sigma_{\min}^2(AB) &= \min_{x \neq 0} \frac{x^\dagger B^\dagger A^\dagger ABx}{x^\dagger B^\dagger Bx} \frac{x^\dagger B^\dagger Bx}{x^\dagger x} \\ &\geq \min_{x \neq 0} \frac{x^\dagger B^\dagger A^\dagger ABx}{x^\dagger B^\dagger Bx} \min_{x \neq 0} \frac{x^\dagger B^\dagger Bx}{x^\dagger x} \\ &= \min_{x \neq 0} \frac{x^\dagger B^\dagger A^\dagger ABx}{x^\dagger B^\dagger Bx} \sigma_{\min}^2(B), \end{aligned} \tag{C.49}$$

where we substituted Eq. (C.48) for $M = B$.

Analogous to Eq. (C.46), we bound from below the first term in the last line of Eq. (C.49). Thus, we write

$$\min_{x \neq 0} \frac{x^\dagger B^\dagger A^\dagger ABx}{x^\dagger B^\dagger Bx} \geq \min_{y \neq 0} \frac{y^\dagger A^\dagger Ay}{y^\dagger y} = \sigma_{\min}^2(A). \tag{C.50}$$

The inequality in Eq. (C.50) becomes an equality if and only if a right singular vector of A with its smallest singular value is in the range of B . Again, this is the case if B is square and of full rank. Substituting Eq. (C.50) into Eq. (C.49), we obtain the desired bound, Eq. (C.43), for $\sigma_{\min}(AB)$.

If $Bx = 0$ for some $x \neq 0$, then $\sigma_{\min}(B) = 0$. Then Eq. (C.43) is trivially satisfied all singular values is non-negative by definition, so $\sigma_{\min}(AB) \geq 0$.

Lastly, one may prove that if the left singular vector of B corresponding to $\sigma_{\min}(B)$ equals the right singular vector of A corresponding to $\sigma_{\min}(A)$, then Eq. (C.43) becomes an equality. To do so, one need only to follow reasoning analogous to Eq. (C.47).

Appendix D

Quantum-optical description of AFC in coupled microrings

As discussed in Chapter 3, a classical electromagnetic field in a time-varying medium generally does not conserve its total electromagnetic energy. However, it is of interest for both conceptual and quantum-technological purposes to determine whether the photon statistics of the field are preserved under temporal modulation in general, and under AFC in particular. To this end, in this appendix, we discuss AFC quantum-optically and examine its photon-number and energy statistics.

To complement the discussion of Chapter 7, we consider a bus waveguide coupled to two simultaneously-modulated rings. Nonetheless, it is straightforward to generalize the analysis to a single ring or several independently-modulated rings. So the results of this appendix are independent of the number of rings and modulation scheme.

In Section D.1, we obtain explicit expressions for the system's Hamiltonian under various simplifying assumptions. Then, we show that the total-photon-statistics of the system are conserved, but the total-energy statistics are not. We show that this is a consequence of the facts that the system's Hamiltonian is time-dependent, and that the total-photon-number operator is still a constant of the motion.

In Section D.2, we derive the input-output description of the rings-waveguide system. To do this, we employ the Weisskopf-Wigner analysis to obtain two sets of Heisenberg-Langevin equations for the ring-modes' annihilation operators: one in terms of the waveguide operators in an earlier time, and one in terms of the waveguide operators in a later time. Then, we combine these two sets of Heisenberg-Langevin equations to obtain the system's input-output relation. In contrast to conventional analyses [81–84], we discuss sufficient approximations for the accuracy of the input-output formulation and we extend it to account for time-dependent resonance frequencies using an approach analogous to Section 3.5.

In Section D.3, we utilize the input-output formalism to analyze the time-evolution of the rings-waveguide system when it is initially in the product state of a coherent waveguide state and the rings' vacuum state. We show that the output state is also the product state of a coherent waveguide state and the rings' vacuum state. Furthermore, the output waveguide state has identical total-photon-statistics as the input one. Lastly, we show that, to the accuracy of the input-output formalism, the mean fraction of frequency-shifted photons equals the AFC energy efficiency predicted by TCMT.

D.1 Hamiltonian and constants of the motion

In the framework of quantum-optical theory, we model the electromagnetic field in the system of bus waveguide and time-modulated rings as a collection of coupled quantum harmonic oscillators [63, 89]. Furthermore, as usual in quantum mechanics, we write the Hamiltonian operator $\hat{H}(t)$ of this coupled system can be written as a sum of three contributions: $H_r(t)$, modeling the coupled rings' electromagnetic field in isolation; H_b , modeling the bus-waveguide field in isolation; and H_i , modeling the interaction between the field in the rings and the field in the bus waveguide, e.g.,

$$\hat{H}(t) = \hat{H}_r(t) + \hat{H}_b + \hat{H}_i. \quad (\text{D.1})$$

For simplicity, we neglect coupling of the bus-ring system to the environment's electromagnetic modes.

To write explicit expressions for the terms on the right-hand side of Eq. (D.1), we introduce simplifying assumptions. First, we assume that the initial state of the field in the bus waveguide has a definite polarization and is narrow-

band compared to the rings' free spectral range. Hence, the waveguide's field may only excite electromagnetic one mode per ring. Second, we assume the modes of the rings and bus waveguide are weakly coupled. Then, the system's normal modes can be approximated as those of the individual rings and waveguide, coupled through an interaction quadratic on the fields [89]. Third, we assume that modulation is either spatially homogeneous over each ring or temporally non-resonant with the rings' roundtrip time. Then, we may safely neglect coupling among longitudinal modes of the ring due to the applied modulation. Fourth, we assume that coupling is sufficiently weak for the rotating-wave approximation to hold. Under these assumptions, the terms in Eq. (D.1) are given by

$$\begin{aligned}\hat{H}_r(t) &= \hbar\omega_r(t) \left(\hat{a}_1^\dagger \hat{a}_1 + \hat{a}_2^\dagger \hat{a}_2 \right) + \hbar \left(\kappa_{12} \hat{a}_1^\dagger \hat{a}_2 + \kappa_{12}^* \hat{a}_2^\dagger \hat{a}_1 \right), \\ \hat{H}_b &= \hbar \int_0^\infty d\omega \omega \hat{a}^\dagger(\omega) \hat{a}(\omega), \\ \hat{H}_i &= \hbar \int_0^\infty d\omega \left[\kappa(\omega) \hat{a}_1^\dagger \hat{a}(\omega) + \kappa^*(\omega) \hat{a}^\dagger(\omega) \hat{a}_1 \right].\end{aligned}\tag{D.2}$$

Here \hbar is Planck's reduced constant; \hat{a}_j ($j = 1, 2$), the annihilation operator of the mode in the j th resonator; $\hat{a}(\omega)$, the annihilation operator of the bus-waveguide mode with natural frequency ω ; $\omega_r(t)$, the time-dependent resonance frequency of the bare rings' resonant modes; κ_{12} , the complex-valued coupling between the rings' modes; and $\kappa(\omega)$, the complex-valued coupling between Ring 1's mode, and the bus's mode of natural frequency ω . As usual in quantum mechanics, the dagger \dagger denotes Hermitian adjoint. Since \hat{a}_j ($j = 1, 2$) and $\hat{a}(\omega)$ are bosonic annihilation operators, they satisfy the commutation relations [62, 63]

$$\begin{aligned}[\hat{a}_i, \hat{a}_j^\dagger] &= \delta_{ij}, \\ [\hat{a}(\omega), \hat{a}^\dagger(\omega')] &= \delta(\omega - \omega').\end{aligned}\tag{D.3}$$

Here, δ_{ij} is the Kronecker delta symbol; and $\delta(\omega - \omega')$, the Dirac delta function.

Even though the Hamiltonian $\hat{H}(t)$ is time-dependent, it is well known and straightforward to verify that a dynamical system with Hamiltonian of the type of Eq. (D.1) (with its terms given by Eq. (D.2)) has a constant of the motion \hat{N} corresponding to the total photon number. Mathematically, \hat{N} is given by

$$\hat{N} = \hat{a}_1^\dagger \hat{a}_1 + \hat{a}_2^\dagger \hat{a}_2 + \int_0^\infty d\omega \hat{a}^\dagger(\omega) \hat{a}(\omega).\tag{D.4}$$

Since \hat{N} is a constant of the motion (i.e., it commutes with $\hat{H}(t)$ for all t), then its characteristic function $\langle \exp(i\hat{N}\phi) \rangle$ [170] with independent variable ϕ ¹ is time-independent. Hence, it follows that the statistical distribution of the system's total photon number is time-independent, even if $\hat{H}(t)$ is time-dependent [70].

In contrast, because the Hamiltonian is explicitly time-dependent, its characteristic function $\langle \exp[i\hat{H}(t)\phi] \rangle$ is clearly time-dependent. Thus, the energy statistics in general (and the mean energy $\langle H(t) \rangle$ in particular) vary in time. We emphasize that these results rely only on the aforementioned assumptions that the optical field has a definite polarization and narrow bandwidth compared to the rings' free spectral range; that the rings and bus are weakly coupled; that ring modulation is either spatially homogeneous or temporally non-resonant; and that the rotating-wave approximation holds for inter-ring and ring-waveguide coupling.

D.2 General input-output formalism

In quantum optics, The closest analog of classical temporal coupled mode theory (TCMT) is the so-called input-output formalism (IOF) [81–84]. Thus, it is useful to apply it to our system to compare its results with those of TCMT. The IOF is an approximate analytical scheme to find the evolution of the Heisenberg-picture annihilation operators of a continuum of optical modes when the latter is coupled to a discrete, resonant system, e.g., an optical resonator or a two-level atom.

¹or more properly, its probability generating function $\langle z^{\hat{N}} \rangle$ with independent variable z , as the spectrum of \hat{N} consists of the set of non-negative integers

For our waveguide-ring system with Hamiltonian Eq. (D.1), the IOF can be derived by applying the Weisskopf-Wigner (WW) analysis [21] to the Heisenberg equations of motion for the rings' and bus's annihilation operators. In this way, the Heisenberg equations for $\hat{a}_1(t)$ and $\hat{a}_2(t)$ can be approximated by the Heisenberg-Langevin equations (in matrix notation) [89, 90]

$$i \frac{d}{dt} \begin{pmatrix} \hat{a}_1 \\ \hat{a}_2 \end{pmatrix} = M(t) \begin{pmatrix} \hat{a}_1 \\ \hat{a}_2 \end{pmatrix} + \begin{pmatrix} \sqrt{2\gamma_e} \exp(i\phi) \\ 0 \end{pmatrix} \hat{b}(t-t_0, t_0). \quad (\text{D.5})$$

In Eq. (D.5), $M(t)$ is the 2×2 matrix

$$M(t) = \begin{pmatrix} \omega_r(t) + \delta - i\gamma_e & \kappa_{12} \\ \kappa_{12}^* & \omega_r(t) \end{pmatrix}. \quad (\text{D.6})$$

In Eqs. (D.5) and (D.6), the parameters γ_e , δ , and ϕ are given by

$$\begin{aligned} \gamma_e &= \pi |\kappa(\omega_0)|^2, \\ \delta &= \text{P.V.} \int_0^\infty d\omega \frac{|\kappa(\omega)|^2}{\omega_0 - \omega}, \\ \exp(i\phi) &= \kappa(\omega_0) / |\kappa(\omega_0)|. \end{aligned} \quad (\text{D.7})$$

The frequency ω_0 is the value of the rings' bare resonance frequency $\omega_r(t)$ before modulation. As usual, P.V. denotes Cauchy principal value. In Eq. (D.5), the operator $\hat{b}(t-t_0, t_0)$ is defined as the integral

$$\hat{b}(t, t') = \frac{1}{\sqrt{2\pi}} \int_0^\infty d\omega \hat{a}(\omega, t') \exp(-i\omega t). \quad (\text{D.8})$$

From Eq. (D.8), $\hat{b}(t, t')$ is a Heisenberg-picture operator at time t' . Its first argument t is merely a label for its degree of freedom. The second argument t_0 of $\hat{b}(t-t_0, t_0)$ is a time earlier than t , i.e., satisfying $t_0 < t$.

An equation analogous to Eq. (D.5) can be derived via the same WW analysis, but integrating the waveguide annihilation operator \hat{b} from t to a future time t_1 , such that $t < t_1$. In this manner, we obtain

$$i \frac{d}{dt} \begin{pmatrix} \hat{a}_1 \\ \hat{a}_2 \end{pmatrix} = M^\dagger(t) \begin{pmatrix} \hat{a}_1 \\ \hat{a}_2 \end{pmatrix} + \begin{pmatrix} \sqrt{2\gamma_e} \exp(i\phi) \\ 0 \end{pmatrix} \hat{b}(t-t_1, t_1). \quad (\text{D.9})$$

Equating the right-hand sides of Eqs. (D.5) and (D.9), we obtain the input-output relation

$$\hat{b}(t-t_1, t_1) = \hat{b}(t-t_0, t_0) - i\sqrt{2\gamma_e} \exp(-i\phi) \hat{a}_1(t). \quad (\text{D.10})$$

Of course, the Heisenberg-Langevin equations, (D.5) and (D.9), are only approximations to the exact Heisenberg equations of motion. Via WW analysis, we find sufficient conditions for Eqs. (D.5) and (D.9) to approximate the Heisenberg equations. Let B_κ be the bandwidth around ω over which $\kappa(\omega)$ is approximately constant; and B_b , the bandwidth of the initial optical excitation in the bus waveguide. Then, these sufficient conditions can be written as

$$\exp(i\omega_0 t) \hat{a}_1(t) \approx \exp(i\omega_0 t') \hat{a}_1(t'), \quad \text{for } |t-t'| \lesssim 2\pi/B_\kappa, \quad (\text{D.11})$$

$$B_b \ll B_\kappa, \quad (\text{D.12})$$

$$t-t_0 \gg 2\pi/B_\kappa, \quad (\text{D.13})$$

$$t_1-t \gg 2\pi/B_\kappa. \quad (\text{D.14})$$

Eq. (D.11) is a "memory-less" approximation [21]. Eq. (D.12) states that the initial optical excitation needs to be narrowband compared to B_κ . Eq. (D.13) indicates that t_0 must be in the far past of t on a timescale of $2\pi/B_\kappa$; and Eq. (D.14), that t_1 must be in the far future of t on a timescale of $2\pi/B_\kappa$. As a consequence of Eq. (D.11), we must have the time-rates γ_e , δ , $|\kappa_{12}|$, $|\omega_r(t) - \omega_0|$ be small compared to B_κ . In summary, Eqs. (D.11) to (D.14) can be interpreted as stating that the IOF cannot accurately resolve temporal dynamics over a timescale comparable or smaller than $2\pi/B_\kappa$, given by the bandwidth B_κ of the coupling coefficient $\kappa(\omega)$.

Because of the expression for $M(t)$ in Eq. (D.6), $M(t)$ commutes with $M(t')$ for any pair of times t and t' . Thus we may integrate Eq. (D.9) and take its adjoint to express the creation operator $\hat{a}_1^\dagger(t)$ of Ring 1's mode at time t in terms of creation operators at later times. The resulting relation is given by

$$\hat{a}_1^\dagger(t) = \hat{a}_1^\dagger(t_i) u_{11}(t_i, t) + \hat{a}_2^\dagger(t_i) u_{21}(t_i, t) - i\sqrt{2\gamma_e} \exp(i\phi) \int_t^{t_i} dt' \hat{b}^\dagger(t'-t_1, t_1) u_{11}(t', t). \quad (\text{D.15})$$

Here, $u_{nm}(t, t')$ is the (n, m) matrix element of the time-evolution matrix $U(t, t')$ defined as

$$U(t, t') = \exp \left[-i \int_{t'}^t dt'' M(t'') \right]. \quad (\text{D.16})$$

In Eq. (D.15), t_i is some future time $t_i > t$ such that $(t_1 - t_i) \gg 2\pi/B_\kappa$. This ensures that $(t_1 - t') \gg 2\pi/B_\kappa$ for all $t' \in [t, t_i]$. Hence that Eq. (D.14) holds for all the integration times in Eq. (D.15).

D.3 Input-output analysis of a coherent waveguide state

Lastly, we use the IOF to analyze the time-evolution of the bus-rings system when it is initially in the product state of a coherent waveguide state and the rings' vacuum state. Mathematically, the initial waveguide coherent state $|\psi(t_0)\rangle$ at the initial time t_0 can be expressed as [62, 63]

$$|\psi(t_0)\rangle = \exp \left[\hat{b}_f^\dagger(t_0) - \hat{b}_f(t_0) \right] |0\rangle. \quad (\text{D.17})$$

Here, $|0\rangle$ is the vacuum state for the full rings-waveguide system; and $\hat{b}_f^\dagger(t_0)$, a waveguide wavepacket creation operator. For a wavepacket of narrow bandwidth relative to its carrier frequency, its creation operator $\hat{b}_f^\dagger(t_0)$ can be expressed as a superposition of the "time-domain" creation operators $\hat{b}^\dagger(t - t_0, t_0)$ at time t_0 , as

$$\hat{b}_f^\dagger(t_0) = \int_{-\infty}^{\infty} dt f_{\text{in}}(t) \hat{b}^\dagger(t - t_0, t_0). \quad (\text{D.18})$$

Here, $f_{\text{in}}(t)$ is the "input" wavepacket amplitude. From Eq. (D.4) for the total photon number operator \hat{N} , and Eq. (D.17) for the initial state $|\psi(t_0)\rangle$, it can be shown [62, 63] that the expectation value $\langle \hat{N} \rangle$ is given by

$$\langle \psi(t_0) | \hat{N} | \psi(t_0) \rangle = \int_{-\infty}^{\infty} dt |f_{\text{in}}(t)|^2. \quad (\text{D.19})$$

Next, we utilize the IOF to express $\hat{b}_f(t_0)$, and hence $|\psi(t_0)\rangle$, in terms of operators at the later time t_1 . To do so, we use Eqs. (D.10) and (D.15) to write $\hat{b}^\dagger(t - t_0, t_0)$ in terms of $\hat{b}^\dagger(t - t_1, t_1)$, $\hat{a}_1^\dagger(t_i)$, and $\hat{a}_2^\dagger(t_i)$. Then, we substitute this expression for $\hat{b}^\dagger(t - t_0, t_0)$ in Eq. (D.18). Then, we assume that the wavepacket amplitude $f_{\text{in}}(t)$ has finite duration so that it becomes relatively negligible for $t < \tau_0$ and $\tau_1 < t$. Lastly, we assume t_1 and τ_1 are sufficiently large so that $\gamma_e(t_1 - \tau_1) \gg 1$ and $\gamma_e(t_i - \tau_1) \gg 1$. Thus we obtain

$$\hat{b}_f(t_0) = \int_{-\infty}^{\infty} f_{\text{out}}(t) \hat{b}^\dagger(t - t_1, t_1). \quad (\text{D.20})$$

From analogy to Eq. (D.18), $f_{\text{out}}(t)$ in Eq. (D.20) is the "output" wavepacket amplitude. From our IOF-based analysis, $f_{\text{out}}(t)$ is related to the input wavepacket amplitude, $f_{\text{in}}(t)$, through

$$f_{\text{out}}(t) = f_{\text{in}}(t) - 2\gamma_e \int_{-\infty}^t dt' f_{\text{in}}(t') u_{11}(t, t'). \quad (\text{D.21})$$

Substituting Eq. (D.20) into Eq. (D.17), it follows that the state $|\psi(t_0)\rangle$, corresponding to a waveguide coherent state with wavepacket amplitude $f_{\text{in}}(t)$ at time t_0 , corresponds to a waveguide coherent state with amplitude $f_{\text{out}}(t)$ (given by Eq. (D.21)) at time t_1 . Furthermore, Eq. (D.21) states that the linear relation between $f_{\text{in}}(t)$ and $f_{\text{out}}(t)$ predicted by the IOF is identical to that between the power-normalized input $s_{\text{in}}(t)$ and the power-normalized output $s_{\text{out}}(t)$ predicted by classical, phenomenological TCMT in the absence of intrinsic loss ($\gamma_0 = 0$).

Because \hat{N} is a constant of the motion, it follows from Eq. (D.19) that

$$\int_{-\infty}^{\infty} dt |f_{\text{out}}(t)|^2 = \int_{-\infty}^{\infty} dt |f_{\text{in}}(t)|^2. \quad (\text{D.22})$$

This can be verified explicitly for the case of time-independent resonance frequency $\omega_r(t)$ using the Fourier transform's Parseval theorem. In other words, Eq. (D.22) states that the output coherent state at later time t_1 has the same mean

photon number as the input coherent state at time t_0 . This is just an instance of the more general result that the input state at the past time t_0 and the output state at the future time t_1 have identical photon-number statistics, as follows from Section D.1.

Next, we analyze the number of photons in a target frequency band at the output. To do so, we introduce the observable $\hat{A}(\omega_i, \omega_f; t)$, which measures the number of photons in the waveguide with natural frequencies between ω_i and ω_f . In the Heisenberg picture, it is a time-dependent operator, given by

$$\hat{A}(\omega_i, \omega_f; t) = \int_{\omega_i}^{\omega_f} d\omega \hat{a}^\dagger(\omega, t) \hat{a}(\omega, t). \quad (\text{D.23})$$

Lastly, we consider η_N , defined as the mean fraction of waveguide photons in the target frequency band at time t_1 . Assuming again that the bandwidth of $f_{\text{out}}(t)$ is small compared to its carrier frequency, we utilize Eq. (D.22), Eq. (D.23), and elementary properties of continuum-mode coherent states [62, 63] to evaluate η_N as

$$\eta_N = \frac{\langle \psi(t_0) | \hat{A}(\omega, \omega_f; t_1) | \psi(t_0) \rangle}{\langle \psi(t_0) | \hat{N} | \psi(t_0) \rangle} = \frac{\int_{\omega_i}^{\omega_f} d\omega |F_{\text{out}}(\omega)|^2}{\int_{-\infty}^{\infty} dt |f_{\text{in}}(t)|^2} = \frac{\int_{\omega_i}^{\omega_f} d\omega |F_{\text{out}}(\omega)|^2}{\int_{-\infty}^{\infty} d\omega |F_{\text{out}}(\omega)|^2}. \quad (\text{D.24})$$

Here, $F_{\text{out}}(\omega)$ is the Fourier transform of $f_{\text{out}}(t)$. The last expression on Eq. (D.24) demonstrates that η_N has a tight upper bound of unity. Moreover, from Eqs. (D.21) and (D.24), we see that Eq. (D.24) for η_N , obtained via a quantum-optical IOF, equals the expression for energy fraction η in the same target frequency-range predicted by classical TCMT.

Appendix E

Analytical expression for the CAFC output

In this appendix, we derive the expression for the frequency-shifted CAFC output $s_{\text{out}}(t)$ provided in Chapter 8. In Section E.1, we provide the complete, exact solution of the TCMT equations for the full CAFC process and the corresponding exact CAFC output. Nonetheless, this expression is unwieldy for subsequent analysis in Chapter 8. So we simplify it in the remaining sections of this appendix, under suitable approximations. Because the rings' modulation is piecewise continuous, we find it useful to examine $s_{\text{out}}(t)$ before, during, and after modulation. In Section E.2, we analyze the CAFC output before modulation. In Section E.3, we analyze it during modulation. And in Section E.4, we analyze it after modulation.

E.1 Exact solution for piece-wise constant detuning

The modulation applied to the rings is piece-wise constant in time. Thus, the temporal coupled-mode theory (TCMT) equations can be solved exactly for the ring-amplitude column vector $a(t)$ in terms of matrix exponentials. In this way, we obtain

$$\begin{aligned}
 a(t) &= \int_{-\infty}^t dt' \exp[-iH_0(t-t')] k_{\text{in}} s_{\text{in}}(t'), & \text{for } t \leq t_1, \\
 a(t) &= \exp[-iH_m(t-t_1)] a(t_1) + \int_{t_1}^t dt' \exp[-iH_m(t-t')] k_{\text{in}} s_{\text{in}}(t'), & \text{for } t_1 < t \leq t_2, \\
 a(t) &= \exp[-iH_0(t-t_2)] a(t_2) + \int_{t_2}^t dt' \exp[-iH_0(t-t')] k_{\text{in}} s_{\text{in}}(t'), & \text{for } t_2 < t.
 \end{aligned} \tag{E.1}$$

Of course, to evaluate the solution in Eq. (E.1) for $a(t)$, we require explicit expressions for the matrix exponentials $\exp(-iH_0 t)$ and $\exp(-iH_m t)$. These can be evaluated as the inverse Laplace transforms of the resolvents $(sI + iH_0)^{-1}$ and $(sI + iH_m)^{-1}$, respectively, via calculus of residues. Here s is the independent variable of the Laplace transform; and I , the 2×2 identity matrix. In this evaluation, we only assume that the resolvents' poles (equivalently, the eigenvalues of H_0 and H_m) are simple. This is true when $|\kappa| \gg |\gamma_e|$, which is a necessary condition for efficient CAFC, as discussed in the Chapter 8. In this manner, we get

$$\begin{aligned}
 \exp(-iH_0 t) &= \exp(-i\bar{\omega}t - \bar{\gamma}t) \tilde{U}(t, \Delta_0), \\
 \exp(-iH_m t) &= \exp(-i\bar{\omega}t - \bar{\gamma}t) \tilde{U}(t, 0).
 \end{aligned} \tag{E.2}$$

Here $\bar{\gamma} = (\gamma_1 + \gamma_2)/2$ is the ring-averaged decay rate; and $\tilde{U}(t, \Delta)$, an auxiliary matrix depending on the time t and the ring detuning $\Delta = (\omega_1 - \omega_2)$. Let $\tilde{u}_{nm}(t, \Delta)$ be the element of $\tilde{U}(t, \Delta)$ in its n th row and m th column. Then explicit

expressions for the matrix elements $\tilde{u}_{nm}(t, \Delta)$ of $\tilde{U}(t, \Delta)$ are

$$\begin{aligned}\tilde{u}_{11}(t, \Delta) &= \frac{1}{2} \left(1 - \frac{\Delta - i\delta}{\Omega} \right) \exp(i\Omega t/2) + \frac{1}{2} \left(1 + \frac{\Delta - i\delta}{\Omega} \right) \exp(-i\Omega t/2), \\ \tilde{u}_{12}(t, \Delta) &= -\frac{\kappa_{12}}{\Omega} \exp(i\Omega t/2) + \frac{\kappa_{12}}{\Omega} \exp(-i\Omega t/2), \\ \tilde{u}_{21}(t, \Delta) &= -\frac{\kappa_{21}}{\Omega} \exp(i\Omega t/2) + \frac{\kappa_{21}}{\Omega} \exp(-i\Omega t/2), \\ \tilde{u}_{22}(t, \Delta) &= \frac{1}{2} \left(1 + \frac{\Delta - i\delta}{\Omega} \right) \exp(i\Omega t/2) + \frac{1}{2} \left(1 - \frac{\Delta - i\delta}{\Omega} \right) \exp(-i\Omega t/2).\end{aligned}\tag{E.3}$$

In Eq. (E.3), δ is the decay rate difference; and Ω , the rings' complex-valued frequency splitting. These quantities are given by

$$\begin{aligned}\delta &\equiv \gamma_1 - \gamma_2, \\ \Omega &\equiv \sqrt{(\Delta - i\delta)^2 + 4|\kappa|^2}, \quad \text{Re}\{\Omega\} > 0.\end{aligned}\tag{E.4}$$

We note that, in Eq. (E.4), we choose the value of the square root in the expression for Ω such that $\text{Re}\{\Omega\} > 0$. This choice is only made for concreteness, as clearly Eq. (E.3) is invariant under the substitution $\Omega \rightarrow -\Omega$.

For subsequent analysis, we find it convenient to introduce the impulse-response matrix $U(t, \Delta)$ for constant ring-detuning Δ . This matrix can be succinctly expressed in terms of the auxiliary matrix $\tilde{U}(t, \Delta)$ of Eq. (E.2) as

$$U(t, \Delta) = \exp(-i\bar{\omega}t - \bar{\gamma}t)\Theta(t)\tilde{U}(t, \Delta).\tag{E.5}$$

In Eq. (E.5), as in Chapters 6 to 8, $\Theta(t)$ represents the Heaviside step function. Analogously to $\tilde{U}(t, \Delta)$, we write $u_{nm}(t, \Delta)$ for the matrix element of $U(t, \Delta)$ in its n th row and m th column. Given Eqs. (E.3) and (E.5), the matrix elements $u_{nm}(t, \Delta)$ are straightforward to evaluate.

E.2 Output before modulation

In this section, we examine $s_{\text{out}}(t)$ before ring modulation is applied; i.e., for values of t satisfying $t \leq t_1$, where t_1 is the time at which ring modulation starts to be applied. Using Eq. (E.1) for $t \leq t_1$ and the input-output relation from TCMT, we obtain

$$s_{\text{out}}(t) = 2\sqrt{\gamma_{1e}\gamma_{2e}} \int_{-\infty}^{\infty} dt' u_{21}(t-t', \Delta_0) s_{\text{in}}(t'), \quad t \leq t_1.\tag{E.6}$$

As above and in Chapters 7 and 8, $u_{21}(t, \Delta_0)$ is the element of the matrix $U(t, \Delta_0)$ in its second row and first column; and $U(t, \Delta_0)$, from Eq. (E.5), is the impulse-response matrix for constant inter-ring detuning equal to Δ_0 .

Next, we note that the solution in Eq. (E.6) for $t \leq t_1$ becomes negligible for sufficiently large $|\Delta_0|$ relative to the inter-ring coupling $|\kappa|$ and to the decay-rate discrepancy $|\delta|$. Intuitively, this is because a large detuning $|\Delta_0|$ relative to $|\kappa|$ implies that the field in the rings grow out of phase with each other before they couple significantly. This inhibits accumulation of the energy in Ring 1 into Ring 2.

To demonstrate this rigorously, we note that the total energy in Eq. (E.6) for $s_{\text{out}}(t)$ can be written as

$$\int_{-\infty}^{t_1} dt |s_{\text{out}}(t)|^2 \leq \int_{-\infty}^{\infty} dt |s_{\text{out}}^{(\text{inv})}(t)|^2 = \frac{1}{2\pi} \int_{-\infty}^{\infty} d\omega |S_{\text{out}}^{(\text{inv})}(\omega)|^2.\tag{E.7}$$

Here, $s_{\text{out}}^{(\text{inv})}(t)$ is the system's output in the absence of modulation, i.e., when the inter-ring detuning remains constant as $\Delta(t) = \Delta_0$. $S_{\text{out}}^{(\text{inv})}(\omega)$ is the Fourier transform of $s_{\text{out}}^{(\text{inv})}(t)$, and the equality in Eq. (E.7) follows from Parseval's theorem. Furthermore, from the convolution theorem of Fourier analysis, we have

$$S_{\text{out}}^{(\text{inv})}(\omega) = 2\sqrt{\gamma_{1e}\gamma_{2e}} U_{21}(\omega, \Delta_0) S_{\text{in}}(\omega).\tag{E.8}$$

Here $U_{21}(\omega, \Delta_0)$ is the Fourier transform of $u_{21}(t, \Delta_0)$; and $S_{\text{in}}(\omega)$, the Fourier transform of $s_{\text{in}}(t)$. From Eq. (E.8), it follows that

$$\begin{aligned} \int_{-\infty}^{\infty} d\omega \left| S_{\text{out}}^{(\text{inv})}(\omega) \right|^2 &= 4\gamma_e \gamma_e \int_{-\infty}^{\infty} d\omega |U_{21}(\omega, \Delta_0)|^2 |S_{\text{in}}(\omega)|^2, \\ &\leq 4\gamma_e \gamma_e W_{21}(\Delta_0) \int_{-\infty}^{\infty} d\omega |S_{\text{in}}(\omega)|^2, \\ &= 8\pi\gamma_e \gamma_e W_{21}(\Delta_0) E_{\text{in}}. \end{aligned} \quad (\text{E.9})$$

Here, E_{in} is the total energy of the input pulse and $W_{21}(\Delta_0)$ is the auxiliary constant

$$W_{21}(\Delta_0) = \max_{\omega} |U_{21}(\omega, \Delta_0)|^2. \quad (\text{E.10})$$

Substituting Eq. (E.9) into Eq. (E.7) we then obtain

$$\int_{-\infty}^{t_1} dt |s_{\text{out}}(t)|^2 \leq 4\gamma_e \gamma_e W_{21}(\Delta_0) E_{\text{in}}. \quad (\text{E.11})$$

It is straightforward to verify that $\lim_{|\Delta_0| \rightarrow \infty} W_{21}(\Delta_0) = 0$. Consequently, we find

$$\lim_{|\Delta_0| \rightarrow \infty} \int_{-\infty}^{t_1} dt |s_{\text{out}}(t)|^2 = 0. \quad (\text{E.12})$$

In other words, Eq. (E.12) states that for sufficiently large $|\Delta_0|$, the energy in $s_{\text{out}}(t)$ before the modulation time t_1 can be made arbitrarily small. This completes the desired proof. We make a similar argument to the one of this section for the integral contribution to $s_{\text{out}}(t)$ for $t > t_2$ in Section E.4.

E.3 Output during modulation

During ring modulation, the rings are brought to a common resonance such that their bare resonance frequencies both equal their average $\bar{\omega}$ and their detuning Δ vanishes. From Eq. (E.1), the output $s_{\text{out}}(t)$ during this time (from t_1 to t_2) is given by

$$\begin{aligned} s_{\text{out}}(t) &= k_{\text{out}}^\dagger U(t - t_1, 0) a(t_1) + \int_{t_1}^{\infty} dt' k_{\text{out}}^\dagger U(t - t', 0) k_{\text{in}} s_{\text{in}}(t'), \quad t_1 \leq t \leq t_2. \\ a(t_1) &= \int_{-\infty}^{\infty} dt' U(t_1 - t', \Delta_0) k_{\text{in}} s_{\text{in}}(t'). \end{aligned} \quad (\text{E.13})$$

Nonetheless, if the inter-ring detuning Δ_0 is large compared to the inter-ring coupling $|\kappa|$, their rings' decay-rates γ_j ($j = 1, 2$), and the bandwidth of the input $s_{\text{in}}(t)$, then the output $s_{\text{out}}(t)$ has negligible spectral energy density at the target shifted frequency. So, for the purposes of engineering CAFC, this contribution to $s_{\text{out}}(t)$ can be neglected.

To illustrate this result, we consider the contribution to the Fourier transform $S_{\text{out}}(\omega)$ of $s_{\text{out}}(t)$ of the first term in the right-hand side of Eq. (E.13). This contribution is the Fourier transform of

$$k_{\text{out}}^\dagger U(t - t_1, 0) a(t_1) [\Theta(t - t_1) - \Theta(t - t_2)], \quad (\text{E.14})$$

where $\Theta(x)$ is the Heaviside step function. By the multiplication theorem of the Fourier transform, the Fourier transform of Eq. (E.14) equals the transform of $k_{\text{out}}^\dagger U(t - t_1, 0) a(t_1)$ convolved with that of $[\Theta(t - t_1) - \Theta(t - t_2)]$, i.e., a sinc function of width $2\pi/(t_2 - t_1)$. In Chapter 8, we show that efficient CAFC requires $|\kappa| \gg \gamma_j$, so the Fourier transform of $k_{\text{out}}^\dagger U(t - t_1, 0) a(t_1)$ is non-negligible only over a frequency band of width $|\kappa|$ around the ring-averaged resonance frequency $\bar{\omega}$. Convolution with the Fourier transform of $[\Theta(t - t_1) - \Theta(t - t_2)]$ increases the spectral width of Eq. (E.14) by a term of the order of $2\pi/(t_2 - t_1)$. But, as discussed in Sec. ??, optimal CAFC requires $2\pi/(t_2 - t_1)$ to be of the order of $|\kappa|$. Thus, the Fourier transform of Eq. (E.14) is only appreciable over a bandwidth of order $|\kappa|$ around $\bar{\omega}$. Consequently, there is no appreciable energy spectral density in the contribution of Eq. (E.14) to $S_{\text{out}}(\omega)$, the Fourier transform of $s_{\text{out}}(t)$, at near Ring 2's resonance frequency $\omega = \bar{\omega} - \Delta_0/2$.

We use similar techniques to analyze the contribution due to the second term on the right-hand side of Eq. (E.13). Said contribution equals the Fourier transform of

$$\left\{ \left[k_{\text{out}}^\dagger U(t, 0) k_{\text{in}} \right] * [s_{\text{in}}(t) \Theta(t - t_1)] \right\} [\Theta(t - t_1) - \Theta(t - t_2)]. \quad (\text{E.15})$$

Here, the asterisk $*$ denotes convolution. Again, we invoke the multiplication theorem to identify the transform of Eq. (E.15) with the convolution of the transform of $\left\{ \left[k_{\text{out}}^\dagger U(t, 0) k_{\text{in}} \right] * [s_{\text{in}}(t) \Theta(t - t_1)] \right\}$ with that of $[\Theta(t - t_1) - \Theta(t - t_2)]$. As with Eq. (E.14), convolution with the window function $[\Theta(t - t_1) - \Theta(t - t_2)]$ increases the spectrum of the term in curly brackets from Eq. (E.15) by a term of order $|\kappa|$. Meanwhile, the spectrum of the curly-bracket term is the product of the spectrum of $k_{\text{out}}^\dagger U(t, 0) k_{\text{in}}$ and that of $s_{\text{in}}(t) \Theta(t - t_1)$, according to the convolution theorem of the Fourier transform. As in our discussion of Eq. (E.14), the contribution of Eq. (E.15) to $S(\omega)$ near $\omega = \bar{\omega} - \Delta_0/2$ is negligible if the Fourier transform of $\left\{ \left[k_{\text{out}}^\dagger U(t, 0) k_{\text{in}} \right] * [s_{\text{in}}(t) \Theta(t - t_1)] \right\}$ is itself negligible near $\bar{\omega} - \Delta_0/2$, at a distance of the order of $|\kappa|$. By the convolution theorem, this is the case because the transform of $k_{\text{out}}^\dagger U(t, 0) k_{\text{in}}$ is centered at $\bar{\omega}$ with bandwidth of the order of $|\kappa|$; and $s_{\text{in}}(t) \Theta(t - t_1)$ is centered near Ring 1's frequency $\bar{\omega} + \Delta_0/2$ with bandwidth of the order of $\tilde{\gamma}_1 \ll |\kappa| \ll |\Delta_0|$.

E.4 Output after modulation

After ring modulation, i.e., for $t \geq t_2$, the rings are no longer modulated, so their bare resonances return to their separate original values of $\bar{\omega} \pm \Delta_0/2$. According to Eq. (E.1), the exact solution of the TCMT equations for the output $s_{\text{out}}(t)$ for $t \geq t_2$ is given by

$$s_{\text{out}}(t) = k_{\text{out}}^\dagger U(t - t_2, \Delta_0) a(t_2) + \int_{t_2}^{\infty} dt' k_{\text{out}}^\dagger U(t - t', \Delta_0) k_{\text{in}} s_{\text{in}}(t'), \quad t \geq t_2, \quad (\text{E.16})$$

$$a(t_2) = U(t_2 - t_1, 0) a(t_1) + \int_{t_1}^{\infty} dt' U(t_2 - t', 0) k_{\text{in}} s_{\text{in}}(t'), \quad (\text{E.17})$$

$$a(t_1) = \int_{-\infty}^{\infty} dt' U(t_1 - t', \Delta_0) k_{\text{in}} s_{\text{in}}(t'). \quad (\text{E.18})$$

However, the second terms in the right-hand side of Eqs. (E.16) and (E.17) contribute a negligible energy fraction to $s_{\text{out}}(t)$. Hence, Eqs. (E.16) to (E.18) are equivalent to the solution for $s_{\text{out}}(t)$ in Chapter 8. Essentially, these terms are negligible because the carrier-frequency of the input $s_{\text{in}}(t)$ is drastically mismatched from the bare frequency of either ring during modulation and of Ring 2 after modulation. Thus, the energy in $s_{\text{in}}(t)$ cannot accumulate in either ring and Ring 2, respectively.

That the second terms in the right-hand side of Eqs. (E.16) and (E.17) become negligible for comparatively large $|\Delta_0|$ can be proven rigorously. For the term in Eq. (E.16), this can be done by constructing an argument similar to that in Section E.2 to show that the energy associated with this term converges to zero in the limit of $|\Delta_0| \rightarrow \infty$.

For the term in Eq. (E.17), it is helpful to write it as the column vector

$$\int_{t_1}^{\infty} dt' U(t_2 - t', 0) k_{\text{in}} s_{\text{in}}(t') = \begin{pmatrix} \sqrt{2\gamma_1} \int_{-\infty}^{\infty} dt' u_{11}(t_2 - t', 0) s_{\text{in}}(t') \Theta(t' - t_1) \\ \sqrt{2\gamma_1} \int_{-\infty}^{\infty} dt' u_{21}(t_2 - t', 0) s_{\text{in}}(t') \Theta(t' - t_1) \end{pmatrix}. \quad (\text{E.19})$$

In the form of Eq. (E.19), it is clear it is a two-dimensional vector which elements are given by inner products of two functions. One function is the input pulse $s_{\text{in}}(t)$. The other is the windowed impulse response

$$\sqrt{2\gamma_j} u_{j1}^*(t_2 - t, 0) \Theta(t - t_1), \quad j = 1, 2. \quad (\text{E.20})$$

For efficient CAFC, $s_{\text{in}}(t)$ is a simple pulse of carrier frequency $\sim (\bar{\omega} + \Delta_0/2)$ and bandwidth of the order of γ_1 . On the other hand, the functions in Eq. (E.20) have carrier frequency $\bar{\omega}$ and bandwidth $2\pi/(t_2 - t_1) \sim |\kappa|$. Because $|\Delta_0| \gg |\kappa|$ and $|\Delta_0| \gg \gamma_j$ ($j = 1, 2$), the inner product between $s_{\text{in}}(t)$ and functions in Eq. (E.20) is small. Hence, the column vector of Eq. (E.19) (i.e., the second term on the right-hand side of Eq. (E.17)) is negligible for comparatively large $|\Delta_0|$.

Appendix F

Mathematical description and optimization of CAFC

In this appendix, we collect several analytical and numerical results we utilize in Chapter 8 to examine and optimize CAFC. In Section F.1, we study analytically and numerically the complex-valued frequency splitting between the rings' supermodes for large inter-ring detuning. This analysis is useful to describe the filtered impulse responses which govern the CAFC efficiency, as discussed in Chapter 8. In Section F.2, we consider the energy Rabi oscillation from Ring 1 to Ring 2 while modulation is applied. We analytically evaluate the modulation duration which optimizes energy transfer from Ring 1 to Ring 2. We examine how this optimal duration and the corresponding energy-transfer efficiency depend on the ring parameters in the limit of large pre- and post-modulation inter-ring detuning. In Section F.3, we aim to determine the coupling rate between the input bus and Ring 1 which optimizes two-ring CAFC. This is a subtle problem, even in the limit of large inter-ring detuning. That is because its optimal value must balance the energy efficiency of loading the input pulse from the bus into Ring 1, and the energy leakage in the transfer from Ring 1 to Ring 2 during ring modulation. To tackle this problem, we model the partial efficiencies of bus-Ring 1 transfer and Ring 1-Ring 2 transfer as Taylor polynomials in the coupling rate. Then, we analytically optimize the resulting model for the net CAFC efficiency and use the model's optimum as an initial guess for a local nonlinear optimization routine. In Section F.4, we derive the approximate expression we use to evaluate the CAFC efficiency for finite inter-ring. In Section F.5, we explain our scheme for setting the coupling rate between Ring 2 and the output bus for two-ring CAFC. In it, we assume that the process's timescales are such that this coupling rate has negligible effect on its net efficiency, so we choose its value to tune the CAFC output's bandwidth.

F.1 Analysis of the complex-valued frequency splitting for large inter-ring detuning

In this section, we examine analytically and numerically the complex-valued frequency splitting Ω_0 between the rings' supermodes. Specifically, we consider the case when the inter-ring frequency detuning $\Delta_0 = (\omega_1 - \omega_2)$ between the rings' bare modes is large compared to their complex-valued coupling rate κ and the imbalance between their decay rates, $\delta = (\gamma_1 - \gamma_2)$. We focus in this case as this occurs before and after ring modulation in CAFC.

As in Chapter 8, we define Ω_0 through the exact relation

$$\Omega_0 = \sqrt{(\Delta_0 - i\delta)^2 + 4|\kappa|^2}, \quad \Omega_0^{(r)} \equiv \text{Re}\{\Omega_0\} > 0. \quad (\text{F.1})$$

For concreteness, Ω_0 is defined so that its real part $\Omega_0^{(r)}$ is positive, as indicated in Eq. (F.1).

To begin our analysis, we expand the real $\Omega_0^{(r)}$ and imaginary $\Omega_0^{(i)}$ parts of Ω_0 up to second order in κ and δ . To do so, we apply the Taylor polynomial expansion $\sqrt{1+x} = 1 + x/2 - x^2/8 + \mathcal{O}(x^3)$ to Eq. (F.1) and retain only terms up to second order in κ and δ . In this way, we obtain

$$\begin{aligned} \Omega_0^{(r)} &\approx |\Delta_0| + \frac{|\kappa|^2}{2|\Delta_0|}, \\ \Omega_0^{(i)} &\approx -s\delta. \end{aligned} \quad (\text{F.2})$$

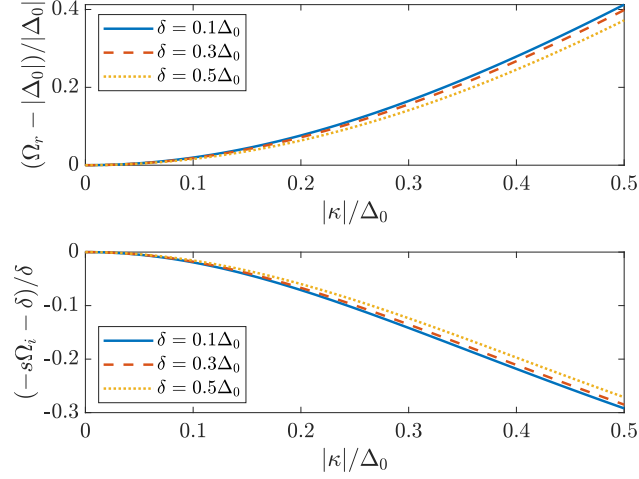


Figure F.1: Relative change in the real part $\Omega_0^{(r)}$ and imaginary part $\Omega_0^{(i)}$ of the complex-valued super-mode frequency splitting Ω for small values of $|\kappa|/\Delta_0$ and δ/Δ_0

Here, as in Chapter 8, s stands for $s = \text{sgn}(\Delta_0)$, where $\text{sgn}(x)$ is the signum function. Thus, to second order in κ and δ , non-zero inter-ring coupling κ increases $\Omega_0^{(r)}$ quadratically beyond $|\Delta_0|$. This is identical to what occurs in quantum mechanical second-order perturbation theory. On the other hand, $\Omega_0^{(i)}$ is unperturbed by inter-ring coupling κ and exactly equals $-s\delta$ to second order in κ and δ .

To analyze $\Omega_0^{(r)}$ and $\Omega_0^{(i)}$ beyond Taylor polynomial approximations, we calculate their value numerically by direct evaluation of Eq. (F.1). We then compare them to their limits $|\Delta_0|$ and $-s\delta$, respectively for vanishingly small κ and δ . For the case of $\Omega_0^{(i)}$, we specifically evaluate $-s\Omega_0^{(i)}$ rather than $\Omega_0^{(i)}$, as the former can be interpreted as the modified decay-rate splitting δ , as follows from Eq. (F.2).

First, we consider the real part, $\Omega_0^{(r)}$. For $\delta = 0$, $\Omega_0^{(r)} = \Omega$ and the plot of $\Omega_0^{(r)}$ as a function of $|\kappa|$ for fixed Δ_0 is a hyperbola. For $\delta \neq 0$, we evaluate $\Omega_0^{(r)}/|\Delta_0|$ numerically and as a function of small $|\kappa|/|\Delta_0|$, and for different small values of δ/Δ_0 . The resulting curves are shown in the upper plot of Fig. F.1. Clearly, $\Omega_0^{(r)}$ as a function of $|\kappa|$ is well-described by the hyperbola, even for non-zero δ . However, increasing non-zero δ decreases $\Omega_0^{(r)}$, although never below $|\Delta_0|$.

Next, we consider the imaginary part, $\Omega_0^{(i)}$. From Eq. (F.1), $\Omega_0^{(i)} = -s\delta$ for $\kappa = 0$. Furthermore, we find from Eq. (F.2) that this equality holds for non-zero κ to second order in δ and κ . By evaluating Eq. (F.1) exactly, we find that the effective decay splitting $-s\Omega_0^{(i)}$ decreases from δ with increasing $|\kappa|/\Delta_0$. Furthermore, this decrease in $-s\Omega_0^{(i)}$ is inhibited by increasing δ/Δ_0 . We note that the derivative of the fractional change $(-s\Omega_0^{(i)} - \delta)/\delta$ with respect to $|\kappa|/\Delta_0$ equals zero at $|\kappa| = 0$ for evaluated all values of δ/Δ_0 . This agrees with the fact that there is no term in Eq. (F.2) for $\Omega_0^{(i)}$ second order in the inter-ring coupling κ .

F.2 Optimization of the duration of inter-ring energy exchange

As discussed in Chapter 8, for optimal CAFC in the high modulation limit, we must choose the difference $(t_2 - t_1)$ between the modulation times (i.e., the modulation duration) to equal t_* , the duration which maximizes the modulus $|u_{21}(t, 0)|^2$. In this section, we obtain explicit expressions for t_* , and the corresponding energy exchange $|u_{21}(t_*, 0)|^2$. Furthermore, we analyze their dependence on the ratio between the rings' decay rates γ_j and the inter-ring coupling $|\kappa|$.

From Appendix E, the expression for $|u_{21}(t, 0)|^2$ is found from Eq. (E.3) as

$$|u_{21}(t, 0)|^2 = 2 \left| \frac{\kappa}{\Omega} \right|^2 \exp(-2\tilde{\gamma}t) [1 - \cos(\tilde{\Omega}t)]. \quad (\text{F.3})$$

Here, the frequency splitting $\tilde{\Omega}$ for $\Delta_0 = 0$ is purely real and given by the positive root of

$$\tilde{\Omega} = \sqrt{4|\kappa|^2 - \delta^2}. \quad (\text{F.4})$$

Of course, a necessary condition for t_* to be the global maximum of $|u_{21}(t, 0)|^2$ is for the derivative of $|u_{21}(t, 0)|^2$ with respect to t at $t = t_*$ to equal zero. This condition is satisfied if either

$$\cos(\tilde{\Omega}t_*) = 1, \quad \sin(\tilde{\Omega}t_*) = 0, \quad (\text{F.5})$$

or

$$\cos(\tilde{\Omega}t_*) = \frac{4\tilde{\gamma}^2 - \tilde{\Omega}^2}{4\tilde{\gamma}^2 + \tilde{\Omega}^2}, \quad \sin(\tilde{\Omega}t_*) = \frac{4\tilde{\gamma}\tilde{\Omega}}{4\tilde{\gamma}^2 + \tilde{\Omega}^2}. \quad (\text{F.6})$$

Eq. (F.5) corresponds to local minima of $|u_{21}(t, 0)|^2$ (where it vanishes exactly); and Eq. (F.6), to its local maxima.

The family of t_* satisfying Eq. (F.6) is a countable set of points separated by a period of $2\pi/\tilde{\Omega}$. Clearly, the global maximum of $|u_{21}(t, 0)|^2$ for positive t is the local maximum occurring at the smallest positive t . Otherwise, there exists another local maximum for smaller value of t (i.e., at $t - 2\pi/\tilde{\Omega}$), with $|u_{21}(t, 0)|^2$ larger by a factor of $\exp(4\pi\tilde{\gamma}/\tilde{\Omega}) > 1$. Furthermore, Eq. (F.6) implies that $\sin(\tilde{\Omega}t_*) > 0$, so the time t_* for the global maximum $|u_{21}(t, 0)|^2$ occurs in the interval $t_* \in (0, \pi/\tilde{\Omega})$. Imposing this restriction on Eq. (F.6), we obtain that the time t_* for the global maximum of $|u_{21}(t, 0)|^2$ is given by

$$\begin{aligned} t_* &= \frac{1}{\tilde{\Omega}} \arccos\left(\frac{4\tilde{\gamma}^2 - \tilde{\Omega}^2}{4\tilde{\gamma}^2 + \tilde{\Omega}^2}\right), \\ &= \frac{2}{\tilde{\Omega}} \arccos\left(\frac{2\tilde{\gamma}}{\sqrt{4\tilde{\gamma}^2 + \tilde{\Omega}^2}}\right), \\ &= \frac{\pi}{\tilde{\Omega}} - \frac{2}{\tilde{\Omega}} \arcsin\left(\frac{2\tilde{\gamma}}{\sqrt{\tilde{\Omega}^2 + 4\tilde{\gamma}^2}}\right). \end{aligned} \quad (\text{F.7})$$

Here, we define the $\arccos(x)$ and $\arcsin(x)$ functions so that $\arccos(x) \in [0, \pi]$ and $\arcsin(x) \in [-\pi/2, \pi/2]$ for $x \in [-1, 1]$, and we utilize the trigonometric identities $\cos 2\theta = \cos^2 \theta - \sin^2 \theta$ and $\arccos(x) = \pi/2 - \arcsin(x)$. Substituting Eq. (F.7) into Eq. (F.3), we readily obtain

$$|u_{21}(t_*, 0)|^2 = \exp\left[-\frac{2\tilde{\gamma}}{\tilde{\Omega}} \arccos\left(\frac{2\tilde{\gamma}}{\sqrt{\tilde{\Omega}^2 + 4\tilde{\gamma}^2}}\right)\right] \frac{|\kappa|^2}{|\kappa|^2 - \delta^2/4} \frac{\tilde{\Omega}^2}{\tilde{\Omega}^2 + 4\tilde{\gamma}^2}. \quad (\text{F.8})$$

To aid the interpretation of Eq. (F.7) and Eq. (F.8), it is useful to approximate them by Taylor polynomials in the ring decay rates γ_j , or, equivalently, their average value $\tilde{\gamma}$ and signed their difference $\delta = (\gamma_1 - \gamma_2)$. Then, to second order in $\tilde{\gamma}$ and δ , the optimal time from Eq. (F.7) is given by

$$t_* = t_*^{(0)} - \frac{\tilde{\gamma}}{|\kappa|^2} + \frac{\pi\delta^2}{16|\kappa|^3} + \mathcal{O}\left(\frac{\gamma_j^3}{|\kappa|^4}\right), \quad (\text{F.9})$$

where

$$t_*^{(0)} = \pi/(2|\kappa|). \quad (\text{F.10})$$

It is interesting to interpret the terms in the right-hand side of Eq. (F.9). The first term, $t_*^{(0)}$, is the optimal time for energy transfer (from Ring 1 to Ring 2) in the absence of ring loss. The second term (proportional to $\tilde{\gamma}$) is a decrease in time, required to account for the exponential decay of the rings' total energy. The third term (proportional to δ^2) reflects a decrease in the rate of inter-ring energy exchange due to the discrepancy in their decay rates.

To second order in $\tilde{\gamma}$ and δ , the maximum energy-transfer ratio $|u_{21}(t, 0)|^2$ is expressed as

$$|u_{21}(t_*, 0)|^2 = 1 - \pi \frac{\tilde{\gamma}}{|\kappa|} + \left(1 + \frac{\pi^2}{2}\right) \left(\frac{\tilde{\gamma}}{|\kappa|}\right)^2 + \frac{1}{4} \left(\frac{\delta}{|\kappa|}\right)^2 + \mathcal{O}\left(\left(\frac{\gamma_j}{|\kappa|}\right)^3\right). \quad (\text{F.11})$$

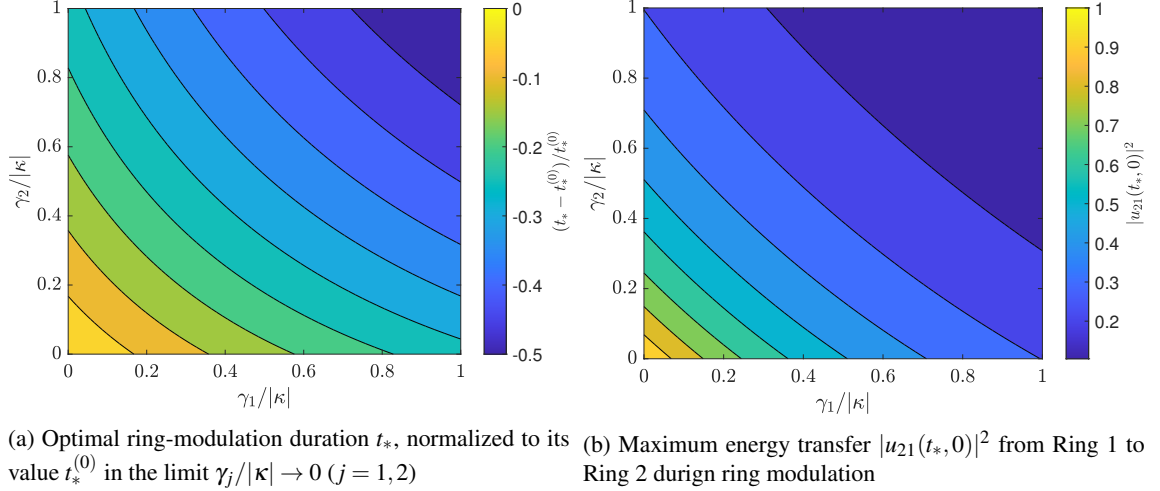


Figure F.2: Parameters for optimal inter-ring energy transfer as functions of the normalized decay rates, γ_j ($j = 1, 2$) normalized to the inter-ring coupling rate $|\kappa|$

The first term in Eq. (F.11) reflects that, in the absence of ring loss, energy transfer achieves efficiency of unity. The second term $-\pi\bar{\gamma}/|\kappa| = -2\bar{\gamma}t_*^{(0)}/t_*$ is the decrease in $|u_{21}(t_*, 0)|^2$ when t_* is taken as $t_*^{(0)}$. The second-order terms in Eq. (F.9) are harder to interpret in a straightforward, physically-intuitive manner.

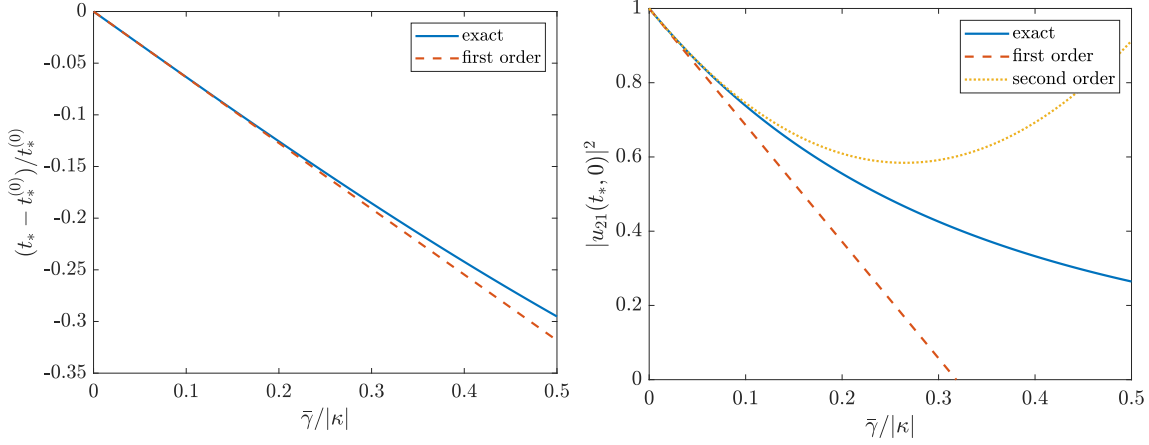
To conclude this section, we study the numerical dependence of the optimal time t_* and the corresponding maximum inter-ring energy exchange $|u_{21}(t_*, 0)|^2$ on the TCMT parameters. From Eq. (F.7) and Eq. (F.8), variation of these quantities depend only on two dimensionless variables, i.e., the ratios of the decay rates γ_j ($j = 1, 2$) to the inter-ring coupling $|\kappa|$. Hence, they are completely characterized by two-dimensional contour plots. In Fig. F.2, we present these contour plots. Fig. F.2a shows the variation of t_* (normalized to $t_*^{(0)}$) with respect to $\gamma_j/|\kappa|$ ($j = 1, 2$); and Fig. F.2b, that of $|u_{21}(t_*, 0)|^2$ with respect to the same ratios.

The dependence of t_* and $|u_{21}(t_*, 0)|^2$ with $\gamma_j/|\kappa|$ share commonalities. Their constant value curves are mostly parallel to lines of constant $(\gamma_1 + \gamma_2)/|\kappa| = 2\bar{\gamma}/|\kappa|$. Hence, they both quantities depend strongly on $\bar{\gamma}/|\kappa|$ and weakly on $\delta/|\kappa| = (\gamma_1 - \gamma_2)/|\kappa|$. Both quantities decrease monotonically with increasing $\bar{\gamma}/|\kappa|$ and constant $\delta/|\kappa|$. As expected, both quantities are invariant under the change $\gamma_1 \rightarrow \gamma_2$, $\gamma_2 \rightarrow \gamma_1$, and hence under the change $\delta \rightarrow -\delta$.

Since both t_* and $|u_{21}(t_*, 0)|^2$ depend only weakly on $\delta/|\kappa|$, we may take $\delta = 0$ and study their dependence on $\bar{\gamma}/|\kappa|$. The results are shown in the plots of Fig. F.3. In them, we plot the exact values of t_* (normalized to $t_*^{(0)}$) and $|u_{21}(t_*, 0)|^2$, in addition to the values predicted by the first- and second-order Taylor polynomials in $\bar{\gamma}/|\kappa|$ from Eqs. (F.9) and (F.11), for $\delta = 0$.

In Fig. F.3a, we first consider the optimal modulation time t_* . In it, we show only its first-order Taylor polynomial because the second-order term in Eq. (F.9) vanishes for $\delta = 0$. From Fig. F.3a, the dependence of t_* is evidently well described by its first-order Taylor polynomial, even for $\bar{\gamma}/|\kappa| \sim 0.5$. Additionally, t_* decreases slowly with $\bar{\gamma}/|\kappa|$, with a relative change of approximately $-0.6\bar{\gamma}/|\kappa|$ over this range.

In Fig. F.3b, we next examine the maximum inter-ring energy exchange $|u_{21}(t_*, 0)|^2$. In contrast to the case of t_* , the first- and second-order Taylor polynomials for $|u_{21}(t_*, 0)|^2$ are distinct, even for $\delta = 0$. Furthermore, the dependence of $|u_{21}(t_*, 0)|^2$ on $\bar{\gamma}/|\kappa|$ is well described by its first-order Taylor polynomial only for $\bar{\gamma}/|\kappa|$ in the order of 0.1 or smaller. And it is well described by its second-order one only up to $\bar{\gamma}/|\kappa| \sim 0.2$. Also, $|u_{21}(t_*, 0)|^2$ decreases more sharply with $\bar{\gamma}/|\kappa|$ than $t_*/t_*^{(0)}$, with an initial rate of π , as predicted by Eq. (F.11). These observations become immediately useful in Sec. F.3 to develop a polynomial model for the partial efficiency η_{02} from the input bus to Ring 2 as a function of bus-ring coupling γ_{1e} .



(a) Optimal ring-modulation duration t_* , normalized to its value $t_*^{(0)}$ in the limit $\gamma_j/|\kappa| \rightarrow 0$ ($j = 1, 2$)

(b) Maximum energy transfer $|u_{21}(t_*, 0)|^2$ from Ring 1 to Ring 2 during ring modulation

Figure F.3: Parameters for optimal inter-ring energy transfer as functions of the ring-averaged decay rate $\bar{\gamma} = (\gamma_1 + \gamma_2)/2$ normalized to the inter-ring coupling rate $|\kappa|$ and for $\gamma_1 = \gamma_2$. Also depicted are their first- and second-order Taylor polynomials around $\bar{\gamma} = 0$.

F.3 Analytical optimization of the input bus coupling

In this section, we aim to determine the optimal coupling rate γ_{1e} between the input bus and Ring 1 for CAFC. This problem is subtle, even in the limit of infinite inter-ring detuning $|\Delta_0|$. This is because the optimal γ_{1e} is governed by two competing processes. On one hand, maximum coupling of the input pulse $s_{\text{in}}(t)$ from the bus waveguide into Ring 1 requires γ_{1e} to be in the order of the input's bandwidth, as discussed in Chapter 6. On the other hand, minimizing energy leakage in the transfer from Ring 1 to Ring 2 requires γ_{1e} to be as small as possible. The optimal value of bus-ring coupling, denoted as γ'_{1e} , must balance these two processes.

We aim to approximate this optimal γ'_{1e} numerically employing the iterative Newton method for local optimization. Nonetheless, to start the Newton method's iteration, we require an accurate initial guess of the value of γ'_{1e} . To obtain this initial guess, we derive an approximate analytical expression for γ'_{1e} , accurate when the ring decay rates γ_j are small compared to the inter-ring coupling $|\kappa|$.

For simplicity, we consider the CAFC efficiency η in the limit $|\Delta_0| \rightarrow \infty$. Then, as discussed in Chapter 8, the overall CAFC efficiency factors into three partial efficiencies, η_{01} , η_{12} , and η_{23} . In the limit $|\Delta_0| \rightarrow \infty$, the coupling rate γ_{1e} affects only the processes of loading the input $s_{\text{in}}(t)$ into Ring 1 and of transferring the energy from Ring 1 to Ring 2. Hence, we need only consider the partial efficiency η_{02} of these two processes in succession. This factors as

$$\eta_{02} = \eta_{01}\eta_{12}. \quad (\text{F.12})$$

As in Chapter 8, η_{01} is the efficiency of loading the input from the bus into Ring 1; and η_{12} , that of transferring energy from Ring 1 to Ring 2.

To optimize η_{02} with respect to γ_{1e} analytically, we require explicit expressions for the dependence of the partial efficiencies η_{01} and η_{12} with respect to γ_{1e} . As shown in Chapter 8, $\eta_{12} = |u_{12}(t_2 - t_1, 0)|^2$. So, if we set the modulation duration $(t_2 - t_1)$ to its optimal value t_* from Eq. (F.7), η_{12} equals the right-hand side of Eq. (F.8). Hence, the dependence of η_{12} on γ_{1e} is generally numerically involved. On the other hand, η_{01} , which explicit expression is given in Chapter 8, depends on the particular shape of the input pulse $s_{\text{in}}(t)$ and is generally complicated. Thus, it is impractical to analyze the general, exact expressions for these partial efficiencies. So we approximate them via Taylor polynomials.

As mentioned above and discussed in Ref. [140], η_{01} is optimized with respect to γ_{1e} when $\gamma_{1e} = k/T_s$, where T_s is the input pulse's duration, and k is a dimensionless constant of the order of unity, depending on the input pulse's shape and the intrinsic decay rate γ_{10} of Ring 1. On the other hand, $\eta_{12} = |u(t_*, 0)|^2$ from Eq. (F.8) with Taylor polynomial (F.11); again assuming that we take the difference $(t_2 - t_1)$ to have its optimal value t_* from Eq. (F.7). Thus, we assume that $|\kappa|$ is large enough compared to γ_{1e} so that $\gamma_{1e}T_s$ can be close to k while $\pi\bar{\gamma}/|\kappa| \ll 1$. Then, we may approximate

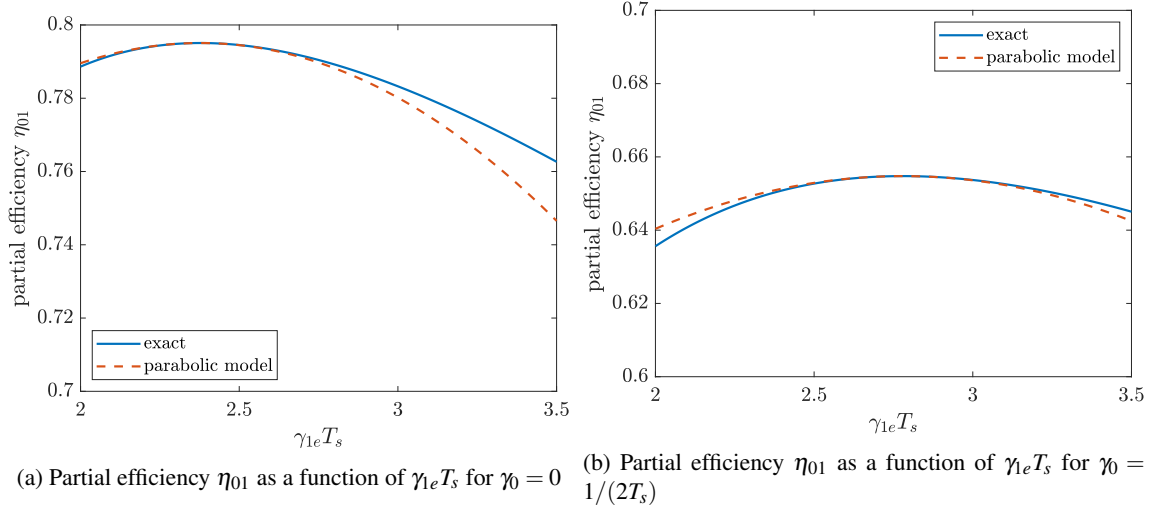


Figure F.4: Plots of the partial CAFC efficiency η_{01} of a raised-cosine input pulse as a function of the bus-ring coupling rate γ_{1e} normalized to the pulse duration T_s and for different values of the intrinsic loss γ_0 . Depicted as a solid blue line is the exact value of η_{01} computed numerically; and as a dashed orange line, its parabolic approximation, from Eq. (F.13).

η_{01} and η_{12} by the Taylor polynomials

$$\begin{aligned}\eta_{01} &= \xi_{01}^{(0)} + \frac{1}{2}\xi_{01}^{(2)}(\gamma_{1e}T_s - k)^2 + \mathcal{O}((\gamma_{1e}T_s - k)^3), \\ \eta_{12} &= 1 - \pi\bar{\gamma}/|\kappa| + \mathcal{O}((\gamma_j/|\kappa|)^2).\end{aligned}\tag{F.13}$$

Here, we recall that $\bar{\gamma} = (\gamma_{1e} + \gamma_{10} + \gamma_2)/2$ is the total, ring-averaged decay rate. $\xi_{01}^{(0)}$ is the value of η_{01} when $\gamma_{1e}T_s = k$; and $\xi_{01}^{(2)}$, the second derivative of η_{01} with respect to $\gamma_{1e}T_s$ at $\gamma_{1e}T_s = k$. Of course, $\xi_{01}^{(2)} < 0$ for $\gamma_{1e}T_s = k$ to be a maximum. In our numerical evaluation of Eq. (F.13), we evaluate $\xi_{01}^{(2)}$ via the well known finite-difference, three-point, midpoint formula for approximation of second-order derivatives [171].

In Section F.2, we studied numerically the accuracy of approximating $\eta_{12} = |u_{21}(t_s, 0)|^2$ by its first-order polynomial in $\bar{\gamma}/|\kappa|$. To complement that discussion, we briefly analyze the Taylor polynomial for η_{01} in Eq. (F.13). To do this, we consider the CAFC of a raised-cosine pulse of duration T_s as in Chapter 8. Then, in Fig. F.4, we plot η_{01} as a function of γ_{1e} , normalized to T_s , for $\gamma_0 = 0$ (Fig. F.4a) and for $\gamma_0 = 1/(2T_s)$ (Fig. F.4b). In these plots, we also depict the parabolic models of Eq. (F.13) with $\xi_{01}^{(0)}$, $\xi_{01}^{(2)}$, and k computed numerically for the corresponding value of γ_0 .

From Fig. F.4, we verify that η_{01} indeed is a concave function of $\gamma_{1e}T_s$, and it exhibits a maximum with respect to γ_{1e} when $\gamma_{1e}T_s$ is of the order of unity. Specifically, this occurs at $\gamma_{1e}T_s = 2.3780$ for $\gamma_0 = 0$ [140]; and at $\gamma_{1e}T_s = 2.7800$ for $\gamma_0 = 1/(2T_s)$. From these maxima, $\xi_{01}^{(0)} = 0.7951$ [140], and $\xi_{01}^{(2)} = -0.0771$ for $\gamma_0 = 0$; and $\xi_{01}^{(0)} = 0.6548$, and $\xi_{01}^{(2)} = -0.0473$ for $\gamma_0 = 1/(2T_s)$. As expected, the maximum partial efficiency η_{01} decreases noticeably from $\gamma_0 = 0$ to $\gamma_0 = 1/(2T_s)$. Nonetheless, for both values of γ_0 , the η_{01} seems well described by the second-order Taylor polynomial of Eq. (F.13) for the values of $\gamma_{1e}T_s$ in Fig. F.4. The largest difference between the exact η_{01} and its second-order Taylor polynomial in these plots is for of ~ 0.2 at $\gamma_{1e}T_s = 3.5$ and $\gamma_0 = 0$.

In Fig. F.5, we analyze more deeply the dependence of the partial efficiency η_{01} for the raised-cosine input on the intrinsic loss γ_0 . In Fig. F.5a, we plot η_{01} as a function of $\gamma_{1e}T_s$ for different values of $\gamma_0 T_s$ from 0 to 0.5. We verify that, for all considered values of γ_0 , and for $\gamma_{1e}T_s$ between 1 and 4, η_{01} is a concave function of $\gamma_{1e}T_s$ and it exhibits a single maximum with respect to $\gamma_{1e}T_s$. In Fig. F.5b, we plot as functions of $\gamma_0 T_s$, the parameters defining the parabolic model of Eq. (F.13) for η_{01} . Specifically, the value k of $\gamma_{1e}T_s$ which maximizes η_{01} ; $\xi_{01}^{(0)}$ the maximum value of η_{01} ; and $\xi_{01}^{(2)}$, the concavity of η_{01} as a function of $\gamma_{1e}T_s$, when $\eta_{01} = \xi_{01}^{(0)}$. We verify that all three parameters are well defined and vary smoothly and monotonically with increasing $\gamma_0 T_s$. As γ_0 increases, the optimal γ_{1e} must increase so coupling from the input bus into Ring 1 occurs more rapidly, and less energy is dissipated into the environment

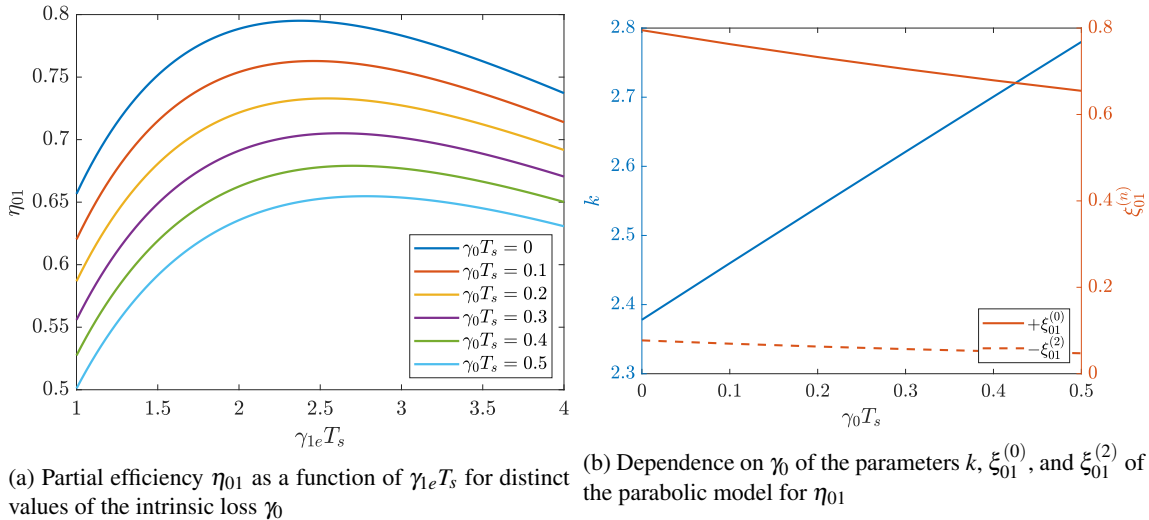


Figure F.5: Dependence on the intrinsic loss γ_0 of the partial efficiency η_{01} and of its parabolic model as a function of $\gamma_{1e} T_s$ from Eq. (F.13).

during this process. Naturally, as the intrinsic dissipation γ_0 increases, the maximum $\xi_{01}^{(0)}$ decreases. Comparatively, the concavity $\xi_{01}^{(2)}$ varies slowly with $\gamma_0 T_s$.

Substituting Eq. (F.13) into Eq. (F.12), we find that, for sufficiently large $|\kappa|$ compared to T_s and $|\Delta_0|$ to all other dynamic rates, the partial efficiency η_{02} from input bus to Ring 2 can be approximated as a third-degree polynomial in γ_{1e} . Hence, the derivative of η_{02} with respect to γ_{1e} is a polynomial of degree two, which roots can be obtained via the quadratic formula. By approximating the optimal bus-ring coupling γ'_{1e} by one of these roots, we find

$$\gamma'_{1e} \approx \frac{\gamma'}{3} + \frac{2k}{3T_s} + \text{sgn}\left(\frac{k}{T_s} - \gamma'\right) \sqrt{\left(\frac{k}{3T_s} - \frac{\gamma'}{3}\right)^2 + \frac{2}{3T_s^2} \left| \frac{\xi_{01}^{(0)}}{\xi_{01}^{(2)}} \right|}. \quad (\text{F.14})$$

In Eq. (F.14), $\text{sgn}(x)$ is the signum function, and γ' is an auxiliary variable, defined as

$$\gamma' = 2|\kappa|/\pi - \gamma_{10} - \gamma_2. \quad (\text{F.15})$$

The sign of the radical in Eq. (F.14) is chosen so that, the limit of $\left| \xi_{01}^{(0)}/\xi_{01}^{(2)} \right| \rightarrow 0$, γ'_{1e} converges to k/T_s . This convergence must occur, as in the limit $\left| \xi_{01}^{(0)}/\xi_{01}^{(2)} \right| \rightarrow 0$, the partial efficiency η_{01} becomes highly susceptible to changes in γ_{1e} , which pulls γ'_{1e} towards the value which optimizes η_{01} , i.e., k/T_s .

In Chapter 8, we evaluate numerically the exact optimum value of γ_{1e} which maximizes η_{02} for $\gamma_0 = 0$. Furthermore, we compare it as a function of $|\kappa|T_s$ with two estimates for it: γ'_{1e} of Eq. (F.14), and the value k/T_s which maximizes η_{01} . There, we find that the optimum γ_{1e} lies always between these two estimates for $\gamma_0 = 0$ and for any $|\kappa|T_s$. Moreover, these three quantities (the exact optimum and its estimates) converge as $|\kappa|T_s$ increases. In the remainder of this section, we verify numerically that these conclusions also hold for $\gamma_0 > 0$.

To do so, we report in Fig. F.6 plots of the exact optimum $\gamma_{1e} T_s$ that maximizes η_{02} as a function of $|\kappa|T_s$ for different values of γ_0 . As in Chapter 8, we show the optimum γ_{1e} alongside its two estimates, γ'_{1e} and k/T_s . We confirm that the optimum γ_{1e} always lies between its two estimates for all the considered values of $|\kappa|T_s$ and $\gamma_0 T_s$. Additionally, as observed for $\gamma_0 = 0$, the exact optimum γ_{1e} and its estimates converge as $|\kappa|T_s$ increases. As seen in Fig. F.5, the estimate k/T_s increases with γ_0 . Accordingly, γ'_{1e} and the exact optimum converge to this larger value as γ_0 increases.

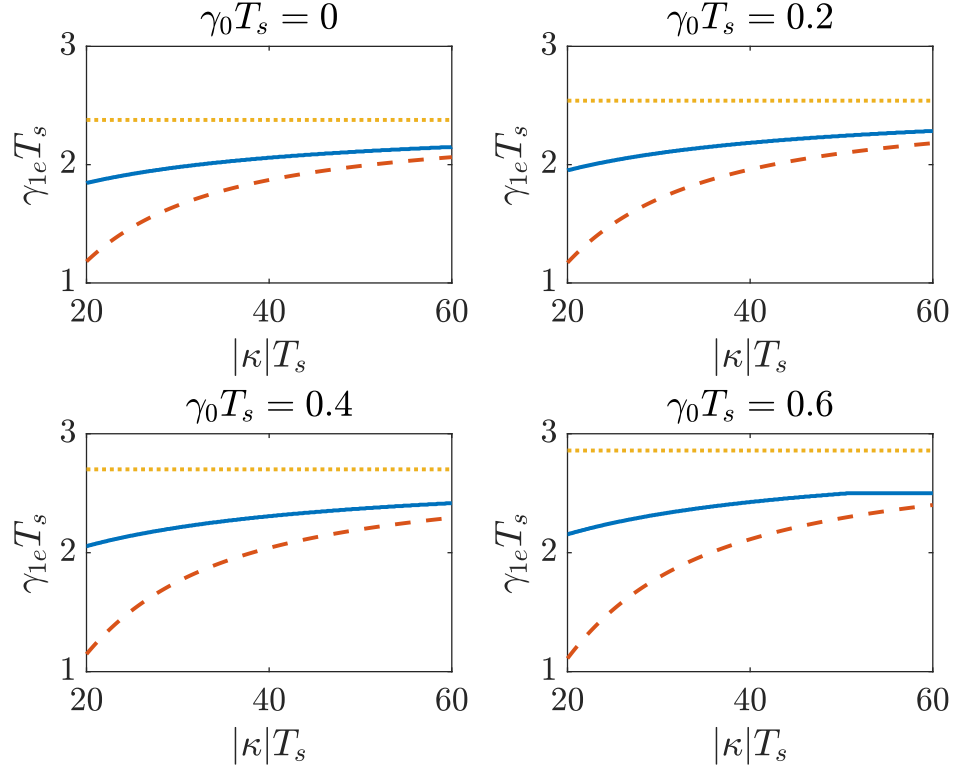


Figure F.6: Plots of the optimum value of γ_{1e} (solid blue) maximizing η_{02} , and its estimates γ'_{1e} (dashed orange) from Eq. (F.14), and k/T_s (dotted yellow) as functions of $|\kappa|T_s$ and for different values of $\gamma_0 T_s$.

F.4 Expression for frequency-converted energy under finite inter-ring detuning

In this section, we obtain the approximate expression we use to numerically evaluate the CAFC efficiency for finite inter-ring detuning $|\Delta_0|$. In accordance with the arguments of Appendix E, we expect that, for $|\Delta_0|$ large compared to the other TCMT rates, the output $s_{\text{out}}(t)$ will oscillate at the output frequency only after the ring modulation concludes, i.e., for $t > t_2$. Thus, according to Appendix E, we may write $s_{\text{out}}(t)$ as

$$\begin{aligned} s_{\text{out}}(t) &= k_{\text{out}}^\dagger U(t - t_2, \Delta_0) a(t_2), \\ &= \sqrt{2\gamma_{2e}} [a_1(t_2) u_{21}(t - t_2, \Delta_0) + a_2(t_2) u_{22}(t - t_2, \Delta_0)]. \end{aligned} \quad (\text{F.16})$$

Then, we may pass the output $s_{\text{out}}(t)$ by an ideal filter centered at the target output frequency $\bar{\omega} - s\Omega_0^{(r)}/2$. If $|\Delta_0|$ is sufficiently large, then the filtered output $s_{\text{out}}^{(F)}(t)$ is given by

$$\begin{aligned} s_{\text{out}}^{(F)}(t) &= \sqrt{2\gamma_{2e}} \left[a_1(t_2) u_{21}^{(F)}(t - t_2, \Delta_0) + a_2(t_2) u_{22}^{(F)}(t - t_2, \Delta_0) \right], \\ &= \sqrt{2\gamma_{2e}} \left[-s \frac{\kappa_{21}}{\Omega_0} a_1(t_2) + \frac{1}{2} \left(1 + s \frac{\Delta_0 - i\delta}{\Omega_0} \right) a_2(t_2) \right] \\ &\quad \times \exp[(-i\bar{\omega} - \bar{\gamma} + is\Omega_0/2)(t - t_2)] \Theta(t - t_2). \end{aligned} \quad (\text{F.17})$$

Here, $u_{2j}^{(F)}(t, \Delta_0)$ are the filtered impulse responses $u_{2j}(t, \Delta_0)$ ($j = 1, 2$); and $s = \text{sgn}(\Delta_0)$, as in Chapter 8.

It follows from Eq. (F.17) that, to this approximation, the inner product $\langle s_{\text{out}}^{(F)}(t) | s_{\text{out}}^{(F)}(t) \rangle$ is the energy in the cascaded-AFC output. We readily evaluate this inner-product as

$$\langle s_{\text{out}}^{(F)}(t) | s_{\text{out}}^{(F)}(t) \rangle = \frac{\gamma_{2e}}{\bar{\gamma}_2} \left| -s \frac{\kappa_{21}}{\Omega_0} a_1(t_2) + \frac{1}{2} \left(1 + s \frac{\Delta_0 - i\delta}{\Omega_0} \right) a_2(t_2) \right|^2. \quad (\text{F.18})$$

Here, as in Chapter 8, $\tilde{\gamma}_2$ is the modified decay rate of Ring 2, $\tilde{\gamma}_2 = \bar{\gamma} + s\Omega_0^{(i)}/2$. If the input $s_{\text{in}}(t)$ is normalized so that its energy, $\langle s_{\text{in}}(t)|s_{\text{in}}(t) \rangle$ equals unity, then the output energy Eq. (F.18) equals the CAFC efficiency η . Thus, we use Eq. (F.18) as our expression for η , ensuring first that $s_{\text{in}}(t)$ is normalized so $\langle s_{\text{in}}(t)|s_{\text{in}}(t) \rangle = 1$. We evaluate the energy amplitude vector $a(t_2) = (a_1(t_2), a_2(t_2))^T$ numerically by solving the TCMT equations via the Runge-Kutta method.

F.5 Output bus coupling efficiency in the high-modulation limit

As explained in Chapter 8, the numerical problem of optimizing the CAFC efficiency η simultaneously with respect to γ_{1e} and γ_{2e} is formidable, even in the limit of $|\Delta_0| \rightarrow \infty$. To circumvent this problem, we assume that the ratios $\gamma_{2e}/|\kappa|$ and γ_0/γ_{2e} are small. Then, we may accurately neglect the effect of γ_{2e} on η , and we rather engineer its effect on the output pulse duration. Specifically, we set γ_{2e} so that the frequency-shifted output $s_{\text{out}}(t)$ has a root-mean-square (RMS) duration T_{RMS} approximately equal to that of the input $s_{\text{in}}(t)$. Consequently, the frequency-shifted $s_{\text{out}}(t)$ shall have a bandwidth comparable to that of $s_{\text{in}}(t)$, in the order of $2\pi/T_{\text{RMS}}$. To achieve this, we note that, as discussed in Chapter 8, $s_{\text{out}}(t)$ decreases exponentially with the modified decay rate $\tilde{\gamma}_2$ of Ring 2, altered by the non-zero inter-ring coupling $|\kappa|$. Thus, its RMS duration equals $(2\tilde{\gamma}_2)^{-1}$. So that both $s_{\text{in}}(t)$ and $s_{\text{out}}(t)$ have approximately the same RMS duration, we should set

$$\tilde{\gamma}_2 = 1/(2T_{\text{RMS}}). \quad (\text{F.19})$$

However, $\tilde{\gamma}_2$ is given by $\tilde{\gamma}_2 = \bar{\gamma} + s\Omega_0^{(i)}/2$ and Ω_0 itself depends on $\delta = \gamma_1 - \gamma_2$, according to Eq. (F.1). So setting γ_{2e} so that $\tilde{\gamma}_2$ satisfies Eq. (F.19) incurs into the same problem of requiring the simultaneous solution of two related nonlinear equations for γ_{1e} and γ_{2e} . Thus, we assume $|\Delta_0|$ is sufficiently large to approximate $\tilde{\gamma}_2 \approx \gamma_2$ in Eq. (F.19) and we set

$$\gamma_2 = 1/(2T_{\text{RMS}}). \quad (\text{F.20})$$

From Eq. (F.2), it follows that the approximation $\tilde{\gamma}_2 \approx \gamma_2$ is accurate to second order in $|\Delta_0|^{-1}$ compared to $|\kappa|$ and $|\delta|$. Thus, Eq. (F.19) is satisfied to second order in $|\Delta_0|^{-1}$ when Eq. (F.20) is satisfied exactly.

Next, we aim to understand how the choice Eq. (F.20) affects the AFC efficiency η . For simplicity, we analyze η in the $|\Delta_0| \rightarrow \infty$ limit through the partial efficiencies $\eta_{j,j+1}$ ($j = 1, 2$). Substituting Eq. (F.20) into the Taylor polynomial in Eq. (F.13) for η_{12} , we obtain, to first order in $|\kappa|^{-1}$,

$$\eta_{12} = 1 - \frac{\pi\gamma_1}{2|\kappa|} - \frac{\pi}{4|\kappa|T_{\text{RMS}}} + \mathcal{O}\left(\left(\frac{\gamma_j}{|\kappa|}\right)^2\right). \quad (\text{F.21})$$

Furthermore, we recall from Ref. [140] that $\gamma_{10} \ll \gamma_{1e}$ and $\gamma_{1e} \sim T_{\text{RMS}}$ for the loading efficiency η_{01} to approach its upper limit, imposed by the Schwarz inequality. Hence, $\gamma_1/|\kappa| \sim (|\kappa|T_{\text{RMS}})^{-1}$. Substituting this into Eq. (F.21), we find that

$$1 - \eta_{12} = \mathcal{O}((|\kappa|T_{\text{RMS}})^{-1}). \quad (\text{F.22})$$

On the other hand, substituting Eq. (F.20) into the definition of η_{23} in Chapter 8, we obtain

$$\eta_{23} = \gamma_{2e}/\gamma_2 = 1 - 2\gamma_{20}T_{\text{RMS}}. \quad (\text{F.23})$$

In Chapter 8, we verify numerically that, in the limit $|\Delta_0| \rightarrow \infty$, η converges to the Schwarz limit of η_{01} as, simultaneously, $\gamma_0T_{\text{RMS}} \rightarrow 0$ and $|\kappa|T_{\text{RMS}} \rightarrow \infty$. This is in agreement with Eqs. (F.22) and (F.23) for η_{12} and η_{23} , respectively.

Appendix G

Analyticity of the CAFC efficiency

In this appendix, we aim to explain the origin of the analyticity of the CAFC efficiency η as a function of the smallness dimensionless parameters $|\kappa/\Delta_0|$, $(|\kappa|T_s)^{-1}$, and $\gamma_0 T_s$, as observed and leveraged in Chapter 8. A fully mathematically rigorous discussion of the analyticity of η is outside the scope of this thesis. Rather, our objective is to provide an intuitive, mathematical explanation of the power-series behavior of the dependence of η on the smallness parameters.

This appendix consists of two sections. First, in Section G.1, we leverage Taylor's theorem of real analysis to justify the polynomial model for the CAFC efficiency η used in Chapter 8, assuming η is a smooth function of the smallness parameters. Then, in Section G.2, we discuss sufficient conditions for η to be a real analytic (and thus smooth) function of the smallness parameters. Specifically, we argue that if the input $s_{\text{in}}(t)$ is a holomorphic (i.e., complex analytic) function of the TCMT parameters, then η is a real analytic function of the three smallness parameters.

G.1 Derivation of the polynomial model for the CAFC efficiency

In this section, we justify the approximation of the CAFC efficiency η as a polynomial function from Chapter 8, assuming η to be a smooth function of the smallness parameters $|\kappa/\Delta_0|$, $(|\kappa|T_s)^{-1}$, and $\gamma_0 T_s$. We discuss sufficient conditions for this assumption of the smoothness of η to hold in Section G.2. Thus, we write

$$\eta = f(|\kappa/\Delta_0|, (|\kappa|T_s)^{-1}, \gamma_0 T_s), \quad (\text{G.1})$$

where f is a smooth function of its three parameters.

In Chapter 8, we showed that η converges to a finite limit η_0 as $|\kappa/\Delta_0|$ tends to zero. Thus, we make f in Eq. (G.1) as a continuous function from the right with respect to $|\kappa/\Delta_0|$ at $|\kappa/\Delta_0| = 0$ through the definition

$$f(0, (|\kappa|T_s)^{-1}, \gamma_0 T_s) = \lim_{|\kappa/\Delta_0| \rightarrow 0} \eta = \eta_0. \quad (\text{G.2})$$

Similarly, we showed that the limit η_0 itself converges to a finite limit as $|\kappa/\Delta_0|$ tends to zero. Specifically, η_0 converges to the product of partial efficiencies $\eta_{01}\eta_{23}$ in this limit. Then, we also define f continuous from the right in the limit $|\kappa|T_s \rightarrow \infty$ according to

$$f(0, 0, \gamma_0 T_s) = \lim_{|\kappa|T_s \rightarrow \infty} \eta_0 = \eta_{01}\eta_{23}. \quad (\text{G.3})$$

In the right-hand side of Eq. (G.3), η_{01} is the efficiency of loading the input $s_{\text{in}}(t)$ into Ring 1 (isolated by the large detuning from Ring 2), maximized over γ_{1e} and t_1 for a fixed value of $\gamma_0 T_s$. Meanwhile, η_{02} is the efficiency of extracting the frequency-shifted output $s_{\text{out}}(t)$ from Ring 2 into the output bus. In our CAFC scheme, η_{23} is given by Eq. (F.23) in Sec. ??.

For simplicity, and for relevance to Chapter 8, we consider the CAFC efficiency η for a fixed value of the normalized intrinsic loss $\gamma_0 T_s$, but variable normalized interring coupling $|\kappa|T_s$ and normalized interring detuning $|\Delta_0/\kappa|$. Physically, this is the case when the intrinsic loss γ_0 and the pulse duration T_s are constant, but the interring coupling $|\kappa|$ and the interring detuning $|\Delta_0|$ are variable. Thus, we henceforth omit the dependence of the function f on

its third argument $\gamma_0 T_s$ for succinctness. Generalization of the following analysis for variable, albeit small, $\gamma_0 T_s$ is straightforward.

With the function f defined via Eqs. (G.1) to (G.3), we next aim to approximate it via a simple polynomial in the smallness parameters. To do so, we note that from Eqs. (G.1) to (G.3), f is then continuous and assumed smooth for sufficiently large $|\kappa|T_s$ and for $|\kappa/\Delta_0| \in [0, h]$ for sufficiently small h . Then, we may utilize Taylor's theorem of real analysis [172, 173] to approximate f via its Taylor polynomial in $|\kappa/\Delta_0|$ as

$$f(|\kappa/\Delta_0|, (|\kappa|T_s)^{-1}) = f(0, (|\kappa|T_s)^{-1}) + \frac{1}{2} \left| \frac{\kappa}{\Delta_0} \right|^2 \frac{\partial^2 f}{\partial |\kappa/\Delta_0|^2} (0, (|\kappa|T_s)^{-1}) + \mathcal{O} \left(\left| \frac{\kappa}{\Delta_0} \right|^3 \right). \quad (\text{G.4})$$

In Eq. (G.4), we neglect the term proportional to $|\kappa/\Delta_0|$ (i.e., the first-order term). This is because we find numerically in the Chapter 8 that η converges approximately quadratically with respect to $|\kappa/\Delta_0|$ to η_0 . Hence we must require Eq. (G.4) to satisfy

$$f(|\kappa/\Delta_0|, (|\kappa|T_s)^{-1}) = f(0, (|\kappa|T_s)^{-1}) + \mathcal{O}(|\kappa/\Delta_0|^2). \quad (\text{G.5})$$

By Taylor's theorem [172, 173], Eq. (G.5) is satisfied if and only if

$$\frac{\partial f}{\partial |\kappa/\Delta_0|} (0, (|\kappa|T_s)^{-1}) = 0, \quad (\text{G.6})$$

in agreement with Eq. (G.4).

We note that we have approximated f via its Taylor polynomial at the boundary $|\kappa/\Delta_0| = 0$ where it is defined. This is not possible according to the usual formulation of Taylor's theorem in complex analysis [169, 174], as it requires the expansion point of f to lie inside some open neighborhood where f is complex analytic. Nonetheless, formulations of Taylor's theorem in real analysis [172, 173] do allow the expansion point to lie at the boundary of the interval of the real axis where f is real analytic. So application of Taylor's theorem at $|\kappa/\Delta_0| = 0$ introduces no subtleties once f is defined to satisfy Eq. (G.2) and the derivative in Eq. (G.4) is assumed to be defined as a right-hand derivative.

Next, we approximate the first term in the right-hand side of Eq. (G.4) as a Taylor polynomial in $(|\kappa|T_s)^{-1}$ around $(|\kappa|T_s)^{-1} = 0$. In this manner, we obtain

$$f(0, (|\kappa|T_s)^{-1}) = f(0, 0) + \frac{1}{|\kappa|T_s} \frac{\partial f}{\partial (|\kappa|T_s)^{-1}} (0, 0) + \mathcal{O}((|\kappa|T_s)^{-2}). \quad (\text{G.7})$$

In Eq. (G.7), we recall that $f(0, 0)$ is defined through Eq. (G.3). Again, expansion of $f(0, (|\kappa|T_s)^{-1})$ at the boundary is allowed via the formulation of Taylor's theorem of real analysis [172, 173].

We now substitute Eq. (G.7) into Eq. (G.4) and retain only the explicit terms, as they are the lowest-order non-vanishing terms in the smallness parameters $|\kappa/\Delta_0|$ and $(|\kappa|T_s)^{-1}$. Then, we substitute the resulting approximation for f in Eq. (G.1) for the CAFC efficiency η to obtain

$$\eta \approx f(0, 0) + \frac{1}{|\kappa|T_s} \frac{\partial f}{\partial (|\kappa|T_s)^{-1}} (0, 0) + \frac{1}{2} \left| \frac{\kappa}{\Delta_0} \right|^2 \frac{\partial^2 f}{\partial |\kappa/\Delta_0|^2} (0, (|\kappa|T_s)^{-1}). \quad (\text{G.8})$$

Although simplified, the right-hand side of Eq. (G.8) is still not yet of the form of a polynomial in the smallness parameters $(|\kappa|T_s)^{-1}$ and $|\kappa/\Delta_0|$, as desired. To put it in this form, we must approximate the last term in Eq. (G.8) itself by a polynomial. To do so, we apply Taylor's theorem again (alternatively, the mean value theorem [172, 173]) to $\partial^2 f(0, (|\kappa|T_s)^{-1})/\partial |\kappa/\Delta_0|^2$ and write

$$\frac{\partial^2 f}{\partial |\kappa/\Delta_0|^2} (0, (|\kappa|T_s)^{-1}) = \frac{\partial^2 f}{\partial |\kappa/\Delta_0|^2} (0, 0) + \mathcal{O}((|\kappa|T_s)^{-1}). \quad (\text{G.9})$$

Substituting Eq. (G.9) into Eq. (G.8), we argue that we can neglect the term proportional to $\mathcal{O}((|\kappa|T_s)^{-1})$ in the resulting expression. This is because this term is proportional to the product of $(|\kappa|T_s)^{-1}$ and $|\kappa/\Delta_0|^2$. Thus, for sufficiently small values of these parameters, this term would be small compared to both $(|\kappa|T_s)^{-1}$ and $|\kappa/\Delta_0|^2$. Thus, after further substituting Eq. (G.3) into Eq. (G.8), we obtain the desired approximate expression for η ,

$$\eta \approx \eta_{01} \eta_{23} + \frac{1}{|\kappa|T_s} \frac{\partial f}{\partial (|\kappa|T_s)^{-1}} (0, 0) + \frac{1}{2} \left| \frac{\kappa}{\Delta_0} \right|^2 \frac{\partial^2 f}{\partial |\kappa/\Delta_0|^2} (0, 0). \quad (\text{G.10})$$

After relabeling the coefficients $\partial f(0, 0)/\partial (|\kappa|T_s)^{-1}$ and $\partial^2 f(0, 0)/\partial |\kappa/\Delta_0|^2$ as $-c_1$ and $-c_2$, respectively, we obtain the polynomial model for the CAFC efficiency η used in Chapter 8.

G.2 Sufficient conditions for the real analyticity of the CAFC efficiency

We recall that, in Section G.1, we assume the CAFC efficiency η to be a smooth function of the normalized smallness parameters $|\kappa/\Delta_0|$, $(|\kappa|T_s)^{-1}$, and $\gamma_0 T_s$. In this section, we aim to discuss sufficient conditions η to be a real analytic, and thus smooth, function of these smallness parameters.

To start, we note that the (filtered) frequency shifted output is given by Eq. (F.17). The expression is clearly holomorphic with respect to the TCMT parameters if $\gamma_{2e} \neq 0$ and $\Omega_0 \neq 0$, and if the ring amplitude vector $a(t_2) = (a_1(t_2), a_2(t_2))^T$ itself is holomorphic with respect to them. The vector $a(t_2)$ is given by Eq. (??). Hence, from Leibnitz's rule of complex analysis [175], $a(t_2)$ is an holomorphic function of the TCMT parameters if the matrices $\exp(-iH_0 t)$ and $\exp(-iH_m t)$, the vector $k_{\text{in}} = (\sqrt{2\gamma_{1e}}, 0)^T$, and the scalar $s_{\text{in}}(t)$ are continuous functions of t (for $t \in (-\infty, t_2]$) and analytic functions of the TCMT parameters. The vector k_{in} clearly meets these conditions if $\gamma_{1e} \neq 0$. And it is straightforward to verify whether the scalar input $s_{\text{in}}(t)$ satisfies them. To determine whether the exponential matrices meet these conditions, some discussion is required.

Thus, we examine the exponential matrices $\exp(-iH_0 t)$ and $\exp(-iH_m t)$ to verify that they indeed satisfy these conditions. First, it is well known [151] that exponential matrices are continuous functions of a scalar multiplying its matrix argument. Hence $\exp(-iH_0 t)$ and $\exp(-iH_m t)$ are continuous functions of t . Second, it is well known from quantum-mechanical time-dependent perturbation theory that exponential matrices can always be expanded as a power series, specifically a Dyson series [70, 110], in terms of perturbations to their matrix arguments. Power series are holomorphic functions inside their radius of convergence [169]. So the exponential matrices $\exp(-iH_0 t)$ and $\exp(-iH_m t)$ are holomorphic functions of the TCMT parameters if the Dyson series are always assumed to converge for sufficiently small perturbations, and if the matrices H_0 and H_m themselves are holomorphic functions of the TCMT parameters. This latter condition is clearly satisfied, provided we consider $|\kappa|$ rather than the complex-valued κ as a TCMT parameter, as H_0 and H_m depend on both κ and κ^* .

Even though the frequency-shifted output $s_{\text{out}}^{(F)}(t)$ is a holomorphic function of the TCMT parameters, the CAFC frequency η is not in general. This is because η is the ratio of the output energy $\langle s_{\text{out}}^{(F)}(t) | s_{\text{out}}^{(F)}(t) \rangle$ to the input energy $\langle s_{\text{in}}(t) | s_{\text{in}}(t) \rangle$, which is evidently not a holomorphic function of $s_{\text{in}}(t)$ and $s_{\text{out}}^{(F)}(t)$. Hence, η does not preserve the complex analyticity of $s_{\text{in}}(t)$ and $s_{\text{out}}^{(F)}(t)$ with respect to the TCMT parameters.

Nonetheless, when $s_{\text{in}}(t)$ and $s_{\text{out}}^{(F)}(t)$ are holomorphic functions of the TCMT parameters, they are complex-analytic. Then, $\langle s_{\text{in}}(t) | s_{\text{in}}(t) \rangle$, $\langle s_{\text{out}}^{(F)}(t) | s_{\text{out}}^{(F)}(t) \rangle$, and hence η (provided $\langle s_{\text{in}}(t) | s_{\text{in}}(t) \rangle \neq 0$), are real-analytic functions of the TCMT parameters [176]. In other words, because $s_{\text{in}}(t)$ and $s_{\text{out}}^{(F)}(t)$ have complex power series representations in the TCMT parameters, η has a real power series representation in these parameters.

As discussed in Chapter 8 and Appendix F, we choose several TCMT timescales to satisfy certain conditions to engineer the CAFC output. Specifically, we set the input bus-ring coupling, γ_{1e} , and the modulation times, t_1 and t_2 , to maximize η in the infinite detuning limit; and we set the output bus-ring coupling γ_{2e} such that the CAFC output has equal RMS duration as the input. This choice reduces the dependence of the CAFC efficiency η to only that on the three dimensionless variables $|\Delta_0/\kappa|$, $|\kappa|T_s$, and $\gamma_0 T_s$. Hence, we next aim to explain the real analyticity of η with respect to these three smallness variables, given the real analyticity of η on all the timescales when they are taken as independent, as explained in the previous paragraph.

To do so, we invoke the implicit function theorem (IFT) for real analytic functions [177]. According to this theorem, if the conditions satisfied by the constrained TCMT parameters (i.e., γ_{1e} , γ_{2e} , t_1 , and t_2) are expressible as real analytic functions of the TCMT parameters set to zero, then these constrained TCMT parameters themselves become real analytic functions of the remaining unconstrained TCMT parameters. This occurs provided the Jacobian determinant related to these conditions is nonvanishing [177], which is generally true, and we assume to be the case.

Evidently, this IFT is applicable to our choice of γ_{2e} . This is because, from Eq. (F.20), γ_{2e} is an explicit, real-analytic function of γ_0 and T_s (for $T_s \neq 0$). To apply the IFT for real analytic functions to γ_{1e} , t_1 , and t_2 , we recall that η is a real analytic function of all TCMT parameters, as argued in this section. Thus, the derivatives of η with respect to γ_{1e} , t_1 , and t_2 are each also real analytic functions of the TCMT parameters [176]. So setting these derivatives η to zero (i.e., extremizing η with respect to these variables) satisfies the hypothesis of the IFT for real analytic functions. Thus, from the IFT, the constrained TCMT parameters are real analytic functions of the unconstrained TCMT parameters. Finally, because η is a real analytic function of all TCMT parameters before maximizing it with respect to the constrained parameters; then η becomes a real analytic function of the unconstrained TCMT parameters after maximization with respect to the constrained TCMT parameters. This follows because the composition of real

analytic functions is real analytic [176]. This explains why the CAFC efficiency η behaves numerically as a real analytic function of the remaining TCMT variables, and thus, of the dimensionless variables $|\kappa/\Delta_0|$, $\gamma_0 T_s$, and $\gamma_0 T_s$.

Appendix H

Efficiency limit of serial AFC

In this appendix, we analyze the energy efficiency of two instances of single-ring AFC in series, i.e., serial AFC. Our objective is to determine the upper limit to the efficiency of serial AFC.

To do this, we first note that the form of the output of the first instance of single-ring AFC is fixed, and that this output is the input of the second instance of single-ring AFC. Let us denote the former by $s_{\text{out}}^{(1)}(t)$ and the latter by $s_{\text{in}}^{(2)}(t)$. According to Chapter 6, these are given by

$$s_{\text{in}}^{(2)}(t) = s_{\text{out}}^{(1)}(t) = \sqrt{2\gamma_1\mu_1 E_{\text{in}}} \exp[-\gamma_1(t-t_1)] \Theta(t-t_1). \quad (\text{H.1})$$

In (H.1), γ_1 is the total decay rate of the first ring; μ_1 , the efficiency of the first instance of AFC; E_{in} , the energy of the input pulse incident on the first ring; and t_1 , the time of modulation of the first ring. As in Chapters 6 to 8 and Appendix E, $\Theta(t)$ is the Heaviside step function. Without loss of generality, we take the output frequency of the first instance of AFC as zero.

From Chapter 6, the output energy E_{out} of the second stage of AFC is given by

$$E_{\text{out}} = (\gamma_e/\gamma_2) |a_2(t_2)|^2. \quad (\text{H.2})$$

In Eq. (H.2), γ_e is the decay rate of the second ring into the bus waveguide; $\gamma_2 \geq \gamma_e$, the total decay rate of the second ring; and $a_2(t_2)$, the energy-normalized amplitude of the field in the second ring at the time t_2 when AFC is induced on the second ring. From Chapter 6, $a_2(t_2)$ is given by

$$a_2(t_2) = \sqrt{2\gamma_e} \int_{-\infty}^{t_2} dt \exp[-\gamma_2(t_2-t)] s_{\text{in}}^{(2)}(t). \quad (\text{H.3})$$

In Eq. (H.3), we assume that the second ring is resonant with the frequency-shifted output of the first ring. It is intuitive and straightforward to show that this maximizes E_{out} with respect to the detuning between $s_{\text{out}}^{(1)}(t)$ and the second ring's resonance frequency. The energy efficiency $\eta \equiv E_{\text{out}}/E_{\text{in}}$ of serial AFC can be evaluated substituting Eq. (H.1) into Eq. (H.3), and Eq. (H.3) into Eq. (H.2). In this way, we obtain

$$\eta = \mu_1 \mu_2. \quad (\text{H.4})$$

In Eq. (H.4), as in Eq. (H.1), μ_1 is the efficiency of the first instance of single-ring AFC. Analogously, μ_2 is that of the second instance of single-ring AFC.

Given Eq. (H.1) to Eq. (H.3), it is straightforward to extremize μ_2 (and thus η) with respect to the parameters governing the second single-ring AFC, i.e., γ_2 , γ_e and t_2 . Subject to the condition of non-vanishing intrinsic loss $0 \leq \gamma_e \leq \gamma_2$, we thus find that μ_2 has the maximum

$$\mu_2 = 4e^{-2} \approx 0.5413, \quad (\text{H.5})$$

and that Eq. (H.5) is attained when

$$\begin{aligned} \gamma_2 &= \gamma_1, \\ \gamma_e &= \gamma_1, \\ t_2 &= t_1 + \gamma_1^{-1}. \end{aligned} \quad (\text{H.6})$$

Bibliography

- [1] Bahaa E. A. Saleh and Malvin Carl Teich. *Fundamentals of photonics*. Wiley series in pure and applied optics. Wiley, Hoboken, NJ, USA, third edition, 2019.
- [2] Amnon Yariv and Pochi Yeh. *Photonics: Optical Electronics in Modern Communications*. The Oxford series in electrical and computer engineering. Oxford University Press, New York, sixth edition, 2007.
- [3] Robert W. Boyd. *Nonlinear optics*. Elsevier, San Diego, fourth edition, 2020.
- [4] Amy C Turner-Foster, Mark A Foster, Reza Salem, Alexander L Gaeta, and Michal Lipson. Frequency conversion over two-thirds of an octave in silicon nanowaveguides. *Optics Express*, 18(3):1904–1908, 2010.
- [5] Qiang Lin, Jidong Zhang, Philippe M Fauchet, and Govind P Agrawal. Ultrabroadband parametric generation and wavelength conversion in silicon waveguides. *Optics Express*, 14(11):4786–4799, 2006.
- [6] Walid Mathlouthi, Haisheng Rong, and Mario Paniccia. Characterization of efficient wavelength conversion by four-wave mixing in sub-micron silicon waveguides. *Optics Express*, 16(21):16735–16745, 2008.
- [7] Sanja Zlatanovic, Jung S Park, Slaven Moro, Jose M Chavez Boggio, Ivan B Divliansky, Nikola Alic, Shayan Mookherjea, and Stojan Radic. Mid-infrared wavelength conversion in silicon waveguides using ultracompact telecom-band-derived pump source. *Nature Photonics*, 4(8):561–564, 2010.
- [8] Mian Zhang, Cheng Wang, Yaowen Hu, Amirhassan Shams-Ansari, Tianhao Ren, Shanhui Fan, and Marko Lončar. Electronically programmable photonic molecule. *Nature Photonics*, 13(1):36–40, 2019.
- [9] Richarda Soref and Brianr Bennett. Electrooptical effects in silicon. *IEEE Journal of Quantum Electronics*, 23(1):123–129, 1987.
- [10] Stefan F Preble, Qianfan Xu, and Michal Lipson. Changing the colour of light in a silicon resonator. *Nature Photonics*, 1(5):293–296, 2007.
- [11] Di Zhu, Linbo Shao, Mengjie Yu, Rebecca Cheng, Boris Desiatov, CJ Xin, Yaowen Hu, Jeffrey Holzgrafe, Soumya Ghosh, Amirhassan Shams-Ansari, et al. Integrated photonics on thin-film lithium niobate. *Advances in Optics and Photonics*, 13(2):242–352, 2021.
- [12] Masayuki Izutsu, Shinsuke Shikama, and Tadasi Sueta. Integrated optical ssb modulator/frequency shifter. *IEEE Journal of Quantum Electronics*, 17(11):2225–2227, 1981.
- [13] Hsin-Pin Lo and Hiroki Takesue. Precise tuning of single-photon frequency using an optical single sideband modulator. *Optica*, 4(8):919–923, 2017.
- [14] Masayuki Izutsu and Tadasi Sueta. Coupled mode analysis of light modulation in dielectric waveguides. *Applied Physics*, 5:307–315, 1975.
- [15] Linran Fan, Chang-Ling Zou, Menno Poot, Risheng Cheng, Xiang Guo, Xu Han, and Hong X Tang. Integrated optomechanical single-photon frequency shifter. *Nature Photonics*, 10(12):766–770, 2016.
- [16] Laura J Wright, Michał Karpiński, Christoph Söller, and Brian J Smith. Spectral shearing of quantum light pulses by electro-optic phase modulation. *Physical Review Letters*, 118(2):023601, 2017.

- [17] M Bruel. Silicon on insulator material technology. *Electronics Letters*, 31(14):1201–1202, 1995.
- [18] Momchil Minkov, Yu Shi, and Shanhui Fan. Exact solution to the steady-state dynamics of a periodically modulated resonator. *APL Photonics*, 2(7):076101, 2017.
- [19] Yaowen Hu, Mengjie Yu, Di Zhu, Neil Sinclair, Amirhassan Shams-Ansari, Linbo Shao, Jeffrey Holzgrafe, Eric Puma, Mian Zhang, and Marko Lončar. On-chip electro-optic frequency shifters and beam splitters. *Nature*, 599(7886):587–593, 2021.
- [20] L. Allen and J. H. Eberly. *Optical resonance and two-level atoms*. Interscience monographs and texts in physics and astronomy. Wiley, New York, 1975.
- [21] Claude Cohen-Tannoudji, Bernard Diu, and Franck Laloë. *Quantum mechanics*. Wiley, New York, 1977.
- [22] Masaya Notomi and Satoshi Mitsugi. Wavelength conversion via dynamic refractive index tuning of a cavity. *Physical Review A*, 73(5):051803, 2006.
- [23] Brian A Daniel, Drew N Maywar, and Govind P Agrawal. Dynamic mode theory of optical resonators undergoing refractive index changes. *Journal of the Optical Society of America B*, 28(9):2207–2215, 2011.
- [24] Mehmet F Yanik and Shanhui Fan. Dynamic photonic structures: stopping, storage, and time reversal of light. *Studies in Applied Mathematics*, 115(2):233–253, 2005.
- [25] Wolfgang Pauli. *Statistical mechanics*. Pauli lectures on physics. Dover Publications, Mineola, New York, 1973.
- [26] Herbert Goldstein, Charles Poole, and John Safko. *Classical mechanics*. Addison Wesley, San Francisco, third edition, 2002.
- [27] Po Dong, Stefan F Preble, Jacob T Robinson, Sasikanth Manipatruni, and Michal Lipson. Inducing photonic transitions between discrete modes in a silicon optical microcavity. *Physical Review Letters*, 100(3):033904, 2008.
- [28] Takasumi Tanabe, Eiichi Kuramochi, Hideaki Taniyama, and Masaya Notomi. Electro-optic adiabatic wavelength shifting and Q switching demonstrated using a pin integrated photonic crystal nanocavity. *Optics Letters*, 35(23):3895–3897, 2010.
- [29] Stefan Preble, Liang Cao, Ali Elshaari, Abdelsalam Aboketaf, and Donald Adams. Single photon adiabatic wavelength conversion. *Applied Physics Letters*, 101(17):171110, 2012.
- [30] Takasumi Tanabe, Masaya Notomi, Hideaki Taniyama, and Eiichi Kuramochi. Dynamic release of trapped light from an ultrahigh-Q nanocavity via adiabatic frequency tuning. *Physical Review Letters*, 102(4):043907, 2009.
- [31] Ryotaro Konoike, Haruyuki Nakagawa, Masahiro Nakadai, Takashi Asano, Yoshinori Tanaka, and Susumu Noda. On-demand transfer of trapped photons on a chip. *Science Advances*, 2(5):e1501690, 2016.
- [32] Nicholas Karl, Polina P Vabishchevich, Maxim R Shcherbakov, Sheng Liu, Michael B Sinclair, Gennady Shvets, and Igal Brener. Frequency conversion in a time-variant dielectric metasurface. *Nano Letters*, 20(10):7052–7058, 2020.
- [33] Wataru Yoshiki, Yoshihiro Honda, Misako Kobayashi, Tomohiro Tetsumoto, and Takasumi Tanabe. Kerr-induced controllable adiabatic frequency conversion in an ultrahigh Q silica toroid microcavity. *Optics Letters*, 41(23):5482–5485, 2016.
- [34] Yannick Minet, Luis Reis, Jan Szabados, Christoph S Werner, Hans Zappe, Karsten Buse, and Ingo Breunig. Pockels-effect-based adiabatic frequency conversion in ultrahigh-Q microresonators. *Optics Express*, 28(3):2939–2947, 2020.
- [35] Andrea Guarino, Gorazd Poberaj, Daniele Rezzonico, Riccardo Degl’Innocenti, and Peter Günter. Electro-optically tunable microring resonators in lithium niobate. *Nature Photonics*, 1(7):407–410, 2007.

- [36] Li Chen, Qiang Xu, Michael G Wood, and Ronald M Reano. Hybrid silicon and lithium niobate electro-optical ring modulator. *Optica*, 1(2):112–118, 2014.
- [37] Cheng Wang, Mian Zhang, Brian Stern, Michal Lipson, and Marko Lončar. Nanophotonic lithium niobate electro-optic modulators. *Optics Express*, 26(2):1547–1555, 2018.
- [38] Mian Zhang, Brandon Buscaino, Cheng Wang, Amirhassan Shams-Ansari, Christian Reimer, Rongrong Zhu, Joseph M Kahn, and Marko Lončar. Broadband electro-optic frequency comb generation in a lithium niobate microring resonator. *Nature*, 568(7752):373–377, 2019.
- [39] Brandon Buscaino, Mian Zhang, Marko Lončar, and Joseph M Kahn. Design of efficient resonator-enhanced electro-optic frequency comb generators. *Journal of Lightwave Technology*, 38(6):1400–1413, 2020.
- [40] Jeffrey Holzgrafe, Neil Sinclair, Di Zhu, Amirhassan Shams-Ansari, Marco Colangelo, Yaowen Hu, Mian Zhang, Karl K Berggren, and Marko Lončar. Cavity electro-optics in thin-film lithium niobate for efficient microwave-to-optical transduction. *Optica*, 7(12):1714–1720, 2020.
- [41] Mohammad Soltani, Mian Zhang, Colm Ryan, Guilhem J Ribeill, Cheng Wang, and Marko Loncar. Efficient quantum microwave-to-optical conversion using electro-optic nanophotonic coupled resonators. *Physical Review A*, 96(4):043808, 2017.
- [42] Yaowen Hu, Christian Reimer, Amirhassan Shams-Ansari, Mian Zhang, and Marko Loncar. Realization of high-dimensional frequency crystals in electro-optic microcombs. *Optica*, 7(9):1189–1194, 2020.
- [43] Xiaotong He, Luis Cortes-Herrera, Kwadwo Opong-Mensah, Yi Zhang, Meiting Song, Govind P Agrawal, and Jaime Cardenas. Electrically induced adiabatic frequency conversion in an integrated lithium niobate ring resonator. *Optics Letters*, 47(22):5849–5852, 2022.
- [44] Zeno Gaburro, Mher Ghulinyan, Francesco Riboli, Lorenzo Pavesi, Alessio Recati, and Iacopo Carusotto. Photon energy lifter. *Optics Express*, 14(16):7270–7278, 2006.
- [45] Wesley D Sacher and Joyce KS Poon. Dynamics of microring resonator modulators. *Optics Express*, 16(20):15741–15753, 2008.
- [46] Yuzhe Xiao, Govind P Agrawal, and Drew N Maywar. Spectral and temporal changes of optical pulses propagating through time-varying linear media. *Optics Letters*, 36(4):505–507, 2011.
- [47] Yuzhe Xiao, Drew N Maywar, and Govind P Agrawal. Optical pulse propagation in dynamic Fabry–Perot resonators. *Journal of the Optical Society of America B*, 28(7):1685–1692, 2011.
- [48] Brian A Daniel, Drew N Maywar, and Govind P Agrawal. Efficient adiabatic wavelength conversion in Gires–Tournois resonators. *Optics Letters*, 36(21):4155–4157, 2011.
- [49] Maxim R Shcherbakov, Pavel Shafirin, and Gennady Shvets. Overcoming the efficiency-bandwidth tradeoff for optical harmonics generation using nonlinear time-variant resonators. *Physical Review A*, 100(6):063847, 2019.
- [50] Momchil Minkov and Shanhui Fan. Localization and time-reversal of light through dynamic modulation. *Physical Review B*, 97(6):060301, 2018.
- [51] Athanasios Papoulis. Maximum response with input energy constraints and the matched filter principle. *IEEE Transactions on Circuit Theory*, 17(2):175–182, 1970.
- [52] Athanasios Papoulis. *Signal Analysis*. McGraw-Hill, New York, 1977.
- [53] H Haus, W Huang, S Kawakami, and N Whitaker. Coupled-mode theory of optical waveguides. *Journal of Lightwave Technology*, 5(1):16–23, 1987.
- [54] Wei-Ping Huang. Coupled-mode theory for optical waveguides: an overview. *Journal of the Optical Society of America A*, 11(3):963–983, 1994.

- [55] Dietrich Marcuse. *Theory of dielectric optical waveguides*. Quantum electronics—principles and applications. Academic Press, Boston, 2nd edition, 1991.
- [56] Steven G Johnson, Mihai Ibanescu, M Skorobogatiy, Ori Weisberg, Torkel D Engeness, Marin Soljačić, Steven A Jacobs, JD Joannopoulos, and Yoel Fink. Low-loss asymptotically single-mode propagation in large-core OmniGuide fibers. *Optics Express*, 9(13):748–779, 2001.
- [57] Maksim Skorobogatiy, Mihai Ibanescu, Steven G Johnson, Ori Weisberg, Torkel D Engeness, Marin Soljačić, Steven A Jacobs, and Yoel Fink. Analysis of general geometric scaling perturbations in a transmitting waveguide: fundamental connection between polarization-mode dispersion and group-velocity dispersion. *Journal of the Optical Society of America B*, 19(12):2867–2875, 2002.
- [58] Brian Adam Daniel. *Nonlinear photonic devices with subwavelength dimensions*. PhD thesis, University of Rochester, Rochester, New York, 2012.
- [59] Dietrich Marcuse. Coupled-mode theory for anisotropic optical waveguides. *The Bell System Technical Journal*, 54(6):985–995, 1975.
- [60] Dietrich Marcuse. *Light transmission optics*. Van Nostrand Reinhold electrical/computer science and engineering series. Van Nostrand Reinhold, New York, 2nd edition, 1982.
- [61] Clifford R. Pollock and Michal. Lipson. *Integrated photonics*. Kluwer Academic, Boston, 2003.
- [62] KJ Blow, Rodney Loudon, Simon JD Phoenix, and TJ Shepherd. Continuum fields in quantum optics. *Physical Review A*, 42(7):4102, 1990.
- [63] Rodney. Loudon. *The quantum theory of light*. Oxford University Press, Oxford, 3rd edition, 2000.
- [64] Amnon Yariv. Coupled-mode theory for guided-wave optics. *IEEE Journal of Quantum Electronics*, 9(9):919–933, 1973.
- [65] Hermann A Haus and Weiping Huang. Coupled-mode theory. *Proceedings of the IEEE*, 79(10):1505–1518, 1991.
- [66] John David Jackson. *Classical electrodynamics*. Wiley, New York, 3rd edition, 1999.
- [67] Max Born and Emil Wolf. *Principles of optics*. Cambridge University Press, Cambridge, seventh (expanded) edition, 2019.
- [68] Rowland A Sammut. Orthogonality and normalization of radiation modes in dielectric waveguides. *Journal of the Optical Society of America*, 72(10):1335–1337, 1982.
- [69] Athanasios Papoulis. *The Fourier integral and its applications*. McGraw-Hill electronic science series. McGraw-Hill, New York, 1962.
- [70] Albert. Messiah. *Quantum mechanics*. North-Holland Pub. Co., Amsterdam, 1961.
- [71] Benyamin Ghojogh, Fakhri Karray, and Mark Crowley. Eigenvalue and generalized eigenvalue problems: Tutorial. *arXiv preprint arXiv:1903.11240*, 2019.
- [72] Joshua N Winn, Shanhui Fan, John D Joannopoulos, and Erich P Ippen. Interband transitions in photonic crystals. *Physical Review B*, 59(3):1551, 1999.
- [73] N Malkova, S Kim, and V Gopalan. Jahn-Teller effect in two-dimensional photonic crystals. *Physical Review B*, 68(4):045105, 2003.
- [74] John D. Joannopoulos, Steven G. Johnson, and Joshua Winn. *Photonic Crystals : Molding the Flow of Light*. Princeton University Press, Princeton, NJ, 2nd edition, 2011.
- [75] Hermann A. Haus. *Waves and Fields in Optoelectronics*. Prentice-Hall series in solid state physical electronics. Prentice-Hall, Englewood Cliffs, NJ, 1984.

- [76] Brent E Little, Sai T Chu, Hermann A Haus, J. Foresi, and J.-P. Laine. Microring resonator channel dropping filters. *Journal of lightwave technology*, 15(6):998–1005, 1997.
- [77] C Manolatou, MJ Khan, Shanhui Fan, Pierre R Villeneuve, HA Haus, and JD Joannopoulos. Coupling of modes analysis of resonant channel add-drop filters. *IEEE Journal of Quantum Electronics*, 35(9):1322–1331, 1999.
- [78] Shanhui Fan, Wonjoo Suh, and John D Joannopoulos. Temporal coupled-mode theory for the Fano resonance in optical resonators. *Journal of the Optical Society of America A*, 20(3):569–572, 2003.
- [79] Wonjoo Suh, Zheng Wang, and Shanhui Fan. Temporal coupled-mode theory and the presence of non-orthogonal modes in lossless multimode cavities. *IEEE Journal of Quantum Electronics*, 40(10):1511–1518, 2004.
- [80] Neil W. Ashcroft and N. David Mermin. *Solid state physics*. Holt, Rinehart and Winston, New York, 1976.
- [81] Crispin W Gardiner and Matthew J Collett. Input and output in damped quantum systems: Quantum stochastic differential equations and the master equation. *Physical Review A*, 31(6):3761, 1985.
- [82] D. F. Walls and Gerard J. Milburn. *Quantum optics*. Springer, Berlin, second edition, 2008.
- [83] Dibyendu Roy, Christopher M Wilson, and Ofer Firstenberg. Colloquium: Strongly interacting photons in one-dimensional continuum. *Reviews of Modern Physics*, 89(2):021001, 2017.
- [84] Shanhui Fan, Şükür Ekin Kocabaş, and Jung-Tsung Shen. Input-output formalism for few-photon transport in one-dimensional nanophotonic waveguides coupled to a qubit. *Physical Review A*, 82(6):063821, 2010.
- [85] V Weisskopf and E Wigner. Berechnung der natürlichen Linienbreite auf Grund der Diracschen Lichttheorie. *Zeitschrift für Physik*, 63:54–73, 1930.
- [86] Emanuele Galiffi, Romain Tirole, Shixiong Yin, Huanan Li, Stefano Vezzoli, Paloma A Huidobro, Mário G Silveirinha, Riccardo Sapienza, Andrea Alù, and John B Pendry. Photonics of time-varying media. *Advanced Photonics*, 4(1):014002–014002, 2022.
- [87] Julius Adams Stratton. *Electromagnetic theory*. International series in physics. McGraw-Hill book company, inc., New York, 1941.
- [88] Stefan F Preble and Michal Lipson. Conversion of a signal wavelength in a dynamically tuned resonator. In *Integrated Photonics Research and Applications*, page IMC5. Optica Publishing Group, 2006.
- [89] William H. Louisell. *Quantum statistical properties of radiation*. Wiley series in pure and applied optics. Wiley, New York, 1973.
- [90] Marlan O. Scully and M. Suhail Zubairy. *Quantum optics*. Cambridge University Press, Cambridge, 1997.
- [91] Ronald Newbold Bracewell. *The Fourier transform and its applications*. McGraw-Hill series in electrical and computer engineering. Circuits and systems. McGraw Hill, Boston, 3rd edition, 2000.
- [92] Govind P. Agrawal. *Fiber-optic communication systems*. Wiley series in microwave and optical engineering. Wiley, Hoboken, N.J, 5th edition, 2014.
- [93] Govind P. Agrawal. *Nonlinear Fiber Optics*. Academic Press, London, England, sixth edition, 2019.
- [94] An Pan, Changran Hu, Cheng Zeng, and Jinsong Xia. Fundamental mode hybridization in a thin film lithium niobate ridge waveguide. *Optics Express*, 27(24):35659–35669, 2019.
- [95] DP Gia Russo and JH Harris. Wave propagation in anisotropic thin-film optical waveguides. *Journal of the Optical Society of America*, 63(2):138–145, 1973.
- [96] RA Steinberg and TG Giallorenzi. Modal fields of anisotropic channel waveguides. *Journal of the Optical Society of America*, 67(4):523–533, 1977.

- [97] Dietrich Marcuse and Ivan Kaminow. Modes of a symmetric slab optical waveguide in birefringent media - Part II: Slab with coplanar optical axis. *IEEE Journal of Quantum Electronics*, 15(2):92–101, 1979.
- [98] Andre Knoesen, Thomas K Gaylord, and MG Moharam. Hybrid guided modes in uniaxial dielectric planar waveguides. *Journal of Lightwave Technology*, 6(6):1083–1104, 1988.
- [99] Weijun Liao, Xianfeng Chen, Yuping Chen, Yuxing Xia, and Yingli Chen. Explicit analysis of anisotropic planar waveguides by the analytical transfer-matrix method. *Journal of the Optical Society of America A*, 21(11):2196–2204, 2004.
- [100] M Lu and MM Fejer. Anisotropic dielectric waveguides. *Journal of the Optical Society of America A*, 10(2):246–261, 1993.
- [101] Charles Vassallo. *Optical waveguide concepts*. Optical wave sciences and technology. Elsevier, Amsterdam, 1991.
- [102] Nagayoshi Morita and R Yamada. Electromagnetic fields in circular bends of slab waveguides. *Journal of lightwave technology*, 8(1):16–22, 1990.
- [103] KR Hiremath, Manfred Hammer, Remco Stoffer, L Prkna, and J Čtyroký. Analytic approach to dielectric optical bent slab waveguides. *Optical and quantum electronics*, 37:37–61, 2005.
- [104] Jon H Shirley. Solution of the Schrödinger equation with a Hamiltonian periodic in time. *Physical Review*, 138(4B):B979, 1965.
- [105] Dietrich Marcuse. Modes of a symmetric slab optical waveguide in birefringent media - Part I: Optical axis not in plane of slab. *IEEE Journal of Quantum Electronics*, 14(10):736–741, 1978.
- [106] Jay N. Damask. *Polarization Optics in Telecommunications*. Springer Series in Optical Sciences, 101. Springer New York, New York, NY, 1st edition, 2005.
- [107] Qiang Lin and Govind P Agrawal. Vector theory of four-wave mixing: polarization effects in fiber-optic parametric amplifiers. *Journal of the Optical Society of America B*, 21(6):1216–1224, 2004.
- [108] MP Silveri, JA Tuorila, EV Thuneberg, and GS Paraoanu. Quantum systems under frequency modulation. *Reports on Progress in Physics*, 80(5):056002, 2017.
- [109] George B. Arfken and Hans J. Weber. *Mathematical methods for physicists*. Elsevier Academic Press, San Diego, 6th edition, 2005.
- [110] Jun John Sakurai and Jim Napolitano. *Modern quantum mechanics*. Addison-Wesley, Boston, 2nd edition, 2011.
- [111] David J. Griffiths. *Introduction to quantum mechanics*. Pearson Prentice Hall, Upper Saddle River, NJ, 2nd edition, 2005.
- [112] AC Aguiar Pinto, MC Nemes, JG Peixoto de Faria, and MT Thomaz. Comment on the adiabatic condition. *American Journal of Physics*, 68(10):955–958, 2000.
- [113] Michael Victor Berry. Quantal phase factors accompanying adiabatic changes. *Proceedings of the Royal Society of London. A. Mathematical and Physical Sciences*, 392(1802):45–57, 1984.
- [114] Dwight W Berreman. Optics in stratified and anisotropic media: 4×4 -matrix formulation. *Journal of the Optical Society of America*, 62(4):502–510, 1972.
- [115] WK Burns and J Warner. Mode dispersion in uniaxial optical waveguides. *Journal of the Optical Society of America*, 64(4):441–446, 1974.
- [116] Luis Cortes-Herrera, Xiaotong He, Jaime Cardenas, and Govind P Agrawal. Coupled-mode theory of the polarization dynamics inside a microring resonator with a uniaxial core. *Physical Review A*, 103(6):063517, 2021.

- [117] Archana Kaushalram, Gopalkrishna Hegde, and Srinivas Talabattula. Mode hybridization analysis in thin film lithium niobate strip multimode waveguides. *Scientific Reports*, 10(1):1–13, 2020.
- [118] Jingyi Wang, Pengxin Chen, Daoxin Dai, and Liu Liu. Polarization coupling of X-cut thin film lithium niobate based waveguides. *IEEE Photonics Journal*, 12(3):1–10, 2020.
- [119] Emi Saitoh, Yuki Kawaguchi, Kunimasa Saitoh, and Masanori Koshiba. TE/TM-pass polarizer based on lithium niobate on insulator ridge waveguide. *IEEE Photonics Journal*, 5(2):6600610–6600610, 2013.
- [120] Yang Liu, Xingrui Huang, Zezheng Li, Yingxin Kuang, Huan Guan, Qingquan Wei, Zhongchao Fan, and Zhiyong Li. TE/TM-pass polarizers based on lateral leakage in a thin film lithium niobate–silicon nitride hybrid platform. *Optics Letters*, 45(17):4915–4918, 2020.
- [121] Zisu Gong, Rui Yin, Wei Ji, Junbao Wang, Chonghao Wu, Xiao Li, and Shicheng Zhang. Optimal design of DC-based polarization beam splitter in lithium niobate on insulator. *Optics Communications*, 396:23–27, 2017.
- [122] Hongnan Xu, Daoxin Dai, Liu Liu, and Yaocheng Shi. Proposal for an ultra-broadband polarization beam splitter using an anisotropy-engineered mach-zehnder interferometer on the X-cut lithium-niobate-on-insulator. *Optics Express*, 28(8):10899–10908, 2020.
- [123] L Zhang, X Fu, and L Yang. Compact, broadband and low-loss polarization beam splitter on lithium-niobate-on-insulator using a silicon nanowire assisted waveguide. *IEEE Photonics Journal*, 12(5):1–6, 2020.
- [124] Jean Schollhammer, Mohammad Amin Baghban, and Katia Gallo. Modal birefringence-free lithium niobate waveguides. *Optics Letters*, 42(18):3578–3581, 2017.
- [125] Archana Kaushalram and Srinivas Talabattula. Zero-birefringence dual mode waveguides and polarization-independent two-mode (de) multiplexer on thin film lithium niobate. *Optics Communications*, 500:127334, 2021.
- [126] Guang Yang, Alexander V Sergienko, and Abdoulaye Ndao. Tunable polarization mode conversion using thin-film lithium niobate ridge waveguide. *Optics Express*, 29(12):18565–18571, 2021.
- [127] Tzyy-Jiann Wang and Yu-Chen Cheng. Integrated-optic polarization rotator with obliquely deposited columnar thin film. *Optics Express*, 20(1):601–606, 2012.
- [128] A Donaldson and KK Wong. Phase-matched mode convertor in LiNbO₃ using near-Z-axis propagation. *Electronics Letters*, 25(23):1378–1379, 1987.
- [129] Jiří Čtyroký. Analysis of polarization effects in near-Z-axis Ti: LiNbO₃ devices. *Journal of Optical Communications*, 14(1):32–38, 1993.
- [130] S Bhandare, R Noé, and D Sandel. Origin of reciprocal circular birefringence observed in X-cut, Z-propagation LiNbO₃ polarization transformers. *Applied Physics B*, 73:549–553, 2001.
- [131] Jeffrey D Bull and Nicolas AF Jaeger. Parasitic mode conversion in Z-propagating lithium-niobate waveguides. *Journal of Lightwave Technology*, 25(1):387–393, 2007.
- [132] Andrei V Tsarev. New compact polarization rotator in anisotropic LiNbO₃ graded-index waveguide. *Optics Express*, 16(3):1653–1658, 2008.
- [133] John Heebner, Rohit Grover, and Tarek Ibrahim. *Optical Microresonators: Theory, Fabrication, and Applications*. Springer series in optical sciences. Springer, New York, NY, 2007.
- [134] Vien Van. *Optical Microring Resonators: Theory, Techniques, and Applications*. Series in Optics and Optoelectronics. CRC Press, 2016.
- [135] Sadri Hassani. *Mathematical Physics: A Modern Introduction to Its Foundations*. Springer International Publishing, Cham, Switzerland, 2nd edition, 2013.

- [136] Viktor S Asadchy, Mohammad Sajjad Mirmoosa, Ana Díaz-Rubio, Shanhui Fan, and Sergei A Tretyakov. Tutorial on electromagnetic nonreciprocity and its origins. *Proceedings of the IEEE*, 108(10):1684–1727, 2020.
- [137] Fredric J Harris. On the use of windows for harmonic analysis with the discrete fourier transform. *Proceedings of the IEEE*, 66(1):51–83, 1978.
- [138] E. Oran Brigham. *The Fast Fourier Transform and its Applications*. Prentice-Hall signal processing series. Prentice Hall, Englewood Cliffs, N.J, 1988.
- [139] Charles K Alexander and Matthew N.O. Sadiku. *Fundamentals of electric circuits*. McGraw-Hill, New York, fifth edition, 2013.
- [140] Luis Cortes-Herrera, Xiaotong He, Jaime Cardenas, and Govind P Agrawal. Optimization of adiabatic frequency conversion in an all-pass resonator. *Physical Review A*, 106(2):023517, 2022.
- [141] Govind P. Agrawal. *Lightwave technology : telecommunication systems*. Wiley-Interscience, Hoboken, N.J, 2005.
- [142] Roger A. Horn and Charles R. Johnson. *Matrix analysis*. Cambridge University Press, Cambridge, 1985.
- [143] Gilbert W. Stewart and Ji-guang Sun. *Matrix perturbation theory*. Computer science and scientific computing. Academic Press, Boston, 1990.
- [144] Lloyd N. Trefethen and David Bau. *Numerical linear algebra*. Society for Industrial and Applied Mathematics, Philadelphia, 1997.
- [145] Stephen T. Thornton and Jerry B. Marion. *Classical dynamics of particles & systems*. Thomson Learning Inc., San Diego, fifth edition, 2004.
- [146] Vernon Barger and Martin Olsson. *Classical mechanics: a modern perspective*. McGraw-Hill, Inc., second edition, 1995.
- [147] Tosio Kato. *Perturbation Theory for Linear Operators*. Classics in Mathematics, 132. Springer Berlin Heidelberg, Berlin, Heidelberg, 2nd edition, 1995.
- [148] Mohammad-Ali Miri and Andrea Alu. Exceptional points in optics and photonics. *Science*, 363(6422):eaar7709, 2019.
- [149] Jan Wiersig. Review of exceptional point-based sensors. *Photonics Research*, 8(9):1457–1467, 2020.
- [150] Aodong Li, Heng Wei, Michele Cotrufo, Weijin Chen, Sander Mann, Xiang Ni, Bingcong Xu, Jianfeng Chen, Jian Wang, Shanhui Fan, et al. Exceptional points and non-Hermitian photonics at the nanoscale. *Nature Nanotechnology*, pages 1–15, 2023.
- [151] Brian C. Hall. *Lie groups, Lie algebras, and representations : an elementary introduction*. Graduate texts in mathematics, 222. Springer, Cham, second edition, 2015.
- [152] Richard P Feynman, Frank L Vernon Jr, and Robert W Hellwarth. Geometrical representation of the Schrödinger equation for solving maser problems. *Journal of Applied Physics*, 28(1):49–52, 1957.
- [153] N Frigo. A generalized geometrical representation of coupled mode theory. *IEEE journal of Quantum Electronics*, 22(11):2131–2140, 1986.
- [154] Govind P. Agrawal. *Fiber-optic communication systems*. Wiley series in microwave and optical engineering. Wiley, Hoboken, NJ, fifth edition, 2022.
- [155] Kuo-Liang Chen and Shyh Wang. Cross-talk problems in optical directional couplers. *Applied Physics Letters*, 44(2):166–168, 1984.
- [156] HA Haus and NA Whitaker. Elimination of cross talk in optical directional couplers. *Applied Physics Letters*, 46(1):1–3, 1985.

- [157] Amos Hardy and William Streifer. Coupled mode theory of parallel waveguides. *Journal of Lightwave Technology*, 3(5):1135–1146, 1985.
- [158] Shun-Lien Chuang. A coupled mode formulation by reciprocity and a variational principle. *Journal of Lightwave Technology*, 5(1):5–15, 1987.
- [159] William Streifer, Marek Osinski, and Amos Hardy. Reformulation of the coupled-mode theory of multiwaveguide systems. *Journal of Lightwave Technology*, 5(1):1–4, 1987.
- [160] Charles Vassallo. About coupled-mode theories for dielectric waveguides. *Journal of Lightwave Technology*, 6(2):294–303, 1988.
- [161] AW Snyder and A Ankiewicz. Fibre couplers composed of unequal cores. *Electronics Letters*, 22(23):1237–1238, 1986.
- [162] Hermann A Haus, Wei-Ping Huang, and Allan W Snyder. Coupled-mode formulations. *Optics Letters*, 14(21):1222–1224, 1989.
- [163] Enrique A.J. Marcetili. Dielectric rectangular waveguide and directional coupler for integrated optics. *The Bell System Technical Journal*, 48(7):2071–2102, 1969.
- [164] Denis G Baranov, Alex Krasnok, and Andrea Alu. Coherent virtual absorption based on complex zero excitation for ideal light capturing. *Optica*, 4(12):1457–1461, 2017.
- [165] G Trainiti, Y Ra’di, M Ruzzene, and A Alù. Coherent virtual absorption of elastodynamic waves. *Science Advances*, 5(8):eaaw3255, 2019.
- [166] Younes Ra’di, Alex Krasnok, and Andrea Alù. Virtual critical coupling. *ACS Photonics*, 7(6):1468–1475, 2020.
- [167] Jakob Hinney, Seunghwi Kim, Graydon JK Flatt, Ipshita Datta, Andrea Alù, and Michal Lipson. Efficient excitation and control of integrated photonic circuits with virtual critical coupling. *Nature Communications*, 15(1):2741, 2024.
- [168] Sophocles J. Orfanidis. Electromagnetic waves and antennas. <https://www.ece.rutgers.edu/~orfanidi/ewa/>, 2016. Accessed: 2024-04-15.
- [169] James Ward Brown and Ruel V. Churchill. *Complex variables and applications*. McGraw-Hill Higher Education, Boston, 7th edition, 2004.
- [170] Alberto Leon-Garcia. *Probability and random processes for electrical engineering*. Addison-Wesley, Reading, Mass, 2nd edition, 1994.
- [171] Richard L. Burden and J. Douglas Faires. *Numerical analysis*. Thomson Brooks/Cole, Belmont, CA, 8th edition, 2005.
- [172] Tom M. Apostol. *Mathematical analysis*. Addison-Wesley series in mathematics. Addison-Wesley, Reading, Mass, 2nd edition, 1974.
- [173] Robert G. Bartle and Donald R. Sherbert. *Introduction to real analysis*. Wiley, Hoboken, NJ, 4th edition, 2011.
- [174] John B. Conway. *Functions of one complex variable*. Graduate texts in mathematics ; 11. Springer-Verlag, New York, 2nd edition, 1978.
- [175] Eberhard Freitag and Rolf Busam. *Complex analysis*. Universitext. Springer, Berlin, 2nd edition, 2009.
- [176] Steven G. Krantz and Harold R. Parks. *A primer of real analytic functions*. Birkhäuser advanced texts. Birkhäuser, Boston, 2nd edition, 2002.
- [177] Steven G. Krantz and Harold R. Parks. *The Implicit Function Theorem History, Theory, and Applications*. Modern Birkhäuser Classics. Springer New York, New York, NY, 1st edition, 2013.